Université catholique de Louvain
Faculté des Sciences appliquées
Laboratoire d'Hyperfréquences

École royale militaire
Faculté Polytechnique
Laboratoire de Traitement d'Images

Accurate Modeling of Ground-Penetrating Radar for Detection and Signature Extraction of Mine-like Targets Buried in Stratified Media

Idesbald van den Bosch

Thesis presented for the Ph.D. degree in Applied Sciences

Jury:

Prof. Jean-Didier Legat (UCL) – Chairman
Prof. Marc Acheroy (ERM) – Supervisor
Prof. Isabelle Huynen (UCL) – Supervisor
Prof. Christophe Craeye (UCL) – Supervision committee
Dr. David Daniels (ERA Technology)
Prof. Christian Pichot (Sophia Antipolis – LEAT)
Prof. Marc Piette (ERM)
Prof. Bart Scheers (ERM)

January 2006

Acknowledgments

This thesis is the first conducted under a joint supervision between the Université catholique de Louvain (UCL) and the Royal Military Academy (RMA). It is also the first thesis conducted at the RMA. I wish to thank both these institutions for their innovative approach of the research and for providing the frame that allowed me to conduct this research. I am also grateful to the Belgian Fund FRIA (Fonds pour la Recherche dans l'Industrie et l'Agriculture), the Belgian NSF (FNRS - Fonds National de la Recherche Scientifique), as well as the Belgian Ministry of Defense for the financial support during these five years. My research work and participations at international conferences would not have been possible without these institutions.

On the personal side, I would like to especially thank my advisors Prof. Isabelle Huynen (UCL) and Prof. Marc Acheroy (RMA) for having supported me so efficiently when times were hard. Their positive suggestions, research advices and restless encouragements have been precious over all those years. Moreover, your mutual collaboration over this work was an example of efficient teamwork aiming at professional results. Please, let other people enjoy it too!

My gratitude also goes to Prof. Christophe Craeye of the telecommunication laboratory at UCL, for his availability as well as deep technical knowledge. It has been a real pleasure to have Christophe as a member of my evaluation committee.

I heartily thank Dr. David Daniels (ERA Technology, UK) and Prof. Christian Pichot (Telecommunication laboratory, Sophia Antipolis, France) for the time they spent reading my thesis as members of the evaluation committee. I daresay your pertinent remarks, backed by years of field expertise, have helped to clarify obscure or imprecise parts of this work. I also thank Prof. Jean-Didier Legat for chairing the evaluation committee.

One of the person that I am probably the most indebted to is Pascal Druyts. I really thank him for his constant availability and interest in problems sometimes

not directly related to his own research interests. His deep understanding of electromagnetic phenomena, alongside his vast scientific culture, have certainly contributed to significantly mark this work. I wish him deserved recognition and success in his own thesis work.

I also wish to thank Dr. Sébastien Lambot for his enthusiastic advices on this research. This work, partly derived from yours, would have been different without you.

I thank the technical staff at the Microwave Laboratory (UCL), especially Robert Platteborze and Pascal Simon, for their invaluable help in setting up some experiments—or even fabricating measurement systems! Who knows what would be possible without people like you ...

I thank my colleagues and friends for the wonderful atmosphere at the Microwave Laboratory (UCL) and at the Signal and Image Center (RMA). I especially thank Dimitri Lederer for his sense of humor and his indefatigable will for playing humiliating (for me) tennis games!

I would like to thank my friends for their joyous presence during those years: Sebouille, Berzingue, John-Eric, Vianney, GC, Carrrro, Fredo, Raphke, and all the others.

Finally, I dedicate this thesis to my family, to which I would like to express my deep gratitude for their love and encouragement.

Abstract

Unexploded ammunitions and landmines pose serious humanitarian problems to the afflicted regions. It is estimated that 45-55 millions of anti-personnel and anti-tank landmines infest at least 1.3 millions square kilometers in more than 100 countries. Around 10,000 people, mostly civilians, are killed or maimed annually, and the average rehabilitation cost of a survivor is US$ 5,000. Landmines are still produced and used nowadays. The average cost of a landmine is US$ 10, and its lifespan can be a few decades.

The demining process is slow and thus costful: the clearance cost of a mine is estimated to be US$ 1,000. For an electromagnetic sensor, such as the metal detector, the main reason for its slowness is the false alarm rate: about 100-1,000 false alarms for one real mine.

A recent approach in electromagnetic detection is the addition of a ground-penetrating radar (GPR) to the metal detector, the former being used for discriminating between mines and innocuous objects, thereby speeding up the detection process by reducing the number of false alarms. However, the performances of the GPR in a given physical environment must be assessed quantitatively before it is used to discriminate between alarms. The goal of this thesis is to pave the way for a model-wise performance assessment.

Therefore, this thesis is devoted to the modeling of GPR with a particular focus on reconciling quantitatively measurements and theory. For this reason, measurements are performed in laboratory conditions (flat soil and no clutter), but could in principle be made in more realistic environments. The proposed model is modular, in the sense that the antenna and the scene under interest can be considered separately. The antenna radiation and reception are modeled by mixing aperture equivalent currents and operational parameters; the soil and target electromagnetic scattering are modeled by the use of integral equations in stratified media, solved by the method of moments. The modeled experiments agree very well with the real experiments. Finally, the method of

moments is used for a parametric study of the soil and target scattering due to changing physical and geometrical conditions. This study, although done for a simple scatterer, yields physically insightful results into the complex scattering phenomena at hand.

Contents

List of Figures

List of publications

International journals

- **I. van den Bosch**, S. Lambot, I. Huynen, M. Acheroy, and P. Druyts. Accurate and Efficient Modeling of Monostatic GPR signal of Dielectric Targets Buried in Stratified Media. *Journal of Electromagnetic Waves and Applications*, volume 20, number 3, page 283-290, 2006.

- **I. van den Bosch**, S. Lambot, P. Druyts, I. Huynen, and M. Acheroy. Buried Target Signature Extraction from Ground-Penetrating Radar Signal. Measurements and Simulations. *Near Surface Geophysics (special issue)*, 2006. Accepted for publication.

- **I. van den Bosch**, M. Acheroy, I. Huynen, and P. Druyts. Accurate Electromagnetic Modeling of a Monostatic Ground-Penetrating Radar for Targets buried in Stratified Media. *IEEE Transactions on Geoscience and Remote Sensing*. In Preparation.

- S. Lambot, **I. van den Bosch**, B. Stockbroeckx, P. Druyts, M. Vanclooster, and E. C. Slob. Frequency Dependence of the Soil Dielectric Properties Derived from Ground-Penetrating Radar Signal Inversion. *Subsurface Sensing Technologies and Applications*, 2005. In press.

- S. Lambot, E. C. Slob, **I. van den Bosch**, B. Stockbroeckx, B. Scheers, and M. Vanclooster. Estimating Soil Electric Properties from Monostatic Ground-Penetrating Radar Signal Inversion in the Frequency Domain. *Water Resources Research*, vol. 40, w04205, doi10.1029/2003WR002095, April 2004.

- S. Lambot, E. C. Slob, **I. van den Bosch**, B. Stockbroeckx, and M. Vanclooster. Modeling of GPR Signal for Accurate Characterization of

the Subsurface Dielectric Properties. *IEEE Transactions on Geoscience and Remote Sensing*, vol. 42, no. 11, November 2004, pp. 2555–2568.

- S. Lambot, J. Rhebergen, **I. van den Bosch**, E. C. Slob, and M. Vanclooster. Measuring the Soil Water Content Profile of a Sandy Soil with an Off-Ground Monostatic Ground-Penetrating Radar. *Vadoze Zone Journal*, vol. 3, November 2004, pp. 1063–1071.

- S. Lambot, M. Antoine, **I. van den Bosch**, E. C. Slob, and M. Vanclooster. Electromagnetic Inversion of GPR Signals and Subsequent Hydrodynamic Inversion to Estimate Effective Vadoze Zone Hydraulic Properties. *Vadoze Zone Journal*, vol. 3, November 2004, pp. 1072–1081.

International conferences

- **I. van den Bosch**, P. Druyts, M. Acheroy and I. Huynen. Numerical Parametric Study of Buried Target Ground-Penetreting Radar Signature. In *Proceedings of SPIE Defense and Security Symposium*, Orlando, Florida, USA, April 2006. Accepted for publication.

- **I. van den Bosch**, P. Druyts, M. Acheroy and I. Huynen. Frequency and Time Domain Error in Buried Target Radar Signature Extraction. In *Proceedings of the Progress in Electromagnetic Research Symposium (PIERS)*, Cambridge, MA, USA, March 2006. Accepted for publication.

- **I. van den Bosch**, P. Druyts, S. Lambot, I. Huynen, and M. Acheroy. Accurate and Efficient Modeling of Monostatic GPR Signal of Dielectric Targets Embedded in Stratified Media. In *Proceedings of the Progress in Electromagnetic Research Symposium (PIERS)*, Hangzhou, Zhejiang, China, August 2005, pp. 251–255.

- **I. van den Bosch**, S. Lambot, M. Acheroy, I. Huynen, and P. Druyts. Accounting for Multiple Reflections and Antenna Radiation Pattern in GPR Signal Modeling and Experimental Validation. In *Proceedings of the Third International Workshop on Advanced Ground Penetrating Radar*, Delft, The Netherlands, May 2005, pp. 135–140.

- O. Lopera, S. Lambot, N. Milisavljevic, B. Scheers, and **I. van den Bosch**. Background Subtraction in the Frequency Domain for Focusing Ground-Penetrating Radar Data. In *Proceedings of the Third Inter-*

national Workshop on Advanced Ground Penetrating Radar, Delft, The Netherlands, May 2005, pp. 25–30.

- S. Lambot, L. Weihermüller, **I. van den Bosch**, M. Vanclooster, and E. C. Slob. Full-Wave Inversion of Off-Ground Monostatic GPR Signal Focused on the Surface Reflection for Identifying Surface Dielectric Permittivity. In *Proceedings of the Third International Workshop on Advanced Ground Penetrating Radar*, Delft, The Netherlands, May 2005, pp. 113–118.

- **I. van den Bosch**, S. Lambot, O. Lopera, and M. Acheroy. Landmine Signature Extraction from GPR Signal: Modeling and Measurements. In *Proceedings of the II International IEEE Andean Region Conference*, IEEE Colombia, Ed., Bogota, Colombia, August 2004.

- S. Lambot, **I. van den Bosch**, O. Lopera, and E. C. Slob. Inverse Identification of the Shallow Subsurface Electric Properties from Frequency Domain GPR Signal for Supporting Humanitarian Demining. In *Proceedings of the II International IEEE Andean Region Conference*, IEEE Colombia, Ed., Bogota, Colombia, August 2004.

- O. Lopera, N. Milisavljevic, B. Macq, **I. van den Bosch**, S. Lambot, and A. Gauthier. Analysis of Segmentation Techniques for Landmine Signature Extraction from 2D Ground Penetrating Radar Data. In *Proceedings of the II International IEEE Andean Region Conference*, IEEE Colombia, Ed., Bogota, Colombia, August 2004.

- **I. van den Bosch**, S. Lambot, and A. Vander Vorst. Buried Target Signature Extraction from Ground-Penetrating Radar Signal Based on the Equivalence Principle. In *Proceedings of the Tenth International Conference on Ground Penetrating Radar*, TU Delft, The Netherlands, June 2004, pp. 287–290.

- S. Lambot, **I. van den Bosch**, M. Vanclooster, and E. C. Slob. Modeling of GPR Signal and Inversion for identifying the Shallow Subsurface Dielectric Properties. In *Proceedings of the Tenth International Conference on Ground Penetrating Radar*, TU Delft, The Netherlands, June 2004, pp. 79–82.

- **I. van den Bosch**, S. Lambot, and A. Vander Vorst. A New Approach for Extracting Landmine Signature from GPR Signal. In *Proceedings of*

the 24th European Association of Remote Sensing Laboratories (EARSeL) Symposium, Dubrovnik, Croatia, May 2004.

- S. Lambot, **I. van den Bosch**, and E. C. Slob. Frequency Domain GPR Signal Forward and Inverse Modeling for Identifying the Subsurface Dielectric Properties. In *Proceedings of the 24th European Association of Remote Sensing Laboratories (EARSeL) Symposium*, Dubrovnik, Croatia, May 2004.

- O. Lopera, **I. van den Bosch**, S. Lambot, N. Milisavljevic, and B. Macq. Simulation and Analysis of Landmine Signatures from Ground Penetrating Radar 2D Data. In *Proceedings of the International Symposium "Humanitarian Demining 2004"*, CROMAC and HCR, Eds., Sibenik, Croatia, April 2004.

- **I. van den Bosch**, S. Lambot, and A. Vander Vorst. A Unified Method for Modeling Radar and Radiometer Measurements. In *Proceedings of the EUDEM2 SCOT 2003 Conference*, H. Sahli, A. M. Bottoms, and J. Cornelis, Eds., vol. 2, VUB, Brussels, September 2003, pp. 523–528.

- S. Lambot, **I. van den Bosch**, and E. C. Slob. Dielectric Characterization of the Shallow Subsurface Using Ground Penetrating Radar for Supporting Humanitarian Demining. In *Proceedings of the EUDEM2 SCOT 2003 Conference*, H. Sahli, A. M. Bottoms, and J. Cornelis, Eds., vol. 2, VUB, Brussels, September 2003, pp. 535–541.

- S. Lambot, E. C. Slob, **I. van den Bosch**, B. Stockbroeckx, B. Scheers, and M. Vanclooster. GPR Design and Modeling for Identifying the Shallow Subsurface Dielectric Properties. In *Proceedings of the 2^{nd} International Workshop on Advanced Ground Penetrating Radar*, A. Yarovoy, Ed., TU Delft, The Nethelands, May 2003, pp. 130–135.

National conferences

- O. Lopera, S. Lambot, **I. van den Bosch**, A. Gauthier, N. Milisavljevic, and B. Macq. A New Signal Processing Approach for Landmine Signature Extraction from Ground Penetrating Radar 2D Data. In *Proceedings of the IV National Congress on Automation and Control*, ACA, Ed., Bogota, Colombia, November 2004.

- **I. van den Bosch**, I. Huynen, and A. Vander Vorst. HuDem 1997–2001: Combining Radar and Radiometry at UCL. In *Proceedings of the Virtual Reality in Mechanical and Production Engineering Symposium (VR-MECH 01)*, Royal Military Academy, Brussels, November 2001, pp. 91–95.

List of abbreviations

AIM	adaptive integral method
AP	anti-personnel
AT	anti-tank
bg	background
c	contrast
CAD	computer-aided design
CFIE	combined field integral equation
CW	continuous wave
DGF	dyadic Green's function
EFIE	electric field integral equation
EM	electromagnetic
EMPIE	electric mixed-potential integral equation
FDTD	finite difference time domain
(I)FFT	(inverse) fast Fourier transform
FMCW	frequency modulated continuous wave
fs	free space
GB	gigabyte
GPR	ground-penetrating radar
hs	homogeneous space
m	measurement system
MB	megabyte
MD	metal detector
menv	mathematical environment
MFIE	magnetic field integral equation
ml	multilayered medium
MLFMA	multi-level fast multipole algorithm
MMPIE	magnetic mixed-potential integral equation

MoM	method of moments
PEC	perfect electric conductor
penv	physical environment
PMCHWT	Poggio-Miller-Chang-Harrington-Wu-Tsai
PO	physical optics
PRF	pulse repetition frequency
RCS	radar cross section
RWG	Rao-Wilton-Glisson
src	source
SFCW	stepped-frequency continuous wave
SIE	surface integral equation
TEM	transverse electro-magnetic
TLGF	transmission-line Green's function
UWB	ultra-wide band
VNA	vector network analyzer
w.r.t.	with respect to

List of symbols

$\triangleq$	variable definition
$\cdot$	scalar product
$\times$	vector product
$\mathcal{F}\{g\}$	Fourier transform of g
$\mathbf{a}$	position or field vector
$\hat{\mathbf{a}}$	unit position vector
$\overline{\overline{\boldsymbol{\mathcal{A}}}}$	dyadic quantity
$\widetilde{\overline{\overline{\boldsymbol{\mathcal{A}}}}}$	dyadic quantity in the spatial frequency domain
$\underline{A}$	1-D array
$\underline{\underline{A}}$	2-D array
$\underline{\underline{A}}^T$	transpose of $\underline{\underline{A}}$
$\underline{\underline{A}}^{-1}$	inverse of $\underline{\underline{A}}$
$\|\underline{\underline{A}}\|$	2-norm of $\underline{\underline{A}}$
$\underline{\underline{I}}$	identity matrix
$\underline{\underline{0}}$	all zero 2-D array
a^*	conjugate of complex quantity a
$\Re\{a\}$	real part of a
$\Im\{a\}$	imaginary part of a
$\|a\|$	absolute value of a
$\delta(\mathbf{r})$	spatial Dirac delta function
Γ	reflection coefficient
ε	dielectric permittivity
μ	magnetic permeability
k	wavenumber
R_T	target radar response
R_S	soil radar response
$\mathbf{E}, \mathbf{e}$	electric field

$\mathbf{H}, \mathbf{h}$	magnetic field
$\mathbf{J}, \mathbf{j}$	electric current
$\mathbf{M}, \mathbf{m}$	magnetic current
$\overline{\boldsymbol{\mathcal{G}}}^{PQ}$	dyadic Green's function for P-fields and Q-currents
$\hat{\mathbf{n}}$	unit normal

Chapter 1

Introduction

1.1 Overview of the landmine problem

Anti-personnel landmines and unexploded ordnance left behind from wars and conflicts constitute a deadly threat to civilians of the affected countries. It is estimated that around 45–55 millions of anti-personnel (AP) and anti-tank (AT) landmines infest at least 1.3 millions sq. km. in more than 100 countries [1]. Approximately 20 of these (*e.g.* Angola, Afghanistan, Cambodia, Croatia, Egypt, Iraq, *etc.*) are heavily affected. These landmines:

- kill or maim a reported 10,000 people annually, with an average rehabilitation cost of US$ 5,000 per person;
- create millions of refugees or internally displaced persons;
- prevent hundreds of thousands of sq. km. of agricultural land from being used;
- deny thousands of km. of roads for travel;
- create food scarcities, causing malnutrition and starvation;
- deny access to potable water, leading to water-borne diseases;
- interrupt health care, increasing sickness and disease;
- inflict long-term psychological trauma on landmine survivors;
- hinder economic development; and

- undermine political stability.

More than a dozen countries (*e.g.* China, Cuba, Egypt, Singapore, Vietnam, *etc.*) still produce landmines, and almost 20 countries or rebel groups use landmines. The problem gets a nasty taint when one knows that AP mines are designed to maim rather than kill, and that their lifespan can be a few decades.

The situation pertaining to every concerned country can be found in an extensive report issued each year by the International Campaign to Ban Landmines[1] (ICBL). Information about the landmine problem and demining technologies is also provided by the U.S. Department of Defense Humanitarian Demining Research and Development Program[2].

The solution to this problem is to be tackled by a multi-level approach. According to ICBL, action is needed to:

- remove mines from the ground;
- ensure that minefields are fenced off and marked and that communities receive education about mine risks;
- destroy mines in stockpiles;
- meet the needs of mine victims—from emergency medical care and rehabilitation to programs for socio-economic reintegration and recognized rights for people with disabilities;
- ensure that all countries joins the Mine Ban Treaty (*i.e.* the Ottawa Convention) and undertake to never again produce, use or sell antipersonnel mines (a list of the members is available at `http://www.icbl.org/treaty/members`);
- make sure that once a State joins, it fully implements the Mine Ban Treaty *e.g.* by submitting transparency reports, meeting deadlines for stockpile destruction and mine clearance, and assisting the victims of landmines;
- ensure that countries outside of the Mine Ban Treaty abide by the spirit of the agreement and refrain from use, production and stockpiling of the weapon;
- persuade non state actors to ban landmines and abide by the spirit of the treaty; and

[1] `http://www.icbl.org/`
[2] `http://www.humanitarian-demining.org/demining/default.asp`

- condemn any use or production by a state or non-state actor.

Let us detail the first item of the above list. Several approaches can be used for removing mines from the ground, which can be classified in two main categories: mechanical mine clearance techniques[3] and mine detection techniques[4].

The first category characterizes itself by the fact that the mines are not detected prior to removal or destruction; instead, the accent is set on the mechanical removal or *in situ* destruction of the mines by "heavyweight" machines that use for example fast rotating flails hitting the ground at high speeds, or that remove a layer of the soil and separate the big objects found therein from the soil itself. The main advantages of this method are speed and security of the operators. The main drawbacks are the impossibility to use this set of methods within "harsh" areas (derelict buildings, forests, rocky hills, irrigation canals,*etc.*), the cost of the machines, and the fact that about 20 % of the landmines remain after such a process.

The mine detection approach is characterized by all techniques that attempt to pinpoint the location of each mine within a minefield, and mark these locations by some visible artifact. Once all the mines within an area have been localized, the process of their removal and/or neutralization can take place. It is to be noted that the mine detection process is obligatory in humanitarian demining and has to take place even if a mechanical clearance process has been done, in order to reach sufficient clearance levels.[5]

1.2 Mine detection methods and technologies

This section is not an exhaustive review of all the methods that are being developed in view of landmine detection, but rather an overview of the current detectors used and the ones that will soon be fielded. For a complete review of all the methods, the reader should consult [2].

1.2.1 Currently used

Traditional manual detection involves teams of deminers that use prodders and metal detectors (MDs). The process is extensively described in [3], and consists in well-defined sequences or procedures that are function of the mine clearance

[3] `http://www.humanitarian-demining.org/demining/clrtech.asp`

[4] `http://www.humanitarian-demining.org/demining/detection.asp`

[5] For example, the U.N. state that, for humanitarian demining purposes, a clearance level of 99.96 % of all mines in a given area should be reached.

scenario, the climate, the vegetation, the variety of mines, the soil, *etc.* For example, a procedure used by the bomb disposal unit of the Belgian Army in Cambodia can be summed up as follows [3]: tripwire removal with help of a long stick, vegetation clearing, MD scanning of an area $1 \times 0.5\text{m}^2$. If there is no alarm, the same process is repeated for the next area. If the MD raises an alarm, the deminer uses a dagger to find the mine and carefully removes the soil above the suspicious target. If the target is found to be a mine, its position is marked, in order to be neutralized or removed. A platoon of 30 well-trained deminers is able to clear approximately 500–2500 m^2 per day, which corresponds to an area of 20–80 m^2 per man per day.

Needless to say, this manual procedure, albeit the most efficient in terms of clearance quality, is very time consuming and expensive. It is estimated that clearance of a mine costs about US$ 1,000. This cost is to be compared to that of a landmine, which is about US$ 10. The main reason of this high cost is the high false alarm rate of the MD, as minefields are often contaminated by a lot of metal fragments that can raise an alarm of the MD. It is estimated that there are about 100–1,000 false alarms for one real mine. These false alarms can also lower the attention level of the deminers, which further slows down the demining process and can augment the risk of accidents. Finally, landmines contain less and less metallic parts, and the explosive contained inside is purely dielectric, which renders their detection with standard levels of sensitivity for the MD difficult; increasing this sensitivity level renders the detection of such low metal content mines possible, but at the cost of a higher false alarm rate.

Mine detection is also accomplished with help of trained dogs, which find mines using their keen sense of smell, and accomplish a defined move to indicate a finding. Dogs are classified under the term "biosensors". The main advantage is that dogs detect explosives present within the ground, and are therefore not subject to the same false alarm problems as the MD. The main drawbacks of this method are:

- cost and time needed to educate the dogs;
- weight of the dog, that in some cases can be sufficient to detonate the mine;
- adaptability under extreme climate conditions;
- the fact that dogs detection capabilities are influenced by the deminer's mood; and

- the fact that dogs are efficient for about half an our.

Figure 1.1: Typical AP landmines found in practice. From left to right: VS 50, PMN, M35BG.

1.2.2 Under development

All methods that are already in use in the field are subject to constant research. For example, modeling of the MD is currently being studied at the RMA, and the technology involved undergoes constant enhancements.[6] This research effort has provided dramatic improvements to classical tools such as the MD, in the field of soil compensation or target imaging [4]. Manual prodders can also be augmented by the addition of an ultrasonic sensor at the prodding extremity. This so-called "smart prodder" allows to have a better guess of encountered objects and to exercise less physical pressure on them (in this way reducing the risk of accidents) [2].[7] However, we present in this section the

[6] `http://www.vallon.de`

[7] For prodders, see also `http://www.rand.org/publications/MR/MR1608/MR1608.appw.pdf`

tools that are currently in testing phase, and that are going to be fielded in maximum two years.

1.2.2.1 Rats: the APOPO project

In the area of biosensors, research is focusing on the use of rats in mine detection. The idea of using rats for the detection of landmines came up through a search for a cheap and efficient mine detector tool, which would be able to detect both metal and plastic landmines.[8] Despite the huge research efforts in mine detection during the last decades, the only technological alternative to manual prodding and MD detection that made its way to the field was the use of mine detection dogs. Rats however, show some major potential to be good mine detectors. Indeed, rats

- have a highly developed sense of smell;
- are easy to tame and train;
- are small, light, cheap and easy to maintain and transport;
- are widespread and easily adapt to all environments;
- once taught, the animals love performing repetitive tasks; and
- rats are more easily transferred between trainers compared to dogs.

APOPO has actually started operational work in Mozambique.

1.2.2.2 Ground-penetrating radar

1.2.2.2.1 Generalities Ground-penetrating radar (GPR) is the name for the family of radar systems whose purpose is to retrieve information from the subsurface. Nowadays, the GPR is widely used in:

- roads and runways inspection;
- pipes and cables localization;
- geophysical prospection;
- snow and ice surveys;
- verification of integrity of building structures;

[8] `http://www.apopo.org/`

- archaeological investigations;*etc.*

The above list is not exhaustive, and the reader will find many examples of practical use in [5, 6, 7, 8].

1.2.2.2.2 Operating principle and signal contributions The operating principle of a GPR is similar to a classical radar system. A transmitter is linked with a waveguiding structure (usually a coaxial waveguide) to a transmitting antenna T_X, which is directed towards the ground as shown at Fig. 1.2. The transmitter radiates through T_X electromagnetic (EM) waves that follow various paths before being picked up by a receiving antenna R_X. If $R_X = T_X$, that is, if the transmitting and receiving antennas are confounded, the radar is monostatic. Otherwise, the radar system is bistatic (two antennas) or multistatic (more than two antennas). As sketched in Fig. 1.2, the EM waves travel following different paths:

Path 1: from T_X to R_X There is a coupling between T_X and R_X that can exist even in the absence of the scatterers. As this signal is not useful, it is considered as clutter, and it can vary with antenna type and configuration [9]. The strength of this coupling has no practical importance as long as it does not vary with time, since in this case a simple free space measurement is sufficient to characterize this coupling, which can then be subtracted from the total signal. If the radar system works in monostatic mode, that is, if $T_X = R_X$, this signal is simply constituted by the reflections of the fields at the waveguide-antenna junction and at the aperture of the antenna.

Path 2: ground reflection The soil is a strong scatterer. Its resulting signal is usually called "ground clutter" or "surface reflection". Its scattering strength depends upon its EM parameters dielectric permittivity ε, magnetic permeability μ, and conductivity σ, but is also highly dependent upon the geometry of the system. The soil EM parameters values—which are in general frequency-dependent—are governed by geophysical parameters such as soil water content, type, texture and structure [10]. Those parameters are also strongly space- and time-dependent. Through σ, the soil is also the main attenuator of the radiated EM waves, and the related loss can reach tremendous values. From this, the reader understands that the soil properties will be one of the most important factors on the behavior of the GPR.

In this work, the soil roughness has not been taken into consideration: the first goal of the thesis is to provide an accurate prediction of GPR measurements by means of a new model, and for this a flat soil was needed in order to reduce the complexity of the model and of the measurements. Nevertheless, one must be conscious of the fact that soil roughness *will* greatly influence its radar response, due for example to multiple path scattering or diffusion by small surface irregularities [11].

Path 3: clutter Clutter is due to the reflections of the air-soil interface (see Path 2) as well as of all the undesired targets that populate the subsurface (a metal can, abandoned ammunition shells, rocks,*etc.*). The buried undesired objects have a radar cross section that can be smaller or greater than that of the interesting target, and can be located at the same range as the target. In that case it will be impossible to discriminate between both. However, the antenna radiation pattern, schematically represented by dotted lines at Fig. 1.2, can save the day: if this pattern is "sufficiently" directive, the radiated energy will be focused on the target, and the clutter on the sides will have a negligible participation to the total signal.

Path 4: target The scattering strength of the target depends upon a handful of parameters, among which one of the most significant is the contrast between its own and the soil dielectric permittivity ε (chapter 4). Indeed, the EM waves are reflected whenever a change of propagation properties occur in the medium. The smaller the change, the smaller the amplitude of the corresponding reflection. Other parameters of importance are the target electrical size, *i.e.* its size as compared to the wavelength, its orientation and shape. All these parameters can be summed up in a function, the radar cross section (RCS) of the target.

Since the wavelength in the soil is much shorter than in the air, buried objects appear electrically larger than in free space. In this regard the soil can be thought of as a "lens" that, for a given frequency, magnifies the details of buried structures and objects, like water visually magnifies immersed objects. The level of details that can be attained increases with the bandwidth of the signal, but attenuation in the soil, which increases with frequency, limits in practice the upper limit of the frequency band. Additionally, the transmitted EM fields must first cross the air-ground interface before reaching the target. As a significant fraction of the EM

waves are directly scattered by the soil surface, this results in a dramatic decrease of the amplitudes of the EM fields traveling towards the target. Moreover, this "interface effect" must be squared, since the part of the EM fields reflected by the target must once again cross the interface before being picked up by R_X. Practically, it means that in most cases the amplitude of the signal due to the target will participate for at most 10 % of the total signal (see chapter 4). However, if the target is located far enough from the soil interface, it is possible to discriminate it in the time domain.

All these contributions are added at the receiving antenna R_X. Finally, the total EM fields picked up by R_X travel again through a waveguide and reach a receiver that will transform it into what is called "signal". Only subsequent treatment done on the received signal will allow to separate the different contributions to it. All signals but the target are called "clutter".

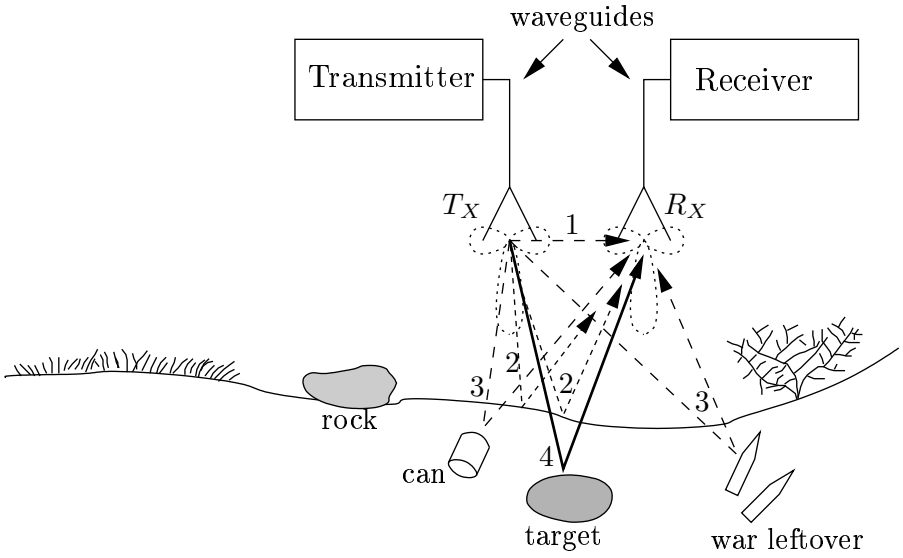

Figure 1.2: Generic working environment of GPR. Dashed lines represents various sources of clutter (defined as "all signals but the target"), such as direct coupling (1), air-soil interface (2), and ground leftovers (3). The soil can reflect following multiple paths. The continuous line (4) is the target contribution to the picked up EM fields at R_X, and is the desired signal. If the radar is monostatic ($T_X = R_X$), the antennas are confounded on the drawing, and the direct coupling simply becomes the internal reflections of the antenna.

1.2.2.2.3 GPR design There are different kinds of hardware implementations of GPRs, that can be separated into two main categories: time domain and frequency domain.[9] As schematically presented at Fig. 1.3, each domain can be further subdivided depending on the modulation of the signal. A complete presentation of these implementations can be found in [5, 3]. The greatest differences come from the underlying hardware used to radiate the EM fields and to sample the resulting signal.

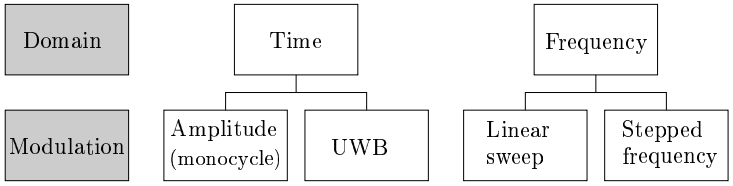

Figure 1.3: Different types of GPR systems (after [3]).

Time domain The time domain GPRs (also called impulse radars), which constitute the majority of commercially available radar systems, send a pulse at a given *pulse repetition frequency* (PRF) into the ground and then "listen" to the backscattered echoes. Time domain GPRs can be further separated in two main categories: amplitude modulated and ultra-wide band (UWB).

Amplitude modulated GPRs send pulses with a carrier at a given frequency, which depends upon the application. This carrier is modulated by a square envelope. In order to have a good spatial resolution in depth, the pulse duration should be as small as possible. This is the reason for using only monocycle pulses for GPR applications (Fig. 1.4). The central frequency f_c of the monocycle (which is the same as the carrier frequency) can vary from some MHz up to GHz, and its 3 dB bandwidth is equal to f_c. For example, a 1 ns (nanosecond) monocycle has f_c and its 3 dB bandwidth equal to 1 GHz.

The need for a larger bandwidth has led to a second and more recent category of time domain GPRs, which produce carrierless pulses. The carrierless pulse can be created by a rapid discharge of stored EM energy into the radiating circuit of the radar. A typical width of the pulse is about 200 ps with a peak amplitude of 30 V, and the shape is in most cases Gaussian-like. These GPRs are called ultra-wide band (UWB) GPRs, because of the very large bandwidth involved.[10] The block diagram of a time domain UWB GPR is given at Fig.

[9] This section is inspired from [3].

[10] To be UWB, a GPR must have a fractional bandwidth larger that 100 %.

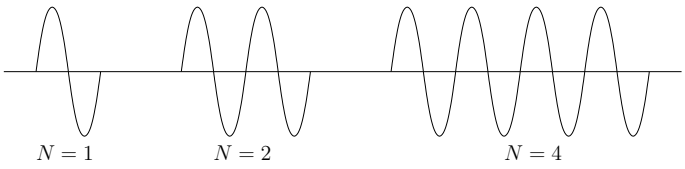

Figure 1.4: Monocycle, two-cycle and four-cycle waveforms for amplitude modulated carrier. Only monocycles are used for amplitude modulated GPRs, due to the need for a good time resolution.

1.5. A detailed presentation of each block is provided in [3, section 2.2.4].

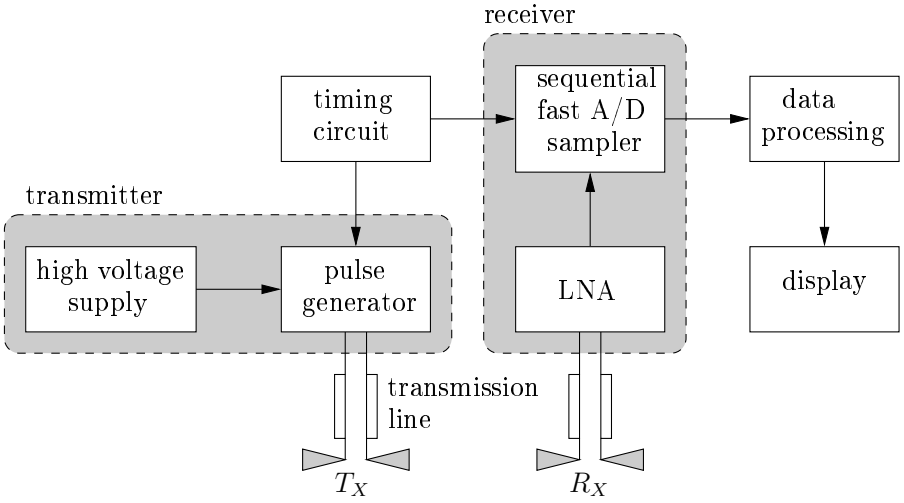

Figure 1.5: Block-diagram of a time domain UWB GPR [3].

Frequency domain The linear sweep radar is also known as frequency modulated continuous wave (FMCW) radar. As its name indicates it, the FMCW radar transmits a carrier whose frequency is modulated linearly with respect to time in a given frequency band, and this modulation is repeated once the upper frequency is reached [9]. By mixing the received signal with a sample of the transmitted waveform, one obtains a difference frequency related to the phase difference between both signals, and hence to the time delay of the target backscattered signal. A detailed description and a list of references about the FMCW radar can be found in [9, section 6.4].

Stepped frequency continuous wave (SFCW) radar can be seen as a simpli-

fied implementation of a FMCW radar, where the frequency modulation is not linear but occurs in a staircase manner. At each frequency, a CW is radiated with a high stability, and a sample of the radiated signal is mixed with the received signal into an I/Q mixer [3]. The I and Q baseband signals can then be sampled using high precision, low speed A/D converters.

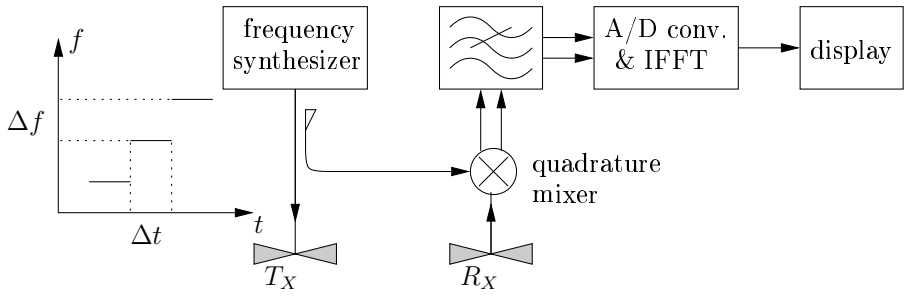

Figure 1.6: Block-diagram of a stepped frequency GPR [3].

The advantages of the SFCW radar over time domain technology are the following. It radiates a higher mean power per frequency[11] and has a more efficient noise rejection than time domain GPRs, because a narrow band coherent receiver can be used. Therefore, its signal-to-noise ratio will be better than a time domain GPR working in the same frequency band. Another advantage is that, by appropriately weighting the amplitudes and phases of the transmitted frequencies, one can synthesize different signals, thus yielding different pulse shapes in the time domain (after an IFFT on the signal). This weighting can be done by software *a posteriori* on the acquired data, thus allowing the hardware to remain that of a simple SFCW radar.

1.2.2.2.4 GPR data The acquired data can be presented in the time domain or in the frequency domain; Fourier transforms can be used for passing from one domain to the other. Time domain representation of data is useful for discriminating reflections from different targets and interfaces, which in turn allows for understanding the subsurface structure. Frequency domain representation allows for studying the frequency dependence of the radar cross section (RCS) of a given buried target, and can thus help in choosing the GPR operating frequency band that maximizes the target radar response.

[11]The USA, Europe and Asia have different regulations concerning GPRs. For an overview of the allowed frequency bands and power levels, check `http://www-rp.lip6.fr/dnac/Bateman.pdf`

Time or frequency domain data acquired for one spatial configuration and localization of the antennas is called an "A-scan". A schematic example of a time domain A-scan is given at Fig. 1.7 (a), where the soil reflection occurs earlier and with a higher amplitude than the target reflection. If the speed of propagation in the soil is known, the time axis can be converted into a distance axis. Examples of time domain and frequency domain A-scans resulting from experiments are shown at Fig. 2.9 and on following figures.

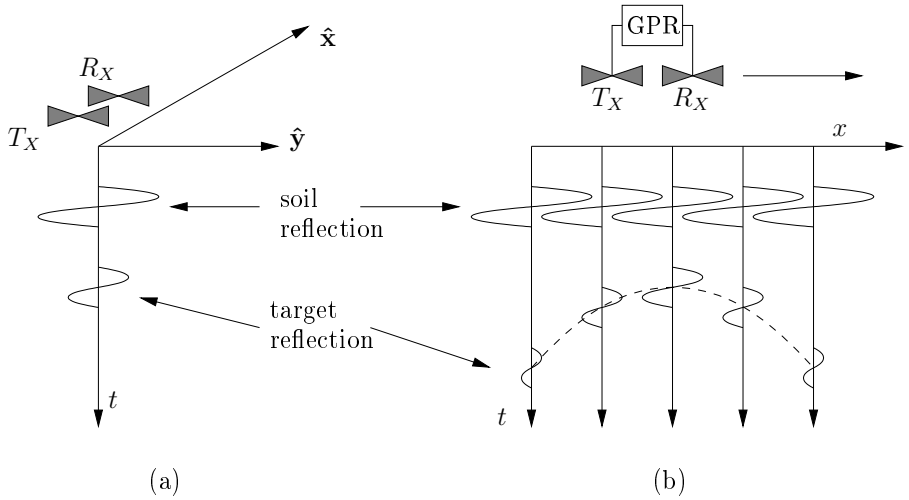

Figure 1.7: (a) Schematic time domain A-scan signal. (b) Schematic time domain B-scan signal.

A "B-scan" is the denomination of a set of A-scans collected alongside a line. Fig. 1.7 (b) schematically illustrates how the GPR signal evolves with the position of the antennas with respect to the target. The time location of the response of the target follows a hyperbolic rule, due to the distance between the target and the antenna system as the latter is moved alongside the line [3]. Moreover, the response of the target decreases as the antennas are moved away from the target, because of the path lengthening and the reduction of the antenna gain in the direction of the target, which depends upon the antenna pattern. The top of the hyperbola corresponds to the antenna system located at nadir of the target. Examples of measured and simulated time domain B-scans are given at Fig. 4.2 and Fig. 4.5 (on those figures, the amplitude of the signal is color-coded).

1.2.2.2.5 Application to mine detection Considerable research effort has been invested in ground-penetrating radar (GPR) technology [9], and this effort began in the early 80's. Since this prospecting tool is based on the principle that the electromagnetic waves penetrate across the structures and are scattered when they impinge upon an inhomogeneity embedded within the host medium, the inhomogeneity being an object with different electromagnetic properties than its immediate surroundings, GPR is therefore in principle able to detect metal as well as plastic mines. However, GPR technology is expensive when compared to more conventional mine detectors. The key issues that have to be solved before any GPR system is accepted by the demining community are: ease of use (as compared to MD), affordability, compactness, small weight, low-power consumption and robustness. Finally, the new technology will present an operational and economic interest only if it leads to a significant decrease of the number of false alarms, while remaining as reliable as other detectors in case of a real mine, thereby providing a significant speed-up of the demining process.

The GPR that approaches the most these requirements is the Minehound^{TM}, which combines a MD developed by Vallon and a time domain GPR unit developed by ERA Technology [12]. The GPR transmits 1 ns pulses at a repetition frequency of 1 MHz. The constructor has ensured that combination of both detectors has no impact on each other's performances. This system is currently being tested in Angola and Cambodia, in order to assess its performances with regards to the indigenous MDs used in clearance operations by the Mines Advisory Group. The principle of use of the Minehound^{TM} can be roughly summed up as follows. The Minehound^{TM} scans the area under interest (the same operational method as exposed in section 1.2.1 is used), with MD turned ON and GPR being OFF. If the MD raises an alarm, the operator tries to locate as precisely as possible its position. Then the GPR is turned ON, and the operator scans again more precisely the problematic zone. Information about position, depth and size (*via* its radar cross section) of the target is encoded in the audio signal produced by the radar. The sound yielded by the GPR being much different from the one provided by the MD, the operator, which wears ear-phones, has no trouble separating both alarms. If the GPR does not yield a consistent alarm, the inhomogeneity is considered to be a false alarm. On the contrary, if the GPR yields a constant and characteristic sound when scanned above the zone, it confirms the alarm raised by the MD and the prodding/excavating/marking operation can take place. The speed-up factor of the

area clearing process is hoped to be in average between 2–7, mainly thanks to the false alarm rate reduction. This parameter is the most important for the viability of the project. Indeed, for being profitable, the economic benefit generated by the increase of speed in the demining operation has to counterbalance the expenses made for buying the Minehound^{TM}, training the operators, changing the procedures,*etc.*

1.2.2.3 Usefulness and state of the art of accurate GPR modeling

The accurate modeling of a GPR is useful for a number of reasons. It can help the GPR designer to conceive a more effective detector, by testing different designs on the same scene without having to actually manufacture them; it can set an upper limit on the performances of a GPR, given the soil and target EM and geometrical properties; it can also be used for testing signal processing algorithms on GPR signals either free from or containing controlled noise measurement; finally one can use it as a benchmark against more approximate but more efficient models.

The modeling of a complete GPR system is a complex and challenging task. The majority of the works in this field use finite-difference time domain (FDTD) algorithms for flat soils [13, 14, 15, 16] and for rough interfaces [17]. A few works compare simulations and measurements [18, 19, 20, 21]. The advantages of FDTD are its widespread use and independence of the algorithm with regards to the medium containing the target. However, with FDTD it is impossible to model separately the antenna and the soil-target system (*i.e.* the model is not *separable*), hence the numerical model is not generic: for another radar setup, such as a different antenna shape or location, one has to rerun the computation process. Due to its non-separability, FDTD does not provide a way for obtaining the target radar signature from measurements. Moreover, the whole volume under consideration must be discretized, leading to high computational and memory costs [19].

Another approach for studying buried target scattering consists in solving a surface or volume integral equation with help of the method of moments (MoM) [22, 23, 24]. Carin *et al.* have also compared GPR simulations to measurements in [25, 26]; however the agreement was only qualitative because the radar system was not calibrated. Two major advantages over a FDTD method are: 1) the limitation of the computation volume to the antenna and scatterer, hence the reduction in computational needs; and 2) the possibility of solving the scattering problem for different excitations simultaneously. Probably the

biggest hurdle in the use of the MoM is the difficulty of its setup for stratified media, since it involves the use of dyadic Green's functions (DGFs) [22, 27]. Additionally, the use of the MoM for inhomogeneous or multivolume bodies remains a challenging task even in free space, mainly due to the complexity of the pertaining surface integral equations.

In both approaches, only simple linear or bow-tie dipole antennas have been modeled. This is because fine geometries demand a very high level of discretization, which anyway does not guarantee that the result will be accurate, since small differences between the real and modeled geometries can lead to important discrepancies between measured and computed quantities [28].

1.3 Objectives of present work

The aim of this thesis is to provide the designer and scientist with a complete, accurate, efficient and separable modeling method for GPR systems, which moreover provides an extraction procedure of the target radar response. More specifically:

- the completeness of the model, which means that the signal is modeled from the electromagnetic (EM) quantities up to the signal observed by the operator, is important for being able to reach both the scientist and the designer—who may not be an expert in the EM modeling aspects—, but also because too many works limit themselves to the EM phenomena pertaining to the scene (soil and target) and/or the antenna without going all the way to the actual measured signal;

- in laboratory conditions, the model should be *quantitatively* accurate to the point that measured and computed signals agree almost perfectly in the frequency and time domain;

- the efficiency is mainly related to the numerical method used in the model, which should be general, reliable, reasonably fast, precise, resource-saving, and able to solve the scattering problem for different excitations at once;

- the fact that the antenna and soil-target system should be modeled separately potentially provides a great flexibility to the user of the model, who can therefore study independently each subsystem, and afterwards examine their interactions with help of an intuitive yet rigorous approach;

- a clean target radar response extraction procedure is highly desirable, mainly for identification purposes; for this, the model should decompose the radar signal in such a way that this extraction is easy to perform on measured data.

1.4 Scientific contributions

In the wake of the objectives, the scientific contributions can be summarized as follows:

- elaboration of a generic radar model for monostatic stepped-frequency continuous wave radar, which
  - is complete from the EM quantities all the way to the signal displayed on the screen of the radar system
  - is separable, with an efficient mixed (experimental characterization)-(equivalent currents) approach for the antenna, very precise yet more simple than a full numerical approach, and independent from the presence of the soil and target
  - is of an accuracy that, to the best knowledge of the author, quantitatively outperforms everything that has been published until now
  - naturally provides a means for obtaining the target radar signature from a measurement
  - presents all the concepts, theory and formalism that allow for a generalization to more complicated situations, such as antenna "very close" to the soil (in the near field), inhomogeneous soils, and multiple antennas systems
- theoretical derivation of the surface integral equations and their MoM solution for multivolume bodies embedded in stratified media, and implementation of a robust and efficient MoM computer code
- study of the sources of error that can affect the target signature extraction, thereby providing the theoretical and practical framework for exploring the limits of the GPR model
- parametric study of the soil and target radar signals, which allows for an intuitive yet rigorous overview of the influence of a wide range of parameters on these signatures.

1.5 Limitations of the study

Flat soil The radar model has been used for predicting and extracting radar responses of targets buried in *flat stratified media only*. The soil surface roughness has not been considered in this work. This can be seen as a severe limitation of the study. However, the goal of the thesis was to provide an accurate GPR model, and for testing its accuracy we used the *most complicated yet exactly controllable* experimental configurations: soil roughness is not exactly controllable in the sense that it implies statistical quantities. But if one knows exactly the geometry of the soil surface, the numerical computation of the soil radar response does not pose any problem. Consequently, *with the same GPR model*, one could generate random soil surfaces with given statistical properties, compute the set of corresponding GPR responses which therefore constitute a random variable, and compare the properties of this simulated random variable to the one obtained experimentally for a soil having the same statistical properties as those used in the simulations.

Simplicity of the targets In chapters 2 and 4, simple targets (*i.e.* metallic and plastic cylinders) are used in both the simulations and measurements. As for the preceding point, this is because the main purpose of this work is to validate a generic GPR model. One could use much more complicated targets in the numerical algorithms, *e.g.* real mine structures, without changing the model in principle. Moreover, it can reasonably be stated that the qualitative conclusions of the parametric study of the target radar response drawn in chapter 4 can probably be transposed to more complex targets, since that parametric study is mainly focused on the consequences of the soil EM parameters variations or on the target relative position with respect to the radar system. Finally, the fact that the internal complexity of the target *does* influence its radar response is established and acknowledged numerically at the end of chapter 4.

Antenna-soil distance The GPR model has been experimentally validated for antenna heights above the soil ranging from 40 cm down to 20 cm, and for a frequency band of 0.8–3 GHz. The lowest height to which the model is still correct for a given frequency has not been investigated, and the model remains to be validated—or modified—for antenna heights of a few centimeters.

Frequency domain The GPR model has been elaborated in the frequency domain, and has been validated for a stepped-frequency continuous wave radar system, both in the frequency and time domains. However, the model can be easily transposed in the time domain by means of Fourier transforms of the formulas established in chapter 2. Conversely, a time domain radar can be characterized in the frequency domain, hence rendering possible its modeling by means of transfer functions in the frequency domain.

Monostatic radar system While established for a monostatic antenna for practical reasons, the GPR model can easily be extended to bistatic systems. The main difference is that the internal reflections are replaced by a direct coupling between the emitting and receiving antennas, but this coupling is also an operational parameter that can be characterized [3].

All the limitations listed above—except the "antenna-soil distance"—could be overcome by using more accurate geometrical descriptions of the targets under consideration (mine *and* soil), or by a straighforward extension/transposition of the GPR model. As a final goal, one could use such a model to perform a study aiming at finding the best possible geometry-radar antennas-frequency band for a given target and a given soil.

1.6 Organization of this document

The content of each chapter following this introduction is described hereafter.

Chapter 2: Accurate and efficient modeling of monostatic ground-penetrating radar

First the state of the art in GPR modeling is depicted, and the approach followed in this work is presented. We then go on with a brief description of the radar system used for our measurements. The following sections are very important, as they establish the expressions of the radar response of a contrast embedded in a general background, and examine thoroughly the scattering of the antenna. The expressions obtained are then specialized to the case of a target embedded in a multilayered medium, and further simplified for being experimentally usable. Measurements and simulations for increasingly complicated cases are presented. This chapter is inspired from [29, 30].

Chapter 3: Target numerical electromagnetic modeling

This chapter deals with the establishment of the surface integral equations (SIEs) for multiple perfectly conducting (PEC) and penetrable inhomogeneous scatterers embedded in stratified media. The integral equations systems will be exposed with gradual generality. First the Huygens surface equivalence principle is established for homogeneous and stratified medium. Then these results are used for establishing the SIEs for homogeneous bodies (PEC and dielectric) embedded in multilayered media. We go one step further by generalizing these SIEs for inhomogeneous bodies. At this point the basic SIEs are combined under the Poggio-Miller-Chang-Harrington-Wu-Tsai (PMCHWT) and combined field integral equation (CFIE) formulations in order to equate the number of integral equations to that of the unknowns. Finally, we derive the MoM solution for the various formulations of the system of SIEs (basic and combined), and the resulting computer code is extensively tested.

Chapter 4: Practical applications of the GPR model

This chapter, inspired from [31, 32], focuses more on the practical aspects and limitations of the GPR model, although comparisons between measured and computed radar signals are already presented at chapter 2. We first present practical examples of buried target signature extraction and the consequent enhancement of the target visual discrimination. The first example studies the effect of soil moisture on the target signature extraction, while the second example is focused on a B-scan. We then spend some time on studying the influence of each term of the GPR equation on the error that arises in the process of the target signature extraction. The parametric study of the soil and target signatures is then performed.

Chapter 5: Summary and perspectives

This chapter summarizes our research work and gives a survey of future research needed in order to apply the model to more complete and/or complicated sceneries, further generalize and enhance the speed of the numerical algorithms in order to broaden its application range, and use the model to predict the performances of commercial GPRs in given sceneries.

Appendixes

Appendixes represent a significant part of this work; they are needed in order to leave only the main ideas and concepts in the core of the text, without having the underlying complex and varied mathematical formalism in the way. Appendix A contains demonstrations needed for chapter 2; appendix B details the computation of the terms needed in the MoM solution, for both homogeneous and multilayered media; appendix C exposes the multilayered medium dyadic Green's functions (DGFs) needed in the MoM; and appendix D details the Fourier transforms and Sommerfeld integrals that are needed to compute the spatial DGFs.

Chapter 2

Accurate and efficient modeling of monostatic GPR

2.1 State of the art and approach in this work

Accurate GPR modeling can be useful to the designer for a number of reasons. Firstly, it can allow for a physical understanding of the complex scattering phenomena involved, and of the influence of fundamental parameters on the soil and target radar response. It can thereby provide a means for enhancing the design of the GPR system. Secondly, if the model is sufficiently accurate, it can help setting an upper limit on the performances of a particular GPR system for a given physical configuration. Thirdly, an accurate model can be a standard against which other approximate models can be compared. Finally, such accurate modeling can be used for generating "virtual experiments", free from or involving controlled measurement errors, which can afterwards be used for testing signal processing algorithms.

The accurate modeling of a GPR is a complex task. Indeed, four main difficulties arise in this process: 1) the emission and measurement process which include the source, the waveguide linking the source with the antenna through the connector and antenna feed, and the antenna itself, must be properly described; 2) the antenna may be close to the ground, and therefore the excitation fields can significantly differ from a plane wave; 3) the antenna radiation pattern must be accounted for; 4) the soil contributes for a significant part to the total radar signal, modifies the target radar signal w.r.t. free space, and

finally induces multiple reflections between itself and the antenna [20], which in turn can change significantly antenna radiation currents and henceforth the measured radar signal.

Modeling of complete GPR systems in presence of soil and target has been done by using a finite difference time domain (FDTD) algorithm in [20, 18, 19, 21], which compared the simulations to measurements. This numerical approach has proven to be quantitatively good, and the algorithm addresses automatically the four difficulties mentioned above. However, FDTD yields hundreds of millions of unknowns for the problem at hand, which necessitate huge memory space (several Gbytes) and a considerable amount of computing power [19], even for the simple dipole antennas that were considered in the above papers.

Another approach relies on using a numerical method which limits the computation volume to the scatterer, such as integral equations solved by the Method of Moments (MoM), or Physical Optics (PO) [33, 25, 26], where the soil is taken into account by using appropriate half-space dyadic Green's functions (DGFs) [22]. Comparisons between measured and computed radar SAR images in Carin *et al.* showed only qualitative similarities, because the measurement system was not calibrated [26].

Recent studies aim at modeling more complex GPR antennas by means of FDTD [34, 35] or MoM [36, 37, 28]; yet it is difficult to set up correctly a precise numerical model of a complex antenna, as fine details in the geometry, as well as manufacturing imperfections, have a great impact on the measured quantities. This is especially true for the ridged-horn antenna used in our measurements [28]. As the waveguide-antenna connection and the antenna internal reflections can contribute significantly to the measured radar signal [20], it is easy to understand that small mistakes in antenna description can greatly hamper the precision of calculated parameters, and hence radar signal prediction.

In a recently developed approach, aiming at modeling the radar signal of the soil without a target, the antenna model is based upon complex scalar transmittances, which account for connector and antenna internal reflections, transmission and reception gains, and multiple reflections between the soil and the antenna [38]. The model is augmented by using the *simplest* antenna current distribution—a dipole—together with an *exact* computation of the electromagnetic (EM) fields propagation in the soil—considered as a multilayered medium—by means of DGFs. Only a few measurements above a metal plane

are needed for determining these unknown transmittances, *i.e.* for system calibration. Yet the accuracy and efficiency of the method is demonstrated in its use for subsurface EM parameters extraction by model inversion.

Extension of this method to describe the signal measured by a monostatic GPR in presence of an inhomogeneity embedded in a multilayered medium has been initiated in [32]. In this case the antenna was also considered as an infinitesimal dipole. This choice, motivated by the sake of simplicity, is based on the assumption that the EM fields produced by the antenna in the solid angle subtended by the target was the same as that produced by a dipole. The latter assumption has been verified in free space at a sufficiently large distance from the antenna, for a target located near or on the main beam axis. However, as it is conceived, this model is not able to take into account the variations of antenna emission and reception characteristics with changes of the target angular position, unless a proper angular dependent calibration is performed. The estimated transmittances would then be a function of the angle, and compensate for the error in the current distribution, at the cost of more and possibly awkward calibration measurements.

This chapter further extends [32], as it formally demonstrates expressions of the GPR response produced by a contrast embedded within an arbitrary background, for any antenna equivalent current distribution, and taking into account the multiple reflections between the antenna and the background and contrast. The scattering of the antenna is studied by decomposing the antenna (emission and scattering) equivalent currents and incoming fields into current and field basis functions respectively. The antenna scattering currents coefficients in the basis are obtained as a function of the free space emission currents and of a feedback matrix, which relates the current basis to the field basis. The expression for the *monostatic GPR response* is then derived, and is shown to have three contributions: 1) the antenna internal reflections 2) the soil response and 3) the buried target response. Target scattering is studied with help of the MoM. In the simulations, two antenna equivalent current distributions are considered: a dipole of electric current located at the phase center of the antenna [38, 32], and a Huygens cosinusoidal distribution of electric and magnetic currents located on the aperture of the antenna [39]. This latter distribution, which represents well the antenna radiation pattern, yields a compact model usable for all angles of interest, as well as for targets that intercept a large part of the main beam.

The approach of this chapter provides a methodology for extracting the

target signature from the measured GPR response. Moreover, it presents the advantages of modeling the complex antenna effects by a well-chosen equivalent currents distribution and a few operational parameters, independent of the environment and determinable through a simple calibration procedure as in [38], while retaining an excellent precision in response prediction, and allowing for a physical insight of the scattering processes at hand. However, this method could also make an advantageous use of a numerical modeling of the antenna, able to compute more precisely the distribution of the antenna emission and scattering currents: the hard-to-model part, due to the small imperfections, would be accounted for by operational parameters. The antenna and environment models remain decoupled, thereby providing a significant advantage over the global numerical model mentioned earlier.

This chapter is organized as follows. Section 2.2 briefly describes the radar system used in our measurements. Section 2.3 gives expressions of the radar response of a contrast embedded in a general background, and examines thoroughly the scattering of the antenna. Section 2.4 applies the general theory to the case of a target embedded in a stratified medium. Measurements and simulations are compared in section 2.5, and section 2.6 concludes the chapter.

2.2 Radar system choice and description

The measurements have been done by means of a stepped-frequency continuous wave (SFCW) radar, emulated by a vector-network analyzer (VNA), as it possesses several advantages over time domain technology [38]. Its very large bandwidth (0.8–3 GHz in this study) allows for attaining a good spatial resolution and depth of penetration. The lower limit is set by the operational range of the antenna (0.8–18 GHz), while the higher limit is due to the VNA capabilities.

A transverse electromagnetic (TEM) ultra-wide band (UWB) metallic ridged-horn antenna (Fig. 2.1) has been used in the measurements. The isotropic gain of the antenna as function of the frequency is given at Table 2.1 (`http://www.schwarzbeck.de/Datenblatt/k9120l3f.pdf`). The system is config-

Table 2.1: Isotropic gain of the antenna as function of the frequency.

Freq (GHz)	0.8	0.9	1.0	1.5	2.0	2.5	3.0
Gain (dB)	0.91	5.30	6.97	9.51	9.43	10.67	11.54

ured in monostatic mode, for a very practical reason: for bistatic systems, the relative position of the antennas is subject to small variations. Hence, even if the direct coupling of the antennas has been characterized before a measurement campaign, these geometrical variations can lead to errors in the cancellation of this coupling. The monostatic mode was therefore chosen in order to avoid this source of possible errors.

The horn antenna has aperture dimensions of 24 × 14 cm and is 20 cm deep. This antenna can therefore be a strong scatterer at the scale of the radar-soil-target system. Since it is located relatively close to the soil (between 20–40 cm), one can expect important late-time resonances between the soil and the antenna. In the time domain, these resonances can have signal components that coincide with the signal of the target. Nevertheless, since in the model these multiple reflections are accounted for by an operational parameter, they can be cancelled; even more, this antenna allows to bring to light this resonance effect. Finally, due to the modularity of the model, *any* antenna could have been used instead of this one.

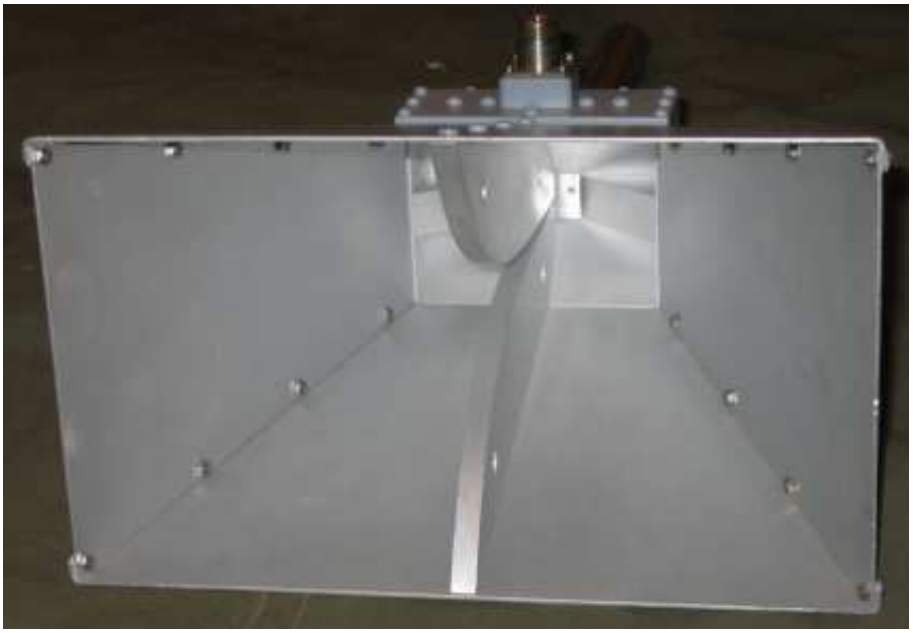

Figure 2.1: Schwarzbeck BBHA TEM ridged-horn ultra-wide band (1–18 GHz) antenna used in the measurements. Aperture size is 24 cm × 14 cm.

In monostatic mode the measured signal is the complex reflection coefficient

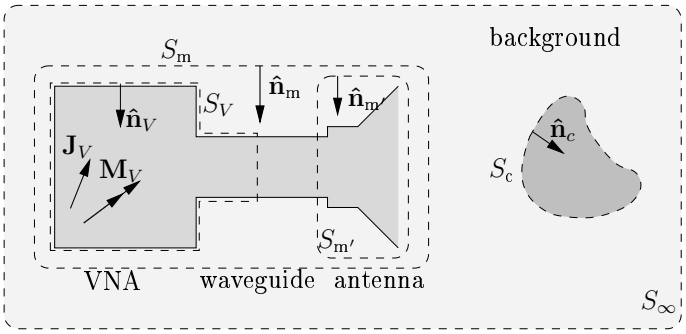

Figure 2.2: Physical configuration of measurement system in presence of contrast. Different surfaces enclosing different volumes will be used for reciprocity. S_m encloses whole measurement system. S_c encloses contrasting body.

Γ (or S_{11}).

2.3 Monostatic GPR signal of a contrast embedded in a general background

2.3.1 Configuration and hypotheses

The considered configuration is shown at Fig. 2.2. No assumption is made about the internals of the VNA: there might be non-linear and non-reciprocal materials. However, the world outside of the VNA is supposed to be linear and reciprocal (hypothesis h1). The VNA and the waveguide linking the antenna to the measurement system are supposed to be perfectly shielded or to present a surface impedance (hypothesis h2), and only the fundamental mode propagates in the waveguide in the frequency band of interest (hypothesis h3).

2.3.2 Notations and definitions

$a^{(\mathrm{penv})}$ and $b^{(\mathrm{penv})}$ are respectively the forward and backward traveling waves in the waveguide, and are function of the physical environment "penv" of the antenna, where "penv" is either "bg" or "bg, c", where "bg" is the background medium, and "c" identifies the contrast put in the background (the word "contrast" will receive a precise context-dependent meaning in the next sections).

The measured GPR response is given by:

$$\Gamma^{(\text{penv})} = \frac{b^{(\text{penv})}}{a^{(\text{penv})}} \tag{2.1}$$

We denote by $\left(\mathbf{E}_{\text{src}}^{(\text{menv})}, \mathbf{H}_{\text{src}}^{(\text{menv})}\right)$ fields radiated in a mathematical environment "menv" by currents $\left(\mathbf{J}_{\text{src}}, \mathbf{M}_{\text{src}}\right)$. Environment "menv" can be different from "penv". It takes the form "bg, obj", where "obj" identifies the objects put in the background: "m" for measurement system, "c" for contrast, or "m, c" for their combination. Subscript "src" identifies the source. The only physical source "V" is in the VNA, and it is constituted by currents $\left(\mathbf{J}_V, \mathbf{M}_V\right)$. We also define the surface electric and magnetic equivalent currents "AT(penv)" for the antenna at emission which are function of "penv", and "C" for the contrast equivalent currents:

$$\mathbf{J}_{AT(\text{penv})} \triangleq (-\hat{\mathbf{n}}_{\text{m}}) \times \mathbf{H}_V^{(\text{penv, m})} \quad \text{on } S_{\text{m}} \tag{2.2a}$$

$$\mathbf{J}_C \triangleq (-\hat{\mathbf{n}}_{\text{c}}) \times \mathbf{H}_V^{(\text{bg, m, c})} \quad \text{on } S_{\text{c}}. \tag{2.2b}$$

Furthermore we call "AS(bg)" and "AS(c)" the antenna scattering currents, which describe the change of "AT" induced by the background and the contrast respectively:

$$\mathbf{J}_{AS(\text{bg})} \triangleq \mathbf{J}_{AT(\text{bg})} - \mathbf{J}_{AT} \quad \text{on } S_{\text{m}} \tag{2.3a}$$

$$\mathbf{J}_{AS(\text{c})} \triangleq \mathbf{J}_{AT(\text{bg, c})} - \mathbf{J}_{AT(\text{bg})} \quad \text{on } S_{\text{m}} \tag{2.3b}$$

The surface magnetic equivalent currents are obtained by applying duality to equations (2.2)–(2.3). Finally, to each "AT" and "AS" we associate equivalent sources "AT'" and "AS'" located inside or on $S_{\text{m}'}$. This set of currents can be a continuous volume or surface distribution, or a set of dipoles, and are defined such as to produce the same fields as sources "AT" and "AS" on S_c (Fig. 2.2).

Thanks to the equivalence principle, in the volume bounded by S_{m} and S_∞, fields $\left(\mathbf{E}_V^{(\text{bg, m})}, \mathbf{H}_V^{(\text{bg, m})}\right)$ can be computed from sources "AT(bg)" radiating in the background alone (Fig. 2.2). Similarly, in the volume bounded by S_{m}, S_{c} and S_∞, $\left(\mathbf{E}_V^{(\text{bg, m, c})}, \mathbf{H}_V^{(\text{bg, m, c})}\right)$ can be computed from "AT(bg, c)" and "C". This can be written as:

$$\left(\mathbf{E}_V^{(\text{bg, m})}, \mathbf{H}_V^{(\text{bg, m})}\right) = \left(\mathbf{E}_{AT(\text{bg})}^{(\text{bg})}, \mathbf{H}_{AT(\text{bg})}^{(\text{bg})}\right) \tag{2.4}$$

$$\left(\mathbf{E}_V^{(\text{bg, m, c})}, \mathbf{H}_V^{(\text{bg, m, c})}\right) = \left(\mathbf{E}_{AT(\text{bg,c})}^{(\text{bg})}, \mathbf{H}_{AT(\text{bg, c})}^{(\text{bg})}\right) + \left(\mathbf{E}_C^{(\text{bg})}, \mathbf{H}_C^{(\text{bg})}\right). \tag{2.5}$$

Starting from a normalized excitation ($a^{(\text{bg})} = 1$), we will show in the next sections how to compute the corresponding normalized currents $\left(\mathbf{j}_{\text{src}}, \mathbf{m}_{\text{src}}\right)$ and

fields $\left(\mathbf{e}_{\mathrm{src}}^{(\mathrm{menv})}, \mathbf{h}_{\mathrm{src}}^{(\mathrm{menv})}\right)$. Since the outer medium is linear (h1), the physical fields and equivalent currents are all proportional to $a^{(\mathrm{bg})}$:

$$(\mathbf{J}_{\mathrm{src}}, \mathbf{M}_{\mathrm{src}}) = a^{(\mathrm{bg})} \, (\mathbf{j}_{\mathrm{src}}, \mathbf{m}_{\mathrm{src}}) \tag{2.6}$$

$$\left(\mathbf{E}_{\mathrm{src}}^{(\mathrm{menv})}, \mathbf{H}_{\mathrm{src}}^{(\mathrm{menv})}\right) = a^{(\mathrm{bg})} \left(\mathbf{e}_{\mathrm{src}}^{(\mathrm{menv})}, \mathbf{h}_{\mathrm{src}}^{(\mathrm{menv})}\right). \tag{2.7}$$

This relation does not necessarily hold for sources "V", as non linear components may exist inside the VNA.

2.3.3 Formulations of contrast contribution to radar signal

In this section we use reciprocity [40] to establish the radar signal due to a contrast embedded in a background in terms of an integral of electromagnetic quantities 1) on the surface of the contrast and 2) on the surface or in the volume supporting the antenna equivalent currents. Reciprocity can be applied in any volume excluding the VNA (h1).

2.3.3.1 Definition of reciprocity states

2.3.3.1.1 State T Sources $(\mathbf{J}_V, \mathbf{M}_V)$ radiate in presence of measurement system and background, *i.e.*

$$(\mathbf{E}_T, \mathbf{H}_T) \triangleq \left(\mathbf{E}_V^{(\mathrm{bg,\ m})}, \mathbf{H}_V^{(\mathrm{bg,\ m})}\right) \tag{2.8}$$

2.3.3.1.2 State R Sources $(\mathbf{J}_V, \mathbf{M}_V)$ radiate in presence of measurement system, background and contrast. This is the "physical" state, with

$$(\mathbf{E}_R, \mathbf{H}_R) \triangleq \left(\mathbf{E}_V^{(\mathrm{bg,\ m,\ c})}, \mathbf{H}_V^{(\mathrm{bg,\ m,\ c})}\right). \tag{2.9}$$

2.3.3.1.3 State T' Equivalent currents $\left(\mathbf{j}_{AT'(\mathrm{bg})}, \mathbf{m}_{AT'(\mathrm{bg})}\right)$ radiate in presence of background only:

$$(\mathbf{E}_{T'}, \mathbf{H}_{T'}) \triangleq \left(\mathbf{e}_{AT'(\mathrm{bg})}^{(\mathrm{bg})}, \mathbf{h}_{AT'(\mathrm{bg})}^{(\mathrm{bg})}\right). \tag{2.10}$$

2.3.3.1.4 State R' Equivalent currents $(\mathbf{j}_C, \mathbf{m}_C)$ radiate in presence of background only:

$$(\mathbf{E}_{R'}, \mathbf{H}_{R'}) \triangleq \left(\mathbf{e}_C^{(\mathrm{bg})}, \mathbf{h}_C^{(\mathrm{bg})}\right). \tag{2.11}$$

2.3.3.2 Integral over contrast surface

We apply reciprocity between states T and R in the volume enclosed by S_V, S_c and S_∞. This volume contains no real sources (Fig. 2.2). Within this volume, the reciprocity relation between $(\mathbf{E}_T, \mathbf{H}_T)$ and $(\mathbf{E}_R, \mathbf{H}_R)$ is:

$$\int_{S_V+S_\mathrm{c}+S_\infty} (\mathbf{E}_T \times \mathbf{H}_R - \mathbf{E}_R \times \mathbf{H}_T) \cdot \hat{\mathbf{n}} \, \mathrm{d}S = 0. \tag{2.12}$$

Assuming that, far away, the background can be replaced by a homogeneous medium without changing the fields on S_V and S_c, integration over S_∞ is zero [40, p. 296]. The integral on S_V demands a particular treatment done in appendix A.1. For the coaxial waveguide used, $K = 1$. Using $a_T = a^{(\mathrm{bg})}$, $b_T = b^{(\mathrm{bg})}$, $a_R = a^{(\mathrm{bg,\,c})}$ and $b_R = b^{(\mathrm{bg,\,c})}$ in (A.4), we get:

$$\int_{S_V} (\mathbf{E}_T \times \mathbf{H}_R - \mathbf{E}_R \times \mathbf{H}_T) \cdot \hat{\mathbf{n}}_V \, \mathrm{d}S = -2 \left(a^{(\mathrm{bg,\,c})} b^{(\mathrm{bg})} - a^{(\mathrm{bg})} b^{(\mathrm{bg,\,c})} \right). \tag{2.13}$$

Using (2.13) in (2.12) and (2.4) in (2.8), we find that

$$\begin{aligned} 2 \left(a^{(\mathrm{bg,\,c})} b^{(\mathrm{bg})} - a^{(\mathrm{bg})} b^{(\mathrm{bg,\,c})} \right) &= \int_{S_\mathrm{c}} \Big(\mathbf{E}^{(\mathrm{bg})}_{AT(\mathrm{bg})} \times \mathbf{H}^{(\mathrm{bg,\,m,\,c})}_{V} \\ &\qquad - \mathbf{E}^{(\mathrm{bg,\,m,\,c})}_{V} \times \mathbf{H}^{(\mathrm{bg})}_{AT(\mathrm{bg})} \Big) \cdot \hat{\mathbf{n}}_\mathrm{c} \, \mathrm{d}S \\ &= \int_{S_\mathrm{c}} \left(\mathbf{E}^{(\mathrm{bg})}_{AT(\mathrm{bg})} \cdot \mathbf{J}_C - \mathbf{H}^{(\mathrm{bg})}_{AT(\mathrm{bg})} \cdot \mathbf{M}_C \right) \mathrm{d}S \end{aligned} \tag{2.14}$$

where the last equality has been obtained by using (2.2b). By dividing both sides by $a^{(\mathrm{bg})} a^{(\mathrm{bg})}$, and using (2.6) and (2.7), one gets:

$$\Gamma^{(\mathrm{bg,\,c})} = \Gamma^{(\mathrm{bg})} + \Gamma^{(\mathrm{c})} \tag{2.15}$$

where $\Gamma^{(\mathrm{bg})}$ and $\Gamma^{(\mathrm{c})}$, the radar signals from the background and the contrast within the background respectively, are given by:

$$\Gamma^{(\mathrm{bg})} \triangleq \frac{b^{(\mathrm{bg})}}{a^{(\mathrm{bg})}} \tag{2.16}$$

$$\begin{aligned} \Gamma^{(\mathrm{c})} &\triangleq -\frac{1}{2} \frac{a^{(\mathrm{bg})}}{a^{(\mathrm{bg,\,c})}} \int_{S_\mathrm{c}} \left(\mathbf{e}^{(\mathrm{bg})}_{AT(\mathrm{bg})} \cdot \mathbf{j}_{C,\gamma} - \mathbf{h}^{(\mathrm{bg})}_{AT(\mathrm{bg})} \cdot \mathbf{m}_{C,\gamma} \right) \mathrm{d}S \\ &= -\frac{1}{2} \frac{a^{(\mathrm{bg})}}{a^{(\mathrm{bg,\,c})}} \int_{S_\mathrm{c}} \left(\mathbf{e}^{(\mathrm{bg})}_{AT'(\mathrm{bg})} \cdot \mathbf{j}_{C,\gamma} - \mathbf{h}^{(\mathrm{bg})}_{AT'(\mathrm{bg})} \cdot \mathbf{m}_{C,\gamma} \right) \mathrm{d}S \end{aligned} \tag{2.17}$$

where the last equality stems from the fact that AT' produces the same fields as AT on S_c (section 2.3.2). γ, which is the reflection coefficient at the entrance of

the VNA if its impedance does not perfectly match the waveguide impedance, has been added as a subscript to $(\mathbf{j}_C, \mathbf{m}_C)$ to indicate that those currents depend upon the reflexion of the traveling waves at the entrance of the VNA. Moreover, from (A.35) derived in appendix A.7 we have that

$$\frac{a^{(\mathrm{bg})}}{a^{(\mathrm{bg,\ c})}} = \frac{1 - \gamma\Gamma^{(\mathrm{bg,\ c})}}{1 - \gamma\Gamma^{(\mathrm{bg})}}. \tag{2.18}$$

Fortunately, as is demonstrated in appendix A.5, $\Gamma^{(\mathrm{c})}$ is independent of γ. That subscript will therefore be ignored in the remainder of the text.

Instead of traveling waves a and b, one could have used the voltages V and currents I in the transmission line. They are related by the following equations [41]:

$$a^{(\mathrm{x})} = \frac{V^{(\mathrm{x})} + Z_0 I^{(\mathrm{x})}}{2\sqrt{\Re\{Z_0\}}} \tag{2.19a}$$

$$b^{(\mathrm{x})} = \frac{V^{(\mathrm{x})} - Z_0 I^{(\mathrm{x})}}{2\sqrt{\Re\{Z_0\}}} \tag{2.19b}$$

where Z_0 is the characteristic impedance of the waveguide. Replacing in (2.14) $a^{(\mathrm{x})}$ and $b^{(\mathrm{x})}$—where (x) = (bg) or (x) = (bg, c)—by their above expressions given in (2.19), one obtains:

$$V^{(\mathrm{bg})} I^{(\mathrm{bg,\ c})} - V^{(\mathrm{bg,\ c})} I^{(\mathrm{bg})} = \int_{S_\mathrm{c}} \left(\mathbf{E}^{(\mathrm{bg})}_{AT(\mathrm{bg})} \cdot \mathbf{J}_C - \mathbf{H}^{(\mathrm{bg})}_{AT(\mathrm{bg})} \cdot \mathbf{M}_C \right) \mathrm{d}S. \tag{2.20}$$

Dividing both sides by $I^{(\mathrm{bg})} I^{(\mathrm{bg})}$ and manipulating yields:

$$Z^{(\mathrm{bg,\ c})} = Z^{(\mathrm{bg})} + Z^{(\mathrm{c})} \tag{2.21}$$

where $Z^{(\mathrm{bg})}$ and $Z^{(\mathrm{c})}$ are given by:

$$Z^{(\mathrm{bg})} \triangleq \frac{V^{(\mathrm{bg})}}{I^{(\mathrm{bg})}} \tag{2.22}$$

$$Z^{(\mathrm{c})} \triangleq -\frac{I^{(\mathrm{bg})}}{I^{(\mathrm{bg,\ c})}} \int_{S_\mathrm{c}} \left(\underset{I^{(\mathrm{bg})}}{\mathbf{e}}{}^{(\mathrm{bg})}_{AT'(\mathrm{bg})} \cdot \underset{I^{(\mathrm{bg})}}{\mathbf{j}}{}_C - \underset{I^{(\mathrm{bg})}}{\mathbf{h}}{}^{(\mathrm{bg})}_{AT'(\mathrm{bg})} \cdot \underset{I^{(\mathrm{bg})}}{\mathbf{m}}{}_C \right) \mathrm{d}S \tag{2.23}$$

where notation $\underset{y}{x}$ means that X has been normalized by y.

A simplified version of (2.20), valid for open circuit reception and done for a coaxial waveguide, appears in [40, chapter 5]. The development presented here is however more general because we do not make any assumption on the waveguide. It is also more straightforward and natural because the waves a

and b have a precise and unique physical interpretation, whereas V and I may be more difficult to define for a generic waveguide. Furthermore the signal measured by the VNA is a reflection coefficient Γ and not an impedance. This is due to the fact that, at high frequencies, it is in practice easier to measure a power ratio than manufacture a load on which V and I are measurable on a wide frequency band. Finally, the normalized quantities depend upon the fact that one uses traveling waves or voltages and currents. We will show in section 2.3.4 that the normalization by traveling waves must be used to appropriately take into account the antenna scattering.

2.3.3.3 Integral over antenna sources

Applying reciprocity between states T' and R' (section 2.3.3.1) in the volume enclosed by S_c and S_∞, we get that

$$\begin{aligned}
&\int_{V_{\mathrm{m}'}} \left(\mathbf{e}_C^{(\mathrm{bg})} \cdot \mathbf{j}_{AT'(\mathrm{bg})} - \mathbf{h}_C^{(\mathrm{bg})} \cdot \mathbf{m}_{AT'(\mathrm{bg})}\right) \mathrm{d}V \\
&\quad = \int_{S_\mathrm{c}} \left(\mathbf{e}_{AT'(\mathrm{bg})}^{(\mathrm{bg})} \times \mathbf{h}_C^{(\mathrm{bg})} - \mathbf{e}_C^{(\mathrm{bg})} \times \mathbf{h}_{AT'(\mathrm{bg})}^{(\mathrm{bg})}\right) \cdot \hat{\mathbf{n}}_\mathrm{c} \, \mathrm{d}S \\
&\quad = \int_{S_\mathrm{c}} \left(\mathbf{e}_{AT'(\mathrm{bg})}^{(\mathrm{bg})} \times \mathbf{h}_V^{(\mathrm{bg,\ m,\ c})} - \mathbf{e}_V^{(\mathrm{bg,\ m,\ c})} \times \mathbf{h}_{AT'(\mathrm{bg})}^{(\mathrm{bg})}\right) \cdot \hat{\mathbf{n}}_\mathrm{c} \, \mathrm{d}S \\
&\quad = \int_{S_\mathrm{c}} \left(\mathbf{e}_{AT'(\mathrm{bg})}^{(\mathrm{bg})} \cdot \mathbf{j}_C - \mathbf{h}_{AT'(\mathrm{bg})}^{(\mathrm{bg})} \cdot \mathbf{m}_C\right) \mathrm{d}S
\end{aligned} \tag{2.24}$$

because, by (2.5), the difference between the second and third lines is:

$$\int_{S_\mathrm{c}} \left(\mathbf{e}_{AT'(\mathrm{bg})}^{(\mathrm{bg})} \times \mathbf{h}_{AT(\mathrm{bg,\ c})}^{(\mathrm{bg})} - \mathbf{e}_{AT(\mathrm{bg,\ c})}^{(\mathrm{bg})} \times \mathbf{h}_{AT'(\mathrm{bg})}^{(\mathrm{bg})}\right) \cdot \hat{\mathbf{n}}_\mathrm{c} \, \mathrm{d}S = 0. \tag{2.25}$$

The above left-hand side is in fact reciprocity in V_c between fields produced by $AT'(\mathrm{bg})$ and $AT(\mathrm{bg,\ c})$, which is equal to zero because no sources are present within V_c for neither state. The last equality in (2.24) stems from (2.2b). Comparing the last line of (2.24) with the right-hand side of (2.17), one gets another expression for $\Gamma^{(\mathrm{c})}$:

$$\Gamma^{(\mathrm{c})} = -\frac{1}{2} \int_{V_{\mathrm{m}'}} \left(\mathbf{e}_C^{(\mathrm{bg})} \cdot \mathbf{j}_{AT'(\mathrm{bg})} - \mathbf{h}_C^{(\mathrm{bg})} \cdot \mathbf{m}_{AT'(\mathrm{bg})}\right) \mathrm{d}V. \tag{2.26}$$

If $\left(\mathbf{j}_{AT'(\mathrm{bg})}, \mathbf{m}_{AT'(\mathrm{bg})}\right)$ are located on $S_{\mathrm{m}'}$, we easily obtain:

$$\Gamma^{(\mathrm{c})} \triangleq -\frac{1}{2} \int_{S_{\mathrm{m}'}} \left(\mathbf{e}_C^{(\mathrm{bg})} \cdot \mathbf{j}_{AT'(\mathrm{bg})} - \mathbf{h}_C^{(\mathrm{bg})} \cdot \mathbf{m}_{AT'(\mathrm{bg})}\right) \mathrm{d}S. \tag{2.27}$$

Finally, if, for approximating the real antenna equivalent currents for example, we use N_J and N_M electric and magnetic equivalent current point densities respectively, such that

$$\mathbf{j}_{AT'(\mathrm{bg})} \simeq \sum_{i=1}^{N_J} \mathbf{j}_i \delta(\mathbf{r}-\mathbf{r}_i) \quad \text{and} \quad \mathbf{m}_{AT'(\mathrm{bg})} \simeq \sum_{j=1}^{N_M} \mathbf{m}_j \delta(\mathbf{r}-\mathbf{r}_j)\,,$$

we have that:

$$\Gamma^{(\mathrm{c})} \triangleq -\frac{1}{2}\left(\sum_{i=1}^{N_J}\left(\mathbf{e}_C^{(\mathrm{bg})}\cdot\mathbf{j}_i\right)_{\mathbf{r}_i} - \sum_{j=1}^{N_M}\left(\mathbf{h}_C^{(\mathrm{bg})}\cdot\mathbf{m}_j\right)_{\mathbf{r}_j}\right). \tag{2.28}$$

The evaluation of $\Gamma^{(\mathrm{c})}$ necessitates the knowledge of the equivalent currents $(\mathbf{j}_C, \mathbf{m}_C)$ or of the fields $(\mathbf{e}_C^{(\mathrm{bg})}, \mathbf{h}_C^{(\mathrm{bg})})$ (see (2.17) and (2.26)–(2.28)). We show at section 2.4 that these fields and equivalent currents can be computed from the excitation fields $(\mathbf{e}^{(\mathrm{bg})}_{AT'(\mathrm{bg,\ c})}, \mathbf{h}^{(\mathrm{bg})}_{AT'(\mathrm{bg,\ c})})$, which are produced by the antenna equivalent currents $(\mathbf{j}_{AT'(\mathrm{bg,\ c})}, \mathbf{m}_{AT'(\mathrm{bg,\ c})})$. The knowledge of these currents requires to study the antenna scattering, which is done in the next section.

2.3.4 Antenna scattering

Strong interactions between the antenna and the contrast can occur, even if they are located within each other's far field region: it suffices that the antenna and contrast are strong scatterers for having multiple reflections that can contribute significantly to the resulting radar signal [20]. This is especially true for our horn antenna, which presents an aperture 24×13 cm^2 of size, and is located at about 30 cm above the soil. Of course, the strength of these interactions increases with smaller antenna-soil distances. In the case of a target embedded within a stratified medium, the multiple reflections between the soil and the antenna can mask the radar signal of the target.

To determine the antenna scattering currents, we first project the fields $(\mathbf{e}_C^{(\mathrm{bg})}, \mathbf{h}_C^{(\mathrm{bg})})$, scattered by the contrast and incident on the antenna (but produced in its absence), on a subspace spanned by a basis $(\mathbf{e}_i, \mathbf{h}_i)$:

$$\left(\mathbf{e}_C^{(\mathrm{bg})}, \mathbf{h}_C^{(\mathrm{bg})}\right) = \sum_{i=1}^{N} F_{C,i}^{(\mathrm{bg})}\left(\mathbf{e}_i, \mathbf{h}_i\right) + \left(\mathbf{e}_r, \mathbf{h}_r\right) \tag{2.29}$$

where $F_{C,i}^{(\mathrm{bg})}$ is chosen in order to minimize the norm of the truncation residual field, $\left|\left(\mathbf{e}_r, \mathbf{h}_r\right)\right|$. When the norm is defined by an inner product $\langle ; \rangle$, we have that

$$\underline{F}_C^{(\mathrm{bg})} = \underline{\underline{P}}^{-1}\underline{Q}^{(\mathrm{c})} \tag{2.30}$$

where $P_{kl} = \langle (\mathbf{e}_k, \mathbf{h}_k); (\mathbf{e}_l, \mathbf{h}_l) \rangle$ and $Q_l^{(c)} = \left\langle (\mathbf{e}_l, \mathbf{h}_l); (\mathbf{e}_C^{(bg)}, \mathbf{h}_C^{(bg)}) \right\rangle$. For example, we could define

$$\langle (\mathbf{e}_i, \mathbf{h}_i); (\mathbf{e}_j, \mathbf{h}_j) \rangle_S \triangleq \int_S \left(\mathbf{e}_i^* \cdot \mathbf{e}_j + \eta_0^2 \mathbf{h}_i^* \cdot \mathbf{h}_j \right) \, \mathrm{d}S \tag{2.31}$$

where S is a surface surrounding the antenna, and η_0 is the free space impedance. Indeed, with this definition, if $\left| (\mathbf{e}_r, \mathbf{h}_r) \right|$ is zero, the residual fields are zero everywhere in the volume bounded by S. The field basis functions could be a truncated multipole development (well suited for electrically small antennas), N plane waves, or the fields caused by N dipoles located on a surface surrounding the antenna.

Then, we develop the antenna equivalent currents into a basis:

$$\left(\mathbf{j}_{AT'(\mathrm{bg})}, \mathbf{m}_{AT'(\mathrm{bg})} \right) = \sum_{i=1}^{M} I_{AT,i}^{(\mathrm{bg})} \left(\mathbf{j}_i, \mathbf{m}_i \right) \tag{2.32}$$

$$\left(\mathbf{j}_{AS'(\mathrm{c})}, \mathbf{m}_{AS'(\mathrm{c})} \right) = \sum_{i=1}^{M} I_{AS,i}^{(\mathrm{c})} \left(\mathbf{j}_i, \mathbf{m}_i \right). \tag{2.33}$$

Each element of the field basis is scattered by the antenna, and thus creates scattering currents. The *feedback* matrix $\underline{\underline{H}}_f$ relates the scattering coefficients of the currents to those of the antenna incident fields by the following relationship:

$$\underline{I}_{AS}^{(\mathrm{c})} = \underline{\underline{H}}_f^{(\mathrm{bg})} \underline{F}_C^{(\mathrm{bg})}. \tag{2.34}$$

In free space, $\underline{I}_{AT}^{(\mathrm{fs})}$ and $\underline{\underline{H}}_f^{(\mathrm{fs})}$—denoted by $\underline{I}_{AT}$ and $\underline{\underline{H}}_f$ for simplicity—are characteristic of the antenna and depend upon the choice of the current and field basis. They can be obtained through a calibration (section 2.4.5), and are therefore operational parameters of the model.

On the other hand, if the current coefficients are known, the fields incident on the antenna can be computed and projected on the field basis to yield:

$$\underline{F}_C^{(\mathrm{bg})} = \underline{\underline{G}}^{(\mathrm{c})} \left(\underline{I}_{AT}^{(\mathrm{bg})} + \underline{I}_{AS}^{(\mathrm{c})} \right) \tag{2.35}$$

where

$$\underline{\underline{G}}^{(\mathrm{c})} = \underline{\underline{P}}^{-1} \underline{\underline{Q}}^{(\mathrm{c})} \tag{2.36}$$

with $Q_{kl}^{(\mathrm{c})} = \left\langle (\mathbf{e}_k, \mathbf{h}_k); (\mathbf{e}_{C,l}^{(\mathrm{bg})}, \mathbf{h}_{C,l}^{(\mathrm{bg})}) \right\rangle$, and $(\mathbf{e}_{C,l}^{(\mathrm{bg})}, \mathbf{h}_{C,l}^{(\mathrm{bg})})$ being the fields scattered by the contrast and due to current basis $(\mathbf{j}_l, \mathbf{m}_l)$. The name $\underline{\underline{G}}^{(\mathrm{c})}$ stems from the fact that it relates fields to current sources, like a dyadic Green's

function (DGF); however this analogy stops there because here current distributions and field projections are involved. Furthermore, only the scattered field is considered. Hence, the direct contribution must be removed. Combining (2.34) and (2.35), we obtain that

$$\underline{F}_C^{(\mathrm{bg})} = \left(\underline{\underline{I}} - \underline{\underline{G}}^{(\mathrm{c})}\underline{\underline{H}}_f^{(\mathrm{bg})}\right)^{-1} \underline{\underline{G}}^{(\mathrm{c})}\underline{I}_{AT}^{(\mathrm{bg})} \tag{2.37a}$$

$$= \underline{\underline{G}}^{(\mathrm{c})}\left(\underline{\underline{I}} - \underline{\underline{H}}_f^{(\mathrm{bg})}\underline{\underline{G}}^{(\mathrm{c})}\right)^{-1} \underline{I}_{AT}^{(\mathrm{bg})} \tag{2.37b}$$

(where (A.8) is used to move $\underline{\underline{G}}^{(\mathrm{c})}$ on the left side of the inverse term) and that

$$\underline{I}_{AS}^{(\mathrm{c})} = \underline{\underline{H}}_f^{(\mathrm{bg})}\left(\underline{\underline{I}} - \underline{\underline{G}}^{(\mathrm{c})}\underline{\underline{H}}_f^{(\mathrm{bg})}\right)^{-1} \underline{\underline{G}}^{(\mathrm{c})}\underline{I}_{AT}^{(\mathrm{bg})}. \tag{2.38}$$

From (2.38) we can compute $\underline{I}_{AT}^{(\mathrm{bg,\ c})}$:

$$\begin{aligned}
\underline{I}_{AT}^{(\mathrm{bg,\ c})} &= \underline{I}_{AT}^{(\mathrm{bg})} + \underline{I}_{AS}^{(\mathrm{c})} \\
&= \underline{I}_{AT}^{(\mathrm{bg})} + \underline{\underline{H}}_f^{(\mathrm{bg})}\left(\underline{\underline{I}} - \underline{\underline{G}}^{(\mathrm{c})}\underline{\underline{H}}_f^{(\mathrm{bg})}\right)^{-1} \underline{\underline{G}}^{(\mathrm{c})}\underline{I}_{AT}^{(\mathrm{bg})} \\
&= \left[\underline{\underline{I}} + \underline{\underline{H}}_f^{(\mathrm{bg})}\left(\underline{\underline{I}} - \underline{\underline{G}}^{(\mathrm{c})}\underline{\underline{H}}_f^{(\mathrm{bg})}\right)^{-1} \underline{\underline{G}}^{(\mathrm{c})}\right] \underline{I}_{AT}^{(\mathrm{bg})} \\
&= \left(\underline{\underline{I}} - \underline{\underline{H}}_f^{(\mathrm{bg})}\underline{\underline{G}}^{(\mathrm{c})}\right)^{-1} \underline{I}_{AT}^{(\mathrm{bg})}
\end{aligned} \tag{2.39}$$

where the last equality is obtained thanks to (A.7) using $\underline{\underline{B}} = \underline{\underline{H}}_f^{(\mathrm{bg})}$ and $\underline{\underline{C}} = \underline{\underline{G}}^{(\mathrm{c})}$.

2.3.5 Radar signal of a contrast embedded in a general background

Using the decomposition of section 2.3.4, we can now rewrite (2.27) involving surface equivalent currents. The development for (2.26) and (2.28) is straightforward. This can be done by decomposing $\left(\mathbf{e}_C^{(\mathrm{bg})}, \mathbf{h}_C^{(\mathrm{bg})}\right)$ in two ways: 1) by projecting $\left(\mathbf{e}_C^{(\mathrm{bg})}, \mathbf{h}_C^{(\mathrm{bg})}\right)$ on the field basis; 2) by using the fields $\left(\mathbf{e}_{C,k}^{(\mathrm{bg})}, \mathbf{h}_{C,k}^{(\mathrm{bg})}\right)$ due to basis $\left(\mathbf{j}_k, \mathbf{m}_k\right)$.

By decomposing $\left(\mathbf{e}_C^{(\mathrm{bg})}, \mathbf{h}_C^{(\mathrm{bg})}\right)$ in the field basis $\left(\mathbf{e}_k, \mathbf{h}_k\right)$, and by using (2.32) and (2.37b), (2.27) yields:

$$\begin{aligned}
\Gamma^{(\mathrm{c})} &= \left(\underline{I}_{AT}^{(\mathrm{bg})}\right)^T \left(\underline{R}_F \underline{\underline{G}}^{(\mathrm{c})}\left(\underline{\underline{I}} - \underline{\underline{G}}^{(\mathrm{c})}\underline{\underline{H}}_f^{(\mathrm{bg})}\right)^{-1} \underline{I}_{AT}^{(\mathrm{bg})} + \underline{R}_r\right) \\
&= \left(\underline{I}_{AT}^{(\mathrm{bg})}\right)^T \underline{R}_F \underline{\underline{G}}^{(\mathrm{c})} \underline{I}_{AT}^{(\mathrm{bg,\ c})} + \left(\underline{I}_{AT}^{(\mathrm{bg})}\right)^T \underline{R}_r
\end{aligned} \tag{2.40}$$

by recognizing $\underline{I}_{AT}^{(\mathrm{bg},\,\mathrm{c})}$ given at (2.39), and by defining:

$$R_{F,lk} \triangleq -\frac{1}{2}\int_{S_{m'}} (\mathbf{e}_k \cdot \mathbf{j}_l - \mathbf{h}_k \cdot \mathbf{m}_l)\,\mathrm{d}S \tag{2.41}$$

$$R_{r,l} \triangleq -\frac{1}{2}\int_{S_{m'}} (\mathbf{e}_r \cdot \mathbf{j}_l - \mathbf{h}_r \cdot \mathbf{m}_l)\,\mathrm{d}S. \tag{2.42}$$

$R_{F,lk}$ is independent of the environment and can be interpreted as the response of an ideal monostatic radar system (no antenna internal reflections and scattering) to incident fields $(\mathbf{e}_k, \mathbf{h}_k)$, and for which the emission currents are $(\mathbf{j}_{AT'(\mathrm{bg})}, \mathbf{m}_{AT'(\mathrm{bg})}) = (\mathbf{j}_l, \mathbf{m}_l)$. $R_{r,l}$ is the response caused by the residual field $(\mathbf{e}_r, \mathbf{h}_r)$.

By using the fields $(\mathbf{e}_{C,k}^{(\mathrm{bg})}, \mathbf{h}_{C,k}^{(\mathrm{bg})})$ due to current basis $(\mathbf{j}_k, \mathbf{m}_k)$, we have that

$$\left(\mathbf{e}_C^{(\mathrm{bg})}, \mathbf{h}_C^{(\mathrm{bg})}\right) = \sum_{k=1}^{M} \left(I_{AT,k}^{(\mathrm{bg})} + I_{AS,k}^{(\mathrm{c})}\right) \left(\mathbf{e}_{C,k}^{(\mathrm{bg})}, \mathbf{h}_{C,k}^{(\mathrm{bg})}\right). \tag{2.43}$$

Using this decomposition and (2.32) in (2.27), we get:

$$\Gamma^{(\mathrm{c})} = \left(\underline{I}_{AT}^{(\mathrm{bg})}\right)^T \underline{\underline{R}}^{(\mathrm{c})} \underline{I}_{AT}^{(\mathrm{bg},\,\mathrm{c})} \tag{2.44}$$

where

$$R_{kl}^{(\mathrm{c})} = -\frac{1}{2}\int_{S_{m'}} \left(\mathbf{e}_{C,k}^{(\mathrm{bg})} \cdot \mathbf{j}_l - \mathbf{h}_{C,k}^{(\mathrm{bg})} \cdot \mathbf{m}_l\right) \mathrm{d}S. \tag{2.45}$$

Comparing (2.40) to (2.44) shows that $\underline{\underline{R}}_F \underline{\underline{G}}^{(\mathrm{c})} \simeq \underline{\underline{R}}^{(\mathrm{c})}$, where the difference comes from the residual term $\underline{R}_r$ which will become negligible if the field basis includes enough well-chosen elements.

The three terms present in (2.44) can be physically interpreted as follows. $\underline{I}_{AT}^{(\mathrm{bg})}$ and $\underline{I}_{AT}^{(\mathrm{bg},\,\mathrm{c})}$ characterize the antenna equivalent currents in presence of the background alone and of the background and contrast respectively. Those environments are related to the two states used for applying reciprocity. $R_{kl}^{(\mathrm{c})}$ is the "reaction" of the contrast, and represents the response of an ideal bistatic radar system (*i.e.* no antenna internal or multiple reflections) to a contrast where the emission and reception antenna equivalent currents are $(\mathbf{j}_k, \mathbf{m}_k)$ and $(\mathbf{j}_l, \mathbf{m}_l)$ respectively. Eq. (2.45) is an integral over the antenna surface, and it can also be computed on the contrast surface:

$$R_{kl}^{(\mathrm{c})} = -\frac{1}{2}\int_{S_{\mathrm{c}}} \left(\mathbf{e}_l^{(\mathrm{bg})} \cdot \mathbf{j}_{C,k} - \mathbf{h}_l^{(\mathrm{bg})} \cdot \mathbf{m}_{C,k}\right) \mathrm{d}S \tag{2.46}$$

where $(\mathbf{e}_l^{(\mathrm{bg})}, \mathbf{h}_l^{(\mathrm{bg})})$ are the fields produced by current basis $(\mathbf{j}_l, \mathbf{m}_l)$, and $(\mathbf{j}_{C,k}, \mathbf{m}_{C,k})$ are the contrast equivalent currents due to excitation by current ba-

sis $(\mathbf{j}_k, \mathbf{m}_k)$. The choice of using (2.45) or (2.46) will be guided by practical considerations.

2.4 Monostatic GPR response for a target embedded in a multilayered medium

Equation (2.15) shows that the radar signal is due to two contributions: the background and the contrast embedded within the background responses. There are two ways to apply that formula, and they both should lead to the same result.

2.4.1 Total approach

We consider the stratified soil with the target as the contrast, plunged into a background that is free space. In this case, combining (2.15) and (2.44) yields the radar response:

$$\Gamma^{(\text{fs, (soil, t)})} = \Gamma^{(\text{fs})} + \left(\underline{I}_{AT}^{(\text{fs})}\right)^T \underline{\underline{R}}^{(\text{soil, t})} \underline{I}_{AT}^{(\text{fs, (soil, t)})} \tag{2.47}$$

where the fact that $\mathbf{e}_C^{(\text{bg})} = \mathbf{e}_{\text{soil}}^{(\text{fs})} + \mathbf{e}_{\text{t}}^{(\text{fs})}$ allows us to write:

$$\underline{\underline{R}}^{(\text{soil, t})} = \underline{\underline{R}}^{(\text{soil})} + \underline{\underline{R}}^{(\text{t})} \tag{2.48}$$

and where, by (2.39) and additivity applied to (2.36),

$$\underline{I}_{AT}^{(\text{fs, (soil, t)})} = \left(\underline{\underline{I}} - \underline{\underline{H}}_f \left(\underline{\underline{G}}^{(\text{soil})} + \underline{\underline{G}}^{(\text{t})}\right)\right)^{-1} \underline{I}_{AT}. \tag{2.49}$$

2.4.2 Recursive approach

Here, the multilayered medium is the background and the target is the contrast. The contribution of the target can be computed by using (2.44)–(2.46) where "bg" and "c" are replaced by "ml" (multilayered medium) and "t" (target) respectively. Since the multilayered medium is composed of the soil and the air located above it, the soil can be seen as a contrast in free space, and its contribution can be computed by using (2.44)–(2.46) where "bg" and "c" are replaced by "fs" and "soil" respectively. Developing (2.15) accordingly yields:

$$\begin{aligned}
\Gamma^{(\text{ml, t})} &= \Gamma^{(\text{ml})} + \Gamma^{(\text{t})} \\
&= \Gamma^{(\text{fs})} + \Gamma^{(\text{soil})} + \Gamma^{(\text{t})} \\
&= \Gamma^{(\text{fs})} + (\underline{I}_{AT1})^T \underline{\underline{R}}_1^{(\text{soil})} \underline{I}_{AT1}^{(\text{ml})} + \left(\underline{I}_{AT2}^{(\text{ml})}\right)^T \underline{\underline{R}}_2^{(\text{t})} \underline{I}_{AT2}^{(\text{ml, t})}
\end{aligned} \tag{2.50}$$

where for the middle term we have used the fact that $\underline{H}_{t1}^{(\mathrm{ml})} = \underline{H}_{t1}^{(\mathrm{fs,\ soil})}$. Subscripts "1" and "2" are introduced to emphasize the fact that current and field basis that differ by shape and size can be used for the soil and target contributions (they can also differ from those used in the total approach). By direct application of (2.39) we have that

$$\underline{I}_{AT1}^{(\mathrm{ml})} = \left(\underline{\underline{I}} - \underline{\underline{H}}_{f1}\underline{\underline{G}}_1^{(\mathrm{soil})}\right)^{-1} \underline{I}_{AT1} \tag{2.51}$$

$$\underline{I}_{AT2}^{(\mathrm{ml,\ t})} = \left(\underline{\underline{I}} - \underline{\underline{H}}_{f2}^{(\mathrm{ml})}\underline{\underline{G}}_2^{(\mathrm{t})}\right)^{-1} \underline{I}_{AT2}^{(\mathrm{ml})}. \tag{2.52}$$

Finally, it is shown in appendix A.3 that

$$\underline{\underline{H}}_f^{(\mathrm{ml})} = \left(\underline{\underline{I}} - \underline{\underline{H}}_f\underline{\underline{G}}^{(\mathrm{soil})}\right)^{-1} \underline{\underline{H}}_f. \tag{2.53}$$

To compute $\underline{\underline{G}}^{(\mathrm{soil})}$ using (2.36), we need $\left(\mathbf{e}_{\mathrm{soil},l}^{(\mathrm{fs})}, \mathbf{h}_{\mathrm{soil},l}^{(\mathrm{fs})}\right)$, which are given by (2.55) and its dual expression (section 2.4.4.2).

2.4.3 Comparison of both approaches

As in (2.50) contributions of the soil and of the target appear separately, we can use current and field basis of different sizes and shapes for each problem, which is not the case for (2.47). However, when using the same current and field basis for the soil and target responses in (2.50), it is easy to demonstrate that (2.47) and (2.50) are equivalent (appendix A.4).

For calculating the response of a contrast, the field impinging upon it should be known on its whole surface. The soil surface is infinite, but if the soil is in the far field of the antenna, it is sufficient to model the latter by a dipole and we are still able to accurately predict the soil response [38]. This can be explained by a simple geometrical optics (GO) reasoning. GO replaces the effect of the soil by images of the radiating source, of which the first is obtained through the first soil interface [42]. This image intercepts a small solid angle of the radiation pattern, and therefore the current source must model correctly the radiation pattern only on this small portion of solid angle.

For the response of a target in the soil, the reasoning above is not valid anymore: it suffices that the target intercepts a wide solid angle, or that a scanning is performed above the target, for a description of antenna radiation in terms of a single dipole to become insufficient. In short, a single dipole modeling the antenna suffices for calculating the soil response, while the radiation pattern must be more precisely described for localized targets.

On the contrary, if the antenna approaches the soil, its first image due to the soil intercepts a growing solid angle of its radiation pattern, until the current basis used does not predict accurately enough the fields impinging upon the antenna image. Moreover GO will be invalidated if the soil is not in the far field of the antenna anymore. In those cases a more complete current basis must be used for calculating the soil response. Finally, the fields scattered by the soil and coming back to the antenna will grow in complexity and need a more complete basis for an appropriate description. But if the target still intercepts a small solid angle of the radiation pattern, a simpler current basis can still be used for calculating its response.

Finally, if the antenna is close to the soil to the point that modeling its response would be very imprecise, the recursive formulation makes it possible to measure the soil response, and characterize the antenna properties in the presence of the soil, which still enables the computation of the target response. For this characterization, a new calibration procedure should be defined. We investigate the possibility of using a standard target placed in the ground.

2.4.4 Analysis of each contribution

2.4.4.1 Contribution of the free space

$\Gamma^{(\mathrm{fs})}$ is generated by the reflections occurring within the antenna, and can be obtained as in [38] by making a free space measurement. As it is characteristic of the antenna, it is the third operational parameter of the model (after $\underline{I}_{AT}$ and $\underline{\underline{H}}_f$), and will be called H_i in order to keep consistent notations with them.

2.4.4.2 Contribution of the soil

We will make use of (2.45) in (2.50) for computing $\Gamma^{(\mathrm{soil})}$, as we cannot use (2.46) for contrasts of infinite size. Equation (2.45) necessitates the knowledge of fields $\left(\mathbf{e}^{(\mathrm{fs})}_{\mathrm{soil},k}, \mathbf{h}^{(\mathrm{fs})}_{\mathrm{soil},k}\right)$ produced by the current basis function $\left(\mathbf{j}_k, \mathbf{m}_k\right)$.

We note that the total electric field at any point due to a current basis $\left(\mathbf{j}_k, \mathbf{m}_k\right)$ can be computed using the multilayered media DGFs [27]:

$$\begin{aligned} \mathbf{e}^{(\mathrm{ml})}_k &= \int_{S_{\mathrm{m}'}} \left(\overline{\boldsymbol{\mathcal{G}}}^{(\mathrm{ml})}_{EJ} \cdot \mathbf{j}_k + \overline{\boldsymbol{\mathcal{G}}}^{(\mathrm{ml})}_{EM} \cdot \mathbf{m}_k \right) \mathrm{d}S' \\ &= \mathbf{e}^{(\mathrm{fs})}_{\mathrm{soil},k} + \int_{S_{\mathrm{m}'}} \left(\overline{\boldsymbol{\mathcal{G}}}^{(\mathrm{fs})}_{EJ} \cdot \mathbf{j}_k + \overline{\boldsymbol{\mathcal{G}}}^{(\mathrm{fs})}_{EM} \cdot \mathbf{m}_k \right) \mathrm{d}S' \end{aligned} \tag{2.54}$$

where the electric field $\mathbf{e}^{(\mathrm{fs})}_{\mathrm{soil},k}$ is produced by the soil equivalent currents, and

is therefore given by:

$$\mathbf{e}^{(\mathrm{fs})}_{\mathrm{soil},k} = \int_{S_{\mathrm{m}'}} \left(\overline{\boldsymbol{\mathcal{G}}}^{(\mathrm{soil})}_{EJ} \cdot \mathbf{j}_k + \overline{\boldsymbol{\mathcal{G}}}^{(\mathrm{soil})}_{EM} \cdot \mathbf{m}_k \right) \mathrm{d}S' \tag{2.55}$$

where $\overline{\boldsymbol{\mathcal{G}}}^{(\mathrm{soil})}_{PQ} \triangleq \overline{\boldsymbol{\mathcal{G}}}^{(\mathrm{ml})}_{PQ} - \overline{\boldsymbol{\mathcal{G}}}^{(\mathrm{fs})}_{PQ}$, and $\overline{\boldsymbol{\mathcal{G}}}^{(\mathrm{ml/fs})}_{PQ} = \overline{\boldsymbol{\mathcal{G}}}^{(\mathrm{ml/fs})}_{PQ}(\mathbf{r}, \mathbf{r}')$ is the DGF that links P-type field at $\mathbf{r}$ to Q-type current at $\mathbf{r}'$ in medium (ml/fs). A similar expression for $\mathbf{h}^{(\mathrm{fs})}_{\mathrm{soil},k}$ can be obtained from the above equation by duality.

It has been shown in [22] that the main contributing term to $\overline{\boldsymbol{\mathcal{G}}}^{(\mathrm{soil})}_{PQ}$ is due to the air-soil reflection, and that it decreases as $\frac{1}{|\mathbf{r}+\mathbf{r}'|}$, where $\mathbf{r}$ and $\mathbf{r}'$ are the position vectors of the observation and source points respectively, with the coordinate system being located on the air-soil interface. Therefore, the magnitude of each "element" $R^{(\mathrm{soil})}_{kl}$ of the soil response $\underline{\underline{R}}^{(\mathrm{soil})}$ will decrease as the inverse of twice the antenna height h above the soil, or $\frac{1}{2h}$, and its associated power will decrease as $\frac{1}{(2h)^2}$.

2.4.4.3 Contribution of the target

$\Gamma^{(\mathrm{t})}$ will be computed by using (2.46) in (2.44). The equivalence principle allows one to replace the contrast by equivalent currents $\left(\mathbf{j}_{\mathrm{t},l}, \mathbf{m}_{\mathrm{t},l}\right)$, proportional to the excitation fields $\left(\mathbf{e}^{(\mathrm{ml})}_l, \mathbf{h}^{(\mathrm{ml})}_l\right)$ emitted by $\left(\mathbf{j}_l, \mathbf{m}_l\right)$, and which radiate in the outside and inside medium for the external and internal equivalent problem respectively [43]. For the external (internal) problem, the physical fields are produced outside (inside) of the contrast, and null fields are produced inside (outside). Therefore, in the external equivalent problem, the contrast can be replaced by the currents $\left(\mathbf{j}_{\mathrm{t},l}, \mathbf{m}_{\mathrm{t},l}\right)$ radiating in the whole space filled by the external multilayered medium. Hence the field $\mathbf{e}^{(\mathrm{ml})}_{\mathrm{t},l}$ can be computed from the currents $\left(\mathbf{j}_{\mathrm{t},l}, \mathbf{m}_{\mathrm{t},l}\right)$ by using the DGFs pertaining to multilayered media in a source-field relationship [27]. Practically, the mixed-potential source-field relationship is preferred for its lower order singularities:

$$\begin{aligned}\mathbf{e}^{(\mathrm{ml})}_{\mathrm{t},l} = -j\omega \int_{S_{\mathrm{t}}} \overline{\boldsymbol{\mathcal{K}}}^{(\mathrm{ml})}_{AJ}(\mathbf{r}, \mathbf{r}') \cdot \mathbf{j}_{\mathrm{t},l}(\mathbf{r}')\, \mathrm{d}S' - \frac{j}{\omega} \nabla \int_{S_{\mathrm{t}}} K^{(\mathrm{ml})}_{\phi}(\mathbf{r}, \mathbf{r}')\, \nabla' \cdot \mathbf{j}_{\mathrm{t},l}(\mathbf{r}')\, \mathrm{d}S' \\ + \int_{S_{\mathrm{t}}} \overline{\boldsymbol{\mathcal{G}}}^{(\mathrm{ml})}_{EM}(\mathbf{r}, \mathbf{r}') \cdot \mathbf{m}_{\mathrm{t},l}(\mathbf{r}')\, \mathrm{d}S'\end{aligned} \tag{2.56}$$

where $\overline{\boldsymbol{\mathcal{K}}}^{(\mathrm{ml})}_{AJ}$ is the DGF for the vector potential $\mathbf{A}$, $K^{(\mathrm{ml})}_{\phi}$ is the Green's function for the scalar potential ϕ, and $\overline{\boldsymbol{\mathcal{G}}}^{(\mathrm{ml})}_{EM}$ is the DGF which yields the electric field due to magnetic current [27]. Similar expressions can be obtained by duality for $\mathbf{h}^{(\mathrm{ml})}_{\mathrm{t},l}$ [27]. Combining (2.56) and their dual forms for $\mathbf{h}^{(\mathrm{ml})}_{\mathrm{t},l}$ to the set of

integral equations obtained from the internal problem, and enforcing boundary conditions at the surface of the contrast yield a system of integral equations. These integral equations can be combined in various ways [44], yielding several formulations, such as the combined field integral equation (CFIE) or the Poggio-Miller-Chang-Harrington-Wu-Tsai (PMCHWT) formulation.

A MoM code is used for solving the integral equation formulation, with Rao-Wilton-Glisson (RWG) basis functions for the development of the unknown target equivalent currents $(\mathbf{j}_{t,l}, \mathbf{m}_{t,l})$ and for the testing of the integral equations [45]. The CFIE is used under its transverse-electric/transverse-magnetic/normal-magnetic (tEtHnH) formulation (see section 3.7.3), because the resulting matrix condition number was 1–3 orders of magnitude lower than the CFIE tEnEnH or the PMCHWT formulations (for more details on the formulations, refer to chapter 3). The multilayered medium is taken into account through DGFs implemented following [27], obtained by Sommerfeld integrals of the transmission-line Green's functions and the use of the weighted-average algorithm for their acceleration [46].

As said above, each element of the target response is expressed by the reaction integral (2.46) of the excitation fields multiplied by the target equivalent currents. By linearity, these equivalent currents are proportional to the excitation fields. Since the latter decrease as $\frac{1}{R}$, where R is the distance between the antenna and the target, the target equivalent currents also follow the $\frac{1}{R}$ decrease rule. Therefore, the target reaction integral decreases as $\frac{1}{R^2}$, the target response magnitude also decreases as $\frac{1}{R^2}$ and its associated power as $\frac{1}{R^4}$. Remembering the discussion in the preceding section about the antenna height influence on the magnitude of the soil response, we can deduce that, if the antenna is lifted up, the magnitude of the target response will decrease faster than that of the soil response. This will be numerically demonstrated in section 4.3.2.

2.4.5 Particularization to single current and field basis function

We assume that "AT'" and "AS'" have the same shape, and can be described by a single basis function $(\mathbf{j}_1, \mathbf{m}_1)$. Let us also choose the simplest field basis function, a plane wave propagating vertically, and linearly polarized following the E-plane of the antenna. If we assume that, on the aperture of the antenna, the impinging wave has always the same shape, *i.e.* that of the field basis function, the fields coefficient will be proportional to any linear operation, such

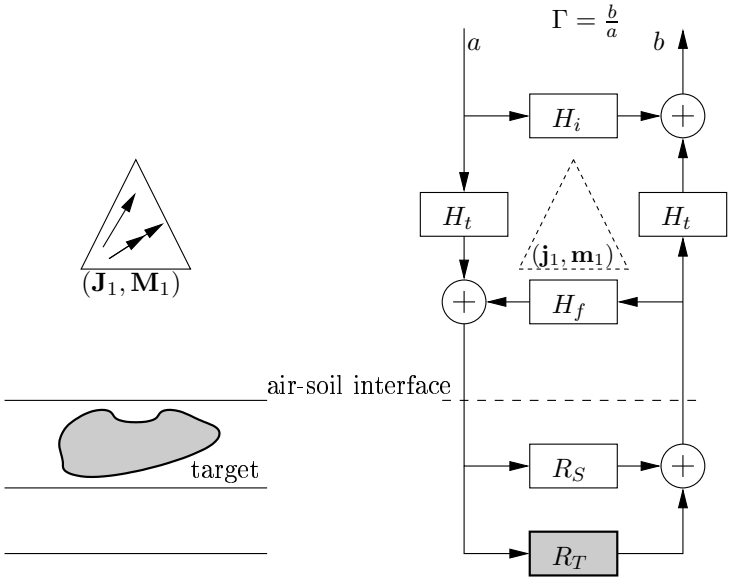

Figure 2.3: Block diagram representation of (2.57). Target is embedded in a stratified medium.

as (2.45), applied to the fields of this wave. Therefore, one can choose the amplitude of the basis plane wave such that $G_{11}^{(\mathrm{c})} = R_{11}^{(\mathrm{c})}$, and (2.47) can be particularized as follows by using (2.48) and (2.49):

$$\Gamma^{(\mathrm{ml,\ t})} = H_i + H_t \left(R_S + R_T\right) \frac{H_t}{1 - H_f \left(R_S + R_T\right)}, \tag{2.57}$$

where $R_S \triangleq R_{11}^{(\mathrm{soil})}$ and $R_T \triangleq R_{11}^{(\mathrm{t})}$ are given by (2.45) and (2.46) respectively, and where $H_t \triangleq I_{AT}^{(\mathrm{fs})}$.

Operational parameters H_i, H_t^2 and H_f can be determined as described in [38], by making measurements in free space and above a PEC plane (considered infinite) at several heights, since for this configuration it is easy to compute $\Gamma^{(\mathrm{soil})} = \Gamma^{(\mathrm{PEC})}$, and $\Gamma^{(\mathrm{t})} = 0$. Equation (2.57) shows that H_t and H_f will depend through R_S upon the choice of the current distribution.

Equation (2.57) can best be understood by representing it under the form of a block diagram as sketched at Fig. 2.3. This representation was first introduced in [47] and later completed by the H_f transfer function in [38], in which the multiple reflections between the soil and the antenna were introduced in the model. The enhancements brought by (2.57) to the model of Lambot—which is limited to the soil alone—are 1) the rigorous establishment of the analytic

expressions for the different contributions to the GPR signal GPR, 2) the addition of the transfer function of the target R_T, and 3) the use of equivalent currents distributions $(\mathbf{j}_1, \mathbf{m}_1)$ allowing to account for the antenna radiation pattern.

The modification of the amplitude and phase of the antenna equivalent currents due to the presence of the soil is accounted for by the multiple reflections operational parameter H_f. However, as said in section 1.5, the model has not been tested for an antenna-soil distance smaller than 20 cm and for frequencies outside the band 0.8–3 GHz. In reality, if the antenna-soil distance is below a given (unknown) limit for a given frequency, the distribution of the antenna equivalent currents will be modified, as will the antenna internal impedance; thereby, the validity and precision of the model will be affected. That limit has not been studied in this work.

2.4.5.1 Dipole basis function

As in [38], let us take the simplest current basis function, a dipole of electric current, located at the phase center of the antenna and directed along $\hat{\mathbf{x}}$:

$$(\mathbf{j}_1, \mathbf{m}_1) = (J_1\, \delta(\mathbf{r} - \mathbf{r}_{\mathrm{pc}})\, \hat{\mathbf{x}}, \mathbf{0})\,. \tag{2.58}$$

J_1 can be chosen to radiate a unit power. With this distribution, (2.45) and (2.46) become respectively:

$$R_S = -\frac{J_1^2}{2}\mathcal{G}^{(\mathrm{soil})}_{E_x J_x} \tag{2.59}$$

$$R_T = -\frac{J_1}{2}\int_{S_{\mathrm{t}}} \left(\hat{\mathbf{x}} \cdot \overline{\boldsymbol{\mathcal{G}}}^{(\mathrm{ml})}_{EJ} \cdot \mathbf{j}_{\mathrm{t},1} - \hat{\mathbf{x}} \cdot \overline{\boldsymbol{\mathcal{G}}}^{(\mathrm{ml})}_{HJ} \cdot \mathbf{m}_{\mathrm{t},1}\right) \mathrm{d}S \tag{2.60}$$

where $\mathcal{G}^{(\mathrm{soil})}_{E_x J_x} \triangleq \hat{\mathbf{x}} \cdot \overline{\boldsymbol{\mathcal{G}}}^{(\mathrm{soil})}_{EJ} \cdot \hat{\mathbf{x}}$ is the $\hat{\mathbf{x}}$-component of the electric field due to a $\hat{\mathbf{x}}$-directed dipole of electric current, and where the last equality is obtained thanks to (2.58) and the reciprocity theorem. In presence of the soil alone, we get the same as (1) in [38], which describes the radar response of the multilayered medium excited by a dipole, where $g^{\uparrow}_{xx} = -\frac{1}{2}\mathcal{G}^{(\mathrm{soil})}_{E_x J_x}$.

2.4.5.2 Huygens cosinusoidal basis function

To better take into account the radiation pattern, a current distribution obtained analytically can be used. Such current distributions are developed for horn antennas in chapter 12 of [39], where it is supposed that contributions from induced currents on other parts of the antenna surface are negligible [36].

Hence the equivalent currents distribution is limited to the aperture of the antenna, and their amplitude distribution is the same as the fundamental TE_{10} mode for a rectangular waveguide having the same dimensions as the aperture; a quadratic phase term accounts for the flaring of the horn transition. This distribution predicts fairly well the main-beam of the far-radiation pattern and the gain of the antenna; that precision is shown to extend to the sidelobes with increasing frequency [36]. The currents are given by:

$$(\mathbf{j}_1, \mathbf{m}_1) = E_0 \cos\left(\frac{\pi}{a}x\right) e^{-\frac{jk}{2}\left(\frac{x^2}{\rho_2}+\frac{y^2}{\rho_1}\right)} \left(-\frac{1}{\eta_0}\hat{\mathbf{y}}_a, \hat{\mathbf{x}}_a\right) \tag{2.61}$$

where E_0 is a constant, x, y is the position in the aperture plane with $(\hat{\mathbf{x}}_a, \hat{\mathbf{y}}_a)$ being the corresponding coordinate system, k is the wavenumber, η_0 is the impedance of plane waves in free space, and a, ρ_1, ρ_2 are geometrical parameters of the antenna. When using this distribution, no simplification of (2.45) and (2.46) can be made. An example of the operational parameters H_i, H_t^2 and H_f, obtained through a calibration for the cosinusoidal distribution, are shown at Fig. 2.4.

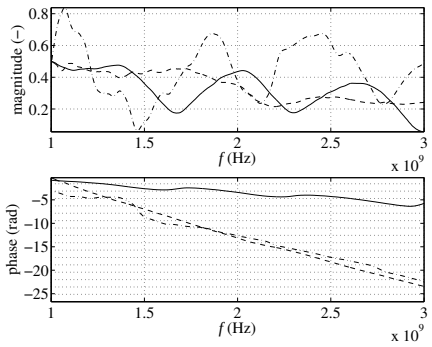

Figure 2.4: Frequency domain H_i (—), H_t^2 (– –) and H_f (– · –) for the cosinusoidal distribution.

2.5 Comparison of measured and simulated GPR signals

In this section we compare measured and computed radar responses of targets embedded within increasingly complex backgrounds: in free space, above a metal plane, and finally buried in a sandbox. As the contribution of the target

to the total radar response can be small, a significant modeling error of its signature might be hardly noticeable in the the total signal. Therefore, we will also compare the computed target signature R_T with its estimated counterpart $\widehat{R}_T$, the latter being obtained by rearranging the measured radar response given by (2.57) as follows:

$$\widehat{R}_T = \frac{\widehat{\gamma}^{(\mathrm{ml,\ t})}}{1 + H_f \widehat{\gamma}^{(\mathrm{ml,\ t})}} - \widehat{R}_S, \tag{2.62}$$

where

$$\begin{aligned} \widehat{\gamma}^{(\mathrm{ml,\ t})} &\triangleq \frac{\Gamma_{\mathrm{meas}}^{(\mathrm{ml,\ t})} - H_i}{H_t^2} \\ &\triangleq \widehat{\gamma}_S + \widehat{\gamma}_T \end{aligned} \tag{2.63}$$

is the estimated radar response of the soil and target, with the antenna internal reflections removed, and normalized by H_t^2. $\widehat{\gamma}_S$ and $\widehat{\gamma}_T$ are intermediate quantities that can be seen as approximations of the soil and target signatures $\widehat{R}_S$ and $\widehat{R}_T$, with the multiple reflections not filtered out. They are defined from (2.57) as follows:

$$\widehat{\gamma}_{S,T} \triangleq \frac{\widehat{R}_{S,T}}{1 - H_f \left(\widehat{R}_S + \widehat{R}_T \right)}. \tag{2.64}$$

Similarly, for the soil we will present its computed R_S and estimated $\widehat{R}_S$, as well as $\widehat{\gamma}_S$. This presentation of the results allows for a validation of both the accuracy of the complete GPR model and the proposed methodology for the target radar signature extraction. Finally, it is worth mentioning that classical background subtraction would only yield $\widehat{\gamma}_T$ but does not provide R_T.

2.5.1 Iron cylinder in free space

The free space configuration serves a double objective: 1) to assess the validity of the target contribution $\Gamma^{(\mathrm{t})}$ in (2.57), and 2) to validate the free space module of the MoM numerical algorithm used to compute the target equivalent currents.

The experimental setup corresponding to Fig. 2.5 consists of an iron cylinder of diameter 11.7 cm and height 6.3 cm, placed at nadir of the horn antenna, 24.3 cm away from the aperture. Fig. 2.5 (b) shows that operational parameter H_i is responsible for the first reflections in the time domain (antenna feed and aperture). Obviously, the radar response of the target has a smaller contribution to the total radar signal than the internal reflections. This is however

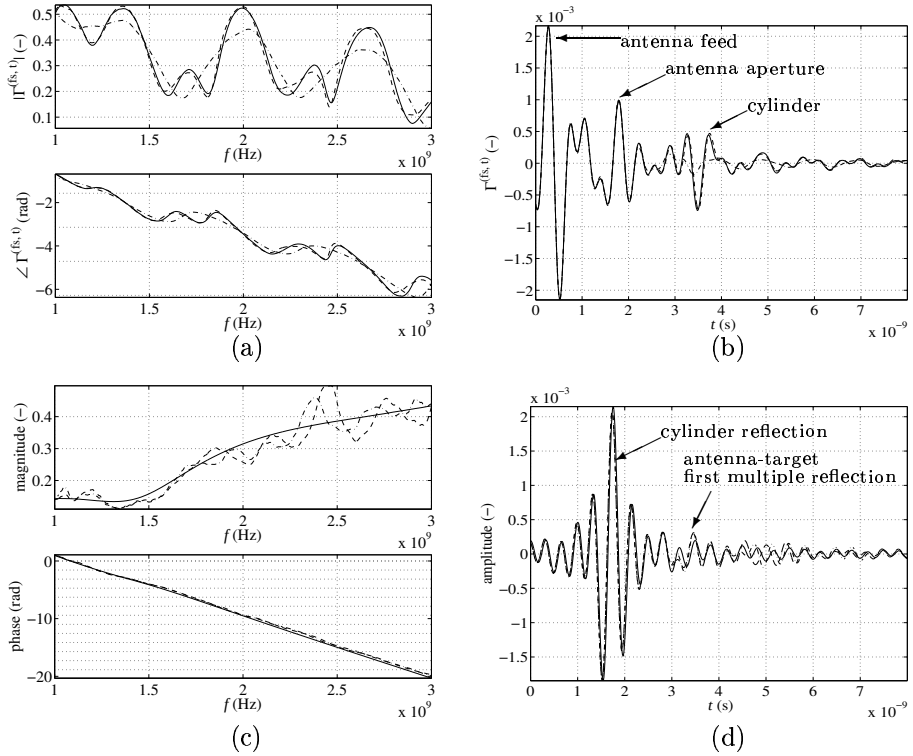

Figure 2.5: Top: (a) frequency and (b) time domain measured (—) and computed (– –) $\Gamma^{(fs,\ t)}$ for iron cylinder in free space. H_i (– · –) is shown for comparison. Bottom: (c) frequency and (d) time domain $\widehat{\gamma}_T$ (– –), $\widehat{R}_T$ (– · –) and R_T (—). Since $\Gamma^{(fs,\ t)}$ is measured at the waveguide-antenna connector and $\widehat{\gamma}_T$ or $\widehat{R}_T$ are quantities estimated on the antenna aperture, arrival time of cylinder signal differs between (b) and (d).

not crucial, since H_i is stable in time and can easily be subtracted from the total signal. Nevertheless, minimizing H_i is a main concern in the design of a monostatic GPR antenna.

Fig. 2.5 (c) demonstrates the effect of extracting $\widehat{R}_T$ by using (2.62): it shows that $\widehat{R}_T$ is "closer" to its computed counterpart R_T than $\widehat{\gamma}_T$. The filtering of the multiple reflections could still be improved by using more field basis functions, as we attribute the remaining error to the shape of the wavefront scattered by the target, which differs from a plane wave. Indeed, the antenna-target first multiple reflection has not been completely filtered from $\widehat{R}_T$. However, while this is obvious at Fig. 2.5 (c) in the frequency domain, it

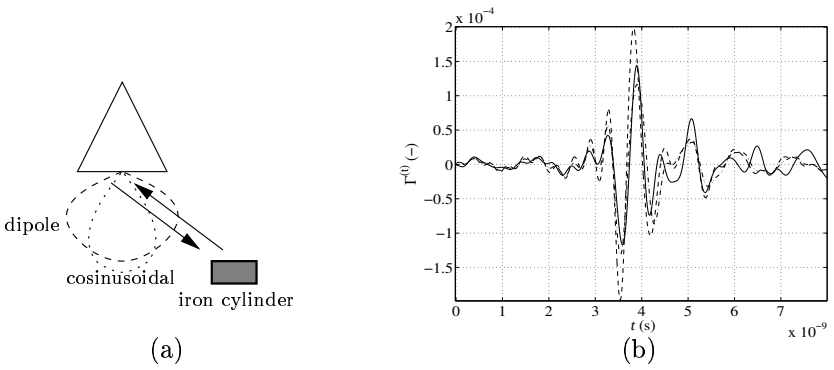

Figure 2.6: (a) Physical configuration for offset iron cylinder experiment. Dipole and cosinusoidal radiation patterns are schematically sketched. Center of cylinder is located at 35° away from main lobe axis. (b) Time domain $\Gamma^{(t)}$ of offset iron cylinder: measured (—), computed for cosinusoidal (– · –) and dipole (– –) distributions.

is much less visible in the time domain as seen at Fig. 2.5 (d). Note that operational parameter H_t^2 introduces a delay, hence filtering it out from $\Gamma^{(\mathrm{fs},\ \mathrm{t})}$ for obtaining $\widehat{\gamma}_T$ or $\widehat{R}_T$—*e.g.*, going from Fig. 2.5 (b) to Fig. 2.5 (d)—will modify the arrival time of the cylinder response. In fact, $\Gamma^{(\mathrm{fs},\ \mathrm{t})}$ is measured at the waveguide-antenna connector, while $\widehat{\gamma}_T$ or $\widehat{R}_T$ are quantities estimated on the antenna aperture, since H_t^2 is the transfer function of the round-trip between the waveguide-antenna connector and the antenna aperture.

To compare the dipole and cosine models, free space experiments were done with the iron cylinder gradually shifted away from the antenna main lobe axis. Fig. 2.6 shows that, if the target is moved away the main lobe axis, the dipole model overestimates the radar signal, while the cosinusoidal model behaves correctly. This is because the cosinusoidal model predicts much better the antenna radiation pattern than the dipole. Moreover, the cosinusoidal model takes into account the variation of this pattern with frequency.

2.5.2 Iron cylinder above a metal plane

This configuration is a simple test where all terms in (2.57) and the multilayer module of the MoM algorithm are involved. We used the iron cylinder of diameter 11.7 cm and height 6.3 cm, placed at nadir of horn antenna at 18.7 cm away from the aperture, above a metal plane (supposed infinite) placed

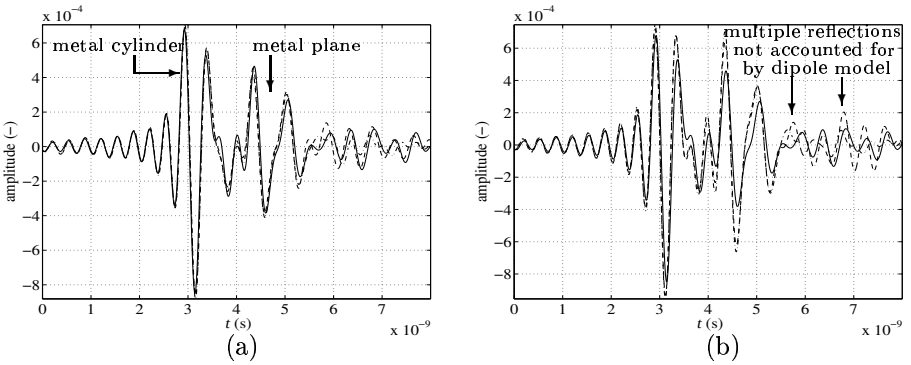

Figure 2.7: Measured (—) and simulated with $H_f \neq 0$ (– · –) and with $H_f = 0$ (– –) radar signals $\Gamma^{(ml,\ t)} - H_i$ of iron cylinder above metal plane. (a) Cosinusoidal and (b) dipole distribution.

at 37.9 cm from the aperture. Fig. 2.7 (a), which concerns the cosinusoidal distribution, validates (2.57) and shows that little error is made in removing the contribution of H_i from $\Gamma_{\text{meas}}^{(\text{ml},\ \text{t})}$.

Comparison between Fig. 2.7 (a) and (b) illustrates the need for having a more "physical" antenna current distribution than the electric dipole of current. With the dipole model, the metal plane reflection is overestimated because the real radiation pattern is more focused. Therefore, because the solid angle subtended by the cylinder covers a large part of the beamwidth, the cylinder intercepts in reality more of the radiated power than what would be the case for the dipole. Therefore the cosinusoidal distribution better predicts the power incident on the metal plane. Moreover, if one compares the late time signatures of Fig. 2.7 (a) and (b), it can be seen that the multiple reflections are better filtered out by the cosinusoidal model than by the dipole model.

2.5.3 Iron cylinder buried in a multilayered medium

This test is the next logical step with regards to the setup complexity. A schematic drawing of the experiment configuration is given at Fig. 2.8. The complex relative permittivity of the soil was obtained from a radar measurement and by using the method of Lambot *et al.* for the soil EM parameters extraction [38], and was found to be $\varepsilon_r = 4.4 - j0.33$ in the frequency band (1–3 GHz).

Fig. 2.9 shows that the agreement between $\widehat{R}_{S,T}$ and their computed coun-

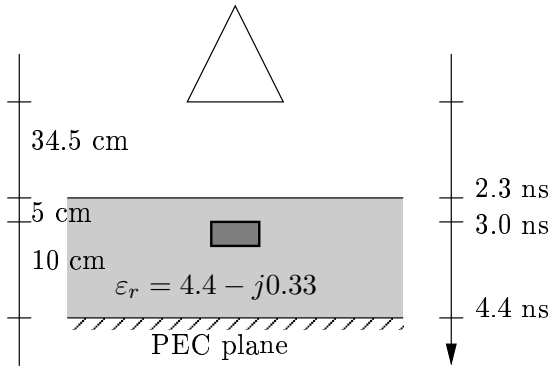

Figure 2.8: Locations and corresponding round-trip times of the different elements of the buried iron cylinder experimental setup (drawing not on scale).

terparts $R_{S,T}$ is very good. Moreover, the time information of Fig. 2.9 (b) and (d) for R_S and R_T corresponds exactly to that given at Fig. 2.8. Finally, the filtering of the multiple reflections does not seem to induce significant changes from $\widehat{\gamma}_{S,T}$ to $\widehat{R}_{S,T}$.

2.5.4 Air-filled target buried in a multilayered medium

This test validates the entire radar model and the MoM algorithm for penetrable scatterers. The setup is similar to that of section 2.5.3. It consists in an air-filled cylindrical target, of 5 cm in height and 10 cm in diameter, buried 2.5 cm deep in a multilayered medium with three layers: air, dry sand layer of 14.5 cm thickness, and a metal plane for controlling the boundary conditions. The complex relative permittivity of the soil was found to be $\varepsilon_r = 2.55 - j0.0$ in the frequency band (0.8–3 GHz). The antenna aperture is at 26.8 cm from the sand surface. Again, the time information of Fig. 2.10 (b) and (d) for R_S and R_T corresponds to that given by simple paths lengths calculations.

Fig. 2.10 shows the accuracy of the entire radar model, as $\widehat{R}_S$ (top) and $\widehat{R}_T$ (bottom) agree very well with their respective computed counterparts. The magnitude of R_S is in average larger than that of R_T. This can be explained by the fact that the target scatters less energy than the soil, especially for large antenna-target distance and/or small soil-target dielectric contrast. Furthermore, the target signal is caused by excitation fields that have to go through the air-soil interface, are scattered by the target, and those scattered fields have to cross the interface again before being picked up by the antenna.

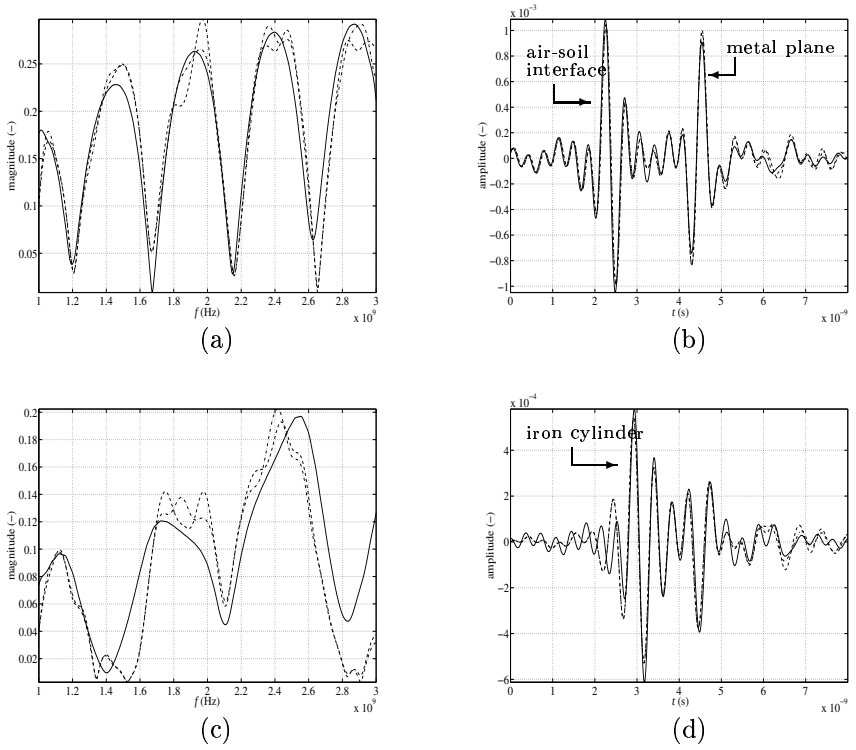

Figure 2.9: Top: (a) frequency and (b) time domain $\widehat{\gamma}_S$ (– –), $\widehat{R}_S$ (– · –) and computed R_S (—). Bottom: (c) frequency and (d) time domain $\widehat{\gamma}_T$ (– –), $\widehat{R}_T$ (– · –) and computed R_T (—).

As seen in (2.57), the magnitude of the scattering currents induced by the multiple reflections is dictated by the product $H_f R_S$ and $H_f R_T$ respectively for soil- and target-antenna multiple reflections. H_f is relatively significant for our antenna (see Fig. 2.4) and, as just said, $R_S > R_T$. Moreover, the soil multiple reflections act on soil and target contributions. Therefore, Fig. 2.10 (a) shows a large improvement of the soil signature estimation when the antenna-soil multiple reflections are filtered out of $\widehat{\gamma}_S$, while Fig. 2.4 (c) demonstrates that the filtering of both multiple reflections from $\widehat{\gamma}_T$ improves the result, but less significantly for the antenna-target multiple reflections.

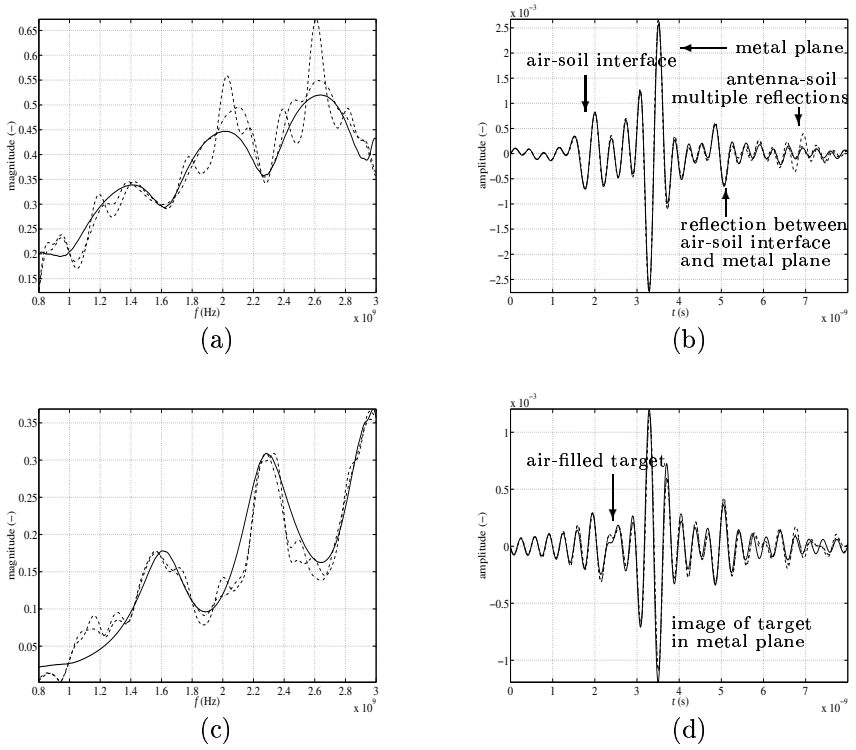

Figure 2.10: Top: (a) frequency and (b) time domain $\widehat{\gamma}_S$ (– –), $\widehat{R}_S$ (– · –) and computed R_S (—). Bottom: (c) frequency and (d) time domain $\widehat{\gamma}_T$ (– –), $\widehat{R}_T$ (– · –) and computed R_T (—).

2.5.5 Multibody buried in a multilayered medium

It is interesting to see how the response of the target is modified by the presence of another close-by scattering body. In this regard, an experiment involving an air-filled Tupperware (the desired target) and a metal parallelepiped (the clutter) buried side-by-side was performed. The geometry of the experiment is depicted at Fig. 2.11. The resulting target is therefore the "multibody" composed of the Tupperware and the parallelepiped. Fig. 2.12 (a) shows that, besides an unexplained discrepancy between 1.7 and 2.2 GHz, agreement between estimated and computed radar responses of the target is good. We must also note that the filtering of the multiple reflections does not enhance significantly the extraction of the target signature.

Finally, in order to see which part of the target contributes most to the com-

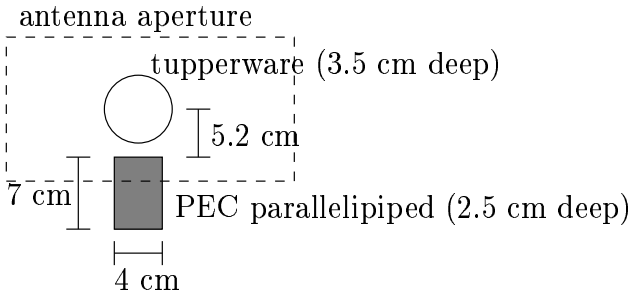

Figure 2.11: Locations of the different elements of the experimental setup (drawing not on scale). Tupperware has diameter of 6 cm and height of 5 cm. Parallelepiped has dimensions 4 *cm*×4 *cm*×7 *cm.*

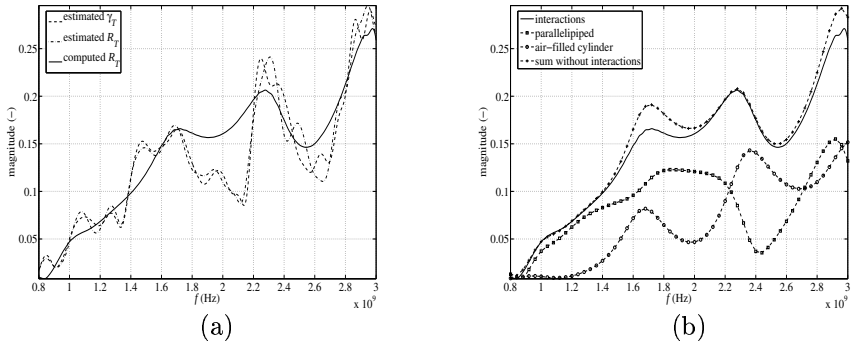

Figure 2.12: (a) Comparison of $\widehat{\gamma}_T$ *and* $\widehat{R}_T$ *with computed* R_T*. (b) Comparison of total* R_T *with radar responses of Tupperware and parallelepiped taken separately, and with cumulated Tupperware and parallelepiped radar responses but where mutual interactions have been ignored.*

plete radar signature, we have computed the Tupperware and parallelepiped signatures separately. Fig. 2.12 (b) shows that neither of these signatures resembles the signature of the multibody system. However, the signal made up of the addition of these two signatures—which is the multibody signature but with the interactions between the Tupperware and the parallelepiped neglected—is close to the true multibody signature. This result is however particular to the experiment, and we cannot extrapolate it to another situation.

2.6 Summary and perspectives

The setup of an accurate model of a monostatic SFCW GPR in presence of buried targets has been presented. The antenna is described by its current distribution and by operational parameters that describe the complex radiation processes occurring in the presence of the soil and target. These parameters can be estimated by a simple calibration procedure, obviating the difficulty of setting up a precise numerical model of the antenna. The model, derived for arbitrary antenna equivalent current distributions, has been applied using dipole and cosinusoidal distributions. It yielded very good quantitative similarities between estimated and simulated target signatures, especially for the cosinusoidal distribution, thereby validating the complete radar equation and its associated methodology for signature estimation, as well as the numerical algorithms used in the computations. The results also showed that accounting for the antenna-soil and to a lesser extent antenna-target multiple reflections in the process of target signature estimation slightly enhances the quality of the signature estimation with respect to a classical background subtraction. Finally, the decoupling of the antenna and target modeling allows for a great modularity in the use of the complete model, as the soil and target radar responses R_S and R_T can be computed independently and combined in (2.57) with the operational parameters H_i, H_t and H_f resulting from the characterization of a given radar system for having its complete simulated Γ.

We did not investigate the effect of the soil roughness on the GPR responses. This is however perfectly possible without modifying the model. The comparison between measured and simulated radar responses would then port solely on their respective statistical properties, since they both become random variables (see section 1.5 for a more detailed discussion).

The GPR model has been experimentally validated for antenna heights above the soil ranging from 40 cm down to 20 cm, and for a frequency band of 0.8–3 GHz. The lowest height to which the model is still correct for a given frequency has not been investigated, and the model remains to be validated—or modified—for antenna heights above the soil of a few centimeters.

Finally, it must be recalled that horn antennas have a phase center whose position w.r.t. the aperture varies with the frequency [39]. Although the effect of the phase center position on the phase of the aperture equivalent currents is characterized through a calibration, it is possible that it causes an additional error in the soil radar response computation. This, combined with the fact that the ridged-horn antenna is a strong scatterer, pleads in favor of using a more

appropriate antenna such as a bow-tie.

Future works include the extension of the model to bistatic and multistatic systems. The extension to more general antenna currents and incident fields, and the corresponding generalization of the characterization procedure, is also foreseen, this for taking into account multiple reflections in case of scattering by targets located away the main beam axis. In order to simplify the characterization we consider the possibility to partly compute $\underline{\underline{H}}_f$ by numerical modeling of the antenna.

Chapter 3

Target numerical electromagnetic modeling

3.1 Introduction

Recently, research has focused on studying the scattering of multiple inhomogeneous bodies embedded in a homogeneous medium *via* the MoM [48, 24, 49]. More recently, the generalization went one step further when Taskinen *et al.* tackled thoroughly the problems caused by junctions [50], which arise when dielectric bodies interpenetrate each other. On another hand, Carin *et al.* explored the problem caused by a homogeneous body (PEC or dielectric) embedded in a two-layers medium [33]. However, no publications are available for multiple scatterers, possibly inhomogeneous, embedded within a multilayered medium. Yet the possibility of studying the scattering by inhomogeneous bodies is necessary if, for example, one wants to evaluate the effect of an air void within the target on its radar response (see section 4.3.5).

This chapter deals with the establishment of the surface integral equations (SIEs) for multiple perfectly conducting (PEC) and penetrable inhomogeneous scatterers embedded in stratified media. The integral equations systems will be exposed with gradual generality. In section 3.2 the Huygens surface equivalence principle is established for homogeneous and stratified medium. These results are used in section 3.3 for establishing the SIEs for homogeneous bodies (PEC and dielectric) embedded in multilayered media. Sections 3.4 and 3.5 go one step further by deriving these SIEs for inhomogeneous bodies. As the resulting

systems of SIEs contain more equations than unknowns (which are the surface equivalent currents), it is necessary to combine these equations in order to equate their number to that of the unknowns. This is done in section 3.6. Finally, section 3.7 develops the MoM solution for the various formulations of the system of SIEs, and section 3.8 concludes this chapter.

3.2 The Huygens surface equivalence principle

3.2.1 Derivation for homogeneous media

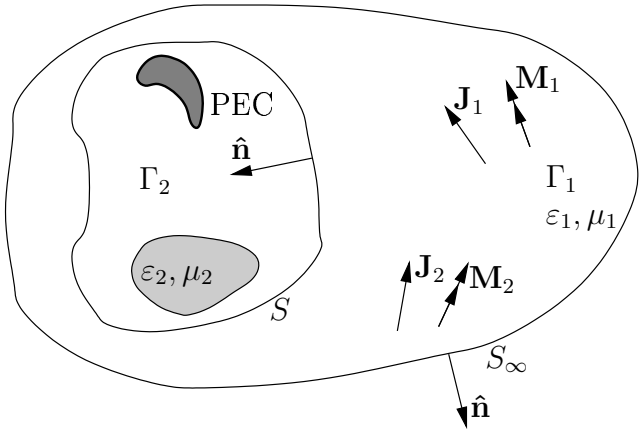

Figure 3.1: Two regions Γ_1 and Γ_2 separated by mathematical surface S.

The derivation of the surface equivalence principle is inspired from [51, chapter 1], but is presented differently here. To derive the surface equivalence principle, consider the hypothetical situation depicted at Fig. 3.1, which shows two regions of space separated by a mathematical surface S. Region 1 is homogeneous, with EM parameters $\varepsilon_1 = \varepsilon_0\varepsilon_{r1}$ and $\mu_1 = \mu_0\mu_{r1}$, whereas region 2 contains perfect electric conducting (PEC) and dielectric inhomogeneities characterized by $\varepsilon_2 = \varepsilon_0\varepsilon_{r2}, \mu_2 = \mu_0\mu_{r2}$. ε_{ri} and μ_{ri} are respectively the relative dielectric permittivity and magnetic permeability of medium i. A first source $(\mathbf{J}_1, \mathbf{M}_1)$, located in Γ_1, radiates in homogeneous space with the same EM parameters as Γ_1, and produces fields $(\mathbf{E}_1, \mathbf{H}_1)$ throughout Γ_1. A second source $(\mathbf{J}_2, \mathbf{M}_2)$, located in Γ_1, radiates in the presence of the inhomogeneities and produces fields $(\mathbf{E}_2, \mathbf{H}_2)$ throughout Γ_1. In Peterson *et al.* [51], the source $(\mathbf{J}_2, \mathbf{M}_2)$ was considered located in Γ_2, which leads to a different expression of

the surface equivalence principle. We will compare our result to those derived in [51] at the end of this section. The fields of both sources satisfy the radiation condition at infinity (S_∞).

Throughout Γ_1, Maxwell's curl equations can be written

$$\nabla \times \mathbf{E}_1 = -j\omega\mu_1\mathbf{H}_1 - \mathbf{M}_1 \tag{3.1}$$
$$\nabla \times \mathbf{H}_1 = j\omega\varepsilon_1\mathbf{E}_1 + \mathbf{J}_1 \tag{3.2}$$
$$\nabla \times \mathbf{E}_2 = -j\omega\mu_1\mathbf{H}_2 - \mathbf{M}_2 \tag{3.3}$$
$$\nabla \times \mathbf{H}_2 = j\omega\varepsilon_1\mathbf{E}_2 + \mathbf{J}_2. \tag{3.4}$$

Therefore, in Γ_1 we can construct the following equations:

$$\mathbf{H}_2 \cdot \nabla \times \mathbf{E}_1 = -j\omega\mu_1\mathbf{H}_2 \cdot \mathbf{H}_1 - \mathbf{H}_2 \cdot \mathbf{M}_1 \tag{3.5}$$
$$\mathbf{E}_2 \cdot \nabla \times \mathbf{H}_1 = j\omega\varepsilon_1\mathbf{E}_2 \cdot \mathbf{E}_1 + \mathbf{E}_2 \cdot \mathbf{J}_1 \tag{3.6}$$
$$\mathbf{H}_1 \cdot \nabla \times \mathbf{E}_2 = -j\omega\mu_1\mathbf{H}_1 \cdot \mathbf{H}_2 - \mathbf{H}_1 \cdot \mathbf{M}_2 \tag{3.7}$$
$$\mathbf{E}_1 \cdot \nabla \times \mathbf{H}_2 = j\omega\varepsilon_1\mathbf{E}_1 \cdot \mathbf{E}_2 + \mathbf{E}_1 \cdot \mathbf{J}_2. \tag{3.8}$$

By combining these equations, we obtain:

$$\begin{aligned}\mathbf{H}_2 \cdot \nabla \times \mathbf{E}_1 - \mathbf{E}_1 \cdot \nabla \times \mathbf{H}_2 + \mathbf{E}_2 \cdot \nabla \times \mathbf{H}_1 - \mathbf{H}_1 \cdot \nabla \times \mathbf{E}_2 = \\ - j\omega\mu_1\mathbf{H}_2 \cdot \mathbf{H}_1 - \mathbf{H}_2 \cdot \mathbf{M}_1 - j\omega\varepsilon_1\mathbf{E}_1 \cdot \mathbf{E}_2 - \mathbf{E}_1 \cdot \mathbf{J}_2 \\ + j\omega\varepsilon_1\mathbf{E}_2 \cdot \mathbf{E}_1 + \mathbf{E}_2 \cdot \mathbf{J}_1 + j\omega\mu_1\mathbf{H}_1 \cdot \mathbf{H}_2 + \mathbf{H}_1 \cdot \mathbf{M}_2\end{aligned} \tag{3.9}$$

which can be further simplified as

$$\nabla \cdot (\mathbf{E}_1 \times \mathbf{H}_2 - \mathbf{E}_2 \times \mathbf{H}_1) = \mathbf{E}_2 \cdot \mathbf{J}_1 - \mathbf{H}_2 \cdot \mathbf{M}_1 - \mathbf{E}_1 \cdot \mathbf{J}_2 + \mathbf{H}_1 \cdot \mathbf{M}_2. \tag{3.10}$$

Eq. (3.10) is the *Lorentz reciprocity theorem* [43]. Integrating both sides of (3.10) over Γ_1 and applying the divergence theorem

$$\iiint_{\Gamma_1} \nabla \cdot \mathbf{Q} \mathrm{d}v = \iint_S \mathbf{Q} \cdot \hat{\mathbf{n}} \mathrm{d}S + \iint_{S_\infty} \mathbf{Q} \cdot \hat{\mathbf{n}} \mathrm{d}S \tag{3.11}$$

where the normal vector $\hat{\mathbf{n}}$ points outside Γ_1, produce

$$\begin{aligned}\iint_S (\mathbf{E}_1 \times \mathbf{H}_2 - \mathbf{E}_2 \times \mathbf{H}_1) \cdot \hat{\mathbf{n}} \mathrm{d}S = \\ \iiint_{\Gamma_1} (\mathbf{E}_2 \cdot \mathbf{J}_1 - \mathbf{H}_2 \cdot \mathbf{M}_1 - \mathbf{E}_1 \cdot \mathbf{J}_2 + \mathbf{H}_1 \cdot \mathbf{M}_2) \ \mathrm{d}v.\end{aligned} \tag{3.12}$$

Thanks to the vector identity $\mathbf{c}\cdot(\mathbf{a}\times\mathbf{b}) = (\mathbf{c}\times\mathbf{a})\cdot\mathbf{b} = (-\mathbf{a}\times\mathbf{c})\cdot\mathbf{b}$, (3.12) can be rewritten as

$$\iint_S (\mathbf{E}_1\cdot(-\hat{\mathbf{n}}\times\mathbf{H}_2) - \mathbf{H}_1\cdot(-\mathbf{E}_2\times\hat{\mathbf{n}}))\ \mathrm{d}S = \iiint_{\Gamma_1} (\mathbf{E}_2\cdot\mathbf{J}_1 - \mathbf{H}_2\cdot\mathbf{M}_1 - \mathbf{E}_1\cdot\mathbf{J}_2 + \mathbf{H}_1\cdot\mathbf{M}_2)\ \mathrm{d}v \quad (3.13)$$

which is a generalized statement of reciprocity. Now, let us suppose that the sources $(\mathbf{J}_1, \mathbf{M}_1)$ are

$$\mathbf{J}_1 = \hat{\mathbf{u}}\delta(\mathbf{r}-\mathbf{r}') \quad (3.14)$$

$$\mathbf{M}_1 = 0 \quad (3.15)$$

where $\mathbf{r}$ denotes the source point in region 1, and $\mathbf{r}'$ represents the integration variable in (3.13). For these sources, (3.13) can be rewritten as

$$\hat{\mathbf{u}}\cdot\mathbf{E}_2|_{\mathbf{r}} = \iint_S [\mathbf{E}_1\cdot(-\hat{\mathbf{n}}\times\mathbf{H}_2) - \mathbf{H}_1\cdot(-\mathbf{E}_2\times\hat{\mathbf{n}})]\ \mathrm{d}S' + \iiint_{\Gamma_1} (\mathbf{E}_1\cdot\mathbf{J}_2 - \mathbf{H}_1\cdot\mathbf{M}_2)\ \mathrm{d}v' \quad (3.16)$$

where $\mathbf{E}_1$ and $\mathbf{H}_1$ are the fields produced at location $\mathbf{r}'$ in an infinite homogeneous space by sources $(\mathbf{J}_1, \mathbf{M}_1)$ located at $\mathbf{r}$. These fields can be obtained in terms of the homogeneous space Green's function by the following source-field relationships [51]

$$\mathbf{E}_1(\mathbf{r}') = \frac{\nabla'\nabla'\cdot + k_1^2}{j\omega\varepsilon_1}\left(\hat{\mathbf{u}}\frac{e^{-jk_1|\mathbf{r}-\mathbf{r}'|}}{4\pi|\mathbf{r}-\mathbf{r}'|}\right) \quad (3.17)$$

$$\mathbf{H}_1(\mathbf{r}') = \nabla'\times\left(\hat{\mathbf{u}}\frac{e^{-jk_1|\mathbf{r}-\mathbf{r}'|}}{4\pi|\mathbf{r}-\mathbf{r}'|}\right) \quad (3.18)$$

where $k_1 = \omega\sqrt{\varepsilon_1\mu_1}$. Note that the derivatives are taken with respect to the prime coordinates. However, thanks to the symmetry of the Green's function, it is easily shown that

$$\nabla'\nabla'\cdot\left(\hat{\mathbf{u}}\frac{e^{-jk_1|\mathbf{r}-\mathbf{r}'|}}{4\pi|\mathbf{r}-\mathbf{r}'|}\right) = \nabla\nabla\cdot\left(\hat{\mathbf{u}}\frac{e^{-jk_1|\mathbf{r}-\mathbf{r}'|}}{4\pi|\mathbf{r}-\mathbf{r}'|}\right) \quad (3.19)$$

$$\nabla'\times\left(\hat{\mathbf{u}}\frac{e^{-jk_1|\mathbf{r}-\mathbf{r}'|}}{4\pi|\mathbf{r}-\mathbf{r}'|}\right) = -\nabla\times\left(\hat{\mathbf{u}}\frac{e^{-jk_1|\mathbf{r}-\mathbf{r}'|}}{4\pi|\mathbf{r}-\mathbf{r}'|}\right). \quad (3.20)$$

With this in hand, (3.16) becomes

$$\hat{\mathbf{u}}\cdot\mathbf{E}_2|_{\mathbf{r}} = \iint_S \left[\frac{\nabla\nabla\cdot + k_1^2}{j\omega\varepsilon_1}\left(\hat{\mathbf{u}}\frac{e^{-jk_1|\mathbf{r}-\mathbf{r}'|}}{4\pi|\mathbf{r}-\mathbf{r}'|}\right)\cdot(-\hat{\mathbf{n}}\times\mathbf{H}_2)\right.$$
$$\left. +\nabla\times\left(\hat{\mathbf{u}}\frac{e^{-jk_1|\mathbf{r}-\mathbf{r}'|}}{4\pi|\mathbf{r}-\mathbf{r}'|}\right)\cdot(-\mathbf{E}_2\times\hat{\mathbf{n}})\right]\,\mathrm{d}S'$$
$$+\iiint_{\Gamma_1}\left[\frac{\nabla\nabla\cdot+k_1^2}{j\omega\varepsilon_1}\left(\hat{\mathbf{u}}\frac{e^{-jk_1|\mathbf{r}-\mathbf{r}'|}}{4\pi|\mathbf{r}-\mathbf{r}'|}\right)\cdot\mathbf{J}_2+\nabla\times\left(\hat{\mathbf{u}}\frac{e^{-jk_1|\mathbf{r}-\mathbf{r}'|}}{4\pi|\mathbf{r}-\mathbf{r}'|}\right)\cdot\mathbf{M}_2\right]\,\mathrm{d}v'. \tag{3.21}$$

The derivations appearing in the surface integral of (3.21) are taken with respect to the unprimed coordinates, while the surface integration is to be performed in primed coordinates, with $(\mathbf{E}_2,\mathbf{H}_2)$ functions of these primed coordinates. Therefore, the first term of the surface integral in (3.21) can be modified using:

$$\begin{aligned}(-\hat{\mathbf{n}}\times\mathbf{H}_2)\cdot\nabla\nabla\cdot\left(\hat{\mathbf{u}}\frac{e^{-jk_1|\mathbf{r}-\mathbf{r}'|}}{4\pi|\mathbf{r}-\mathbf{r}'|}\right) &= \sum_{i=1}^{3}\hat{\mathbf{x}}_i\cdot(-\hat{\mathbf{n}}\times\mathbf{H}_2)\frac{\partial}{\partial x_i}\frac{\partial}{\partial u}\left(\frac{e^{-jk_1|\mathbf{r}-\mathbf{r}'|}}{4\pi|\mathbf{r}-\mathbf{r}'|}\right)\\ &= \frac{\partial}{\partial u}\sum_{i=1}^{3}\frac{\partial}{\partial x_i}\left(\hat{\mathbf{x}}_i\cdot(-\hat{\mathbf{n}}\times\mathbf{H}_2)\frac{e^{-jk_1|\mathbf{r}-\mathbf{r}'|}}{4\pi|\mathbf{r}-\mathbf{r}'|}\right)\\ &= \hat{\mathbf{u}}\cdot\nabla\nabla\cdot\left((-\hat{\mathbf{n}}\times\mathbf{H}_2)\frac{e^{-jk_1|\mathbf{r}-\mathbf{r}'|}}{4\pi|\mathbf{r}-\mathbf{r}'|}\right)\end{aligned} \tag{3.22}$$

where $\{x_i\}$ denote the three Cartesian variables and u is a variable defined along $\hat{\mathbf{u}}$. Furthermore, the second term of the surface integral in (3.21) can be modified using vector identities and the fact that $\hat{\mathbf{u}}$ is a constant:

$$\begin{aligned}\nabla\times\left(\hat{\mathbf{u}}\frac{e^{-jk_1|\mathbf{r}-\mathbf{r}'|}}{4\pi|\mathbf{r}-\mathbf{r}'|}\right)\cdot(-\mathbf{E}_2\times\hat{\mathbf{n}}) &= \nabla\left(\frac{e^{-jk_1|\mathbf{r}-\mathbf{r}'|}}{4\pi|\mathbf{r}-\mathbf{r}'|}\right)\times\hat{\mathbf{u}}\cdot(-\mathbf{E}_2\times\hat{\mathbf{n}})\\ &= -\hat{\mathbf{u}}\cdot\nabla\left(\frac{e^{-jk_1|\mathbf{r}-\mathbf{r}'|}}{4\pi|\mathbf{r}-\mathbf{r}'|}\right)\times(-\mathbf{E}_2\times\hat{\mathbf{n}})\\ &= -\hat{\mathbf{u}}\cdot\nabla\times\left((-\mathbf{E}_2\times\hat{\mathbf{n}})\frac{e^{-jk_1|\mathbf{r}-\mathbf{r}'|}}{4\pi|\mathbf{r}-\mathbf{r}'|}\right).\end{aligned} \tag{3.23}$$

Proceeding in the same way for the terms in the volume integral, substituting these results in (3.21), and moving the derivatives taken with respect to

unprimed variables out of the surface and volume integrals yield:

$$\hat{\mathbf{u}}\cdot\mathbf{E}_2|_{\mathbf{r}} = \hat{\mathbf{u}}\cdot\frac{\nabla\nabla\cdot+k_1^2}{j\omega\varepsilon_1}\iint_S(-\hat{\mathbf{n}}\times\mathbf{H}_2)\,\frac{e^{-jk_1|\mathbf{r}-\mathbf{r}'|}}{4\pi\,|\mathbf{r}-\mathbf{r}'|}\,\mathrm{d}S'$$
$$-\hat{\mathbf{u}}\cdot\nabla\times\iint_S(-\mathbf{E}_2\times\hat{\mathbf{n}})\,\frac{e^{-jk_1|\mathbf{r}-\mathbf{r}'|}}{4\pi\,|\mathbf{r}-\mathbf{r}'|}\,\mathrm{d}S'+\hat{\mathbf{u}}\cdot\frac{\nabla\nabla\cdot+k_1^2}{j\omega\varepsilon_1}\iiint_{\Gamma_1}\mathbf{J}_2\frac{e^{-jk_1|\mathbf{r}-\mathbf{r}'|}}{4\pi\,|\mathbf{r}-\mathbf{r}'|}\,\mathrm{d}v'$$
$$-\hat{\mathbf{u}}\cdot\nabla\times\iiint_{\Gamma_1}\mathbf{M}_2\frac{e^{-jk_1|\mathbf{r}-\mathbf{r}'|}}{4\pi\,|\mathbf{r}-\mathbf{r}'|}\,\mathrm{d}v'. \quad (3.24)$$

Since $\hat{\mathbf{u}}$ was arbitrary, we can withdraw it from (3.24) to obtain:

$$\mathbf{E}_2|_{\mathbf{r}} = \frac{\nabla\nabla\cdot+k_1^2}{j\omega\varepsilon_1}\left\langle G_1(\mathbf{r},\mathbf{r}'),-\hat{\mathbf{n}}\times\mathbf{H}_2(\mathbf{r}')\right\rangle_S-\nabla\times\left\langle G_1(\mathbf{r},\mathbf{r}'),-\mathbf{E}_2(\mathbf{r}')\times\hat{\mathbf{n}}\right\rangle_S$$
$$+\frac{\nabla\nabla\cdot+k_1^2}{j\omega\varepsilon_1}\left\langle G_1(\mathbf{r},\mathbf{r}'),\mathbf{J}_2(\mathbf{r}')\right\rangle_{\Gamma_1}-\nabla\times\left\langle G_1(\mathbf{r},\mathbf{r}'),\mathbf{M}_2(\mathbf{r}')\right\rangle_{\Gamma_1} \quad (3.25)$$

where

$$G_1(\mathbf{r},\mathbf{r}') = \frac{e^{-jk_1|\mathbf{r}-\mathbf{r}'|}}{4\pi\,|\mathbf{r}-\mathbf{r}'|}. \quad (3.26)$$

In (3.25) we have introduced the following compact notation [27]:

$$\left\langle G(\mathbf{r},\mathbf{r}'),F(\mathbf{r}')\right\rangle_\Gamma \triangleq \iiint_\Gamma F(\mathbf{r}')\,G(\mathbf{r},\mathbf{r}')\;\mathrm{d}r', \quad (3.27)$$

where $\langle,\rangle$ denotes an integral of product of two functions $G(\mathbf{r},\mathbf{r}')$ and $F(\mathbf{r}')$ separated by the comma over their common spatial support Γ, with a dot or a cross over the comma indicating a dot or a cross product (if F and G are vector quantities). Field $\mathbf{H}_2$ can be obtained from (3.25) by duality. Eq. (3.25) is a statement that the fields $(\mathbf{E}_2,\mathbf{H}_2)$, produced by the sources $(\mathbf{J}_2,\mathbf{M}_2)$ radiating in presence of the inhomogeneities contained within S, can be expressed in the form of an integration over tangential fields on the surface S of region 2, to which is to be added the direct contribution of the sources as if radiating in the homogeneous space filled by ε_1,μ_1. We can indeed recognize in the volume integration term the well-known source field relation for the electric field in a homogeneous medium [51, p. 7]:

$$\mathbf{E} = \frac{\nabla\nabla\cdot\mathbf{A}_2+k_1^2\mathbf{A}_2}{j\omega\varepsilon_1}-\nabla\times\mathbf{F}_2 \quad (3.28)$$

where $\mathbf{A}_2$, the magnetic vector potential, and $\mathbf{F}_2$, the electric vector potential, are given by a three-dimensional convolution:

$$\mathbf{A}_2(\mathbf{r}') = \left\langle G_1(\mathbf{r},\mathbf{r}'),\mathbf{J}_2(\mathbf{r})\right\rangle \quad (3.29a)$$
$$\mathbf{F}_2(\mathbf{r}') = \left\langle G_1(\mathbf{r},\mathbf{r}'),\mathbf{M}_2(\mathbf{r})\right\rangle \quad (3.29b)$$

Moreover, if we define

$$\mathbf{J}_S \triangleq -\hat{\mathbf{n}} \times \mathbf{H}_2 \tag{3.30}$$

$$\mathbf{M}_S \triangleq -\mathbf{E}_2 \times \hat{\mathbf{n}}, \tag{3.31}$$

it is immediately apparent from the similarity between the surface and volume integration in (3.25) that $\mathbf{E}_2\big|_{\mathbf{r}}$ is the sum of the fields produced by

- the surface current densities $(\mathbf{J}_S, \mathbf{M}_S)$, located on S, which radiate in homogeneous space having constitutive parameters ε_1, μ_1
- the current densities $(\mathbf{J}_2, \mathbf{M}_2)$, also radiating in homogeneous space having constitutive parameters ε_1, μ_1.

A last remark concerns the derivation done in [51], where the source $(\mathbf{J}_2, \mathbf{M}_2)$ was supposed to be located inside Γ_2. This makes disappear the volume integral term in (3.25), leaving only the surface integration contribution. This property is a fundamental theorem of electromagnetics, called the *Huygens surface equivalence principle*: the effect of the source inside Γ_2 is described by the surface currents densities $(\mathbf{J}_S, \mathbf{M}_S)$, which are therefore "equivalent" from the point of view of an observer located outside Γ_2. This explains the name of this principle.

3.2.2 Huygens surface equivalence principle for stratified media

At the preceding section, we have seen how currents $(\mathbf{J}_2, \mathbf{M}_2)$, together with equivalent currents $(\mathbf{J}_S, \mathbf{M}_S)$, were used for "representing" through source-field integral relations $\mathbf{E}_2$ and $\mathbf{H}_2$ in Γ_1. Although derived for a homogeneous Γ_1, (3.25) is in its principle not different for a multilayered medium, *i.e.*, a medium having its constitutive parameters ε, μ homogeneous following two perpendicular directions, but step-changing following the third axis; however, the source-field relationship used within must be modified to account for this stratification. Namely, the relationships linking fields $\mathbf{E}$ and $\mathbf{H}$ to currents $\mathbf{J}$ and $\mathbf{M}$ are [27]:

$$\mathbf{E}(\mathbf{r}) = \left\langle \overline{\boldsymbol{\mathcal{G}}}^{EJ}(\mathbf{r}, \mathbf{r}') ; \mathbf{J}(\mathbf{r}') \right\rangle + \left\langle \overline{\boldsymbol{\mathcal{G}}}^{EM}(\mathbf{r}, \mathbf{r}') ; \mathbf{M}(\mathbf{r}') \right\rangle \tag{3.32a}$$

$$\mathbf{H}(\mathbf{r}) = \left\langle \overline{\boldsymbol{\mathcal{G}}}^{HJ}(\mathbf{r}, \mathbf{r}') ; \mathbf{J}(\mathbf{r}') \right\rangle + \left\langle \overline{\boldsymbol{\mathcal{G}}}^{HM}(\mathbf{r}, \mathbf{r}') ; \mathbf{M}(\mathbf{r}') \right\rangle \tag{3.32b}$$

where the integration is performed on the spatial support of the sources. $\overline{\boldsymbol{\mathcal{G}}}^{PQ}(\mathbf{r}, \mathbf{r}')$ is the dyadic Green's function linking P-type fields at $\mathbf{r}$ to Q-type

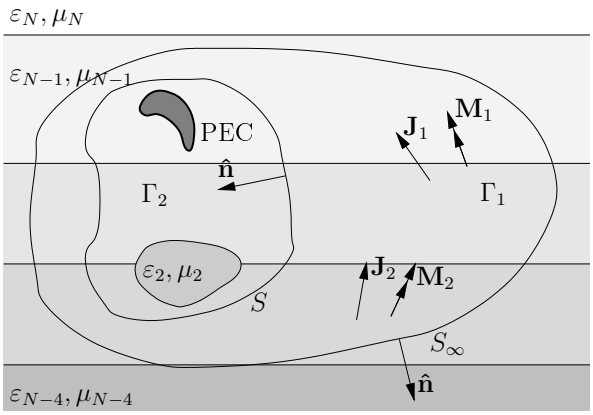

Figure 3.2: Same configuration than Fig. 3.1, but with Γ_1 having stratification of EM parameters ε, μ along one axis. N is the number of layers.

currents at $\mathbf{r}'$, and they are detailed at section C.1. Using these source-field relationships and definitions (3.30)–(3.31), (3.25) can be rewritten as:

$$\begin{aligned}\mathbf{E}_2|_{\mathbf{r}} = &\left\langle \overline{\boldsymbol{\mathcal{G}}}^{EJ}(\mathbf{r},\mathbf{r}')\,;\mathbf{J}_S(\mathbf{r}')\right\rangle_S + \left\langle \overline{\boldsymbol{\mathcal{G}}}^{EM}(\mathbf{r},\mathbf{r}')\,;\mathbf{M}_S(\mathbf{r}')\right\rangle_S \\ &+ \left\langle \overline{\boldsymbol{\mathcal{G}}}^{EJ}(\mathbf{r},\mathbf{r}')\,;\mathbf{J}_2(\mathbf{r}')\right\rangle_{\Gamma_1} + \left\langle \overline{\boldsymbol{\mathcal{G}}}^{EM}(\mathbf{r},\mathbf{r}')\,;\mathbf{M}_2(\mathbf{r}')\right\rangle_{\Gamma_1}\end{aligned} \tag{3.33}$$

As usual, a dual expression for $\mathbf{H}_2$ can be obtained by making the appropriate replacements of symbols (see section C.1).

In view of the hypersingular behavior of $\overline{\boldsymbol{\mathcal{G}}}^{EJ}$ and $\overline{\boldsymbol{\mathcal{G}}}^{HM}$ when $\mathbf{r}$ approaches $\mathbf{r}'$, which renders them of awkward use in numerical algorithms, it is preferable to use the mixed-potential source-field relationships in (3.33) [22, 27]. Using (C.9) for rewriting $\overline{\boldsymbol{\mathcal{G}}}^{EJ}$ allows us to rewrite (3.33):

$$\begin{aligned}\mathbf{E}_2|_{\mathbf{r}} = &-j\omega\left\langle \overline{\boldsymbol{\mathcal{K}}}^{AJ}(\mathbf{r},\mathbf{r}')\,;\mathbf{J}_S(\mathbf{r}')\right\rangle_S + \frac{1}{j\omega\varepsilon_0}\nabla\left\langle K^{\Phi}(\mathbf{r},\mathbf{r}')\,,\nabla'\cdot\mathbf{J}_S(\mathbf{r}')\right\rangle_S \\ &+ \left\langle \overline{\boldsymbol{\mathcal{G}}}^{EM}(\mathbf{r},\mathbf{r}')\,;\mathbf{M}_S(\mathbf{r}')\right\rangle_S \\ &- j\omega\left\langle \overline{\boldsymbol{\mathcal{K}}}^{AJ}(\mathbf{r},\mathbf{r}')\,;\mathbf{J}_2(\mathbf{r}')\right\rangle_{\Gamma_1} + \frac{1}{j\omega\varepsilon_0}\nabla\left\langle K^{\Phi}(\mathbf{r},\mathbf{r}')\,,\nabla'\cdot\mathbf{J}_2(\mathbf{r}')\right\rangle_{\Gamma_1} \\ &+ \left\langle \overline{\boldsymbol{\mathcal{G}}}^{EM}(\mathbf{r},\mathbf{r}')\,;\mathbf{M}_2(\mathbf{r}')\right\rangle_{\Gamma_1}\end{aligned} \tag{3.34}$$

and its dual expression for $\mathbf{H}_2$ is likely found:

$$\begin{aligned}\mathbf{H}_2|_{\mathbf{r}} = -j\omega \left\langle \overline{\boldsymbol{\mathcal{K}}}^{FM}(\mathbf{r},\mathbf{r}')\,;\mathbf{M}_S(\mathbf{r}')\right\rangle_S + \frac{1}{j\omega\mu_0}\nabla\left\langle K^{\Psi}(\mathbf{r},\mathbf{r}')\,,\nabla'\cdot\mathbf{M}_S(\mathbf{r}')\right\rangle_S \\ + \left\langle \overline{\boldsymbol{\mathcal{G}}}^{HJ}(\mathbf{r},\mathbf{r}')\,;\mathbf{J}_S(\mathbf{r}')\right\rangle_S \\ - j\omega \left\langle \overline{\boldsymbol{\mathcal{K}}}^{FM}(\mathbf{r},\mathbf{r}')\,;\mathbf{M}_2(\mathbf{r}')\right\rangle_{\Gamma_1} + \frac{1}{j\omega\mu_0}\nabla\left\langle K^{\Psi}(\mathbf{r},\mathbf{r}')\,,\nabla'\cdot\mathbf{M}_2(\mathbf{r}')\right\rangle_{\Gamma_1} \\ + \left\langle \overline{\boldsymbol{\mathcal{G}}}^{HJ}(\mathbf{r},\mathbf{r}')\,;\mathbf{J}_2(\mathbf{r}')\right\rangle_{\Gamma_1}\end{aligned} \tag{3.35}$$

In (3.34) and its dual form, $\overline{\boldsymbol{\mathcal{K}}}^{AJ}$ and $\overline{\boldsymbol{\mathcal{K}}}^{FM}$ are the DGFs for the corrected vector magnetic and electric potentials respectively and are given by (C.15) and it dual form, and K^{Φ} and K^{Ψ} are the scalar potential kernels for the electric and magnetic fields respectively, yielded by (C.16) and its dual form.

3.2.3 Application of the equivalence principle: construction of an exterior equivalent problem

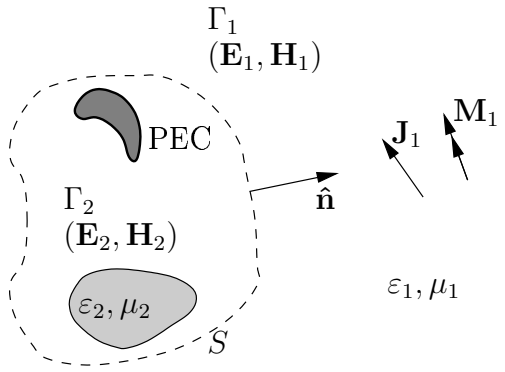

Figure 3.3: Electromagnetic source in region 1 radiating in presence of inhomogeneities located in region 2. Mathematical surface S separates two regions.

Consider Fig. 3.3, which shows a source $(\mathbf{J}_1, \mathbf{M}_1)$ radiating in the presence of inhomogeneities located in region 2. Fields produced in region 1 and 2 are denoted $(\mathbf{E}_1, \mathbf{H}_1)$ and $(\mathbf{E}_2, \mathbf{H}_2)$ respectively. Now, let us place on S equivalent sources $\mathbf{J}_S$ and $\mathbf{M}_S$ satisfying

$$\mathbf{J}_S \triangleq \hat{\mathbf{n}} \times \mathbf{H}_1 \tag{3.36a}$$

$$\mathbf{M}_S \triangleq \mathbf{E}_1 \times \hat{\mathbf{n}} \tag{3.36b}$$

where $\hat{\mathbf{n}}$ is the outward normal to S (Fig. 3.4). According to the equivalence principle, mathematically expressed by (3.25) and its dual form for $\mathbf{H}$, the combination of the original and equivalent sources produce fields $(\mathbf{E}_1, \mathbf{H}_1)$ identical to those of the original problem. The fields in region 2 are not identical to those

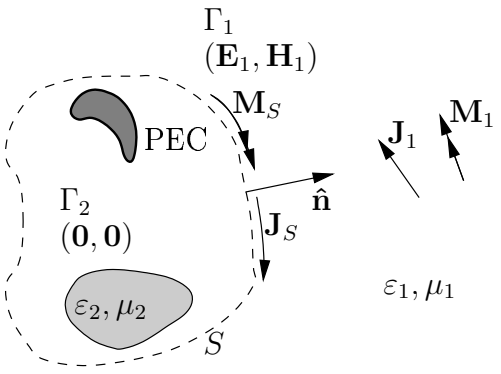

Figure 3.4: Intermediate step in construction of equivalent exterior problem associated with Fig. 3.3. Equivalent sources $\mathbf{J}_S$ and $\mathbf{M}_S$ are introduced on S and are combined with $(\mathbf{J}_1, \mathbf{M}_1)$ to replicate $(\mathbf{E}_1, \mathbf{H}_1)$ in region 1. Null fields are produced in region 2.

of the original problem: this is due to the change of boundary conditions for the fields $(\mathbf{E}_1, \mathbf{H}_1)$ caused by the introduction of $(\mathbf{J}_S, \mathbf{M}_S)$. In fact, null fields are produced within region 2. This effect is called the *extinction theorem.*

Since the fields within region 2 of the modified problem vanish, any inhomogeneity contained therein may be replaced at will without affecting the fields in region 1. For example, one could remove all inhomogeneities contained within region 2, and replace all matter by the constitutive parameters ε_1, μ_1 (or by the ε, μ corresponding to the stratification of Γ_1). This approach leaves us with sources $(\mathbf{J}_1, \mathbf{M}_1)$ and $(\mathbf{J}_S, \mathbf{M}_S)$, radiating in a homogeneous (stratified) medium, and producing the original fields in region 1 and null fields in region 2. This is often the approach followed in practice, since it effectively replaces the original problem involving complicated inhomogeneous media with a problem involving sources radiating in a homogeneous (stratified) space, from which the fields can be calculated by using the homogeneous space (multilayered space) Green's functions in the source-field relationships. Note that $\mathbf{J}_S$ and $\mathbf{M}_S$ are still unknowns that need to be determined. The objective of the next section is to establish equations for these unknowns that can be solved by a numerical method.

3.3 Surface integral equations for homogeneous bodies

3.3.1 Surface integral equations for perfectly conducting surfaces

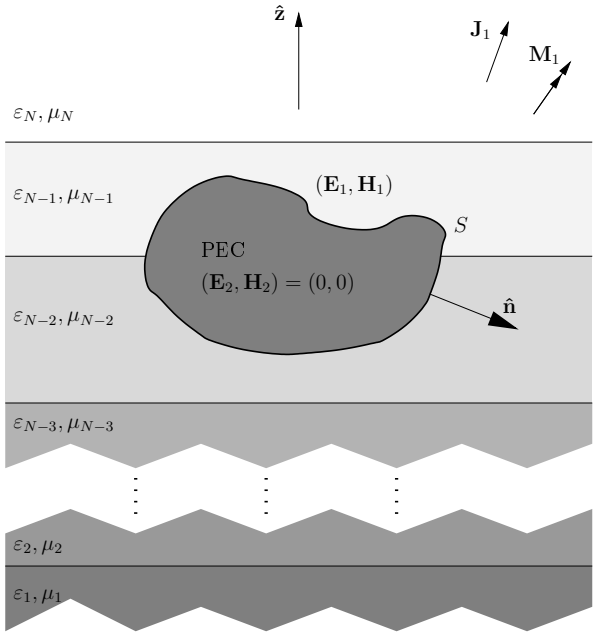

Figure 3.5: Original problem involving a PEC scatterer embedded in a stratified medium.

Figure 3.5 shows a perfectly conducting (PEC) closed surface embedded in a multilayered medium. Let us call $\left(\mathbf{E}^{\text{inc}}, \mathbf{H}^{\text{inc}}\right)$ the fields due to the sources $\left(\mathbf{J}_1, \mathbf{M}_1\right)$ as if radiating in the absence of the scatterer. They are given by looking at (3.34), with $\left(\mathbf{J}_2, \mathbf{M}_2\right)$ now replaced by $\left(\mathbf{J}_1, \mathbf{M}_1\right)$:

$$\mathbf{E}^{\text{inc}}(\mathbf{r}) = -j\omega \left\langle \overline{\boldsymbol{\mathcal{K}}}^{AJ}(\mathbf{r}, \mathbf{r}') ; \mathbf{J}_1(\mathbf{r}') \right\rangle_{\Gamma_1} + \frac{1}{j\omega\varepsilon_0} \nabla \left\langle K^{\Phi}(\mathbf{r}, \mathbf{r}') , \nabla' \cdot \mathbf{J}_1(\mathbf{r}') \right\rangle_{\Gamma_1} + \left\langle \overline{\boldsymbol{\mathcal{G}}}^{EM}(\mathbf{r}, \mathbf{r}') ; \mathbf{M}_1(\mathbf{r}') \right\rangle_{\Gamma_1} \quad (3.37a)$$

$$\mathbf{H}^{\text{inc}}(\mathbf{r}) = -j\omega \left\langle \overline{\boldsymbol{\mathcal{K}}}^{FM}(\mathbf{r},\mathbf{r}')\,;\mathbf{M}_1(\mathbf{r}')\right\rangle_{\Gamma_1} + \frac{1}{j\omega\mu_0}\nabla\left\langle K^{\Psi}(\mathbf{r},\mathbf{r}')\,,\nabla'\cdot\mathbf{M}_1(\mathbf{r}')\right\rangle_{\Gamma_1} + \left\langle \overline{\boldsymbol{\mathcal{G}}}^{HJ}(\mathbf{r},\mathbf{r}')\,;\mathbf{J}_1(\mathbf{r}')\right\rangle_{\Gamma_1}. \quad (3.37b)$$

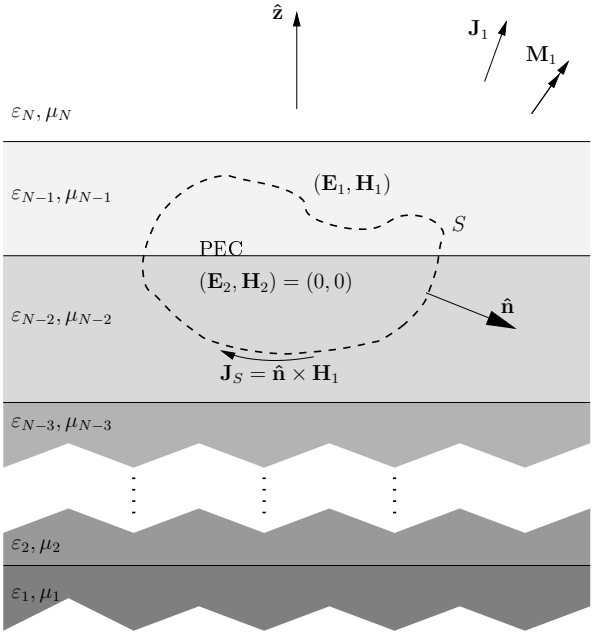

Figure 3.6: Equivalent exterior problem associated with Figure 3.5. An equivalent source $\mathbf{J}_S$ is introduced along the location of the conducting surface, and the conductor is replaced by a homogeneous medium with the same constitutive parameters as the exterior region.

$(\mathbf{E}_1, \mathbf{H}_1)$ are the fields radiated by $(\mathbf{J}_1, \mathbf{M}_1)$ in the presence of the scatterer. Let us place equivalent sources $(\mathbf{J}_S, \mathbf{M}_S)$ on a mathematical surface enclosing the scatterer, with $\hat{\mathbf{n}}$ being the normal to that surface. On the surface of a PEC, $(\mathbf{E}_1, \mathbf{H}_1)$ must satisfy the boundary conditions

$$\hat{\mathbf{n}} \times \mathbf{E}_1 = 0 \quad (3.38a)$$

$$\hat{\mathbf{n}} \times \mathbf{H}_1 = \mathbf{J}_S. \quad (3.38b)$$

Consequently, if we allow the mathematical surface S supporting the equivalent currents to shrink until it coincides with the surface of the scatterer, the

equivalent sources become

$$\mathbf{M}_S = 0 \tag{3.39a}$$

$$\mathbf{J}_S = \hat{\mathbf{n}} \times \mathbf{H}_1, \tag{3.39b}$$

which, when combined with $(\mathbf{J}_1, \mathbf{M}_1)$, will produce the correct fields $(\mathbf{E}_1, \mathbf{H}_1)$ outside of the surface S and null fields inside (as the inhomogeneity is a PEC, the null fields are also correct, therefore the interior equivalent problem is described simultaneously). As the fields inside the scatterer are zero, this latter can be replaced by the surrounding medium (Fig. 3.6). Therefore the equivalent sources $(\mathbf{J}_S, \mathbf{M}_S)$ radiate in the absence of the scatterer, which allows for the use of the DGFs for determining the fields generated by them. Making use of (3.37) and (3.39) in (3.34) yields the following equations:

$$\mathbf{E}_1 = \mathbf{E}^{\text{inc}} - j\omega \left\langle \overline{\boldsymbol{\mathcal{K}}}^{AJ}; \mathbf{J}_S \right\rangle_S + \frac{1}{j\omega\varepsilon_0} \nabla \left\langle K^{\Phi}, \nabla' \cdot \mathbf{J}_S \right\rangle_S \tag{3.40a}$$

$$\mathbf{H}_1 = \mathbf{H}^{\text{inc}} + \left\langle \overline{\boldsymbol{\mathcal{G}}}^{HJ}; \mathbf{J}_S \right\rangle_S \tag{3.40b}$$

which have been defined as the *integral representation* of fields $(\mathbf{E}_1, \mathbf{H}_1)$ by Morita *et al.* [52]. In (3.40) the fields are evaluated at $\mathbf{r}$ outside of S. Finally, evaluating the fields for $\mathbf{r}$ located on S and enforcing the boundary conditions (3.38) yield the following equations:

$$\hat{\mathbf{n}} \times \mathbf{E}^{\text{inc}} = \hat{\mathbf{n}} \times \left\{ j\omega \left\langle \overline{\boldsymbol{\mathcal{K}}}^{AJ}; \mathbf{J}_S \right\rangle_S - \frac{1}{j\omega\varepsilon_0} \nabla \left\langle K^{\Phi}, \nabla' \cdot \mathbf{J}_S \right\rangle_S \right\}_S \tag{3.41a}$$

$$\hat{\mathbf{n}} \times \mathbf{H}^{\text{inc}} = \mathbf{J}_S - \hat{\mathbf{n}} \times \left\{ \left\langle \overline{\boldsymbol{\mathcal{G}}}^{HJ}; \mathbf{J}_S \right\rangle_S \right\}_{S^+}. \tag{3.41b}$$

These expressions are two integro-differential equations for the unknown equivalent surface current density $\mathbf{J}_S$. Eq. (3.41a) is a mixed-potential form of the *electric field integral equation* (EFIE), and holds only for points located on S. The term "mixed-potential" stems from the use of potentials $\overline{\boldsymbol{\mathcal{K}}}^{AJ}$ and K^{Φ} instead of $\overline{\boldsymbol{\mathcal{G}}}^{EJ}$. The resulting name of (3.41a) will be *electric mixed-potential integral equation* (EMPIE). Similarly, (3.41b) is the *magnetic mixed-potential integral equation* (MMPIE), and is to be enforced at an infinitesimal distance outside the scatterer surface (S^+) [51].

Any of these two equations can be solved to produce the unknown equivalent source $\mathbf{J}_S$. Once $\mathbf{J}_S$ is determined, the electric and magnetic fields everywhere may be found from the source-field relationships in stratified media presented previously, by combining fields due to $\mathbf{J}_S$ and $(\mathbf{E}^{\text{inc}}, \mathbf{H}^{\text{inc}})$. In case of a planar scatterer, only the EFIE may be used, as the MMPIE is limited to closed bodies [51, p. 18].

3.3.2 Surface integral equations for homogeneous penetrable scatterers

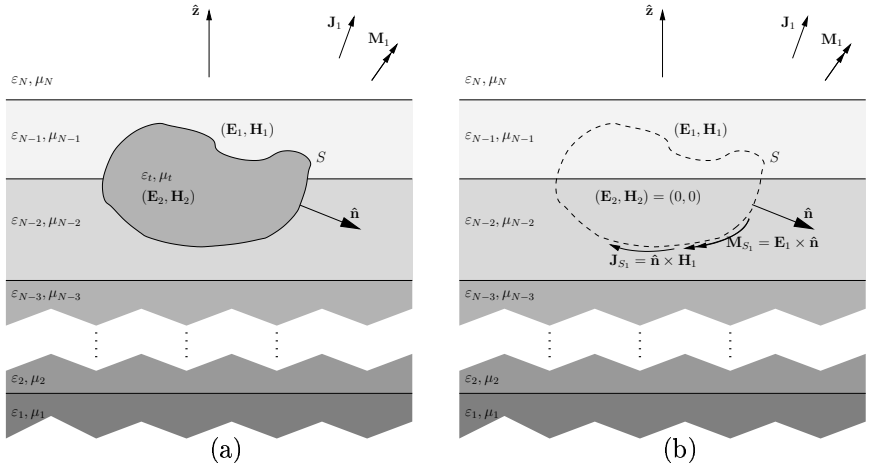

Figure 3.7: (a) Original problem involving a dielectric scatterer with EM parameters ε_t and μ_t embedded in a stratified medium. (b) Equivalent exterior problem.

Fig. 3.7 (a) depicts a homogeneous and penetrable target illuminated by a source $(\mathbf{J}_1, \mathbf{M}_1)$. Region 1 is a stratified medium and region 2 is characterized by constant $\varepsilon_t = \varepsilon_0 \varepsilon_{rt}, \mu_t = \mu_0 \mu_{rt}$. $(\mathbf{E}_1, \mathbf{H}_1)$ and $(\mathbf{E}_2, \mathbf{H}_2)$ are the fields produced in regions 1 and 2 respectively. We wish to define the equivalent currents on the scatterer surface that yield equivalent problems for both the outside and inside of the scatterer.

As shown at Fig. 3.7 (b), the exterior equivalent problem is constructed by placing equivalent sources $(\mathbf{J}_{S_1}, \mathbf{M}_{S_1})$ accordingly to (3.36) on S:

$$\mathbf{J}_{S_1} = \hat{\mathbf{n}} \times \mathbf{H}_1 \tag{3.42a}$$

$$\mathbf{M}_{S_1} = \mathbf{E}_1 \times \hat{\mathbf{n}}. \tag{3.42b}$$

According to the equivalence principle, these sources, combined with the original sources $(\mathbf{J}_1, \mathbf{M}_1)$, produce the correct fields outside of S and null fields inside S. The interior of S may therefore be replaced by the stratified medium without changing the fields outside of S, and thus the exterior equivalent problem is constituted by the sources $(\mathbf{J}_1, \mathbf{M}_1)$ and $(\mathbf{J}_{S_1}, \mathbf{M}_{S_1})$ radiating in the stratified medium in the absence of the target. Making use of (3.37) and of

(3.42) in (3.34) yields the following integral representations of $(\mathbf{E}_1, \mathbf{H}_1)$:

$$\mathbf{E}_1 = \mathbf{E}^{\text{inc}} - j\omega \left\langle \overline{\boldsymbol{\mathcal{K}}}^{AJ}; \mathbf{J}_S \right\rangle_S + \frac{1}{j\omega\varepsilon_0} \nabla \left\langle K^{\Phi}, \nabla' \cdot \mathbf{J}_S \right\rangle_S + \left\langle \overline{\boldsymbol{\mathcal{G}}}^{EM}; \mathbf{M}_S \right\rangle_S \tag{3.43a}$$

$$\mathbf{H}_1 = \mathbf{H}^{\text{inc}} - j\omega \left\langle \overline{\boldsymbol{\mathcal{K}}}^{FM}; \mathbf{M}_S \right\rangle_S + \frac{1}{j\omega\mu_0} \nabla \left\langle K^{\Psi}, \nabla' \cdot \mathbf{M}_S \right\rangle_S + \left\langle \overline{\boldsymbol{\mathcal{G}}}^{HJ}; \mathbf{J}_S \right\rangle_S \tag{3.43b}$$

where the fields are evaluated at $\mathbf{r}$ outside of S. The integral representation for $\mathbf{H}_1$ can be obtained from its $\mathbf{E}_1$ counterpart by duality (see appendix C.1).

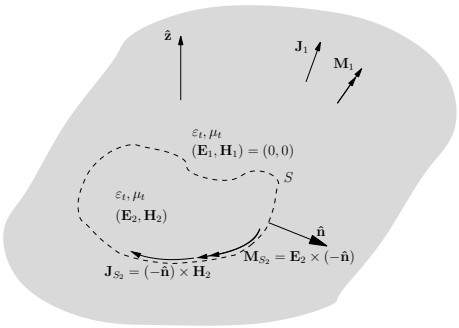

Figure 3.8: Interior equivalent problem associated with Fig. 3.7 (a).

The interior equivalent problem is depicted at Fig. 3.8, where sources $(\mathbf{J}_{S_1}, \mathbf{M}_{S_1})$ are defined according to (3.42) but with regards to the interior fields $(\mathbf{E}_2, \mathbf{H}_2)$ and with the normal pointing inside region 2:

$$\mathbf{J}_{S_2} = (-\hat{\mathbf{n}}) \times \mathbf{H}_2 \tag{3.44a}$$

$$\mathbf{M}_{S_2} = \mathbf{E}_2 \times (-\hat{\mathbf{n}}) \,. \tag{3.44b}$$

Radiating *in the absence* of the original source $(\mathbf{J}_1, \mathbf{M}_1)$ (see section 3.2), these equivalent sources replicate the original fields throughout region 2 and produce null fields throughout region 1. Therefore, alike the procedure followed for the exterior equivalent problem, one can replace the multilayered EM parameters of region 1 by those present in the target, *i.e.* ε_t and μ_t, without changing the fields in region 2, thus converting the problem to one involving infinite homogeneous space. Therefore the interior equivalent problem is constituted by the equivalent sources $(\mathbf{J}_{S_2}, \mathbf{M}_{S_2})$ radiating in homogeneous medium having constitutive parameters ε_t, μ_t. Using (3.44) in (3.25), with the part corresponding

to $(\mathbf{E}^{\text{inc}}, \mathbf{H}^{\text{inc}})$ suppressed since $(\mathbf{J}_1, \mathbf{M}_1)$ are absent in this configuration, we obtain the integral representations:

$$\mathbf{E}_2 = \frac{\nabla\nabla\cdot + k_t^2}{j\omega\varepsilon_t} \langle G_t, \mathbf{J}_{S_2} \rangle_S - \nabla \times \langle G_t, \mathbf{M}_{S_2} \rangle_S \tag{3.45a}$$

$$\mathbf{H}_2 = \frac{\nabla\nabla\cdot + k_t^2}{j\omega\mu_t} \langle G_t, \mathbf{M}_{S_2} \rangle_S + \nabla \times \langle G_t, \mathbf{J}_{S_2} \rangle_S \tag{3.45b}$$

where

$$G_t = \frac{e^{-jk_t|\mathbf{r}-\mathbf{r}'|}}{4\pi|\mathbf{r}-\mathbf{r}'|} \tag{3.46}$$

and $k_t = \omega\sqrt{\varepsilon_t\mu_t}$. The fields are evaluated at $\mathbf{r}$ inside of S. If the inside of the body is a inhomogeneous medium for which we possess DGFs—for example a spherically layered structure or a medium stratified following one direction—, the integral representations (3.45) have to be modified accordingly.

The continuity of the tangential part of fields $\mathbf{E}$ and $\mathbf{H}$ on S dictates that

$$\mathbf{J}_{S_1} = -\mathbf{J}_{S_2} \tag{3.47a}$$

$$\mathbf{M}_{S_1} = -\mathbf{M}_{S_2} \tag{3.47b}$$

and therefore only one set of unknowns, for example $(\mathbf{J}_{S_1}, \mathbf{M}_{S_1})$, must be determined. Finally, approaching the observation point at an infinitesimal distance from S for the outside and inside equivalent problems and plugging (3.43) and (3.45) into (3.42) and (3.44) respectively yields two coupled EMPIEs:

$$\hat{\mathbf{n}} \times \mathbf{E}^{\text{inc}} = -\mathbf{M}_{S_1} - \hat{\mathbf{n}} \times \left\{ -j\omega \left\langle \overline{\boldsymbol{\mathcal{K}}}^{AJ}; \mathbf{J}_{S_1} \right\rangle_S + \frac{1}{j\omega\varepsilon_0} \nabla \left\langle K^{\Phi}, \nabla' \cdot \mathbf{J}_{S_1} \right\rangle_S + \left\langle \overline{\boldsymbol{\mathcal{G}}}^{EM}; \mathbf{M}_{S_1} \right\rangle_S \right\}_{S^+} \tag{3.48a}$$

$$0 = \mathbf{M}_{S_1} - \hat{\mathbf{n}} \times \left\{ \frac{\nabla\nabla\cdot + k_t^2}{j\omega\varepsilon_t} \langle G_t, \mathbf{J}_{S_1} \rangle_S - \nabla \times \langle G_t, \mathbf{M}_{S_1} \rangle_S \right\}_{S^-} \tag{3.48b}$$

where for (3.48b), $(\mathbf{J}_{S_2}, \mathbf{M}_{S_2})$ have been replaced by $(-\mathbf{J}_{S_1}, -\mathbf{M}_{S_1})$ according to (3.47). Eqs. (3.48a) and (3.48b) are evaluated at an infinitesimal distance outside and inside the scatterer surface S respectively. The above approach

also yields two coupled MMPIEs:

$$\hat{\mathbf{n}} \times \mathbf{H}^{\text{inc}} = \mathbf{J}_{S_1} - \hat{\mathbf{n}} \times \left\{ -j\omega \left\langle \overline{\boldsymbol{\mathcal{K}}}^{FM}; \mathbf{M}_{S_1} \right\rangle_S + \frac{1}{j\omega\mu_0} \nabla \left\langle K^{\Psi}, \nabla' \cdot \mathbf{M}_{S_1} \right\rangle_S + \left\langle \overline{\boldsymbol{\mathcal{G}}}^{HJ}; \mathbf{J}_{S_1} \right\rangle_S \right\}_{S^+} \tag{3.49a}$$

$$0 = -\mathbf{J}_{S_1} - \hat{\mathbf{n}} \times \left\{ \frac{\nabla\nabla\cdot + k_t^2}{j\omega\mu_t} \langle G_t, \mathbf{M}_{S_1} \rangle_S + \nabla \times \langle G_t, \mathbf{J}_{S_1} \rangle_S \right\}_{S^-} . \tag{3.49b}$$

Note that (3.49) could have been obtained by duality applied to (3.48). Since there are two unknowns in each of these systems of two coupled equations, either system could in principle be used for finding the solution. We will see later that usually a combination of these systems is employed, for enhancing the conditioning of the matrix system that results from the discretization.

3.4 Surface integral equations for inhomogeneous bodies

In this section the developments of the surface integrals EMPIE and MMPIE are extended to scattering problems involving an inhomogeneity (dielectric or PEC) embedded inside another dielectric body, and two inhomogeneities contained in a given medium (free space or multilayered).

3.4.1 Body contained inside dielectric body

This first case is proposed as an exercise in [51, chapter 1], albeit in free space only. It is sketched at Fig. 3.9, and consists in a multilayered medium (not shown on the figure) characterized by 1-D arrays $\underline{\varepsilon}_s$ and $\underline{\mu}_s$, in which an inhomogeneity made up of two different materials ε_2, μ_2 and ε_3, μ_3 has been inserted. There are three regions denoted by R_i, which are separated by two surfaces: $S_{2,1}$ between R_2 and R_1, and $S_{3,2}$ between R_3 and R_2. In general the notation $S_{i,j}$ is used for a surface separating regions R_i and R_j [49]. Normals are defined with the same convention, with the second subscript indicating that the normal $\hat{\mathbf{n}}_{i,j}$ points into R_j. Source $(\mathbf{J}_1, \mathbf{M}_1)$ produces fields $(\mathbf{E}_i, \mathbf{H}_i)$ in R_i.

The EMPIE for region R_1 is given directly by (3.48a) (with fields $(\mathbf{E}^{\text{inc}},$

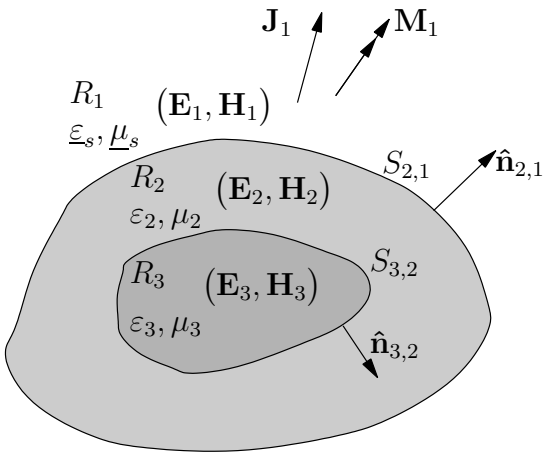

Figure 3.9: A system composed of two bodies. The multilayered medium is not shown on the figure. ε_s, μ_s are arrays representing the EM parameters of the surrounding multilayered medium.

$\mathbf{H}^{\text{inc}}\big)$ radiated by $\big(\mathbf{J}_1, \mathbf{M}_1\big)$ in the absence of the inhomogeneity):

$$\hat{\mathbf{n}}_{2,1} \times \mathbf{E}^{\text{inc}} = -\mathbf{M}_{S_{2,1}} - \hat{\mathbf{n}}_{2,1} \times \Big\{ -j\omega \left\langle \overline{\boldsymbol{\mathcal{K}}}^{AJ}; \mathbf{J}_{S_{2,1}} \right\rangle_{S_{2,1}} + \frac{1}{j\omega\varepsilon_0} \nabla \left\langle K^{\Phi}, \nabla' \cdot \mathbf{J}_{S_{2,1}} \right\rangle_{S_{2,1}} + \left\langle \overline{\boldsymbol{\mathcal{G}}}^{EM}; \mathbf{M}_{S_{2,1}} \right\rangle_{S_{2,1}} \Big\}_{S_{2,1}^{+}} \tag{3.50}$$

with $\big(\mathbf{J}_{S_{2,1}}, \mathbf{M}_{S_{2,1}}\big) = \hat{\mathbf{n}}_{2,1} \times \big(\mathbf{H}_1, -\mathbf{E}_1\big)$. As usual, this combination of currents produces the correct fields $\big(\mathbf{E}_1, \mathbf{H}_1\big)$ in R_1, while null fields are produced inside the inhomogeneity, and the latter is replaced by the multilayered medium.

Let us now construct the equivalent problem for R_2. We know from the boundary condition (3.47) that on $S_{2,1}$ we have to put $\big(-\mathbf{J}_{S_{2,1}}, -\mathbf{M}_{S_{2,1}}\big)$. If we define currents $\big(\mathbf{J}_{S_{3,2}}, \mathbf{M}_{S_{3,2}}\big)$ on $S_{3,2}$ such that:

$$\mathbf{M}_{S_{3,2}} = \mathbf{E}_2 \times \hat{\mathbf{n}}_{3,2} \tag{3.51a}$$

$$\mathbf{J}_{S_{3,2}} = \hat{\mathbf{n}}_{3,2} \times \mathbf{H}_2, \tag{3.51b}$$

the combination of the fields radiated by $\big(-\mathbf{J}_{S_{2,1}}, -\mathbf{M}_{S_{2,1}}\big)$ and $\big(\mathbf{J}_{S_{3,2}}, \mathbf{M}_{S_{3,2}}\big)$ will produce null fields outside R_2 and the original fields $\big(\mathbf{E}_2, \mathbf{H}_2\big)$ inside. This result stems directly from the surface equivalence principle. We may therefore replace all matter outside R_2 by ε_2, μ_2 and use the homogeneous space source-

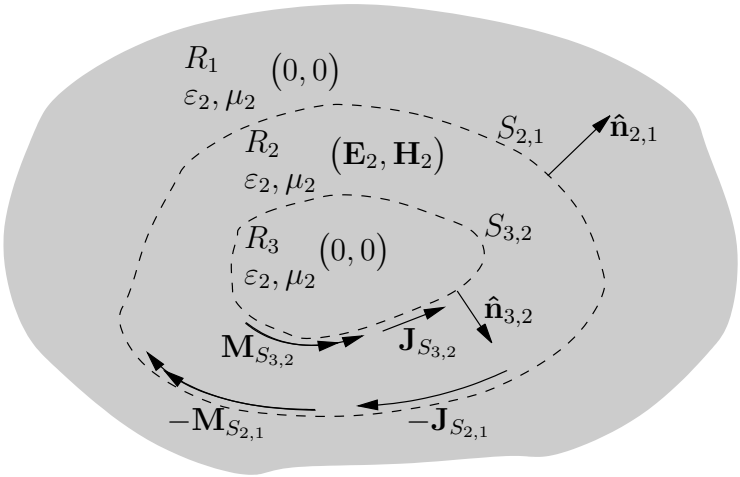

Figure 3.10: Equivalent problem for region 2.

field relationships (3.28) to obtain the integral representation for $\mathbf{E}_2$:

$$\mathbf{E}_2 = \frac{\nabla\nabla\cdot + k_2^2}{j\omega\varepsilon_2}\left\langle G_2, -\mathbf{J}_{S_{2,1}}\right\rangle_{S_{2,1}} - \nabla\times\left\langle G_2, -\mathbf{M}_{S_{2,1}}\right\rangle_{S_{2,1}} + \frac{\nabla\nabla\cdot + k_2^2}{j\omega\varepsilon_2}\left\langle G_2, \mathbf{J}_{S_{3,2}}\right\rangle_{S_{3,2}} - \nabla\times\left\langle G_2, \mathbf{M}_{S_{3,2}}\right\rangle_{S_{3,2}}. \quad (3.52)$$

This equation is the same as (3.45), where contributions of the equivalent currents $\left(-\mathbf{J}_{S_{2,1}}, -\mathbf{M}_{S_{2,1}}\right)$ and $\left(\mathbf{J}_{S_{3,2}}, \mathbf{M}_{S_{3,2}}\right)$ have simply been added. Plugging back these two equations into the equivalent currents definitions on $S_{2,1}$ and $S_{3,2}$, such as (3.51) for example, yields respectively two EMPIEs:

$$0 = \mathbf{M}_{S_{2,1}} - \hat{\mathbf{n}}_{2,1}\times\left\{\frac{\nabla\nabla\cdot + k_2^2}{j\omega\varepsilon_2}\left\langle G_2, \mathbf{J}_{S_{2,1}}\right\rangle_{S_{2,1}} - \nabla\times\left\langle G_2, \mathbf{M}_{S_{2,1}}\right\rangle_{S_{2,1}}\right\}_{S_{2,1}^-} + \hat{\mathbf{n}}_{2,1}\times\left\{\frac{\nabla\nabla\cdot + k_2^2}{j\omega\varepsilon_2}\left\langle G_2, \mathbf{J}_{S_{3,2}}\right\rangle_{S_{3,2}} - \nabla\times\left\langle G_2, \mathbf{M}_{S_{3,2}}\right\rangle_{S_{3,2}}\right\}_{S_{2,1}^-} \quad (3.53a)$$

$$0 = \mathbf{M}_{S_{3,2}} - \hat{\mathbf{n}}_{3,2}\times\left\{\frac{\nabla\nabla\cdot + k_2^2}{j\omega\varepsilon_2}\left\langle G_2, \mathbf{J}_{S_{2,1}}\right\rangle_{S_{2,1}} - \nabla\times\left\langle G_2, \mathbf{M}_{S_{2,1}}\right\rangle_{S_{2,1}}\right\}_{S_{3,2}^+} + \hat{\mathbf{n}}_{3,2}\times\left\{\frac{\nabla\nabla\cdot + k_2^2}{j\omega\varepsilon_2}\left\langle G_2, \mathbf{J}_{S_{3,2}}\right\rangle_{S_{3,2}} - \nabla\times\left\langle G_2, \mathbf{M}_{S_{3,2}}\right\rangle_{S_{3,2}}\right\}_{S_{3,2}^+}. \quad (3.53b)$$

Finally, the equivalent problem for region 3 is obtained in a straightforward

manner, by using $\left(-\mathbf{J}_{S_{3,2}}, -\mathbf{M}_{S_{3,2}}\right)$ as equivalent currents:

$$0 = \mathbf{M}_{S_{3,2}} - \hat{\mathbf{n}}_{3,2} \times \left\{ \frac{\nabla\nabla\cdot + k_3^2}{j\omega\varepsilon_3} \left\langle G_3, \mathbf{J}_{S_{3,2}} \right\rangle_{S_{3,2}} - \nabla \times \left\langle G_3, \mathbf{M}_{S_{3,2}} \right\rangle_{S_{3,2}} \right\}_{S_{3,2}^-} \tag{3.54}$$

Proceeding the same for $\mathbf{H}$, one easily obtains the following coupled MMP-IEs:

$$\hat{\mathbf{n}}_{2,1} \times \mathbf{H}^{\text{inc}} = \mathbf{J}_{S_{2,1}} - \hat{\mathbf{n}}_{2,1} \times \left\{ -j\omega \left\langle \overline{\boldsymbol{\mathcal{K}}}^{FM}; \mathbf{M}_{S_{2,1}} \right\rangle_{S_{2,1}} + \frac{1}{j\omega\mu_0} \nabla \left\langle K^{\Psi}, \nabla' \cdot \mathbf{M}_{S_{2,1}} \right\rangle_{S_{2,1}} + \left\langle \overline{\boldsymbol{\mathcal{G}}}^{HJ}; \mathbf{J}_{S_{2,1}} \right\rangle_{S_{2,1}} \right\}_{S_{2,1}^+} \tag{3.55a}$$

$$0 = -\mathbf{J}_{S_{2,1}} - \hat{\mathbf{n}}_{2,1} \times \left\{ \frac{\nabla\nabla\cdot + k_2^2}{j\omega\mu_2} \left\langle G_2, \mathbf{M}_{S_{2,1}} \right\rangle_{S_{2,1}} + \nabla \times \left\langle G_2, \mathbf{J}_{S_{2,1}} \right\rangle_{S_{2,1}} \right\}_{S_{2,1}^-} + \hat{\mathbf{n}}_{2,1} \times \left\{ \frac{\nabla\nabla\cdot + k_2^2}{j\omega\mu_2} \left\langle G_2, \mathbf{M}_{S_{3,2}} \right\rangle_{S_{3,2}} + \nabla \times \left\langle G_2, \mathbf{J}_{S_{3,2}} \right\rangle_{S_{3,2}} \right\}_{S_{2,1}^-} \tag{3.55b}$$

$$0 = -\mathbf{J}_{S_{3,2}} - \hat{\mathbf{n}}_{3,2} \times \left\{ \frac{\nabla\nabla\cdot + k_2^2}{j\omega\mu_2} \left\langle G_2, \mathbf{M}_{S_{2,1}} \right\rangle_{S_{2,1}} + \nabla \times \left\langle G_2, \mathbf{J}_{S_{2,1}} \right\rangle_{S_{2,1}} \right\}_{S_{3,2}^+} + \hat{\mathbf{n}}_{3,2} \times \left\{ \frac{\nabla\nabla\cdot + k_2^2}{j\omega\mu_2} \left\langle G_2, \mathbf{M}_{S_{3,2}} \right\rangle_{S_{3,2}} + \nabla \times \left\langle G_2, \mathbf{J}_{S_{3,2}} \right\rangle_{S_{3,2}} \right\}_{S_{3,2}^+} \tag{3.55c}$$

$$0 = -\mathbf{J}_{S_{3,2}} - \hat{\mathbf{n}}_{3,2} \times \left\{ \frac{\nabla\nabla\cdot + k_3^2}{j\omega\mu_3} \left\langle G_3, \mathbf{M}_{S_{3,2}} \right\rangle_{S_{3,2}} + \nabla \times \left\langle G_3, \mathbf{J}_{S_{3,2}} \right\rangle_{S_{3,2}} \right\}_{S_{3,2}^-} \tag{3.55d}$$

If R_3 is made up of PEC material, null fields are produced inside it. The boundary conditions on a PEC surface states that $\mathbf{M}_{S_{3,2}} = 0$, and there is no equivalent problem for R_3 to be considered. With this in hand the set of EMPIEs becomes:

$$\hat{\mathbf{n}}_{2,1} \times \mathbf{E}^{\text{inc}} = -\mathbf{M}_{S_{2,1}} - \hat{\mathbf{n}}_{2,1} \times \left\{ -j\omega \left\langle \overline{\boldsymbol{\mathcal{K}}}^{AJ}; \mathbf{J}_{S_{2,1}} \right\rangle_{S_{2,1}} + \frac{1}{j\omega\varepsilon_0} \nabla \left\langle K^{\Phi}, \nabla' \cdot \mathbf{J}_{S_{2,1}} \right\rangle_{S_{2,1}} + \left\langle \overline{\boldsymbol{\mathcal{G}}}^{EM}; \mathbf{M}_{S_{2,1}} \right\rangle_{S_{2,1}} \right\}_{S_{2,1}^+} \tag{3.56a}$$

$$0 = \mathbf{M}_{S_{2,1}} - \hat{\mathbf{n}}_{2,1} \times \left\{ \frac{\nabla\nabla\cdot + k_2^2}{j\omega\varepsilon_2} \left\langle G_2, \mathbf{J}_{S_{2,1}} \right\rangle_{S_{2,1}} - \nabla \times \left\langle G_2, \mathbf{M}_{S_{2,1}} \right\rangle_{S_{2,1}} \right\}_{S_{2,1}^-} + \hat{\mathbf{n}}_{2,1} \times \left\{ \frac{\nabla\nabla\cdot + k_2^2}{j\omega\varepsilon_2} \left\langle G_2, \mathbf{J}_{S_{3,2}} \right\rangle_{S_{3,2}} \right\}_{S_{2,1}^-} \tag{3.56b}$$

$$0 = -\hat{\mathbf{n}}_{3,2} \times \left\{ \frac{\nabla\nabla\cdot + k_2^2}{j\omega\varepsilon_2} \left\langle G_2, \mathbf{J}_{S_{2,1}} \right\rangle_{S_{2,1}} - \nabla \times \left\langle G_2, \mathbf{M}_{S_{2,1}} \right\rangle_{S_{2,1}} \right\}_{S_{3,2}^+} + \hat{\mathbf{n}}_{3,2} \times \left\{ \frac{\nabla\nabla\cdot + k_2^2}{j\omega\varepsilon_2} \left\langle G_2, \mathbf{J}_{S_{3,2}} \right\rangle_{S_{3,2}} \right\}_{S_{3,2}^+} . \quad (3.56c)$$

A similar set of MMPIEs can be obtained directly from (3.55), with $\mathbf{M}_{S_{3,2}} = 0$. We recall here that MMPIEs are applicable only to closed bodies.

For each surface there are at most two unknowns, $\mathbf{J}_S$ and $\mathbf{M}_S$. Therefore, if both bodies are dielectric, the number of unknowns is 4. If the inner surface is a PEC, only $\mathbf{J}_S$ will be used on it, and we have 3 unknowns to determine. On the other hand, if R_2 and R_3 are dielectrics, the set of EMPIEs and of MMPIEs each yield 4 equations (2 equations per surface). Both yield 3 equations if R_3 is a closed PEC, and MMPIE yields only 2 equations if R_3 is an open PEC. In all cases the number of equations is at least equal to that of the unknowns (for problems involving only open PEC scatterers) and at most equal to twice that of the unknowns (for problems involving dielectric and closed PEC scatterers), which in most cases makes the whole system composed of the EMPIEs and MMPIEs over-determined. Section 3.6 presents the techniques used for reducing the number of equations, in view of obtaining a well-determined and conditioned system.

3.4.2 Two bodies contained in the same region

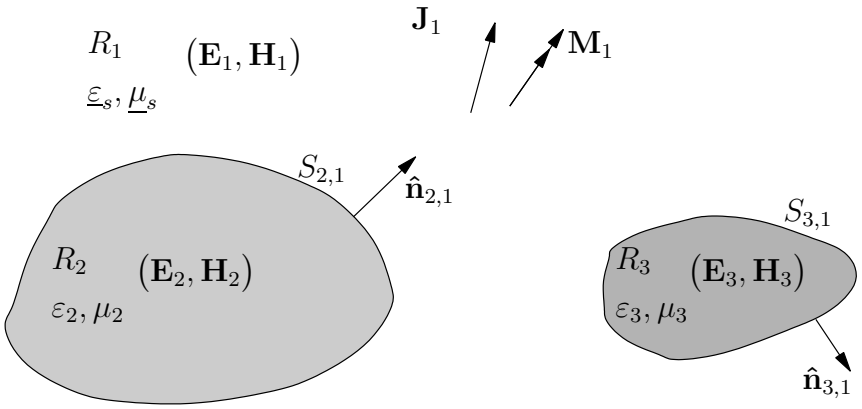

Figure 3.11: Two bodies contained within same region R_1. ε_s, μ_s are arrays representing the EM parameters of the surrounding multilayered medium.

This situation is sketched at Fig. 3.11, where two dielectric bodies are in-

troduced inside R_1 (a multilayered medium). Again defining the appropriate equivalent currents and deriving the integral representations for $\mathbf{E}$ in each region yield the EMPIEs:

$$\begin{aligned}\hat{\mathbf{n}}_{2,1}\times\mathbf{E}^{\text{inc}} = -\mathbf{M}_{S_{2,1}} &- \hat{\mathbf{n}}_{2,1}\times\Big\{-j\omega\left\langle\overline{\boldsymbol{\mathcal{K}}}^{AJ};\mathbf{J}_{S_{2,1}}\right\rangle_{S_{2,1}} \\ &+\frac{1}{j\omega\varepsilon_0}\nabla\left\langle K^{\Phi},\nabla'\cdot\mathbf{J}_{S_{2,1}}\right\rangle_{S_{2,1}}+\left\langle\overline{\boldsymbol{\mathcal{G}}}^{EM};\mathbf{M}_{S_{2,1}}\right\rangle_{S_{2,1}}\Big\}_{S_{2,1}^{+}} \\ &-\hat{\mathbf{n}}_{2,1}\times\Big\{-j\omega\left\langle\overline{\boldsymbol{\mathcal{K}}}^{AJ};\mathbf{J}_{S_{3,1}}\right\rangle_{S_{3,1}} \\ &+\frac{1}{j\omega\varepsilon_0}\nabla\left\langle K^{\Phi},\nabla'\cdot\mathbf{J}_{S_{3,1}}\right\rangle_{S_{3,1}}+\left\langle\overline{\boldsymbol{\mathcal{G}}}^{EM};\mathbf{M}_{S_{3,1}}\right\rangle_{S_{3,1}}\Big\}_{S_{2,1}^{+}}\end{aligned} \tag{3.57a}$$

$$\begin{aligned}\hat{\mathbf{n}}_{3,1}\times\mathbf{E}^{\text{inc}} = -\mathbf{M}_{S_{3,1}} &- \hat{\mathbf{n}}_{3,1}\times\Big\{-j\omega\left\langle\overline{\boldsymbol{\mathcal{K}}}^{AJ};\mathbf{J}_{S_{2,1}}\right\rangle_{S_{2,1}} \\ &+\frac{1}{j\omega\varepsilon_0}\nabla\left\langle K^{\Phi},\nabla'\cdot\mathbf{J}_{S_{2,1}}\right\rangle_{S_{2,1}}+\left\langle\overline{\boldsymbol{\mathcal{G}}}^{EM};\mathbf{M}_{S_{2,1}}\right\rangle_{S_{2,1}}\Big\}_{S_{3,1}^{+}} \\ &-\hat{\mathbf{n}}_{3,1}\times\Big\{-j\omega\left\langle\overline{\boldsymbol{\mathcal{K}}}^{AJ};\mathbf{J}_{S_{3,1}}\right\rangle_{S_{3,1}} \\ &+\frac{1}{j\omega\varepsilon_0}\nabla\left\langle K^{\Phi},\nabla'\cdot\mathbf{J}_{S_{3,1}}\right\rangle_{S_{3,1}}+\left\langle\overline{\boldsymbol{\mathcal{G}}}^{EM};\mathbf{M}_{S_{3,1}}\right\rangle_{S_{3,1}}\Big\}_{S_{3,1}^{+}}\end{aligned} \tag{3.57b}$$

$$0 = \mathbf{M}_{S_{2,1}} \tag{3.57c}$$

$$-\hat{\mathbf{n}}_{2,1}\times\left\{\frac{\nabla\nabla\cdot+k_2^2}{j\omega\varepsilon_2}\left\langle G_2,\mathbf{J}_{S_{2,1}}\right\rangle_{S_{2,1}}-\nabla\times\left\langle G_2,\mathbf{M}_{S_{2,1}}\right\rangle_{S_{2,1}}\right\}_{S_{2,1}^{-}} \tag{3.57d}$$

$$0 = \mathbf{M}_{S_{3,1}} \tag{3.57e}$$

$$-\hat{\mathbf{n}}_{3,1}\times\left\{\frac{\nabla\nabla\cdot+k_3^2}{j\omega\varepsilon_3}\left\langle G_3,\mathbf{J}_{S_{3,1}}\right\rangle_{S_{3,1}}-\nabla\times\left\langle G_3,\mathbf{M}_{S_{3,1}}\right\rangle_{S_{3,1}}\right\}_{S_{3,1}^{-}}. \tag{3.57f}$$

If one of the inhomogeneity is a PEC, its associated magnetic equivalent currents are equal to zero, and the need for an equivalent interior problem vanishes. The MMPIEs are obtained by duality.

3.5 Generalization to more than two inhomogeneities

3.5.1 N bodies embedded within the multilayered medium

The generalization of the equations derived at section 3.4.2 to more than two bodies is rather straightforward. First let us consider that region 1, supposed to be a multilayered medium, contains N_1 surfaces, all closed and dielectric. Moreover, currents $(\mathbf{J}_1, \mathbf{M}_1)$ radiate fields $(\mathbf{E}^{\text{inc}}, \mathbf{H}^{\text{inc}})$ in the absence of the inhomogeneities. Adding to these N_1 dielectric bodies N_2 closed PEC surfaces and N_3 open PEC surfaces, we obtain $N = N_1 + N_2 + N_3$ EMPIEs, expressed on each dielectric surface $S_{i,1}$ as:

$$\begin{aligned}\hat{\mathbf{n}}_{i,1} \times \mathbf{E}^{\text{inc}} = -\mathbf{M}_{S_{i,1}} - \hat{\mathbf{n}}_{i,1} \times \sum_{k=2}^{N_1+1} \Big\{ &- j\omega \left\langle \overline{\boldsymbol{\mathcal{K}}}^{AJ}; \mathbf{J}_{S_{k,1}} \right\rangle_{S_{k,1}} \\ &+ \frac{1}{j\omega\varepsilon_0} \nabla \left\langle K^{\Phi}, \nabla' \cdot \mathbf{J}_{S_{k,1}} \right\rangle_{S_{k,1}} + \left\langle \overline{\boldsymbol{\mathcal{G}}}^{EM}; \mathbf{M}_{S_{k,1}} \right\rangle_{S_{k,1}} \Big\}_{S_{i,1}^+} \\ -\hat{\mathbf{n}}_{i,1} \times \sum_{k=(N_1+1)+1}^{(N_1+1)+(N_2+N_3)} &\left\{ -j\omega \left\langle \overline{\boldsymbol{\mathcal{K}}}^{AJ}; \mathbf{J}_{S_{k,1}} \right\rangle_{S_{k,1}} + \frac{1}{j\omega\varepsilon_0} \nabla \left\langle K^{\Phi}, \nabla' \cdot \mathbf{J}_{S_{k,1}} \right\rangle_{S_{k,1}} \right\}_{S_{i,1}^+}, \\ &i = 2 \ldots (N_1 + 1). \end{aligned} \quad (3.58)$$

and on each PEC surface as:

$$\begin{aligned}\hat{\mathbf{n}}_{i,1} \times \mathbf{E}^{\text{inc}} = -\hat{\mathbf{n}}_{i,1} \times \sum_{k=2}^{N_1+1} \Big\{ &- j\omega \left\langle \overline{\boldsymbol{\mathcal{K}}}^{AJ}; \mathbf{J}_{S_{k,1}} \right\rangle_{S_{k,1}} \\ &+ \frac{1}{j\omega\varepsilon_0} \nabla \left\langle K^{\Phi}, \nabla' \cdot \mathbf{J}_{S_{k,1}} \right\rangle_{S_{k,1}} + \left\langle \overline{\boldsymbol{\mathcal{G}}}^{EM}; \mathbf{M}_{S_{k,1}} \right\rangle_{S_{k,1}} \Big\}_{S_{i,1}^+} \\ -\hat{\mathbf{n}}_{i,1} \times \sum_{k=(N_1+1)+1}^{(N_1+1)+(N_2+N_3)} &\left\{ -j\omega \left\langle \overline{\boldsymbol{\mathcal{K}}}^{AJ}; \mathbf{J}_{S_{k,1}} \right\rangle_{S_{k,1}} + \frac{1}{j\omega\varepsilon_0} \nabla \left\langle K^{\Phi}, \nabla' \cdot \mathbf{J}_{S_{k,1}} \right\rangle_{S_{k,1}} \right\}_{S_{i,1}^+}, \\ &i = \big((N_1 + 1) + 1 \big) \ldots \big((N_1 + 1) + (N_2 + N_3) \big). \end{aligned} \quad (3.59)$$

More care must be taken when considering MMPIEs: indeed, one must recall that a MMPIE cannot be enforced on open PEC surfaces. With this in

mind, the MMPIEs on the dielectric surfaces are expressed as:

$$\hat{\mathbf{n}}_{i,1}\times\mathbf{H}^{\text{inc}}=\mathbf{J}_{S_{i,1}}-\hat{\mathbf{n}}_{i,1}\times\sum_{k=2}^{N_1+1}\Big\{-j\omega\left\langle\overline{\boldsymbol{\mathcal{K}}}^{FM};\mathbf{M}_{S_{k,1}}\right\rangle_{S_{k,1}}+\frac{1}{j\omega\mu_0}\nabla\left\langle K^{\Psi},\nabla'\cdot\mathbf{M}_{S_{k,1}}\right\rangle_{S_{k,1}}+\left\langle\overline{\boldsymbol{\mathcal{G}}}^{HJ};\mathbf{J}_{S_{k,1}}\right\rangle_{S_{k,1}}\Big\}_{S_{i,1}^{+}}-\hat{\mathbf{n}}_{i,1}\times\sum_{k=(N_1+1)+1}^{(N_1+1)+(N_2+N_3)}\Big\{\left\langle\overline{\boldsymbol{\mathcal{G}}}^{HJ};\mathbf{J}_{S_{k,1}}\right\rangle_{S_{k,1}}\Big\}_{S_{i,1}^{+}},\qquad i=2\ldots(N_1+1).\quad(3.60)$$

and on each *closed* PEC surface as:

$$\hat{\mathbf{n}}_{i,1}\times\mathbf{H}^{\text{inc}}=\mathbf{J}_{S_{i,1}}-\hat{\mathbf{n}}_{i,1}\times\sum_{k=2}^{N_1+1}\Big\{-j\omega\left\langle\overline{\boldsymbol{\mathcal{K}}}^{FM};\mathbf{M}_{S_{k,1}}\right\rangle_{S_{k,1}}+\frac{1}{j\omega\mu_0}\nabla\left\langle K^{\Psi},\nabla'\cdot\mathbf{M}_{S_{k,1}}\right\rangle_{S_{k,1}}+\left\langle\overline{\boldsymbol{\mathcal{G}}}^{HJ};\mathbf{J}_{S_{k,1}}\right\rangle_{S_{k,1}}\Big\}_{S_{i,1}^{+}}-\hat{\mathbf{n}}_{i,1}\times\sum_{k=(N_1+1)+1}^{(N_1+1)+(N_2+N_3)}\Big\{\left\langle\overline{\boldsymbol{\mathcal{G}}}^{HJ};\mathbf{J}_{S_{k,1}}\right\rangle_{S_{k,1}}\Big\}_{S_{i,1}^{+}},\qquad i=\big((N_1+1)+1\big)\ldots\big((N_1+1)+N_2\big).\quad(3.61)$$

3.5.2 N bodies embedded within a dielectric body

This generalization is one step further than the previous section. For the clarity of the derivation, we will once again derive the integral representation of the electric fields, which will be used in the equivalent currents definitions in order to get the EMPIEs.

The problem is shown at Fig. 3.12, where there are N_1 dielectric bodies, N_2 closed PEC surfaces and N_3 open PEC surfaces located within R_1, itself a dielectric body. The total number of bodies embedded inside R_1 is $N = N_1 + N_2 + N_3$. Non zero fields $\big(\mathbf{E}_i, \mathbf{H}_i\big)$ exist in region i if it is a dielectric region. The equivalent problem for R_0 has already been done in several sections before and is straightforward to derive by using original currents $\big(\mathbf{J}_0, \mathbf{M}_0\big)$ and equivalent currents defined on $S_{1,0}$ by $\big(\mathbf{J}_{S_{1,0}}, \mathbf{M}_{S_{1,0}}\big) = \hat{\mathbf{n}}_{1,0} \times \big(\mathbf{H}_0, -\mathbf{E}_0\big)$.

Let us now construct the equivalent problem for R_1. We know from the boundary condition (3.47) that on $S_{1,0}$ we have to put $\big(-\mathbf{J}_{S_{1,0}}, -\mathbf{M}_{S_{1,0}}\big)$. We

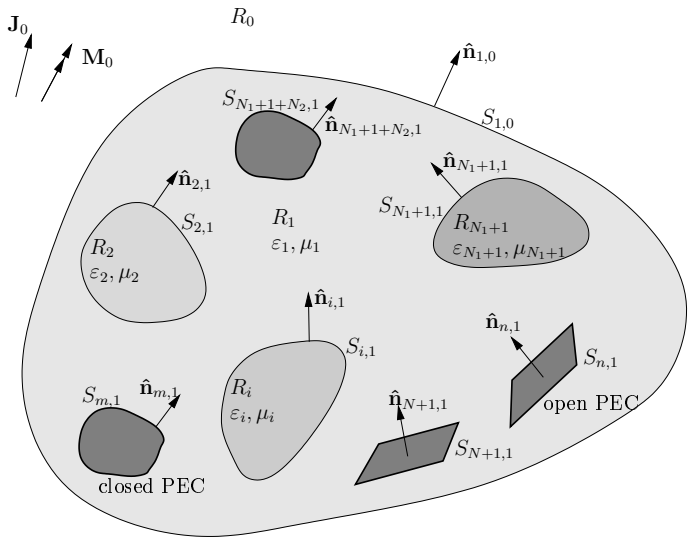

Figure 3.12: N bodies contained within dielectric body R_1.

also define equivalent currents $\left(\mathbf{J}_{S_{i,1}}, \mathbf{M}_{S_{i,1}}\right)$ on all $S_{i,1}$ such that:

$$\mathbf{M}_{S_{i,1}} = \mathbf{E}_1 \times \hat{\mathbf{n}}_{i,1} \tag{3.62a}$$

$$\mathbf{J}_{S_{i,1}} = \hat{\mathbf{n}}_{i,1} \times \mathbf{H}_1, \quad i = 2 \ldots (N_1 + 1) \tag{3.62b}$$

and

$$\mathbf{M}_{S_{i,1}} = 0 \tag{3.63a}$$

$$\mathbf{J}_{S_{i,1}} = \hat{\mathbf{n}}_{i,1} \times \mathbf{H}_1, \quad i = \big((N_1 + 1) + 1\big) \ldots (N + 1)\,. \tag{3.63b}$$

the combination of the fields radiated by $\left(-\mathbf{J}_{S_{1,0}}, -\mathbf{M}_{S_{1,0}}\right)$ and all the $\left(\mathbf{J}_{S_{i,1}}, \mathbf{M}_{S_{i,1}}\right)$ will produce null fields outside R_1 and the original fields $\left(\mathbf{E}_1, \mathbf{H}_1\right)$ inside. We may therefore replace all matter outside R_1 by ε_1, μ_1 and use the homogeneous space source-field relationships (3.28) to obtain the integral representation for $\mathbf{E}_1$:

$$\begin{aligned}\mathbf{E}_1 = {} & \frac{\nabla\nabla\cdot + k_1^2}{j\omega\varepsilon_1} \left\langle G_1, -\mathbf{J}_{S_{1,0}} \right\rangle_{S_{1,0}} - \nabla \times \left\langle G_1, -\mathbf{M}_{S_{1,0}} \right\rangle_{S_{1,0}} \\ & + \sum_{k=2}^{N_1+1} \left[\frac{\nabla\nabla\cdot + k_1^2}{j\omega\varepsilon_1} \left\langle G_1, \mathbf{J}_{S_{k,1}} \right\rangle_{S_{k,1}} - \nabla \times \left\langle G_1, \mathbf{M}_{S_{k,1}} \right\rangle_{S_{k,1}} \right] \\ & + \sum_{k=(N_1+1)+1}^{(N_1+1)+(N_2+N_3)} \frac{\nabla\nabla\cdot + k_1^2}{j\omega\varepsilon_1} \left\langle G_1, \mathbf{J}_{S_{k,1}} \right\rangle_{S_{k,1}}\end{aligned} \tag{3.64}$$

This equation is the same as (3.45), where contributions of the equivalent currents $\left(-\mathbf{J}_{S_{1,0}}, -\mathbf{M}_{S_{1,0}}\right)$ and all $\left(\mathbf{J}_{S_{i,1}}, \mathbf{M}_{S_{i,1}}\right)$ have simply been added. Plugging back these two equations into the equivalent currents definitions on $S_{1,0}$ and $S_{i,1}$ yields respectively 1 and N EMPIEs:

$$\begin{aligned} 0 = \mathbf{M}_{S_{1,0}} &- \hat{\mathbf{n}}_{1,0} \times \left\{ \frac{\nabla\nabla\cdot + k_1^2}{j\omega\varepsilon_1} \left\langle G_1, \mathbf{J}_{S_{1,0}} \right\rangle_{S_{1,0}} - \nabla \times \left\langle G_1, \mathbf{M}_{S_{1,0}} \right\rangle_{S_{1,0}} \right\}_{S_{1,0}^-} \\ &+ \hat{\mathbf{n}}_{1,0} \times \sum_{k=2}^{N_1+1} \left\{ \frac{\nabla\nabla\cdot + k_1^2}{j\omega\varepsilon_1} \left\langle G_1, \mathbf{J}_{S_{k,1}} \right\rangle_{S_{k,1}} - \nabla \times \left\langle G_1, \mathbf{M}_{S_{k,1}} \right\rangle_{S_{k,1}} \right\}_{S_{1,0}^-} \\ &+ \hat{\mathbf{n}}_{1,0} \times \sum_{k=(N_1+1)+1}^{(N_1+1)+(N_2+N_3)} \left\{ \frac{\nabla\nabla\cdot + k_1^2}{j\omega\varepsilon_1} \left\langle G_1, \mathbf{J}_{S_{k,1}} \right\rangle_{S_{k,1}} \right\}_{S_{1,0}^-} \end{aligned} \tag{3.65a}$$

$$\begin{aligned} 0 = \mathbf{M}_{S_{i,1}} &- \hat{\mathbf{n}}_{i,1} \times \left\{ \frac{\nabla\nabla\cdot + k_1^2}{j\omega\varepsilon_1} \left\langle G_1, \mathbf{J}_{S_{1,0}} \right\rangle_{S_{1,0}} - \nabla \times \left\langle G_1, \mathbf{M}_{S_{1,0}} \right\rangle_{S_{1,0}} \right\}_{S_{i,1}^+} \\ &+ \hat{\mathbf{n}}_{i,1} \times \sum_{k=2}^{N_1+1} \left\{ \frac{\nabla\nabla\cdot + k_1^2}{j\omega\varepsilon_1} \left\langle G_1, \mathbf{J}_{S_{k,1}} \right\rangle_{S_{k,1}} - \nabla \times \left\langle G_1, \mathbf{M}_{S_{k,1}} \right\rangle_{S_{k,1}} \right\}_{S_{i,1}^+} \\ &+ \hat{\mathbf{n}}_{i,1} \times \sum_{k=(N_1+1)+1}^{(N_1+1)+(N_2+N_3)} \left\{ \frac{\nabla\nabla\cdot + k_1^2}{j\omega\varepsilon_1} \left\langle G_1, \mathbf{J}_{S_{k,1}} \right\rangle_{S_{k,1}} \right\}_{S_{i,1}^+}, \\ &\qquad\qquad i = 2 \ldots (N_1+1) \end{aligned} \tag{3.65b}$$

The EMPIEs enforced on the PEC bodies, that is, for $i = \big((N_1+1)+1\big) \ldots \big((N_1+1)+(N_2+N_3)\big)$, are exactly the same as for $i = 2 \ldots \big((N_1+1)+1\big)$, but with $\mathbf{M}_{S_{i,1}} = 0$. As usual, the MMPIEs can be obtained by duality.

The reasoning on the number of equations and unknowns used at section 3.4.1 can easily be applied to this general system. The total number of EMPIEs and MMPIEs are given by $2(N_1+1)+N_2+N_3$ and $2(N_1+1)+N_2$ respectively, and their addition yields the total number of equations $N_{\text{eq}} = 4(N_1+1) + 2N_2 + N_3$. On the other hand, the total number of unknowns is given by $N_{\text{u}} = 2(N_1+1) + N_2 + N_3$. If $N_1 = N_2 = 0$ (no dielectrics nor closed PEC bodies), $N_{\text{eq}} = N_{\text{u}}$. If $N_3 = 0$ (no open PEC surfaces), $N_{\text{eq}} = 2N_{\text{u}}$. The techniques for combining the equations in excess are presented at the next section.

No assumption was made about the inside of the penetrable inhomogeneities $R_2 \ldots R_{N_1+1}$. If they themselves contain inhomogeneities, the above formulas

can be applied recursively for each region of the problem. If one of the region consists in a multilayered medium (bounded by the surface of the region), one has to replace the free space Green's functions by the appropriate DGFs. There remains the problem of the junctions, that is, when two or more surfaces touch each other. This problem has been tackled by Taskinen *et al.* [50], but was not considered in this work, as it was not necessary for modeling the mine.

3.6 Reduction of the number of equations

As discussed at sections 3.4.1 and 3.5.2, the number of equations is at least equal to and at most the double of that of the unknowns, which makes in many cases the whole system over-determined. These equations must therefore be combined in order to yield the right number of unknowns and equations [44].

The simplest possible combination is to use only the EMPIEs on all surfaces. If only dielectric or closed PEC bodies are involved, one can use only the MMPIEs. A little more complex is to use EMPIEs on part of the surfaces, and MMPIEs on the remaining surfaces. Unfortunately, when used to describe the exterior equivalent problem, these integral equations may not produce unique solutions if applied to closed geometries that also represent resonant cavities [51, chapter 6]. When the problem is discretized with the method of moments, the corresponding impedance matrix becomes ill-conditioned at the resonance frequencies, and it is not possible to invert it to get the solution. We are going to shortly describe alternative surface integral equations that do not suffer from this resonance problem.

3.6.1 PMCHWT formulation

The first formulation was proposed by Poggio and Miller [53], Chang and Harrington [54] and Wu and Tsai [55], and is called from the name of its inceptors the "PMCHWT" formulation. The PMCHWT formulation is known to yield a solution free of the interior resonance corruption [44]. The principle is explained for a homogeneous target immersed in a multilayered medium. The corresponding EMPIEs and MMPIEs are given at section 3.3.2 by (3.48) and (3.49) respectively. The PMCHWT consists in adding the outside and inside

MPIEs, thereby yielding two equations for two unknowns:

$$\begin{aligned}\hat{\mathbf{n}}\times\mathbf{E}^{\text{inc}} = -\hat{\mathbf{n}}\times\Bigg\{ &-j\omega\left\langle\overline{\boldsymbol{\mathcal{K}}}^{AJ};\mathbf{J}_{S_1}\right\rangle_S + \frac{1}{j\omega\varepsilon_0}\nabla\left\langle K^{\Phi},\nabla'\cdot\mathbf{J}_{S_1}\right\rangle_S \\ &+\left\langle\overline{\boldsymbol{\mathcal{G}}}^{EM};\mathbf{M}_{S_1}\right\rangle_S\Bigg\}_{S^+} \\ -\hat{\mathbf{n}}\times\Bigg\{&\frac{\nabla\nabla\cdot+k_t^2}{j\omega\varepsilon_t}\left\langle G_t,\mathbf{J}_{S_1}\right\rangle_S - \nabla\times\left\langle G_t,\mathbf{M}_{S_1}\right\rangle_S\Bigg\}_{S^-}\end{aligned} \tag{3.66}$$

$$\begin{aligned}\hat{\mathbf{n}}\times\mathbf{H}^{\text{inc}} = -\hat{\mathbf{n}}\times\Bigg\{ &-j\omega\left\langle\overline{\boldsymbol{\mathcal{K}}}^{FM};\mathbf{M}_{S_1}\right\rangle_S + \frac{1}{j\omega\mu_0}\nabla\left\langle K^{\Psi},\nabla'\cdot\mathbf{M}_{S_1}\right\rangle_S \\ &+\left\langle\overline{\boldsymbol{\mathcal{G}}}^{HJ};\mathbf{J}_{S_1}\right\rangle_S\Bigg\}_{S^+} \\ -\hat{\mathbf{n}}\times\Bigg\{&\frac{\nabla\nabla\cdot+k_t^2}{j\omega\mu_t}\left\langle G_t,\mathbf{M}_{S_1}\right\rangle_S + \nabla\times\left\langle G_t,\mathbf{J}_{S_1}\right\rangle_S\Bigg\}_{S^-}.\end{aligned} \tag{3.67}$$

The combination of the exterior and interior MPIEs can be done for every dielectric inhomogeneity, but not for PEC bodies, as there is no interior problem associated to them. Please note that the above equations appear in [51, section 10.7], where the author consider them as forming a "combined field integral equation".

3.6.2 Combined field integral equation formulation

This formulation has been thoroughly studied by Sheng *et al.* [44]. As its name "combined field integral equation" (CFIE) indicates it, it consists of the combination of the exterior EMPIE and MMPIE, and the combination of the interior EMPIE and MMPIE. Again taking the MPIEs for a homogeneous dielectric target immersed in a multilayered medium given by (3.48) and (3.49), such a combination yields the following equations:

$$\begin{aligned}\alpha\left[\hat{\mathbf{n}}\times\mathbf{E}^{\text{inc}}\right] + (1-\alpha)\,\eta_0\left[\hat{\mathbf{n}}\times\mathbf{H}^{\text{inc}}\right] = \alpha\Bigg[&-\mathbf{M}_{S_1} - \hat{\mathbf{n}}\times\Bigg\{-j\omega\left\langle\overline{\boldsymbol{\mathcal{K}}}^{AJ};\mathbf{J}_{S_1}\right\rangle_S \\ &+\frac{1}{j\omega\varepsilon_0}\nabla\left\langle K^{\Phi},\nabla'\cdot\mathbf{J}_{S_1}\right\rangle_S + \left\langle\overline{\boldsymbol{\mathcal{G}}}^{EM};\mathbf{M}_{S_1}\right\rangle_S\Bigg\}_{S^+}\Bigg] \\ +(1-\alpha)\,\eta_0\Bigg[&\mathbf{J}_{S_1} - \hat{\mathbf{n}}\times\Bigg\{-j\omega\left\langle\overline{\boldsymbol{\mathcal{K}}}^{FM};\mathbf{M}_{S_1}\right\rangle_S \\ &+\frac{1}{j\omega\mu_0}\nabla\left\langle K^{\Psi},\nabla'\cdot\mathbf{M}_{S_1}\right\rangle_S + \left\langle\overline{\boldsymbol{\mathcal{G}}}^{HJ};\mathbf{J}_{S_1}\right\rangle_S\Bigg\}_{S^+}\Bigg]\end{aligned} \tag{3.68}$$

$$0 = \alpha \left[\mathbf{M}_{S_1} - \hat{\mathbf{n}} \times \left\{ \frac{\nabla\nabla\cdot + k_t^2}{j\omega\varepsilon_t} \langle G_t, \mathbf{J}_{S_1} \rangle_S - \nabla \times \langle G_t, \mathbf{M}_{S_1} \rangle_S \right\}_{S^-} \right]$$
$$+ (1-\alpha)\,\eta_0 \left[-\mathbf{J}_{S_1} - \hat{\mathbf{n}} \times \left\{ \frac{\nabla\nabla\cdot + k_t^2}{j\omega\mu_t} \langle G_t, \mathbf{M}_{S_1} \rangle_S + \nabla \times \langle G_t, \mathbf{J}_{S_1} \rangle_S \right\}_{S^-} \right] \tag{3.69}$$

where $\eta_0 = \sqrt{\mu_0/\varepsilon_0}$ is the impedance of free space, and $0 < \alpha < 1$. If $\alpha = 0$ ($\alpha = 1$), the MMPIE (EMPIE) is the result of the combination. The CFIE can be applied to all closed bodies, PEC included. For problems involving more inhomogeneities, the CFIE (as the PMCHWT) can—and should—be applied on every surface on which it is possible. Combination of both CFIE and PMCHWT can even be found in [50], with the PMCHWT applied to dielectric bodies, CFIE applied to closed PEC bodies, and the EMPIE used for open PEC surfaces.

3.7 Method of moments solution for the MPIEs

For an introduction to the MoM, a good start is the book written by Harrington [56]. The key idea behind the MoM is that *linear operators*, such as those that appear in integro-differential equations for example, are transformed into *matrix operators*, by means of discretization of the *unknown quantity or function* with help of a set of *basis functions*, and testing of the resulting equation by *testing functions*. After discretization, this matrix operator can be inverted in order to find the solution in the space spanned by the basis. We talk about *Galerkin* scheme if these testing functions are the same as the basis functions. In electromagnetics, the unknown quantity of interest is most often the *electric and/or magnetic surface equivalent current*, on which functionals such as *radar cross section* are based.

During the 70's, researchers used "wire-grid" or "surface patch" models of the surface of the body under consideration. Although successful in the prediction of far-field quantities, the wire-grid model suffered from several problems, ranging from non-applicability to near-field calculations to accuracy problems and difficulties in physical interpretation of computed currents [45]. While the surface patch approaches could overcome most of these limitations, their ability to model arbitrary surfaces was very limited, since those patches were rectangular. Some authors used quadrilateral patches, but those were still presenting heavy computational- and geometrical-related inconveniences to modelers.

A fundamental extension of the surface patch method for conducting bod-

ies of arbitrary shapes has been given by Rao *et al.* [45], who defined a new set of basis functions, called the Rao-Wilton-Glisson (RWG) basis functions, based upon discretization of the body surface by means of triangles. This powerful and versatile set of basis functions has met enormous success, due to its geometrical abilities as well as to its mathematical properties, and is still in heavy use nowadays. Later on, the method was applied to conducting bodies of arbitrary shapes embedded in two-layers media by Zheng and Michalski [22].

The aim of this section is the derivation of the method of moments (MoM) solution to the EMPIEs, MMPIEs and their combinations PMCHWT and CFIE. First the RWG basis functions are briefly introduced, and their use in the decomposition of the target equivalent currents is shown. The discretization of the EMPIEs and MMPIEs is the next logical step, and the testing phase, which yields the integro-differential operator under its matrix form, is presented. The study is particularized to an inhomogeneity contained within a dielectric body (section 3.4.1), and the resulting linear system is explicitly derived. Finally, the numerical algorithms are tested in several cases.

3.7.1 Method of moments formulation

3.7.1.1 Basis functions: definition and properties

First the surface of the body is discretized by triangular patches. Then the electric and magnetic currents are approximated by a sum of RWG *basis functions* such that, for any point on the surface of the body, we have

$$\mathbf{J}(\mathbf{r}) \simeq \sum_{n=1}^{N} J^n \mathbf{f}_n(\mathbf{r}) \quad \text{and} \quad \mathbf{M}(\mathbf{r}) \simeq \sum_{n=1}^{N} M^n \mathbf{f}_n(\mathbf{r}) \tag{3.70}$$

where $\mathbf{f}_n(\mathbf{r})$ are triangular edge-defined basis functions called RWG functions, first introduced by Rao, Wilton and Glisson in [45]. N is the number of basis functions. One can already note that on PEC surfaces the corresponding M^n coefficients will be zero. The n^{th} RWG basis function is defined on the adjacent triangles associated with edge n, and is given by [22]:

$$\mathbf{f}_n(\mathbf{r}) \triangleq \begin{cases} \mathbf{f}_n^+ = \frac{l_n}{2A_n^+}\left(\mathbf{r}^+ - \mathbf{r}_n^+\right), & \mathbf{r} \text{ in } T_n^+ \\ \mathbf{f}_n^- = -\frac{l_n}{2A_n^-}\left(\mathbf{r}^- - \mathbf{r}_n^-\right), & \mathbf{r} \text{ in } T_n^- \\ \mathbf{0}, & \text{otherwise} \end{cases} \tag{3.71}$$

in which l_n is the length of the edge, $A_n^\pm$ is the area of triangle $T_n^\pm$ and $(\mathbf{r}^\pm - \mathbf{r}_n^\pm)$ is the position vector in the triangle plane and relative to the node opposed to

the edge (Fig. 3.13).

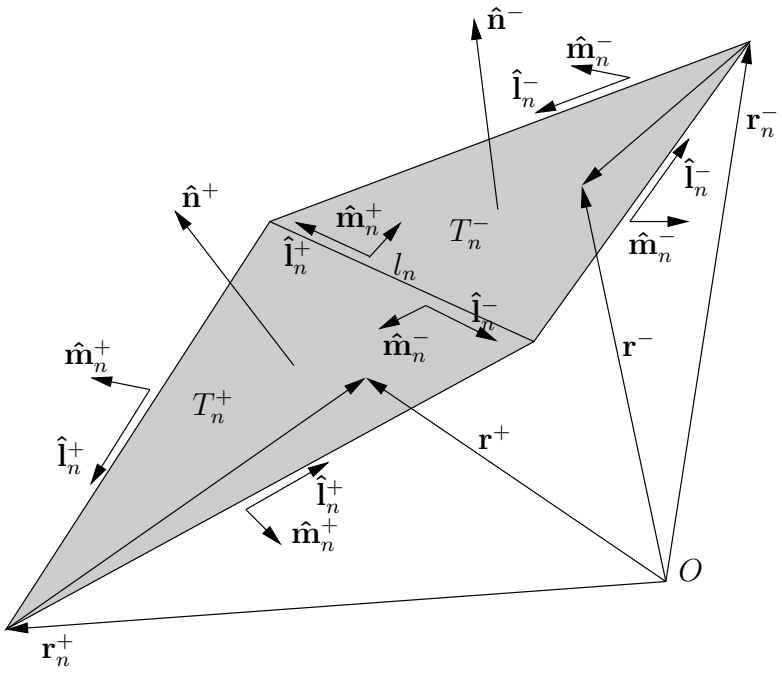

Figure 3.13: n^{th} RWG function $\mathbf{f}_n$ is defined on triangle pair T_n^+ and T_n^-, and starts from or ends on node opposed to edge. $\mathbf{r}^+$ and $\mathbf{r}^-$ are vectors position in T_n^+ and T_n^- respectively. For all triangles, $\hat{\mathbf{n}} = \hat{\mathbf{m}} \times \hat{\mathbf{l}}$.

These RWG basis functions display properties that are very useful in the MoM, among which the most important are given hereafter [45]:

1. the component of current normal to the n^{th} edge is constant and continuous across the edge;

2. all edges of T_n^+ and T_n^- are free of line charges;

3. the surface divergence of $\mathbf{f}_n$, proportional to the surface charge density associated with the basis element, is

$$\nabla_S \cdot \mathbf{f}_n(\mathbf{r}) = \begin{cases} \frac{l_n}{A_n^+}, & \mathbf{r} \text{ in } T_n^+ \\ -\frac{l_n}{A_n^-}, & \mathbf{r} \text{ in } T_n^- \\ 0, & \text{otherwise.} \end{cases} \tag{3.72}$$

The charge density is constant in each triangle and the total charge associated with the triangle pair T_n^+ and T_n^- is zero;

4. a linear superposition of the three basis functions associated with a triangle can represent a linear current flowing through this triangle in an arbitrary direction.

3.7.2 MoM discretization of MPIEs for body contained inside dielectric body

The purpose of this rather involving section is to derive the main steps of an algorithm allowing the computation of the MoM impedance matrix of an arbitrary target embedded within a stratified medium. We first write explicitly the discretization and test of the MPIEs for a body contained inside a dielectric body (Fig. 3.9). We then put the resulting system of equations under a matrix form, the *MoM impedance matrix*, which allows for an easier understanding of the contributions of the terms involved.

3.7.2.1 EMPIEs representation with RWG basis functions

Developing the equivalent currents $(\mathbf{J}_S, \mathbf{M}_S)$ into the basis functions as done in (3.70), the coupled EMPIEs given by (3.50), (3.53) and (3.54) for the inhomogeneous body of section 3.4.1 become

$$\left[-\mathbf{E}^{\text{inc}} = \sum_{n=1}^{N_{S_{2,1}}} J_{S_{2,1}}^n \left\{ -j\omega \left\langle \overline{\boldsymbol{\mathcal{K}}}^{AJ}; \mathbf{f}_n \right\rangle_{D_{S_{2,1}}^n} + \frac{1}{j\omega\varepsilon_0} \nabla \left\langle K^{\Phi}, \nabla' \cdot \mathbf{f}_n \right\rangle_{D_{S_{2,1}}^n} \right\}_{S_{2,1}^+} + \sum_{n=1}^{N_{S_{2,1}}} M_{S_{2,1}}^n \left\{ -\hat{\mathbf{n}}_{2,1} \times \mathbf{f}_n + \left\langle \overline{\boldsymbol{\mathcal{G}}}^{EM}; \mathbf{f}_n \right\rangle_{D_{S_{2,1}}^n} \right\}_{S_{2,1}^+} \right]_{\tan} \tag{3.73a}$$

$$\begin{aligned} 0 = \sum_{n=1}^{N_{S_{2,1}}} & \left[J_{S_{2,1}}^n \left\{ -\frac{\nabla\nabla\cdot + k_2^2}{j\omega\varepsilon_2} \left\langle G_2, \mathbf{f}_n \right\rangle_{D_{S_{2,1}}^n} \right\}_{S_{2,1}^-} \right. \\ & \left. + M_{S_{2,1}}^n \left\{ -\hat{\mathbf{n}}_{2,1} \times \mathbf{f}_n + \nabla \times \left\langle G_2, \mathbf{f}_n \right\rangle_{D_{S_{2,1}}^n} \right\}_{S_{2,1}^-} \right]_{\tan} \\ & + \sum_{n=N_{S_{2,1}}+1}^{N_{S_{2,1}}+N_{S_{3,2}}} \left[J_{S_{3,2}}^n \left\{ \frac{\nabla\nabla\cdot + k_2^2}{j\omega\varepsilon_2} \left\langle G_2, \mathbf{f}_n \right\rangle_{D_{S_{3,2}}^n} \right\}_{S_{2,1}^-} \right. \end{aligned}$$

$$+ M^n_{S_{3,2}} \left\{ -\nabla \times \langle G_2, \mathbf{f}_n \rangle_{D^n_{S_{3,2}}} \right\}_{S^-_{2,1}} \Bigg]_{\tan} \tag{3.73b}$$

$$\begin{aligned} 0 = \sum_{n=1}^{N_{S_{2,1}}} \Bigg[& J^n_{S_{2,1}} \left\{ -\frac{\nabla\nabla\cdot + k_2^2}{j\omega\varepsilon_2} \langle G_2, \mathbf{f}_n \rangle_{D^n_{S_{2,1}}} \right\}_{S^+_{3,2}} \\ & + M^n_{S_{2,1}} \left\{ \nabla \times \langle G_2, \mathbf{f}_n \rangle_{D^n_{S_{2,1}}} \right\}_{S^+_{3,2}} \Bigg]_{\tan} \\ + \sum_{n=N_{S_{2,1}}+1}^{N_{S_{2,1}}+N_{S_{3,2}}} \Bigg[& J^n_{S_{3,2}} \left\{ \frac{\nabla\nabla\cdot + k_2^2}{j\omega\varepsilon_2} \langle G_2, \mathbf{f}_n \rangle_{D^n_{S_{3,2}}} \right\}_{S^+_{3,2}} \\ & + M^n_{S_{3,2}} \left\{ -\hat{\mathbf{n}}_{3,2} \times \mathbf{f}_n - \nabla \times \langle G_2, \mathbf{f}_n \rangle_{D^n_{S_{3,2}}} \right\}_{S^+_{3,2}} \Bigg]_{\tan} \end{aligned} \tag{3.73c}$$

$$\begin{aligned} 0 = \sum_{n=N_{S_{2,1}}+1}^{N_{S_{2,1}}+N_{S_{3,2}}} \Bigg[& J^n_{S_{3,2}} \left\{ -\frac{\nabla\nabla\cdot + k_3^2}{j\omega\varepsilon_3} \langle G_3, \mathbf{f}_n \rangle_{D^n_{S_{3,2}}} \right\}_{S^-_{3,2}} \\ & + M^n_{S_{3,2}} \left\{ -\hat{\mathbf{n}}_{3,2} \times \mathbf{f}_n + \nabla \times \langle G_3, \mathbf{f}_n \rangle_{D^n_{S_{3,2}}} \right\}_{S^-_{3,2}} \Bigg]_{\tan} \end{aligned} \tag{3.73d}$$

where $D^n_{S_{i,j}}$ is the domain of the basis function $\mathbf{f}_n$ located on surface $S_{i,j}$, and the "tan" index means that only the tangential part of the EMPIEs (which have been cross-multiplied by the normals pertaining to the surface on which they are evaluated) have to be taken into account. $N_{S_{i,j}}$ is the number of edges (or basis functions) on surface $S_{i,j}$.

In view of the source-field relationships given by (3.28) and (3.29) for homogeneous space and by the mixed-potential form of (3.32) for multilayered media, we can notice that, for a given region R_j bounded by surfaces $S_{i,j}, i = 1 \ldots N_S$ (N_S is the number of surfaces concerned), the equivalent currents of the innermost surface provides a *positive* contribution to the total electric field, while the equivalent currents of the outermost surface provides a *negative* contribution. The generalization of this observation to an arbitrary number of bodies contained within a dielectric body (see section 3.5.2) is immediate: all the inner surface equivalent currents will have a positive contribution to the total electric field.

3.7.2.2 Testing of the EMPIEs

The next step consists in testing the above equations. The choice of the testing functions is widely debated in the literature, and is of paramount importance for obtaining a precise and well-defined numerical approximation of the solution. Testing is most often done with help of the RWG basis functions, in which case we are in a Galerkin numerical scheme. However, as has been thoroughly discussed in [44], testing with $\hat{\mathbf{n}}\times$RWG functions must also be considered when using the CFIE. The testing function, denoted by $\mathbf{g}_m$, can therefore be:

$$\mathbf{g}_m \triangleq \mathbf{f}_m \qquad \text{or} \qquad \mathbf{g}_m \triangleq \hat{\mathbf{n}} \times \mathbf{f}_m \qquad \text{on } D_m \tag{3.74}$$

where $\hat{\mathbf{n}}$ is the outward normal to the surface, and where D_m is the domain of the test function $\mathbf{g}_m$, defined in the same manner as for $\mathbf{f}_m$.

Testing (3.73) with $\mathbf{g}_m(\mathbf{r})$, with $m = 1 \ldots N_{S_{2,1}} + N_{S_{3,2}}$, yields the MoM EMPIEs:

$$\begin{aligned}
-\left\langle \mathbf{g}_m; \mathbf{E}^{\text{inc}} \right\rangle_{D^m_{S_{2,1}}} = & \sum_{n=1}^{N_{S_{2,1}}} J^n_{S_{2,1}} \left\{ -j\omega \left\langle \mathbf{g}_m; \left\langle \overline{\boldsymbol{\mathcal{K}}}^{AJ}; \mathbf{f}_n \right\rangle_{D^n_{S_{2,1}}} \right\rangle_{D^m_{S_{2,1}}} \right. \\
& \left. + \frac{1}{j\omega\varepsilon_0} \left\langle \mathbf{g}_m; \nabla \left\langle K^{\Phi}, \nabla' \cdot \mathbf{f}_n \right\rangle_{D^n_{S_{2,1}}} \right\rangle_{D^m_{S_{2,1}}} \right\}_{S^+_{2,1}} \\
& + \sum_{n=1}^{N_{S_{2,1}}} M^n_{S_{2,1}} \left\{ -\left\langle \mathbf{g}_m; \hat{\mathbf{n}}_{2,1} \times \mathbf{f}_n \right\rangle_{D^m_{S_{2,1}}} + \left\langle \mathbf{g}_m; \left\langle \overline{\boldsymbol{\mathcal{G}}}^{EM}; \mathbf{f}_n \right\rangle_{D^n_{S_{2,1}}} \right\rangle_{D^m_{S_{2,1}}} \right\}_{S^+_{2,1}}
\end{aligned} \tag{3.75a}$$

$$\begin{aligned}
0 = & \sum_{n=1}^{N_{S_{2,1}}} J^n_{S_{2,1}} \left\{ -\left\langle \mathbf{g}_m; \frac{\nabla\nabla\cdot + k_2^2}{j\omega\varepsilon_2} \left\langle G_2, \mathbf{f}_n \right\rangle_{D^n_{S_{2,1}}} \right\rangle_{D^m_{S_{2,1}}} \right\}_{S^-_{2,1}} \\
& + \sum_{n=1}^{N_{S_{2,1}}} M^n_{S_{2,1}} \left\{ -\left\langle \mathbf{g}_m; \hat{\mathbf{n}}_{2,1} \times \mathbf{f}_n \right\rangle_{D^m_{S_{2,1}}} + \left\langle \mathbf{g}_m; \nabla \times \left\langle G_2, \mathbf{f}_n \right\rangle_{D^n_{S_{2,1}}} \right\rangle_{D^m_{S_{2,1}}} \right\}_{S^-_{2,1}} \\
& + \sum_{n=N_{S_{2,1}}+1}^{N_{S_{2,1}}+N_{S_{3,2}}} J^n_{S_{3,2}} \left\{ \left\langle \mathbf{g}_m; \frac{\nabla\nabla\cdot + k_2^2}{j\omega\varepsilon_2} \left\langle G_2, \mathbf{f}_n \right\rangle_{D^n_{S_{3,2}}} \right\rangle_{D^m_{S_{2,1}}} \right\}_{S^-_{2,1}} \\
& + \sum_{n=N_{S_{2,1}}+1}^{N_{S_{2,1}}+N_{S_{3,2}}} M^n_{S_{3,2}} \left\{ -\left\langle \mathbf{g}_m; \nabla \times \left\langle G_2, \mathbf{f}_n \right\rangle_{D^n_{S_{3,2}}} \right\rangle_{D^m_{S_{2,1}}} \right\}_{S^-_{2,1}}
\end{aligned} \tag{3.75b}$$

$$
\begin{aligned}
0 = \sum_{n=1}^{N_{S_{2,1}}} J^n_{S_{2,1}} \Bigg\{ & - \left\langle \mathbf{g}_m ; \frac{\nabla\nabla\cdot + k_2^2}{j\omega\varepsilon_2} \left\langle G_2, \mathbf{f}_n \right\rangle_{D^n_{S_{2,1}}} \right\rangle_{D^m_{S_{3,2}}} \Bigg\}_{S^+_{3,2}} \\
& + \sum_{n=1}^{N_{S_{2,1}}} M^n_{S_{2,1}} \left\{ \left\langle \mathbf{g}_m ; \nabla \times \left\langle G_2, \mathbf{f}_n \right\rangle_{D^n_{S_{2,1}}} \right\rangle_{D^m_{S_{3,2}}} \right\}_{S^+_{3,2}} \\
& + \sum_{n=N_{S_{2,1}}+1}^{N_{S_{2,1}}+N_{S_{3,2}}} J^n_{S_{3,2}} \left\{ \left\langle \mathbf{g}_m ; \frac{\nabla\nabla\cdot + k_2^2}{j\omega\varepsilon_2} \left\langle G_2, \mathbf{f}_n \right\rangle_{D^n_{S_{3,2}}} \right\rangle_{D^m_{S_{3,2}}} \right\}_{S^+_{3,2}} \\
& + \sum_{n=N_{S_{2,1}}+1}^{N_{S_{2,1}}+N_{S_{3,2}}} M^n_{S_{3,2}} \Bigg\{ - \left\langle \mathbf{g}_m ; \hat{\mathbf{n}}_{3,2} \times \mathbf{f}_n \right\rangle_{D^m_{S_{3,2}}} \\
& \qquad - \left\langle \mathbf{g}_m ; \nabla \times \left\langle G_2, \mathbf{f}_n \right\rangle_{D^n_{S_{3,2}}} \right\rangle_{D^m_{S_{3,2}}} \Bigg\}_{S^+_{3,2}}
\end{aligned} \tag{3.75c}
$$

$$
\begin{aligned}
0 = \sum_{n=N_{S_{2,1}}+1}^{N_{S_{2,1}}+N_{S_{3,2}}} J^n_{S_{3,2}} \Bigg\{ & - \left\langle \mathbf{g}_m ; \frac{\nabla\nabla\cdot + k_3^2}{j\omega\varepsilon_3} \left\langle G_3, \mathbf{f}_n \right\rangle_{D^n_{S_{3,2}}} \right\rangle_{D^m_{S_{3,2}}} \Bigg\}_{S^-_{3,2}} \\
& + \sum_{n=N_{S_{2,1}}+1}^{N_{S_{2,1}}+N_{S_{3,2}}} M^n_{S_{3,2}} \Bigg\{ - \left\langle \mathbf{g}_m ; \hat{\mathbf{n}}_{3,2} \times \mathbf{f}_n \right\rangle_{D^m_{S_{3,2}}} \\
& \qquad + \left\langle \mathbf{g}_m ; \nabla \times \left\langle G_3, \mathbf{f}_n \right\rangle_{D^n_{S_{3,2}}} \right\rangle_{D^m_{S_{3,2}}} \Bigg\}_{S^-_{3,2}} .
\end{aligned} \tag{3.75d}
$$

The system of equations (3.75) can be written in a matrix form:

$$\left(\begin{bmatrix} \underline{\underline{Z}}^{E_{S_{2,1}^+},+J_{S_{2,1}}} \\ \left(N_{S_{2,1}} \times N_{S_{2,1}}\right) \end{bmatrix} \begin{bmatrix} \underline{\underline{0}} \\ \left(N_{S_{2,1}} \times N_{S_{3,2}}\right) \end{bmatrix} \begin{bmatrix} \underline{\underline{Z}}^{E_{S_{2,1}^+},+M_{S_{2,1}}} \\ \left(N_{S_{2,1}} \times N_{S_{2,1}}\right) \end{bmatrix} \begin{bmatrix} \underline{\underline{0}} \\ \left(N_{S_{2,1}} \times N_{S_{3,2}}\right) \end{bmatrix} \right.$$
$$\begin{bmatrix} \underline{\underline{Z}}^{E_{S_{2,1}^-},-J_{S_{2,1}}} \\ \left(N_{S_{2,1}} \times N_{S_{2,1}}\right) \end{bmatrix} \begin{bmatrix} \underline{\underline{Z}}^{E_{S_{2,1}^-},+J_{S_{3,2}}} \\ \left(N_{S_{2,1}} \times N_{S_{3,2}}\right) \end{bmatrix} \begin{bmatrix} \underline{\underline{Z}}^{E_{S_{2,1}^-},-M_{S_{2,1}}} \\ \left(N_{S_{2,1}} \times N_{S_{2,1}}\right) \end{bmatrix} \begin{bmatrix} \underline{\underline{Z}}^{E_{S_{2,1}^-},+M_{S_{3,2}}} \\ \left(N_{S_{2,1}} \times N_{S_{3,2}}\right) \end{bmatrix}$$
$$\begin{bmatrix} \underline{\underline{Z}}^{E_{S_{3,2}^+},-J_{S_{2,1}}} \\ \left(N_{S_{3,2}} \times N_{S_{2,1}}\right) \end{bmatrix} \begin{bmatrix} \underline{\underline{Z}}^{E_{S_{3,2}^+},+J_{S_{3,2}}} \\ \left(N_{S_{3,2}} \times N_{S_{3,2}}\right) \end{bmatrix} \begin{bmatrix} \underline{\underline{Z}}^{E_{S_{3,2}^+},-M_{S_{2,1}}} \\ \left(N_{S_{3,2}} \times N_{S_{2,1}}\right) \end{bmatrix} \begin{bmatrix} \underline{\underline{Z}}^{E_{S_{3,2}^+},+M_{S_{3,2}}} \\ \left(N_{S_{3,2}} \times N_{S_{3,2}}\right) \end{bmatrix}$$
$$\left. \begin{bmatrix} \underline{\underline{0}} \\ \left(N_{S_{3,2}} \times N_{S_{2,1}}\right) \end{bmatrix} \begin{bmatrix} \underline{\underline{Z}}^{E_{S_{3,2}^-},-J_{S_{3,2}}} \\ \left(N_{S_{3,2}} \times N_{S_{3,2}}\right) \end{bmatrix} \begin{bmatrix} \underline{\underline{0}} \\ \left(N_{S_{3,2}} \times N_{S_{2,1}}\right) \end{bmatrix} \begin{bmatrix} \underline{\underline{Z}}^{E_{S_{3,2}^-},-M_{S_{3,2}}} \\ \left(N_{S_{3,2}} \times N_{S_{3,2}}\right) \end{bmatrix} \right) \bullet \left(\begin{bmatrix} \underline{J}_{S_{2,1}} \\ \left(N_{S_{2,1}} \times 1\right) \end{bmatrix} \right.$$
$$\begin{bmatrix} \underline{J}_{S_{3,2}} \\ \left(N_{S_{3,2}} \times 1\right) \end{bmatrix} \begin{bmatrix} \underline{M}_{S_{2,1}} \\ \left(N_{S_{2,1}} \times 1\right) \end{bmatrix} \left. \begin{bmatrix} \underline{M}_{S_{3,2}} \\ \left(N_{S_{3,2}} \times 1\right) \end{bmatrix} \right) = \left(\begin{bmatrix} \underline{V}^{E_{S_{2,1}^+}} \\ \left(N_{S_{2,1}} \times 1\right) \end{bmatrix} \right.$$
$$\begin{bmatrix} \underline{0} \\ \left(N_{S_{2,1}} \times 1\right) \end{bmatrix} \begin{bmatrix} \underline{0} \\ \left(N_{S_{3,2}} \times 1\right) \end{bmatrix} \left. \begin{bmatrix} \underline{0} \\ \left(N_{S_{3,2}} \times 1\right) \end{bmatrix} \right) \tag{3.76}$$

Each matrix block is given by the following equations for multilayered media:

$$Z_{mn}^{E_{S_{k,l}^{\pm}},\pm J_{S_{p,q}}} = \pm \left\{ -j\omega \left\langle \mathbf{g}_m; \langle \overline{\boldsymbol{\mathcal{K}}}^{AJ}; \mathbf{f}_n \rangle_{D_{S_{p,q}}^n} \right\rangle_{D_{S_{k,l}}^m} + \frac{1}{j\omega\varepsilon_0} \left\langle \mathbf{g}_m; \nabla \langle K^{\Phi}, \nabla' \cdot \mathbf{f}_n \rangle_{D_{S_{p,q}}^n} \right\rangle_{D_{S_{k,l}}^m} \right\}_{S_{k,l}^{\pm}} \tag{3.77a}$$

$$Z_{mn}^{E_{S_{k,l}^{\pm}},\pm M_{S_{p,q}}} = \left\{ -\delta_{kp}\delta_{lq} \langle \mathbf{g}_m; \hat{\mathbf{n}}_{k,l} \times \mathbf{f}_n \rangle_{D_{S_{k,l}}^m} \pm \left\langle \mathbf{g}_m; \langle \overline{\boldsymbol{\mathcal{G}}}^{EM}; \mathbf{f}_n \rangle_{D_{S_{p,q}}^n} \right\rangle_{D_{S_{k,l}}^m} \right\}_{S_{k,l}^{\pm}} \tag{3.77b}$$

where δ_{ij}, the Kronecker delta, is 0 for $i \neq j$ and 1 for $i = j$. Superscript $E_{S_{k,l}^{\pm}}$ to Z_{mn} means that for "+" or for "−" we are testing the electric field on surface $S_{k,l}$ in medium l or medium k respectively (we recall here that the normal to surface $S_{k,l}$ is $\hat{\mathbf{n}}_{k,l}$ and points outside $S_{k,l}$ towards region l). Superscript $\pm J_{S_{p,q}}$ tells if we take equivalent current $\mathbf{J}_{S_{p,q}}$ with its positive or negative sign: it will be positive if we are outside $S_{p,q}$ and negative otherwise. We give in appendix B.2 the explicit expressions of the terms involved in Z_{mn}^{EJ} and Z_{mn}^{EM} for multilayered media.

We also have the following equations for homogeneous media with the same conventions applied:

$$Z_{mn}^{E_{S_{k,l}^{\pm}},\pm J_{S_{p,q}}} = \left\{ \pm \left\langle \mathbf{g}_m; \frac{\nabla\nabla\cdot + k_{k,l}^2}{j\omega\varepsilon_{k,l}} \langle G_{k,l}, \mathbf{f}_n \rangle_{D_{S_{p,q}}^n} \right\rangle_{D_{S_{k,l}}^m} \right\}_{S_{k,l}^{\pm}} \tag{3.78a}$$

$$Z_{mn}^{E_{S_{k,l}^{\pm}},\pm M_{S_{p,q}}} = \left\{ -\delta_{kp}\delta_{lq} \langle \mathbf{g}_m; \hat{\mathbf{n}}_{k,l} \times \mathbf{f}_n \rangle_{D_{S_{k,l}}^m} - \pm \left\langle \mathbf{g}_m; \nabla \times \langle G_{k,l}, \mathbf{f}_n \rangle_{D_{S_{p,q}}^n} \right\rangle_{D_{S_{k,l}}^m} \right\}_{S_{k,l}^{\pm}}. \tag{3.78b}$$

The terms appearing above are explicitly given at appendix B.1.

The 1-D array $(\underline{J}, \underline{M})$, which are the coefficients of the equivalent currents,

are the unknowns of the problem. The excitation vector $\underline{V}^E$ is given by:

$$V_m^E = \begin{cases} -\left\langle \mathbf{g}_m; \mathbf{E}^{\text{inc}} \right\rangle_{D^m_{S_{2,1}}} & \text{for } m = 1 \dots N_{S_{2,1}} \\ 0 \quad \text{otherwise.} \end{cases} \tag{3.79}$$

Its computation is done at appendix B.3.

The EMPIE MoM matrix $\underline{\underline{Z}}^E$ in (3.76) is characteristic of the target and is independent of the excitation field $\mathbf{E}^{\text{inc}}$. Its total size is $2\left(N_{S_{2,1}} + N_{S_{3,2}}\right) \times 2\left(N_{S_{2,1}} + N_{S_{3,2}}\right)$. Each line corresponds to a testing function, while each column corresponds to a source basis function. The use of $\mathbf{g}_m = \mathbf{f}_m$ and $\mathbf{g}_m = \hat{\mathbf{n}} \times \mathbf{f}_m$ will be indicated in the superscript of the EMPIE MoM matrix by "t" and "n" respectively, which will give $\underline{\underline{Z}}^{tE}$ and $\underline{\underline{Z}}^{nE}$.

If the innermost body is a PEC, the corresponding magnetic equivalent currents coefficients must be set to zero; the last $N_{S_{3,2}}$ lines of the 1-D array $\left(\underline{J}, \underline{M}\right)$ must be removed, and the last $N_{S_{3,2}}$ columns of $\underline{\underline{Z}}^E$ must be removed as well (no $\mathbf{M}_{S_{3,2}}$). The last $N_{S_{3,2}}$ lines of $\underline{\underline{Z}}^E$ and of $\underline{V}^E$, which correspond to the inner problem for $S_{3,2}$ must also be removed, and the size of the matrix then becomes $\left(2N_{S_{2,1}} + N_{S_{3,2}}\right) \times \left(2N_{S_{2,1}} + N_{S_{3,2}}\right)$.

We can take the inverse of $\underline{\underline{Z}}^E$ and use it by multiplying (3.76) in order to find the coefficients $\left(\underline{J}, \underline{M}\right)$, but this is not a wise solution because of the possibility of resonances, as discussed at section 3.6. We must use a MoM discretization of the PMCHWT and CFIE for having a well-conditioned problem. This discretization will be based on the MoM EMPIEs and MMPIEs.

3.7.2.3 MoM MMPIEs matrix

By duality applied to (3.75), or developing (3.55) with $\mathbf{f}_n$ and testing with $\mathbf{g}_m$ yields the following MoM MMPIEs:

$$\begin{aligned} -\left\langle \mathbf{g}_m; \mathbf{H}^{\text{inc}} \right\rangle_{D^m_{S_{2,1}}} = \sum_{n=1}^{N_{S_{2,1}}} M^n_{S_{2,1}} \Bigg\{ & -j\omega \left\langle \mathbf{g}_m; \left\langle \overline{\boldsymbol{\mathcal{K}}}^{FM}; \mathbf{f}_n \right\rangle_{D^n_{S_{2,1}}} \right\rangle_{D^m_{S_{2,1}}} \\ & + \frac{1}{j\omega\mu_0} \left\langle \mathbf{g}_m; \nabla \left\langle K^{\Psi}, \nabla' \cdot \mathbf{f}_n \right\rangle_{D^n_{S_{2,1}}} \right\rangle_{D^m_{S_{2,1}}} \Bigg\}_{S^+_{2,1}} \\ + \sum_{n=1}^{N_{S_{2,1}}} J^n_{S_{2,1}} \Bigg\{ & \left\langle \mathbf{g}_m; \hat{\mathbf{n}}_{2,1} \times \mathbf{f}_n \right\rangle_{D^m_{S_{2,1}}} + \left\langle \mathbf{g}_m; \left\langle \overline{\boldsymbol{\mathcal{G}}}^{HJ}; \mathbf{f}_n \right\rangle_{D^n_{S_{2,1}}} \right\rangle_{D^m_{S_{2,1}}} \Bigg\}_{S^+_{2,1}} \end{aligned} \tag{3.80a}$$

$$
\begin{aligned}
0 = & \sum_{n=1}^{N_{S_{2,1}}} M_{S_{2,1}}^{n} \left\{ -\left\langle \mathbf{g}_m; \frac{\nabla\nabla\cdot + k_2^2}{j\omega\mu_2} \langle G_2, \mathbf{f}_n \rangle_{D_{S_{2,1}}^n} \right\rangle_{D_{S_{2,1}}^m} \right\}_{S_{2,1}^-} \\
& + \sum_{n=1}^{N_{S_{2,1}}} J_{S_{2,1}}^{n} \left\{ \langle \mathbf{g}_m; \hat{\mathbf{n}}_{2,1} \times \mathbf{f}_n \rangle_{D_{S_{2,1}}^m} - \left\langle \mathbf{g}_m; \nabla \times \langle G_2, \mathbf{f}_n \rangle_{D_{S_{2,1}}^n} \right\rangle_{D_{S_{2,1}}^m} \right\}_{S_{2,1}^-} \\
& + \sum_{n=N_{S_{2,1}}+1}^{N_{S_{2,1}}+N_{S_{3,2}}} M_{S_{3,2}}^{n} \left\{ \left\langle \mathbf{g}_m; \frac{\nabla\nabla\cdot + k_2^2}{j\omega\mu_2} \langle G_2, \mathbf{f}_n \rangle_{D_{S_{3,2}}^n} \right\rangle_{D_{S_{2,1}}^m} \right\}_{S_{2,1}^-} \\
& + \sum_{n=N_{S_{2,1}}+1}^{N_{S_{2,1}}+N_{S_{3,2}}} J_{S_{3,2}}^{n} \left\{ \left\langle \mathbf{g}_m; \nabla \times \langle G_2, \mathbf{f}_n \rangle_{D_{S_{3,2}}^n} \right\rangle_{D_{S_{2,1}}^m} \right\}_{S_{2,1}^-}
\end{aligned} \tag{3.80b}
$$

$$
\begin{aligned}
0 = & \sum_{n=1}^{N_{S_{2,1}}} M_{S_{2,1}}^{n} \left\{ -\left\langle \mathbf{g}_m; \frac{\nabla\nabla\cdot + k_2^2}{j\omega\mu_2} \langle G_2, \mathbf{f}_n \rangle_{D_{S_{2,1}}^n} \right\rangle_{D_{S_{3,2}}^m} \right\}_{S_{3,2}^+} \\
& + \sum_{n=1}^{N_{S_{2,1}}} J_{S_{2,1}}^{n} \left\{ -\left\langle \mathbf{g}_m; \nabla \times \langle G_2, \mathbf{f}_n \rangle_{D_{S_{2,1}}^n} \right\rangle_{D_{S_{3,2}}^m} \right\}_{S_{3,2}^+} \\
& + \sum_{n=N_{S_{2,1}}+1}^{N_{S_{2,1}}+N_{S_{3,2}}} M_{S_{3,2}}^{n} \left\{ \left\langle \mathbf{g}_m; \frac{\nabla\nabla\cdot + k_2^2}{j\omega\mu_2} \langle G_2, \mathbf{f}_n \rangle_{D_{S_{3,2}}^n} \right\rangle_{D_{S_{3,2}}^m} \right\}_{S_{3,2}^+} \\
& + \sum_{n=N_{S_{2,1}}+1}^{N_{S_{2,1}}+N_{S_{3,2}}} J_{S_{3,2}}^{n} \Bigg\{ \{ \langle \mathbf{g}_m; \hat{\mathbf{n}}_{3,2} \times \mathbf{f}_n \rangle_{D_{S_{3,2}}^m} \\
& \qquad + \left\langle \mathbf{g}_m; \nabla \times \langle G_2, \mathbf{f}_n \rangle_{D_{S_{3,2}}^n} \right\rangle_{D_{S_{3,2}}^m} \Bigg\}_{S_{3,2}^+}
\end{aligned} \tag{3.80c}
$$

$$
\begin{aligned}
0 = & \sum_{n=N_{S_{2,1}}+1}^{N_{S_{2,1}}+N_{S_{3,2}}} M_{S_{3,2}}^{n} \left\{ -\left\langle \mathbf{g}_m; \frac{\nabla\nabla\cdot + k_3^2}{j\omega\mu_3} \langle G_3, \mathbf{f}_n \rangle_{D_{S_{3,2}}^n} \right\rangle_{D_{S_{3,2}}^m} \right\}_{S_{3,2}^-} \\
& + \sum_{n=N_{S_{2,1}}+1}^{N_{S_{2,1}}+N_{S_{3,2}}} J_{S_{3,2}}^{n} \Bigg\{ \langle \mathbf{g}_m; \hat{\mathbf{n}}_{3,2} \times \mathbf{f}_n \rangle_{D_{S_{3,2}}^m} \\
& \qquad - \left\langle \mathbf{g}_m; \nabla \times \langle G_3, \mathbf{f}_n \rangle_{D_{S_{3,2}}^n} \right\rangle_{D_{S_{3,2}}^m} \Bigg\}_{S_{3,2}^-} .
\end{aligned} \tag{3.80d}
$$

This system of equations can also be written in a matrix form, which will have exactly the same structure as in (3.76). The blocks of the resulting MoM MMPIE matrix $\underline{\underline{Z}}^H$ are given by expressions dual to the blocks of (3.76), namely:

$$Z_{mn}^{H_{S_{k,l}^{\pm}},\pm M_{S_{p,q}}} = \pm \left\{ -j\omega \left\langle \mathbf{g}_m; \left\langle \overline{\boldsymbol{\mathcal{K}}}^{FM}; \mathbf{f}_n \right\rangle_{D_{S_{p,q}}^n} \right\rangle_{D_{S_{k,l}}^m} + \frac{1}{j\omega\mu_0} \left\langle \mathbf{g}_m; \nabla \left\langle K^{\Psi}, \nabla' \cdot \mathbf{f}_n \right\rangle_{D_{S_{p,q}}^n} \right\rangle_{D_{S_{k,l}}^m} \right\}_{S_{k,l}^{\pm}} \tag{3.81a}$$

$$Z_{mn}^{H_{S_{k,l}^{\pm}},\pm J_{S_{p,q}}} = \left\{ \delta_{kp}\delta_{lq} \left\langle \mathbf{g}_m; \hat{\mathbf{n}}_{k,l} \times \mathbf{f}_n \right\rangle_{D_{S_{k,l}}^m} \pm \left\langle \mathbf{g}_m; \left\langle \overline{\boldsymbol{\mathcal{G}}}^{HJ}; \mathbf{f}_n \right\rangle_{D_{S_{p,q}}^n} \right\rangle_{D_{S_{k,l}}^m} \right\}_{S_{k,l}^{\pm}} \tag{3.81b}$$

in the stratified medium (see annex C.1). The terms appearing above are dual to those that are detailed at appendix B.2. In every other "homogeneous" medium (i.e., the medium which is homogeneous when all bodies have been replaced by the appropriate constitutive parameters), we have the following relations:

$$Z_{mn}^{H_{S_{k,l}^{\pm}},\pm M_{S_{p,q}}} = \left\{ \pm \left\langle \mathbf{g}_m; \frac{\nabla\nabla\cdot + k_{k,l}^2}{j\omega\mu_{k,l}} \left\langle G_{k,l}, \mathbf{f}_n \right\rangle_{D_{S_{p,q}}^n} \right\rangle_{D_{S_{k,l}}^m} \right\}_{S_{k,l}^{\pm}} \tag{3.82a}$$

$$Z_{mn}^{H_{S_{k,l}^{\pm}},\pm J_{S_{p,q}}} = \left\{ \delta_{kp}\delta_{lq} \left\langle \mathbf{g}_m; \hat{\mathbf{n}}_{k,l} \times \mathbf{f}_n \right\rangle_{D_{S_{k,l}}^m} \pm \left\langle \mathbf{g}_m; \nabla \times \left\langle G_{k,l}, \mathbf{f}_n \right\rangle_{D_{S_{p,q}}^n} \right\rangle_{D_{S_{k,l}}^m} \right\}_{S_{k,l}^{\pm}}, \tag{3.82b}$$

where the terms are dual to those detailed at appendix B.1.

Each element of the excitation vector $\underline{V}^H$ is given by:

$$V_m^H = \begin{cases} -\left\langle \mathbf{g}_m; \mathbf{H}^{\text{inc}} \right\rangle_{D_{S_{2,1}}^m} & \text{for } m = 1 \ldots N_{S_{2,1}} \\ 0 \quad \text{otherwise.} \end{cases} \tag{3.83}$$

The nonzero terms are explicitly given at appendix B.3.

As for the MoM EMPIE, the use of $\mathbf{g}_m = \mathbf{f}_m$ and $\mathbf{g}_m = \hat{\mathbf{n}} \times \mathbf{f}_m$ in the testing will be indicated by calling the MMPIE MoM matrix $\underline{\underline{Z}}^{tH}$ and $\underline{\underline{Z}}^{nH}$ respectively. If the innermost body is a closed PEC, the same remarks as for $\underline{\underline{Z}}^{E}$ hold true. Moreover, if the innermost body is an open PEC, one cannot enforce the MMPIE on it, and the corresponding testing lines in $\underline{\underline{Z}}^{H}$ and $\underline{V}^{H}$ must also be removed.

3.7.3 PMCHWT and CFIE MoM matrices

As discussed at section 3.6, these two formulations provide a way to have a well-conditioned system (from which the spurious resonances have been removed) and transform an over-determined system into a well-determined one. As a result, it is the MoM CFIE or PMCHWT resulting matrix system that will be used for finding the unknown coefficients of the equivalent currents.

Although applied to the case of a homogeneous body embedded in a multi-layered medium, the general rule for the PMCHWT is that, for *every* surface enclosing a dielectric body (itself homogeneous or containing inhomogeneities), one adds the corresponding inside and outside EMPIEs and MMPIEs as follows:

$$\begin{aligned} &\mathrm{EMPIE}_{S_{i,j}^{+}} + \mathrm{EMPIE}_{S_{i,j}^{-}} \\ &\mathrm{MMPIE}_{S_{i,j}^{+}} + \mathrm{MMPIE}_{S_{i,j}^{-}}. \end{aligned}$$

In the MoM matrices (and the excitation vectors), it is equivalent to add all the lines corresponding to the inside testing of a surface to the lines corresponding to the outside testing of the same surface. Then all the lines corresponding to the inside testing of a surface are removed from the matrix. The resulting matrices $\underline{\underline{Z}}^{E}$ and $\underline{\underline{Z}}^{H}$ and excitation vectors $\underline{V}^{E}$ and $\underline{V}^{H}$ are then concatenated following the lines to form the MoM PMCHWT matrix, which has therefore

the form:

$$\left(\begin{bmatrix} \underline{\underline{Z}}^{tE_{S_{k,l}^+},\pm J_{S_{p,q}}} + \underline{\underline{Z}}^{tE_{S_{k,l}^-},\pm J_{S_{p,q}}} \end{bmatrix} \quad \begin{bmatrix} \underline{\underline{Z}}^{tE_{S_{k,l}^+},\pm M_{S_{p,q}}} + \underline{\underline{Z}}^{tE_{S_{k,l}^-},\pm M_{S_{p,q}}} \end{bmatrix} \right.$$
$$\left. \begin{bmatrix} \underline{\underline{Z}}^{tH_{S_{k,l}^+},\pm J_{S_{p,q}}} + \underline{\underline{Z}}^{tH_{S_{k,l}^-},\pm J_{S_{p,q}}} \end{bmatrix} \quad \begin{bmatrix} \underline{\underline{Z}}^{tH_{S_{k,l}^+},\pm M_{S_{p,q}}} + \underline{\underline{Z}}^{tH_{S_{k,l}^-},\pm M_{S_{p,q}}} \end{bmatrix} \right)$$
$$\bullet \left(\begin{bmatrix} \underline{J}_{S_{p,q}} \end{bmatrix} \right) = \left(\begin{bmatrix} \underline{V}^{tE_{S_{k,l}^+}} + \underline{V}^{tE_{S_{k,l}^-}} \end{bmatrix} \right)$$
$$\left(\begin{bmatrix} \underline{M}_{S_{p,q}} \end{bmatrix} \right) = \left(\begin{bmatrix} \underline{V}^{tH_{S_{k,l}^+}} + \underline{V}^{tH_{S_{k,l}^-}} \end{bmatrix} \right) \tag{3.85}$$

The MoM PMCHWT matrix is formed with $\underline{\underline{Z}}^{tE}$ and $\underline{\underline{Z}}^{tH}$, that is, its elements are the result of testing the PMCHWT formulation with $\mathbf{g}_m = \mathbf{f}_m$ [44].

The MoM CFIE matrix is simpler to obtain from the MoM EMPIE and MMPIE matrices. For all dielectric-dielectric interfaces and closed PEC surfaces, the CFIE is written as the weighted sum of the EMPIE and MMPIE:

$$\alpha\,\mathrm{EMPIE}_{S_{i,j}^{\pm}} + (1-\alpha)\,\eta_0\,\mathrm{MMPIE}_{S_{i,j}^{\pm}}$$

with $0 < \alpha < 1$. The bottom line is that $\underline{\underline{Z}}^E$ and $\underline{\underline{Z}}^H$ as well as $\underline{V}^E$ and $\underline{V}^H$ are simply added with the appropriate weighting to form the MoM CFIE matrix:

$$\begin{bmatrix} \alpha \left(\mathrm{tE}\, \underline{\underline{Z}}^{tE_{S_{k,l}^{\pm}}} + \mathrm{nE}\, \underline{\underline{Z}}^{nE_{S_{k,l}^{\pm}}} \right) \\ + (1-\alpha)\,\eta_0 \left(\mathrm{tH}\, \underline{\underline{Z}}^{tH_{S_{k,l}^{\pm}}} + \mathrm{nH}\, \underline{\underline{Z}}^{nH_{S_{k,l}^{\pm}}} \right) \end{bmatrix} \bullet \begin{bmatrix} \underline{J}_S \\ \underline{M}_S \end{bmatrix}$$
$$= \begin{bmatrix} \alpha \left(\mathrm{tE}\, \underline{V}^{tE_{S_{k,l}^{\pm}}} + \mathrm{nE}\, \underline{V}^{nE_{S_{k,l}^{\pm}}} \right) \\ + (1-\alpha)\,\eta_0 \left(\mathrm{tH}\, \underline{V}^{tH_{S_{k,l}^{\pm}}} + \mathrm{nH}\, \underline{V}^{nH_{S_{k,l}^{\pm}}} \right) \end{bmatrix}. \tag{3.86}$$

On the contrary to the PMCHWT formulation, the CFIE formulation can be tested with $\mathbf{g}_m = \mathbf{f}_m$ and $\mathbf{g}_m = \hat{\mathbf{n}} \times \mathbf{f}_m$ as well. We note the presence of the factors "tE", "tH", "nE" and "nH" in (3.86): these are booleans, equal to 1 if the corresponding testing is used in the CFIE, and 0 otherwise. So, when we talk about the CFIE, it will for example be qualified "tEtHnH" if the EMPIE part is tested with $\mathbf{g}_m = \mathbf{f}_m$ and the MMPIE part is tested by both $\mathbf{g}_m = \mathbf{f}_m$ and $\mathbf{g}_m = \hat{\mathbf{n}} \times \mathbf{f}_m$. The logic for all other names is similar. The most common form of the CFIE found in the literature is tEnEnH [57], but in fact the combinations tEnEtH, tEtHnH, nEtHnH are all equivalent [44].

3.7.4 Validation of the computer programs

The method of moments solution for the EMPIEs, MMPIEs and their combinations under the PMCHWT and CFIE forms have been implemented into computer programs. The code works for general multibodies configurations (section 3.5.1 and 3.5.2), and the combination of the matrix blocks pertaining to the surfaces is performed automatically for all integral equation formulations. The medium which contains the inhomogeneities can be homogeneous or multilayered.

Before performing any computations, one has to describe the problem at hand, *i.e.*, draw the inhomogeneities with the help of a computer aided design (CAD) tool, and somehow mesh the surfaces of the resulting structure. In this work we used Gmsh[1], an open-source mesh generator that has a built-in CAD engine. After the structure has been meshed, Gmsh can save all the information about the mesh (vertexes coordinates and numbers, triangles,...) into a `*.msh` file.

The `*.msh` file provided by Gmsh must be processed in order to classify the basis functions (*i.e.* the pairs of triangles that define them) by physical surface, direct the normals of all the triangles belonging to a closed surface outside of it, detect the boundaries of open surfaces, *etc.* The `*.msh` file processing routine has been written in MATLAB, which allows for a great flexibility in manipulating the mesh components and in their visualization.

The very heart of the MoM program is the computation of the matrix blocks that appear in the MoM EMPIEs and MMPIEs matrices. It is performed by routines written in C++, which are gathered into a library. The choice for C++ was motivated by its ease of use, cleanness of notations and high performance.

[1] `http://www.geuz.org/gmsh/`

This library is interfaced with MATLAB routines, which do the work of re-assembling the blocks for building up the various MoM matrix formulations, as well as inverting these matrices for finding the currents coefficients $(\underline{J}, \underline{M})$.

3.7.4.1 Layered sphere

We study the scattering of a layered sphere, presented at Fig. 3.14. This problem is described for a layered body of arbitrary shape at section 3.4.1; however, we did not use the explicit integral equations formulations derived for that case. As said above, the matrix EMPIEs and MMPIEs blocks are assembled automatically to form the MoM CFIE and PMCHWT matrices. The total number of basis functions is 2,145 (1,389 and 756 on the outer and inner spheres respectively), and since both spheres are dielectric, the total number of unknowns is 4,290. The fill time of all the $\underline{\underline{Z}}^E$ and $\underline{\underline{Z}}^H$ blocks (on which the PMCHWT and CFIE formulations are based) takes about 300 seconds on a Pentium IV 3.2 GHz, and the solution time is approximately 120 seconds for each formulation. The memory taken is about 800 MB. This high memory consumption for the problem at hand is due to the fact that both the PMCHWT and CFIE matrices are computed and stored in RAM, and each has a memory footprint of $\sim$ 300 MB (a complex double precision digit occupies 16 bytes, and the size of each matrix is 4,290 $\times$ 4,290). We used the analytical Mie solution

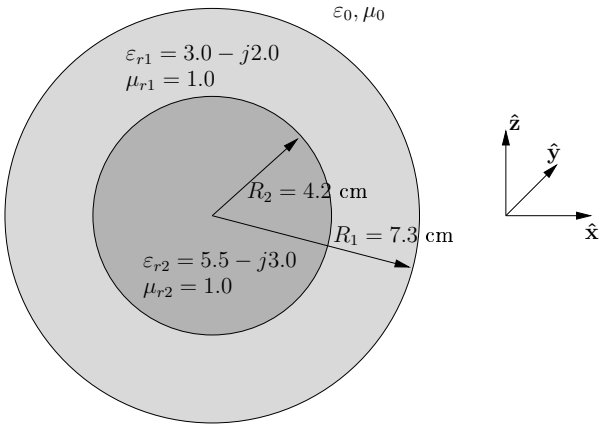

Figure 3.14: A 2-layers sphere, where each layer is lossy. The analytical solution is obtained by the Mie theory.

for layered spheres for comparison [58], which yields the exact solution for the problem at hand.

The spheres are excited by a plane wave at $f = 1.35$ GHz, with its E-field directed following $\hat{\mathbf{x}}$. We first compare at Fig. 3.15 the E_x and H_y scattered fields—that is, radiated by $\left(\mathbf{J}_{S_{1,0}}, \mathbf{M}_{S_{1,0}}\right)$—in region 0. The E-field along di-

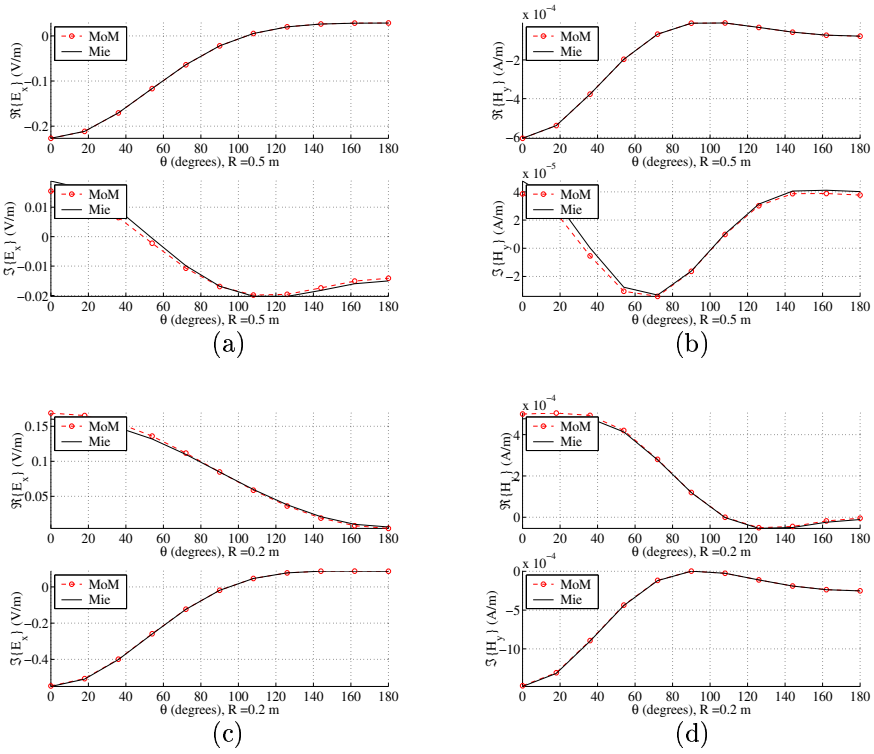

Figure 3.15: Comparison of E_x (left column) and H_y (right column) scattered fields in region 0, at 50 cm and 20 from sphere center. θ is the angle that the observation point position vector forms with the vertical. The observation point is in the zy plane (see Fig. 3.14).

rection $\hat{\mathbf{x}}$ at some point $\mathbf{r}$ in space due to the equivalent currents on $S_{1,0}$ is obtained as follows. We place a dipole of electric current $\mathbf{J}_d = \hat{\mathbf{x}}$ at $\mathbf{r}$ in space. The reciprocity theorem then yields the following relation:

$$E_x = \int_{S_{1,0}} \left(\mathbf{E}_d \cdot \mathbf{J}_{S_{1,0}} - \mathbf{H}_d \cdot \mathbf{M}_{S_{1,0}}\right) \, \mathrm{d}S'. \tag{3.87}$$

where $\left(\mathbf{E}_d, \mathbf{H}_d\right)$ are the fields due to the dipole. The Mie (MoM) E_x field is obtained if the Mie (MoM) surface currents are used in (3.87). If the MoM currents are used, (3.87) can be simplified by using the equivalent currents

decomposition (3.70):

$$\begin{aligned} E_x^{\text{MoM}} &= \sum_{n=1}^{N_{S_{1,0}}} J_{S_{1,0}}^n \langle \mathbf{E}_d; \mathbf{f}_n \rangle_{D_{S_{1,0}}^n} - \sum_{n=1}^{N_{S_{1,0}}} M_{S_{1,0}}^n \langle \mathbf{H}_d; \mathbf{f}_n \rangle_{D_{S_{1,0}}^n} \\ &= -\underline{J}_{S_{1,0}}^T \underline{V}_d^{tE} + \underline{M}_{S_{1,0}}^T \underline{V}_d^{tH} \end{aligned} \tag{3.88}$$

where the last equality has been obtained by using (3.79) and (3.83), with superscript "T" indicating that the corresponding array must be transposed. The magnetic field H_y is obtained by a similar reasoning (or by duality). One can immediately see that, when agreement between real parts is excellent, it is somewhat less good for the imaginary part, and vice-versa.

It is also interesting to compare directly the currents obtained by the MoM algorithm to those obtained through the analytical Mie solution. There is no bias or constant error between the Mie and MoM equivalent currents. Significant standard deviation errors seem to affect J_{Sy} and M_{Sx} more than the other components, as shown at Fig. 3.16. This can be attributed to the fact that the incident E-field and H-field are linearly polarized following x and y respectively. Indeed, at any point $\left(R = R_1, \theta, \phi\right)$ on the outer sphere, we have for the E-field and magnetic current that

$$\begin{aligned} \mathbf{M}_{S_{1,0}} &= \left(E^{\text{inc}}\,\hat{\mathbf{x}} + \mathbf{E}^{\text{scat}}\right) \times \hat{\mathbf{n}}_{S_{1,0}} \\ &= E^{\text{inc}}\left(\sin(\theta)\sin(\phi)\,\hat{\mathbf{z}} - \cos(\theta)\,\hat{\mathbf{y}}\right) + \mathbf{E}^{\text{scat}} \times \hat{\mathbf{n}}_{S_{1,0}} \end{aligned} \tag{3.89}$$

because $\hat{\mathbf{n}}_{S_{1,0}} = \hat{\mathbf{R}} = \sin(\theta)\cos(\phi)\,\hat{\mathbf{x}} + \sin(\theta)\sin(\phi)\,\hat{\mathbf{y}} + \cos(\theta)\,\hat{\mathbf{z}}$, and with $\mathbf{E}^{\text{scat}} = \mathbf{E}_0 - \mathbf{E}^{\text{inc}}$. Therefore, while $\left(\mathbf{E}^{\text{inc}} + \mathbf{E}^{\text{scat}}\right) \times \hat{\mathbf{n}}_{S_{1,0}}$ account for M_{Sy} and M_{Sz}, only $\mathbf{E}^{\text{scat}} \times \hat{\mathbf{n}}_{S_{1,0}}$ accounts for M_{Sx}, making it more prone to numerical errors.

We can further examine the exactness of the equivalent currents by means of histograms for each component, as shown at Fig. 3.17. The MoM equivalent currents can be considered as statistical quantities distributed near their Mie counterparts, and deviations with regards to the exact solution can be studied by means of appropriate statistical tools.

3.7.4.2 Dielectric cube

The cube under consideration has sides of length 7 cm, is made of dielectric material of $\varepsilon_r = 3.0 - j2.0$, and is excited by a dipole of electric current $\mathbf{J}^{\text{inc}} = [1.0, 1.0, 0.0]/\sqrt{2.0}$, which radiates at a frequency $f = 1.35$ GHz and is located at $\mathbf{r}' = [0.1, -0.05, 0.2]$.

As no analytical solution exists for the cube scattering, the only way to verify the validity of the solution is to consider the equivalent currents pertaining

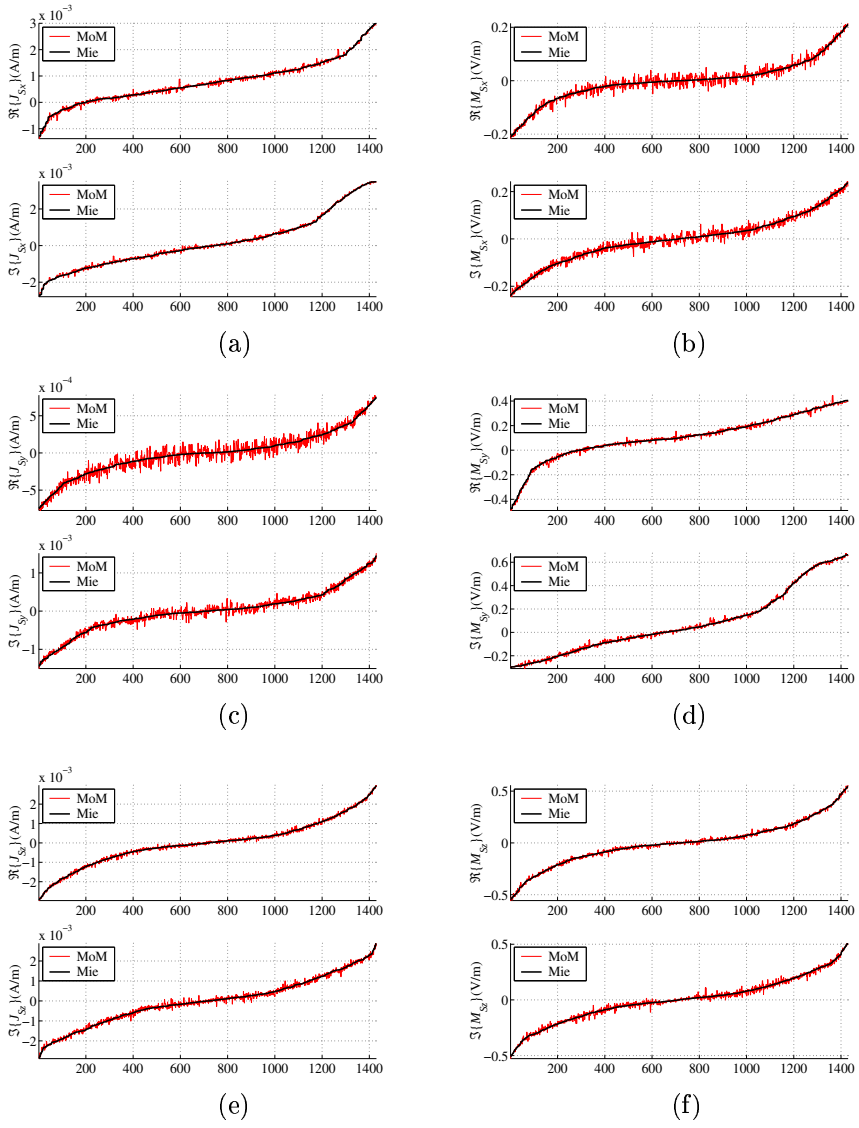

Figure 3.16: Left column: Comparison of the components of the electric currents $\mathbf{J}_S$ given by the MoM CFIE and by Mie theory. Right column: the same but for magnetic currents $\mathbf{M}_S$. Comparisons are made at the centroid of each triangle. Abscissa indicates the triangle number.

to a region and see if in all other regions the fields are zero. Fig. 3.18 shows the equivalent problem for the region outside the cube and, as expected, null fields

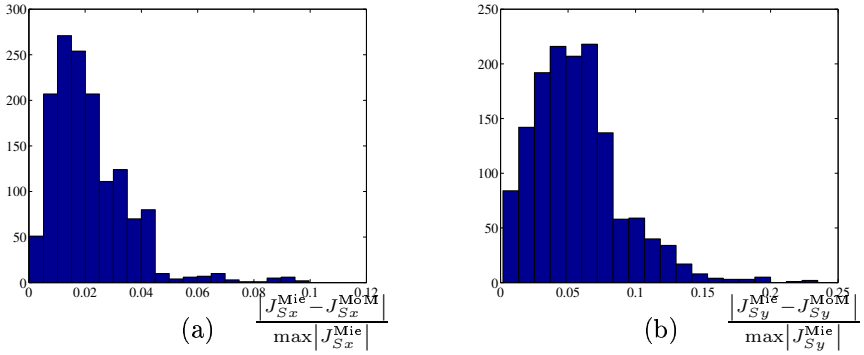

Figure 3.17: Histograms of J_{Sx} and J_{Sy} for the layered sphere show that J_{Sy} is statistically less coherent with its Mie counterpart than J_{Sx}.

are obtained inside the cube. We remind here that, for the exterior equivalent problem, one has to add the fields radiated by the surface equivalent currents and the incident fields produced by $\mathbf{J}^{\mathrm{inc}}$. The discrepancies that occur inside the cube near the boundary for the real parts of the electric and magnetic fields are due to the fact that the singularities of the free space Green's function and its gradient have not been extracted in the computation of the scattered fields.

3.8 Summary and perspectives

In this chapter, we have derived in section 3.2 the Huygens surface equivalence principle for a homogeneous medium in a manner slightly different than the development presented by Peterson *et al.* [51, chapter 1], in order to derive the principle for sources contained within the region for which the equivalence is built. In section 3.2.2 we extended the principle to multilayered media thanks to the source-field relationships written with help of the appropriate DGFs [27]. This equivalence principle has allowed us to write mixed-potential integral representations for the original electric and magnetic fields within a given volume as a sum of fields resulting from source-fields integrals of bounding surface equivalent currents convoluted with the volume Green's functions, combined with the fields produced by the original sources if any. Applying the boundary conditions to the integral representations of these fields has naturally provided the surface mixed-potential integral equations, namely the EMPIE and MMPIE (first defined at section 3.3.1), which in section 3.6 have further been combined

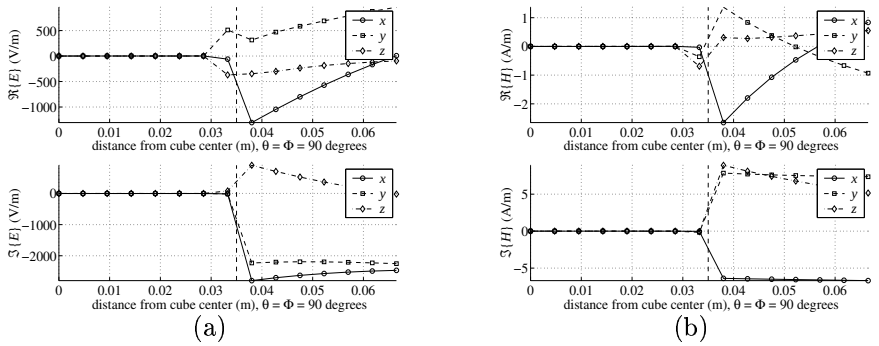

Figure 3.18: Fields of the exterior equivalent problem for the dielectric cube. Vertical dashed line represents cube boundary. Null fields are obtained inside the cube, and the original fields are obtained outside the cube.

under the form of a CFIE and PMCHWT formulation in order to obtain a resonance-free problem and the same number of unknowns and equations. The step-by-step approach followed has evolved from simple PEC scatterers embedded within multilayered media (section 3.3.1) up to arbitrary combinations of dielectric and PEC bodies (section 3.5.2).

In section 3.7 we have introduced the MoM, which allows for solving the surface integral equations by discretizing the surface equivalent currents (which are the unknown quantities searched for) and testing the resulting discretized equations, thereby providing a linear system that has to be solved in order to retrieve the unknown coefficients of the discretized currents. First, the MoM expressions for the EMPIEs pertaining to an inhomogeneous dielectric body (introduced at section 3.4.1) have been derived and written in a matrix system, conveniently subdivided into matrix blocks whose lines and columns are related to testing and source surfaces respectively (section 3.7.2.2). Explicit expressions of the terms appearing in these blocks are given in appendix B. Duality is then used to obtain the MoM matrix formulation for the corresponding MMPIEs; the MoM EMPIEs and MMPIEs matrix blocks are then combined following simple rules to form the MoM matrices for the CFIE and PMCHWT formulations. Although derived for the inhomogeneous dielectric body of section 3.4.1, the MoM matrix systems of section 3.7 are easily generalizable to more complete geometries. Yet it is an unnecessary task to write down the matrix systems for other cases, as the corresponding submatrices assembling and combinations

can be performed by a computer fed by the rules derived from the simpler inhomogeneous dielectric body case.

The MoM computer routines are indeed based on the simple rules of section 3.7 for constituting the MoM matrix systems from the matrix blocks, and on a programs library that computes efficiently the matrix blocks. The user must only draw the geometry at hand and mesh the surfaces, give values to the EM properties of the medium surrounding and filling the inhomogeneities, and define the source strength, distribution, position and orientation. These computer routines have been extensively tested and found to yield accurate solution for geometries involving several volumes (layered sphere), possibly with sharp edges and corners (cube).

Although very general, these computer routines still suffer some limitations:

- the code does not handle bodies penetrating one or more interfaces of the multilayered medium;
- the code does not handle intersections between dielectric and/or metallic surfaces;
- the computational complexity and memory footprint of the code is $\mathcal{O}(N^2)$ if an iterative method is used for solving the linear system, where N is the number of basis functions, which can rapidly render slow or intractable the resolution of problems involving electrically large objects[2].

The first two items can be addressed in a few men-weeks work, and publications are available on these subjects [59, 60, 50]. The extension of the code in order to tackle electrically large objects is however much more challenging, especially for multilayered media. While this has been done for single PEC, single homogeneous target and multiple homogeneous targets embedded in two-layers media by Carin *et al.* [25, 26, 61] by using the multilevel fast multipole algorithm (MLFMA) [44, 48], which allows the complexity and memory cost to drop down to $\mathcal{O}(N \log N)$, the extension of such a method to multivolumes embedded in arbitrary multilayered media remains to be done. However, such an extension was not necessary for the practical applications of the MoM code studied in chapter 4.

[2]This can happen if the soil or the target permittivity or the frequency is high.

Chapter 4

Practical applications of the GPR model

4.1 Introduction

The GPR model developed in chapter 2 allows for the extraction of the target radar signature, in theory free from the antenna signal artifacts (internal reflections, emission and reception equivalent currents amplitudes and the multiple reflections) and from the soil response. For this, the radar system has to be characterized for determining H_i, H_t^2 and H_f, and a measurement above the soil without target has to be performed in order to extract its signature R_S. With this in hand, one is able to recover the target signature by using (2.62). Within this scope, comparisons between extracted and computed target signatures have already been made at chapter 2, and excellent agreement has been found.

However, real world conditions are far from the laboratory settings. The operational parameters of the antenna can be wrongly estimated. In our experience, these parameters are strongly dependent upon the strength with which the waveguide is attached to the VNA. On another hand, the soil EM parameters can—and do—vary greatly from point to point, therefore an estimation of those parameters or of R_S may not correspond to the reality of the ground surrounding the buried target (at this point we do not consider the dependence of R_S upon the soil surface roughness, because it is possible to choose the upper limit of the bandwidth such that the smallest wavelength is still large

enough when compared to the soil surface variations [9, chapter 3]). Finally, as each term of the relative error will depend upon the magnitude of the target signature (section 4.2.3), a parametric study of its variations should also be performed.

This chapter is organized as follows. Section 4.2 presents two practical examples of buried target signature extraction and the consequent enhancement of the target visual discrimination. The first example studies the effect of soil moisture on the target signature extraction, while the second example is focused on a B-scan. Both are laboratory experiments. Sections 4.2.3 and 4.2.4 are devoted to the study of the sources of errors that arise in the process of signature extraction. Finally, section 4.3 presents the parametric study of the target signature.

4.2 Buried target signature extraction

4.2.1 Extraction of a buried AP PMN Russian mine signature

Measurements for a soil subject to various water contents have been made. Fig. 4.1 (a) shows $\Gamma^{(\mathrm{soil},\ t)} = \Gamma^{(\mathrm{ml},\ t)} - \Gamma^{(\mathrm{fs})}$ in the time domain for a 4-layers medium which contains a plastic AP PMN Russian mine, obtained without filtering out the soil response (antenna internal reflections have been subtracted). The figure is a collection of A-scans obtained for different volumetric water contents. The reader can see that the mine is not discernable from the background.

Fig. 4.1 (b) shows the time domain signature of the mine after extraction of the soil response in the frequency domain, which had been previously measured, and filtering of the antenna effect. Note that operational parameter H_t^2 introduces a delay, hence filtering it out from the signal—*e.g.*, going from Fig. 4.1 (a) to Fig. 4.1 (b)—will modify the arrival times of the different signals. In configurations 1–4, the filtered signal shows much more clearly the presence of the mine, and the time position of the target reflection permits to accurately retrieve its depth. In configurations 5–6, the soil reflection has been correctly filtered; however, the mine is not clearly visible, because the attenuation of the EM waves at those water contents becomes too important. Henceforth the EM waves incident upon the target are strongly attenuated, and the resulting scattered waves are also attenuated on their way back to the antenna.

The reason why configurations 7–9 yielded less satisfactory results in terms

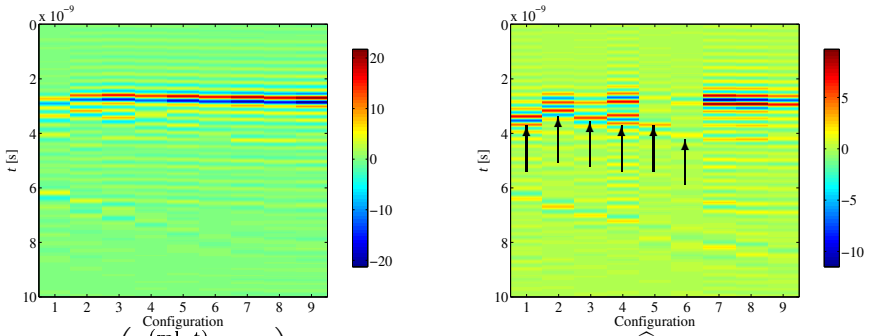

(a) $\left(\Gamma_{\text{meas}}^{(\text{ml, t})} - H_i\right)(t)$ [–] (b) $\widehat{R}_T(t)$ [–]

Figure 4.1: Time domain signal of soil and Russian PMN mine (diameter 11 cm, height 5.5 cm: see Fig. 1.1) for 9 different water contents. Abscissa "configuration" refers to the water content of the layer containing the target: 1 is 0 %, 9 is 25 % of volumetric water content, and progression between water contents is uniform. (a) Mine is hard to see because of strong soil reflection. (b) Soil signal subtraction allows to "see" the mine in some configurations, indicated by a black arrow. Burial depth varies for different configurations.

of soil clutter removal is due to the fact that the height of the antenna above the empty soil was not equal to the height of the antenna above the soil with the mine. This resulted in a phase shift between the estimated soil radar responses that does not allow for a good subtraction of the soil contribution from the total GPR signal (see section 4.2.4.1). Configurations 7–9 also correspond to high water contents, therefore the radar response of the soil is rather strong and the waves are quickly attenuated within the soil, which leads to an overall target response much weaker than for the lower water contents.

The water content increases from configuration 1 to 9, and so does the complex permittivity of the sand. Therefore, if the target is always buried at the same depth, its signal arrival time should also increase with the configuration number. However, this is not the case at Fig. 4.1 (b), because the target was not buried at a constant depth from one configuration to the other, due to a practical reason: the sand had to be thoroughly mixed for each new water content in order to ensure homogeneity of the moisture repartition.

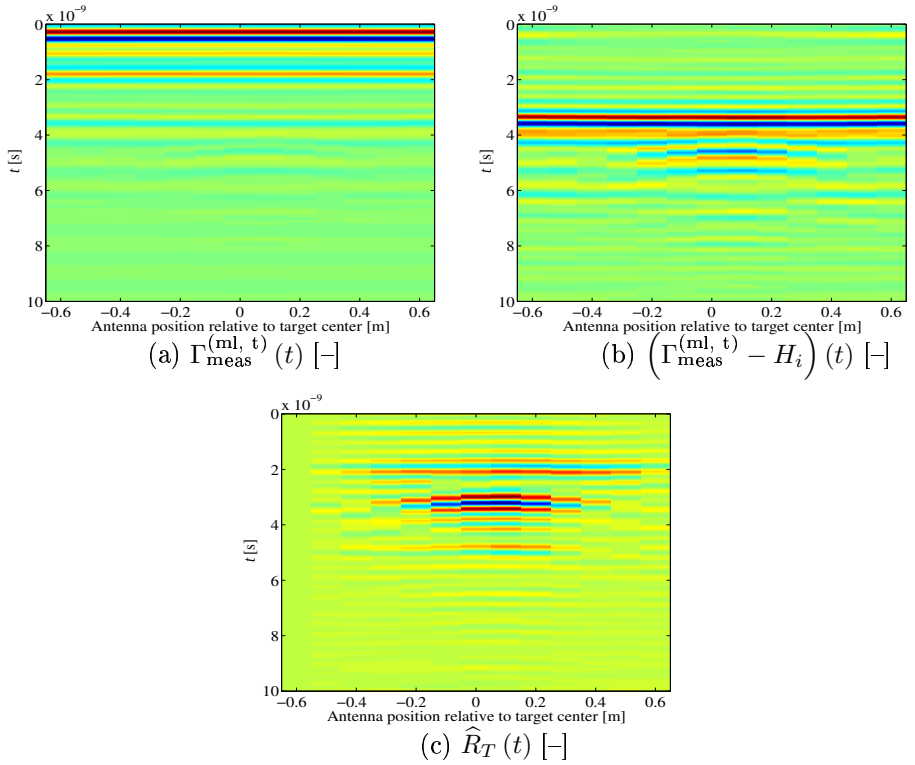

(a) $\Gamma_{\text{meas}}^{(\text{ml, t})}(t)$ [–]

(b) $\left(\Gamma_{\text{meas}}^{(\text{ml, t})} - H_i\right)(t)$ [–]

(c) $\widehat{R}_T(t)$ [–]

Figure 4.2: Extraction of the B-scan produced by metal cylinder embedded in a 4-layers medium. (a) Antenna internal reflections dominate the soil and target radar responses in this measured time domain B-scan. (b) Filtering of antenna internal reflections allows for better understanding of underground structure. Target response is weaker than soil response. (c) Filtering of the soil signal shows much more clearly target signal.

4.2.2 Extraction of the B-scan signature of a buried metal cylinder

The process of soil radar response filtering has been applied to a B-scan (collection of A-scans along a line) of a metal cylinder (diameter 12 cm, height 6.5 cm) buried in a sandy soil with $\varepsilon_r = 5$ and $\sigma = 5.3 \times 10^{-3}$ [S/m]. Fig. 4.2 (a) shows the raw GPR signal in the time domain, with no filtering applied at all. The internal reflections of the antenna make it impossible to see the buried target. This illustrates the importance of filtering out the effect of the antenna from the GPR signal. Fig. 4.2 (b) shows the GPR signal from which the antenna

internal reflections have been removed. Now the soil radar response dominates the target radar response. A target with a weaker radar response would hardly stand out of the background, *i.e.*, the soil. Fig. 4.2 (c) shows the B-scan from which the soil signal has been removed, resulting in a great improvement of the signal to clutter ratio, where "signal" is the target response, and "clutter" is the soil response. Nevertheless, the soil response is still visible: this is due to a small change of the antenna height above the soil while it was moved alongside a line. It is shown at section 4.2.4.1 that an antenna-soil distance error as small as 3 mm can yield bad results when subtracting the soil response from the radar signal. Therefore a simple soil signal subtraction is not usable in practice.

4.2.3 Errors in buried target signature extraction

The target signature is yielded by rewriting (2.57):

$$R_T = \frac{\frac{\Gamma - H_i}{H_t^2}}{1 + H_f \frac{\Gamma - H_i}{H_t^2}} - R_S, \tag{4.1}$$

where $R_T = R_{11}^{(\mathrm{t})}$ and $R_S = R_{11}^{(\mathrm{soil})}$. The above equation is in the frequency domain. The first order error on the target signature is given by differentiating (4.1) and by replacing the differential terms by their corresponding finite increments:

$$\begin{aligned}
\Delta R_T &= \frac{\partial R_T}{\partial \Gamma}\Delta\Gamma + \frac{\partial R_T}{\partial H_i}\Delta H_i + \frac{\partial R_T}{\partial H_t}\Delta H_t + \frac{\partial R_T}{\partial H_f}\Delta H_f + \frac{\partial R_T}{\partial R_S}\Delta R_S \\
&= \frac{1}{H_t^2\left[1 + H_f\frac{\Gamma - H_i}{H_t^2}\right]^2}\left[\Delta\Gamma - \Delta H_i - 2\frac{\Gamma - H_i}{H_t}\Delta H_t - \left(\frac{\Gamma - H_i}{H_t}\right)^2 \Delta H_f\right] \\
&\quad - \Delta R_S.
\end{aligned} \tag{4.2}$$

Finally, the relative error in R_T can be obtained from the relative errors in each of the above terms by dividing both sides of (4.2) by R_T:

$$\begin{aligned}
\frac{\Delta R_T}{R_T} &= \frac{1}{H_t^2\left[1 + H_f\frac{\Gamma - H_i}{H_t^2}\right]^2} \\
&\quad \left[\frac{\Gamma}{R_T}\frac{\Delta\Gamma}{\Gamma} - \frac{H_i}{R_T}\frac{\Delta H_i}{H_i} - 2\frac{\Gamma - H_i}{H_t}\frac{H_t}{R_T}\frac{\Delta H_t}{H_t} - \left(\frac{\Gamma - H_i}{H_t}\right)^2 \frac{H_f}{R_T}\frac{\Delta H_f}{H_f}\right] \\
&\quad - \frac{R_S}{R_T}\frac{\Delta R_S}{R_S}.
\end{aligned} \tag{4.3}$$

Eq. (4.3), called the *GPR determinate relative error equation*, is very important, as it expresses the relative error on R_T as a weighted sum of the relative errors of all the terms that are in (4.1). The coefficient in front of each relative error term yields the magnitude of its contribution to $\frac{\Delta R_T}{R_T}$. It is therefore easy to see from practical measurements which source of error is predominant. For example, we present at Fig. 4.3 the numerical values of these coefficients for the air-filled target buried in multilayered medium (section 2.5.4). Fig. 4.3 tells us that not all errors have the same effects: while, according to (4.3), all the coefficients of the error terms are inversely proportional to $|R_T|$, it is ΔH_i and ΔH_t that have the highest coefficients in the error formula, followed by that of ΔR_S. We remind here that H_i can be obtained by a free space measurement in the GPR characterization process (see section 2.4.5); if the tightening strength that binds the antenna to the waveguide does not vary from the GPR characterization to the actual measurement campaign, ΔH_i will be negligible. A variable tightening strength is also a source of error for the estimated H_t, but another cause concerns the estimation of the radar response of the calibration target (a finite metal plane, considered infinite for the GPR characterization). ΔH_f will have similar causes as ΔH_i and ΔH_t, but its incidence on the target signature estimation error is much less consequential, as seen at Fig. 4.3 (b). Finally, ΔR_S can have different reasons, of which the first is of course the error on the antenna operational parameters. Another source of error is the fact that the soil response can vary greatly from point to point due to varying moisture conditions or soil roughness for example, and a nearby A-scan of a target-free soil can differ significantly from the response of the soil surrounding the target, thereby yielding a bad soil subtraction. ΔR_S can also occur when the height of the antenna above the soil differs for the A-scan with and without the target respectively (see sections 4.2.2 and 4.2.4.1).

4.2.4 Soil clutter in target signature

Clutter should be considered as the main source of the target undetectability. D. Daniels defines the clutter as "the signals that are unrelated to the target scattering characteristics but occur in the same sample-time window and have similar spectral characteristics to the target response" [9]. For GPRs, clutter mainly comes from the air-soil interface, and to a lesser extent from the multiple reflections that occur between the antenna and the ground surface. Clutter can also be generated by inhomogeneities located at the same electrical distance from the antenna than the target, and this has been studied by El-Shenawee

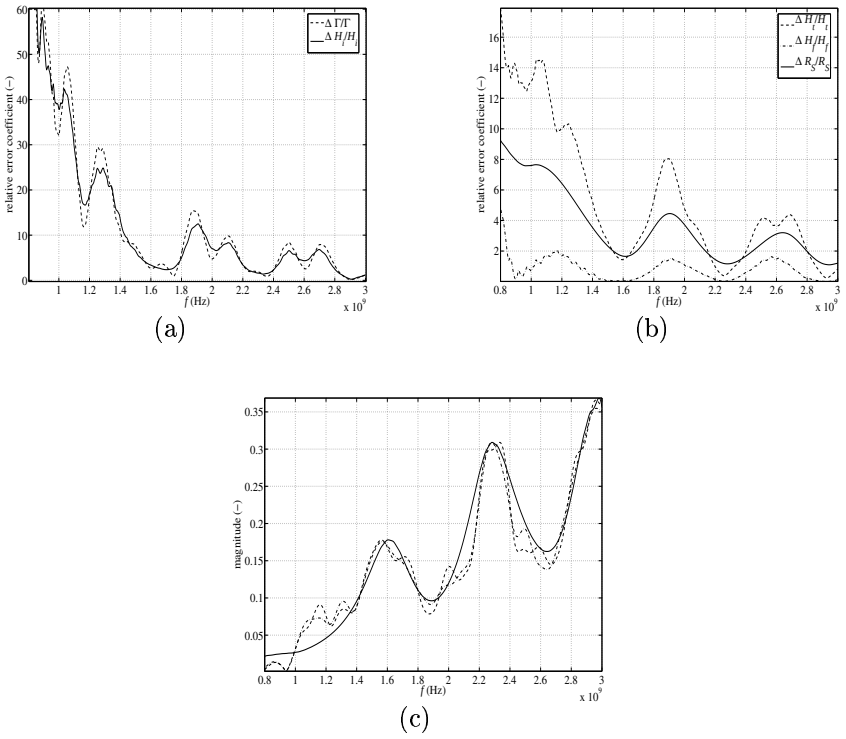

Figure 4.3: Relative errors coefficients for signature of target presented at section 2.5.4: (a) coefficients of $\frac{\Delta\Gamma}{\Gamma}$ and $\frac{\Delta H_i}{H_i}$; (b) coefficients of $\frac{\Delta H_t}{H_t}$, $\frac{\Delta H_f}{H_f}$ and $\frac{\Delta R_S}{R_S}$. These coefficients are inversely proportional to magnitude of R_T shown at (c) (reproduced from Fig. 2.10 (c)).

[24].

Aside the soil or spurious target clutter, the target undetectability level is also related to the dynamic range of the detector [62, 9]. In our experiments we used a Rohde & Schwarz vector network analyzer whose dynamic range can be considered to be $\sim$ 110 dB (see the data sheet at `www.rohde-schwarz.com`). Therefore, the target would have been undetected if the power level associated to $\Gamma^{(\mathrm{t})}$ had been 110 dB below that of $\Gamma^{(\mathrm{fs})} + \Gamma^{(\mathrm{soil})}$. This was not the limiting factor for target detectability in our experiments, and has therefore not been studied.

Simulations done hereafter show at Fig. 4.7, section 4.3.1, that the radar response of a small plastic landmine is at least one order of magnitude smaller than the soil radar response, that is, $|R_T| < 0.1\,|R_S|$. Consequently, rewriting

(2.57) by neglecting the contribution of the target in the retroaction yields:

$$\frac{\Gamma^{(\mathrm{ml,\ t})} - H_i}{H_t^2} = \frac{R_S}{1 - H_f R_S} + \frac{R_T}{1 - H_f R_S}. \tag{4.4}$$

This equation is written in the frequency domain.

Let us suppose now that the system has been characterized, *i.e.*, that we know transmittances H_i, H_t and H_f with good precision, and that we possess for R_S an estimation $\widehat{R}_S = \alpha R_S$, where α is frequency-dependent and should be as close to 1 as possible for every frequency. In order to suppress the soil contribution in (4.4), we subtract from it the estimated (measured or computed) soil response and obtain:

$$\begin{aligned}
\frac{\Gamma^{(\mathrm{ml,\ t})} - H_i}{H_t^2} - \frac{\widehat{R}_S}{1 - H_f \widehat{R}_S} &= \frac{R_S}{1 - H_f R_S} - \frac{\widehat{R}_S}{1 - H_f \widehat{R}_S} + \frac{R_T}{1 - H_f R_S} \\
&= \frac{R_S - \widehat{R}_S}{\left(1 - H_f \widehat{R}_S\right)(1 - H_f R_S)} + \frac{R_T}{1 - H_f R_S} \\
&\simeq \frac{R_S (1 - \alpha)}{1 - H_f R_S (1 + \alpha)} + \frac{R_T}{1 - H_f R_S},
\end{aligned} \tag{4.5}$$

where the last equality has been obtained by neglecting $H_f^2 R_S \widehat{R}_S$ at the denominator, because H_f and R_S are smaller than 1, as can be seen at Fig. 2.4 and 2.10. Finally, developing in series the denominators, retaining only the first-order terms and neglecting the multiple reflections excitation of the target yields:

$$\begin{aligned}
\frac{\Gamma^{(\mathrm{ml,\ t})} - H_i}{H_t^2} - \frac{\widehat{R}_S}{1 - H_f \widehat{R}_S} &\simeq R_S (1 - \alpha)\left(1 + H_f R_S (1 + \alpha)\right) + R_T \\
&\simeq R_S (1 - \alpha) + H_f R_S^2 \left(1 - \alpha^2\right) + R_T.
\end{aligned} \tag{4.6}$$

The above result shows us that two terms are added to the target signature, respectively due to the first air-ground reflection and to the first antenna-soil reflection. This is illustrated at Fig. 4.4.

We therefore have to distinguish two cases, following the target position with respect to the soil clutter. If the target is within a "clutter band", it has to "stand out" in order to be detectable. It can be so through the shape of its corresponding signal if a B-scan is performed (the shape is then a hyperbola: see Fig. 1.7 and the corresponding discussion), or through a larger time domain amplitude of its signature than the soil clutter. On the other side, if the target is outside the clutter bands, it will be time discriminable even within an A-scan.

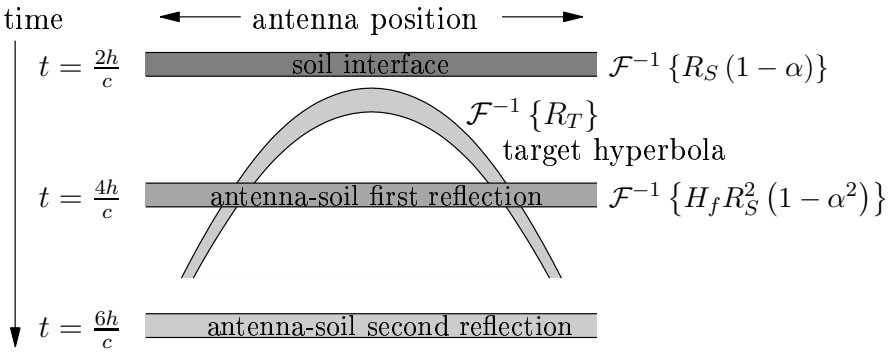

Figure 4.4: Schematic drawing of a B-scan (collection of A-scans along a line) after soil radar signal subtraction. h is the antenna height above the soil. $\mathcal{F}^{-1}$ denotes inverse Fourier transform. If $\widehat{R}_S \neq R_S$, the soil interface radar response and the first antenna-soil reflection pollute the target signal. Higher order multiple reflections terms are neglected in the series development of the denominator in (4.5).

We give in the following two sections two concrete examples of soil interface and antenna-soil reflection clutter.

4.2.4.1 Soil interface clutter

If the target is very close to the soil surface, the time domain equivalent of R_T will get mixed into that of $\Delta R_S = R_S - \widehat{R}_S = R_S(1-\alpha)$. Since $|R_T| < 0.1\,|R_S|$, a 10% error on $\widehat{R}_S$ will have the consequence that $|\Delta R_S| > |R_T|$, which renders the target not discernable in an A-scan with the antenna placed at its nadir. However, if the error does not vary with the antenna horizontal position, the mine can still be discernable in B-scans (with a constant antenna height above the soil surface), as its characteristic hyperbola will stand out of the background. If $\widehat{R}_S = R_S$ ($\alpha = 1$), the soil subtraction is perfect and the clutter is zero.

Let us illustrate the soil interface clutter by a simulated example, where we suppose that $H_f = 0$ (no antenna scattering). Fig. 4.5 (a) shows the theoretical (computed) B-scan of a metallic cylinder buried in a 4-layers soil. Fig. 4.5 (b) presents the B-scan signature of the cylinder, where the soil radar signal extraction is done perfectly, *i.e.* when no error is made on the soil EM parameters or on the height of the antenna above the soil. It is easy to see that the signal due to the different layers has been perfectly removed. The second

reflection apparent on the figure is due to the image of the cylinder in the metal plane at the bottom of the multilayered medium.

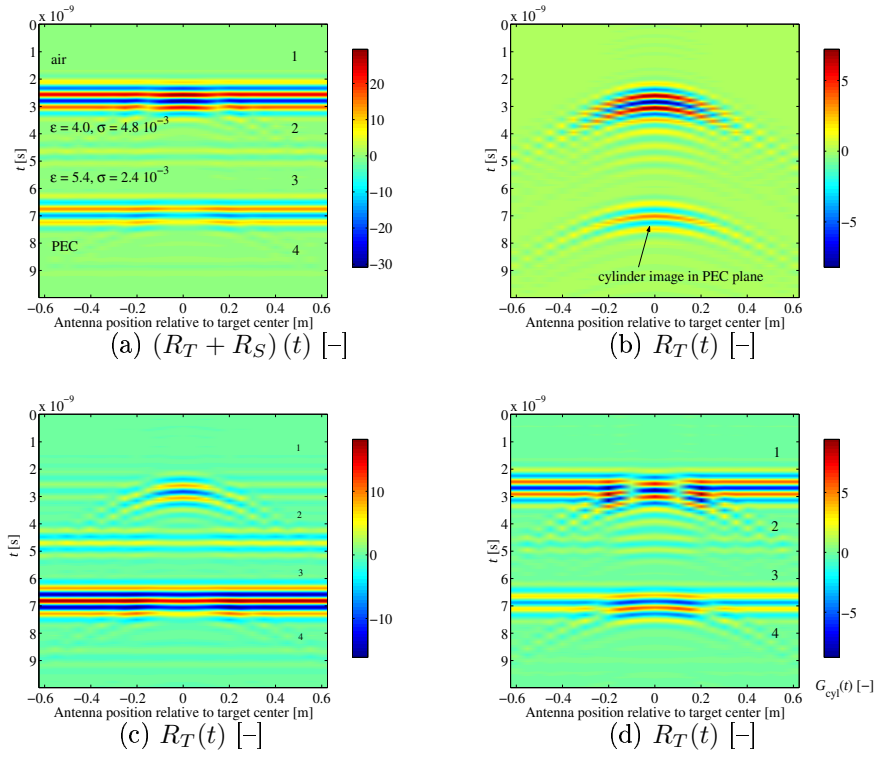

(a) $(R_T + R_S)(t)$ [–] (b) $R_T(t)$ [–]

(c) $R_T(t)$ [–] (d) $R_T(t)$ [–]

Figure 4.5: Simulated time domain B-scan of iron cylinder ($h = 6$ cm, $d = 12$ cm) buried in a 4-layers medium. Last layer is PEC. (a) $R_S + R_T$, i.e. radar signal before soil signature subtraction. (b) Radar signature of buried cylinder when soil EM parameters and antenna height are correctly estimated. (c) Radar signature of buried cylinder when ε_{r2} of layer 2 is incorrectly estimated. (d) Radar signature of buried cylinder when antenna height above the soil is 3 mm lower than in the simulation of the soil alone.

Fig. 4.5 (c) shows the degradation of the signature extraction when an underestimation of 10 % is made on the estimation of the dielectric permittivity of layer 2. The reflection of layer 2 cannot be completely eliminated, but the result of the filtering is still sufficiently low as compared to the reflection due to the cylinder for this latter to be clearly visible. The interface between layer 2 and 3 is also visible, but the main clutter comes from the PEC plane reflection. The explanation is the following. As for layer 2, the amplitude of this reflection

is incorrectly estimated; but, since the EM waves propagation velocity within layer 2 is also not correctly estimated, the time at which this reflection occurs does not correspond to the original time. Therefore, at the PEC plane level, the soil signal subtraction yields a difference between two large quantities (correct and incorrect reflection of PEC surface) that are not in phase, which in turn gives a considerable contribution to the extracted target signature. In fact, this contribution is so strong that the second hyperbola is not visible anymore.

The above reasoning may be reproduced for Fig. 4.5 (d), where an error of 3 mm is made on the estimation of the antenna height above the soil. This error causes a difference in the arrival time of the air-soil interface radar return, and the difference of these two quantities yields an important "phantom reflection", rendering the extraction of the cylinder radar return barely possible. From the above discussions, it is easy to see that mistakes in antenna height lead to more important errors in target radar return extraction than those due to bad estimation of the soil EM parameters. Only the "tails" of the hyperbola are visible at Fig. 4.5 (d), but the top of the hyperbola, which corresponds to the A-scan at nadir of the target, is drowned in the soil interface clutter. However, the B-scan renders the target radar response *space-time discernable* thanks to the tails of the hyperbola. Note that if the antenna is too directive, the tails of the hyperbola will present a small amplitude and might therefore be hard to detect.

4.2.4.2 Antenna-soil multiple reflections clutter

If the target is buried away the air-soil interface, time domain R_T can be mixed in the antenna-soil first reflection clutter. For example, if the antenna is located at $h = 20$ cm above the ground surface, clutter due to antenna-soil multiple reflections will be located at $t = 4h/c = 2.67$ ns (c is the speed of light in free space). Moreover, if the target is buried at $d = 7$ cm deep in a soil having $\varepsilon_{rs} = 8, \mu_{rs} = 1$, its signal will occur at $t = 2\left(h + d\sqrt{\varepsilon_{rs}}\right)/c = 2.65$ ns, which corresponds to antenna-soil clutter time. If we suppose for simplicity that the height of the antenna remains constant while performing a B-scan, the clutter due to the antenna-soil multiple reflections will form a *horizontal band* that will "pollute" the target hyperbolic signal, with the first (and most important) reflection located at a time position that depends upon the antenna-soil distance. This clutter effect is schematically depicted at Fig. 4.4. If the clutter is more important than the target radar response, it can mask a significant part of it, especially if the hyperbola displays a small curvature.

It has already been mentioned (section 2.2) that our antenna is a strong scatterer. We repeat here that this antenna allows to bring to light the "multiple reflections" effect. It must be stressed that, thanks to the modularity of the model, *any* antenna, in particular a weak backscattering one, could have been used instead of this one.

4.3 Parametric study of buried target radar signature

One of the most important question that has to be answered before using the GPR in mine detection activities is: when will GPR perform poorly in detecting mines? Or in other words: when is the signal-to-clutter ratio small to the point that the mine detection becomes hazardous (here, signal is the target signature and noise are all other signals)? We have seen in the previous section that the answer to this question is strongly related to the strength of the soil clutter with respect to the target signature magnitude and its location in the time domain. Eq. 4.3 also shows that the relative error terms are inversely proportional to the magnitude of the target signature. It is therefore of significant interest to study the variation of the soil and target radar responses with respect to the parameters that are susceptible to impact them.

The physical and geometrical parameters that influence the target signature are: the soil EM constitutive parameters $\varepsilon_{rs}, \mu_{rs}, \sigma_s$ (subscripts "r" and "s" stand for "relative" and "soil" respectively), the target depth and orientation with respect to the soil surface, the antenna height and the target EM and geometrical properties. The soil EM characteristics are amongst the most important factors in the mine radar response. As will be seen later in this section, the magnitude of the target signature is indeed strongly correlated with the difference of EM parameters (especially dielectric permittivity) between the soil and the target. Moreover, it is well known that soils which present high losses will prevent the GPR from detecting buried targets, since attenuation can greatly reduce the power incident upon and hence scattered by the target. The target physical properties also play a very important role: its EM properties—which are to be compared to the soil EM properties—, shape and dimensions play a significant part on its radar cross section. Finally, the GPR hardware (antenna type and orientation, polarization, frequency band, ...) also plays an important role in the soil and target signature, since it defines the excitation of the targets. In this work we have only considered the radar

system described in chapter 2.

Measurements can answer the performance assessment question. The main advantage of this approach is that it can be made as close to the terrain reality as possible. However, this method is time-consuming and expensive. Moreover, many parameters can influence the measurements, and it is very difficult to isolate the influence of each parameter in the variations of the signal. Finally, the results provided by this method are bound to the hardware used (antenna type and polarization, detector sensitivity, soil signal filtering, signal modulation, *etc.*), and are by no means extrapolable to another radar system.

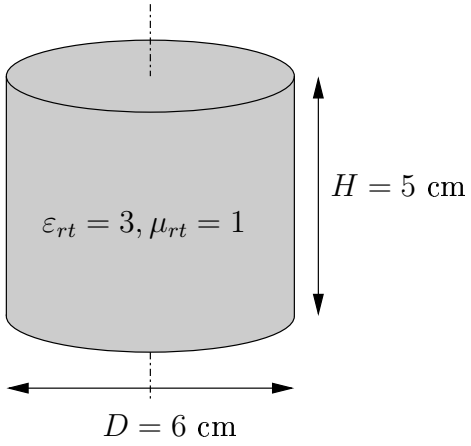

Figure 4.6: The M35BG AP mine simulant used in the parametric calculations. Due to its internal structure, it is probable that a real M35BG AP mine would have a radar response 5–10 dB superior to its simulant.

Another approach consists in a numerical parametric study of the target radar signature. The advantages of the numerical approach are obvious: it allows for a separate study of the influence of the parameters on the radar responses, it is fast, cheap, generic with regards to hardware, and finally it is deterministic and not prone to hardware failures or misuse. Moreover it is always possible to link the numerical experiments with a particular hardware by characterizing this latter, and use (2.57) and the related subsequent equations for determining the signal that would have been measured. The main disadvantage is that it is non-realistic w.r.t. the soil clutter if only flat soil is considered.

In this work we have chosen the numerical approach. The target considered in the remainder of the text is a dielectric cylinder representing an AP mine,

with diameter 6 cm and height 5 cm, and $\varepsilon_{rt} = 3$. These numbers are chosen to approach as much as possible the physical properties of the M35BG AP mine (see Fig. 1.1), which is small and therefore difficult to detect. We could have used a more complicated target in the numerical computations, with a better approximation of a real landmine internals. However, the goal here is to present a parametric study; the qualitative conclusions of the parametric study can probably be extrapolated to more complicated targets since the study is mainly focused on the consequences of the soil EM parameters variations or on the target relative position with respect to the radar system. Nevertheless, one could use much more complicated targets in the study, *e.g.* real mine structures, since the GPR model remains exactly the same. Such a study could be performed for finding the best possible geometry-radar antennas-frequency band for a given target and a given soil.

For all signatures, the target and soil excitation fields are computed with the help of the cosinusoidal equivalent currents distribution on the aperture of the horn antenna (see chapter 2).

4.3.1 Varying soil permittivity

The "physical" situation consists in the cylinder buried 4 cm deep, and the antenna located at 20 cm above the soil. The frequency band is 0.5–3 GHz, and ε_{rs} varies from 2.5 to 10. Fig. 4.7 (a) shows that, for $\tan\delta_s = 0$, the magnitude of the target signature grows with f and with the contrast of dielectric permittivity $\Delta\varepsilon_r = |\varepsilon_{rs} - \varepsilon_{rt}|$.[1] For a small $\tan\delta_s$, this observation seems to remain valid as seen at Fig. 4.7 (c). When losses in the soil become important, it appears that for a given ε_{rs}, the magnitude presents an optimum for a frequency that is not necessarily the upper limit of the band. Please note that, in reality, $\varepsilon_{rs} > 2$, but this value has been used for comparison.

The same observations apply to Fig. 4.7 (b), (d) and (f), which present the most interesting quantity, *i.e.*, the ratio of magnitudes of the target and soil signatures. Please note that, while the numerical values may not correspond accurately to reality, the ratio $|R_T/R_S|$ is always below 0.1, and can go below 0.02 for high losses in the soil. This is an indication that the target response will in most cases be much weaker (at least one order of magnitude) than the soil response.

Finally, it should be noted that, since the target has been considered lossless (which is a valid assumption), augmenting the losses in the soil will make the

[1] The magnitude of the target signature is of course near to zero if $\varepsilon_{rs} \simeq \varepsilon_{rt}$.

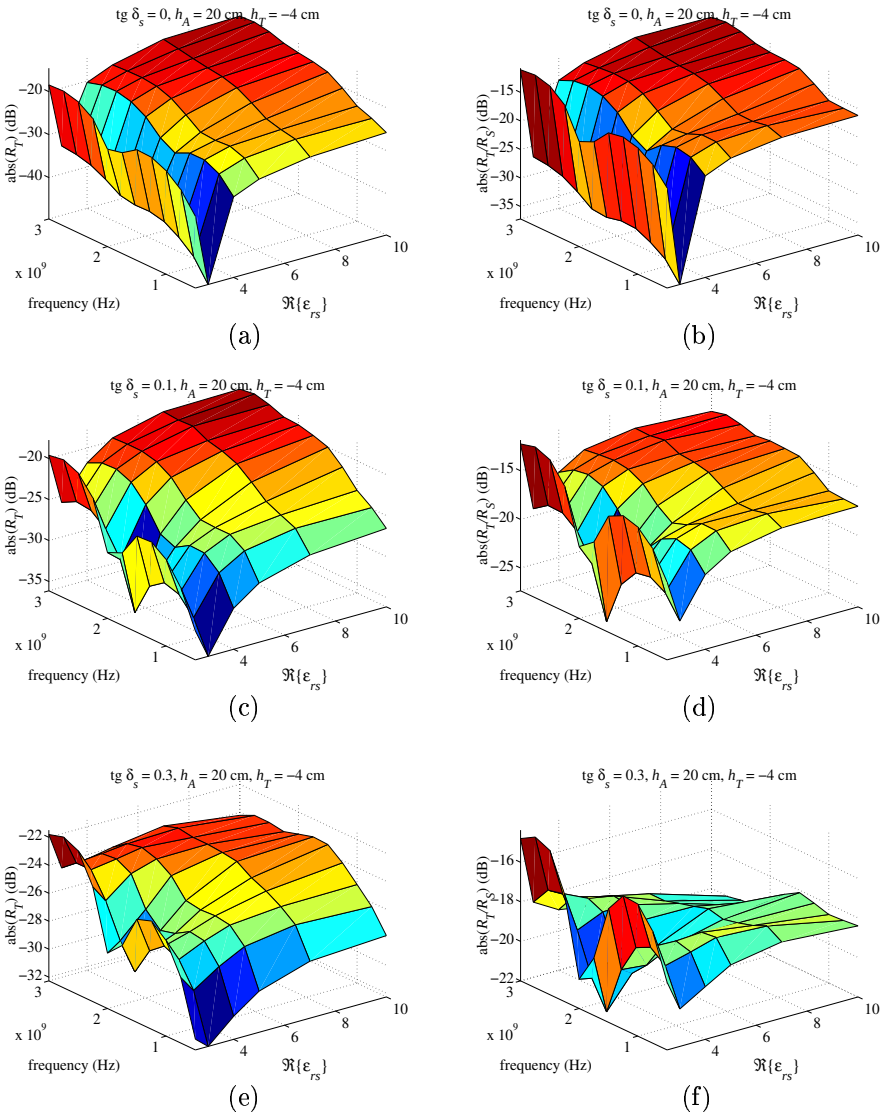

Figure 4.7: Left column: variation of target signature (R_T) magnitude as function of soil EM parameters. Right column: variation of $|R_T/R_S|$, the ratio of magnitudes of target and soil signatures. This ratio is never greater than -10 dB, or $|R_T| < 0.1\,|R_S|$.

target more "visible" for $\varepsilon_{rs} = 3$, this because ε_{rt} is real.

4.3.2 Varying antenna height above the soil

Fig. 4.8 (a) shows that $|R_T|$ decreases if the antenna height above the soil increases. Fig. 4.8 (b) indicates that, when the antenna is moved away from the soil, the target radar response decreases faster than the soil response. Indeed, as explained in sections 2.4.4.2 and 2.4.4.3, the decrease in amplitude of the soil signal is only in R^{-1} while that of a localized target is in R^{-2}. Hence, for increasing the ratio $|R_T/R_S|$, the GPR antennas should be put as close to the soil as possible. When doing so, however, one has to bear in mind that the

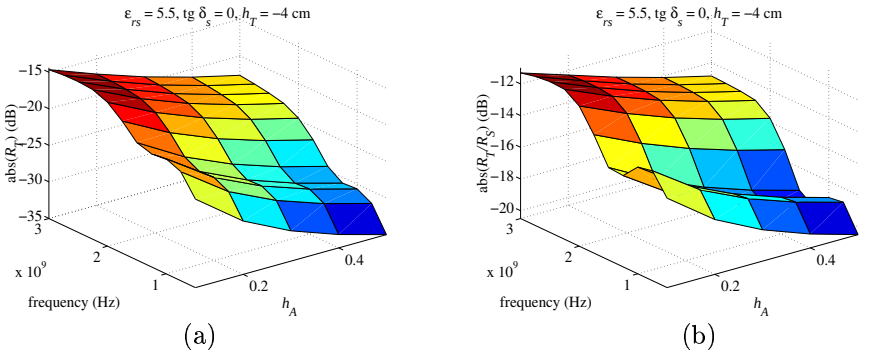

Figure 4.8: (a) Variation of $|R_T|$ as function of antenna height above soil. (b) Variation of $\left|\frac{R_T}{R_S}\right|$.

antenna-soil multiple reflections terms schematically depicted at Fig. 4.4 will get closer to each other, and their time domain amplitudes will grow following a R^{-2} rule. Therefore the probability of polluting the target signature will increase. A study is necessary to evaluate if this disadvantage outweighs the increase of the ratio $|R_T/R_S|$ when the antenna is closer to the soil.

4.3.3 Varying target depth

As we can see at Fig. 4.9 (a), when the soil presents no losses, the decrease of the target signature magnitude with the increase of the target depth is not very significant. However, Fig. 4.9 (b) shows that this decrease adopts an exponential behavior when the soil presents a loss tangent, here $\tan\delta = 0.1$.

A more interesting depth effect is its influence on the MoM matrix $\underline{\underline{Z}}$ of the target. We can see at Fig. 4.10 that the difference between the MoM matrix $\underline{\underline{Z}}^{(\mathrm{ml})}$ of the buried target and the MoM matrix $\underline{\underline{Z}}^{(\mathrm{hs})}$ of the target embedded

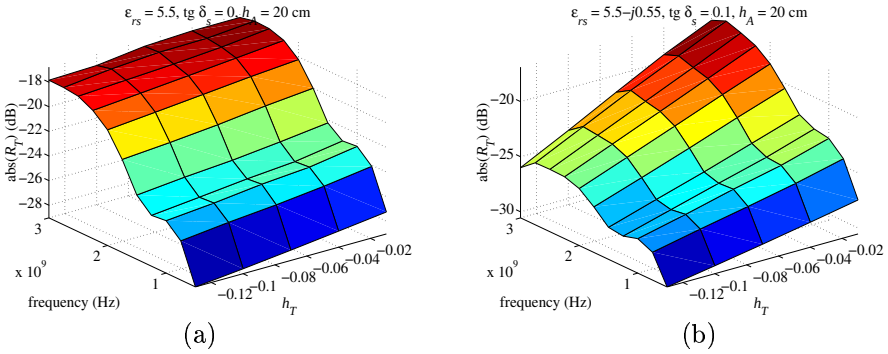

Figure 4.9: Magnitude of target signature for varying target depth with (a) no losses in soil (b) $\tan\delta_s = 0.1$. $\varepsilon_{rs} = 5.5$.

in a homogeneous space having the same ε_{rs} as the soil becomes smaller as the target depth increases. This effect is even more pronounced when the soil is lossy. As the MoM matrix is characteristic of the target, this result simply means that, the deeper the target is, the more its signature resembles its homogeneous space counterpart—provided that the medium has the same EM parameters as the soil. Another way to see this is that the multiple reflections between the air-soil interface and the target play a more and more negligible role as the target depth increases, and this tendency is increased if the soil is lossy.

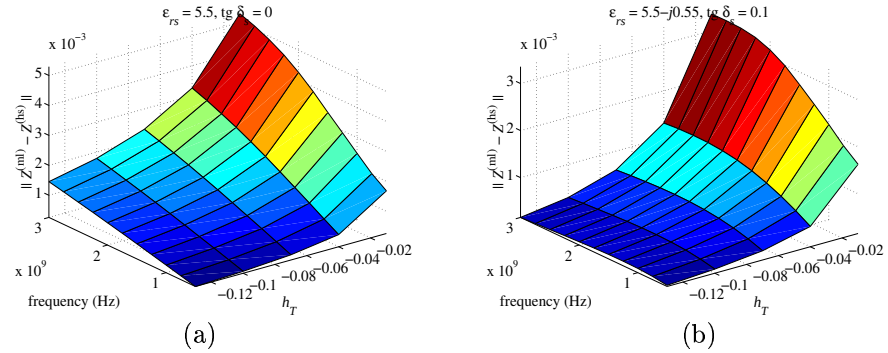

Figure 4.10: $\|\Delta Z\| = \|Z^{(ml)} - Z^{(hs)}\|$ *diminishes with target depth. (a)* $\varepsilon_{rs} = 5.5$ *and no losses in soil. (b)* $\varepsilon_{rs} = 5.5 - j0.55$ *and* $\tan\delta_s = 0.1$.

Since the difference between the MoM matrices diminishes with target depth, it is interesting to check the evolution of the difference between the radar signals $R_T^{(\mathrm{ml})}$ and $R_T^{(\mathrm{hs})}$ computed with the help of the MoM matrix of the buried target and its homogeneous space (hs) counterpart respectively. In this numerical example the antenna is located at 20 cm from the soil, and the incoming fields *in the presence of the soil* are used for computing $R_T^{(\mathrm{ml})}$ and $R_T^{(\mathrm{hs})}$ (buried and homogeneous space targets undergo the same excitation). We can see at Fig. 4.11 that the relative error is in its greater part below 5 %. The

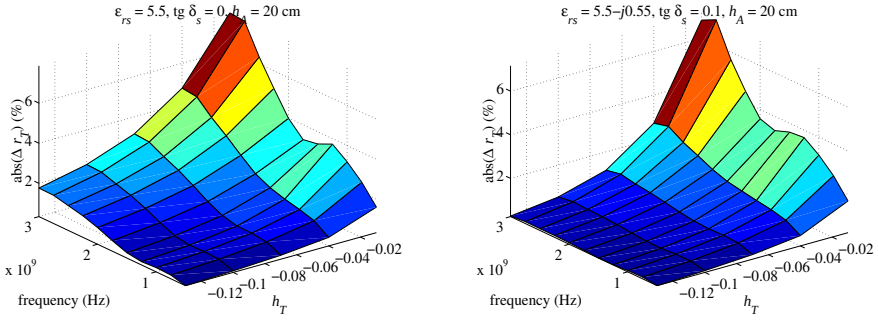

Figure 4.11: $\Delta r_T = \left| \frac{R_T^{(ml)} - R_T^{(hs)}}{R_T^{(ml)}} \right|$ *is the relative error of* $R_T^{(hs)}$ *with regards to* $R_T^{(ml)}$. Δr_T *diminishes rapidly with target depth. (a)* $\varepsilon_{rs} = 5.5$ *and no losses in soil. (b)* $\varepsilon_{rs} = 5.5 - j0.55$ *and* $\tan\delta_s = 0.1$.

above result could be of very important practical consequence in target identification. Indeed, one could compare the target signature measured on the field with its counterpart obtained by measurement or simulation in a homogeneous medium having the same EM properties as the soil, because the orientation and distance of the target with respect to the interface plays a negligible role in its response: only the amplitude and phase of the excitation fields and their angle of illumination of the target matter.

4.3.4 Varying target angle with respect to the vertical

The buried target top surface is not necessarily parallel to the air-soil interface. It means that for monostatic GPRs the specular reflection will not occur, unless the antenna is tilted. In this numerical experiment R_T was computed over the usual frequency band, but with a varying tilting angle θ_T between the soil

surface and the top surface of the target. Fig. 4.12 shows that to an increase of θ_T up to $40°$ corresponds a small increase of R_T at lower frequencies, but that an important decrease of R_T occurs at high frequencies. This, together with Fig. 4.14 (b), shows that the top surface of the target plays a crucial role in the magnitude of its radar response. A possible explanation for the

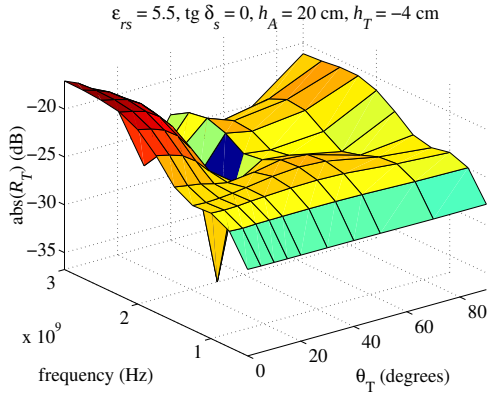

Figure 4.12: Varying target angle with respect to the vertical. $\varepsilon_{rs} = 5.5$.

small increase of R_T at lower frequencies has been suggested by Marc Piette. The scattering of an electrically small object is mainly related to the "visible surface" or "aspect" that it offers to the incoming wave. In this case, since the wave is propagating following the vertical, the aspect of the cylinder is at its maximum when tilted at around 40 degrees w.r.t. the vertical.

Fig. 4.13 shows examples of the time domain R_T for different target angles. One can see that the greatest amplitude is obtained for $\theta_T = 0$.

4.3.5 Varying target diameter, height and shape

The increase of the area of the target top surface has a significant impact, and leads to an important increase of the target response $|R_T|$, as shown at Fig. 4.14 (a). We note also that the height of the target only displaces the loci of the local minima and maxima of $|R_T|$, but does not increase its magnitude. Fig. 4.14 (b) gives an idea of the changes in the magnitude of the target response that can occur if a small change of geometry or a void in the AP mine is added (see Fig. 4.15). The most significant changes appear to occur at 2 GHz and above, but this value is indicative, as a higher soil dielectric permittivity would have a strong influence on these variations. Nevertheless, the introduction

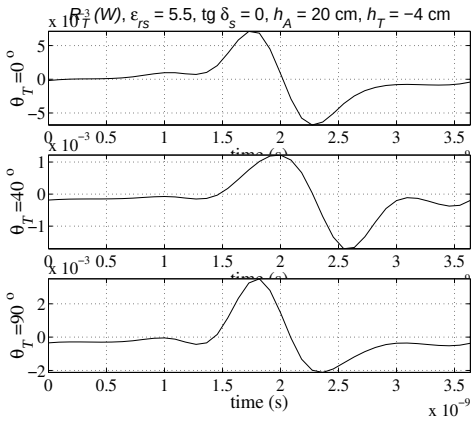

Figure 4.13: Time domain R_T for three different target angles with respect to the vertical. $\varepsilon_{rs} = 5.5$. Maximum amplitude is attained for $\theta_T = 0°$.

of a geometrical or structural modification such as a small bump or an air void modifies in an important manner the target signature, and it emphasizes the importance of taking into account even small geometrical details in the fabrication of inert mines used in GPR testing. Likewise, a precise computer CAD model of the target is needed if one wants to perform more realistic simulations.

4.4 Summary and perspectives

The monostatic GPR equation (2.57) can be used for extracting the target signature from radar measurements. The target radar response is then given by (4.1), where the soil radar signal R_S can be measured or computed once the soil EM parameters are known. We have shown in two laboratory experiments—a soil with varying moisture content containing a Russian PMN mine and a B-scan of a buried metal cylinder—that the subtraction of the antenna and soil contributions to the total radar signal significantly enhances the visual discrimination of the target. Moreover, the ability to retrieve the target signature opens the door to further signal processing treatment that could allow target identification.

However, errors on the estimation of the antenna operational parameters or of the soil radar response lead to errors on the estimated target response, as stated by the GPR determinate relative error equation (4.3). In that equation,

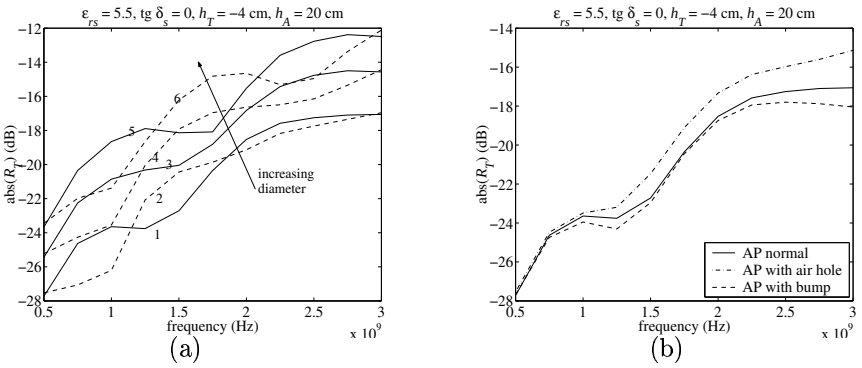

Figure 4.14: (a) Varying target height and diameter. For curves 1, 3, 5: $D = 6, 8, 10$ *cm,* $H = 5$ *cm; for curves 2, 4, 6:* $D = 6, 8, 10$ *cm,* $H = 7.5$ *cm. (b) Different target geometries: standard AP, AP with bump, AP with air hole.* $\varepsilon_{rs} = 5.5$*,* $h_T = -4$ *cm,* $h_A = 20$ *cm.*

the relative error on R_T is expressed as a weighted sum of the relative errors on the terms of (4.1), with all weights inversely proportional to $|R_T|$. In the numerical example given at Fig. 4.3, we can see that the weights before ΔH_i, ΔH_t and ΔR_S are the most important; however, if the antenna-waveguide tightening strength does not change between the GPR characterization and the actual measurement, ΔH_i will be negligible. Moreover, in that case the source of error for H_t comes then from the target used for GPR characterization. Apart from characterization errors, the error on the soil response can be due to the differences in the soil EM properties from point to point, or to the soil roughness, which induces random spatial variations in the soil response. This latter aspect has however not been studied in this work.

The soil clutter, which arises when its response is not properly subtracted from the total radar signal, is the main source of target undetectability. In an A-scan, if the target is flush buried, its radar response can be mixed with the air-soil interface response; if buried deeper, its response can be polluted by the multiple reflections occurring between the soil and the antenna. Fortunately, in this case a B-scan renders the target space-time discernible, thanks to the characteristic hyperbolic shape of the target response. The amplitudes of the hyperbola tails are dependent upon the directivity of the antenna and the losses in the soil. If the antenna is too directive, the target will be "visible" only if it is located on the main beam axis, and its hyperbola tails amplitudes will

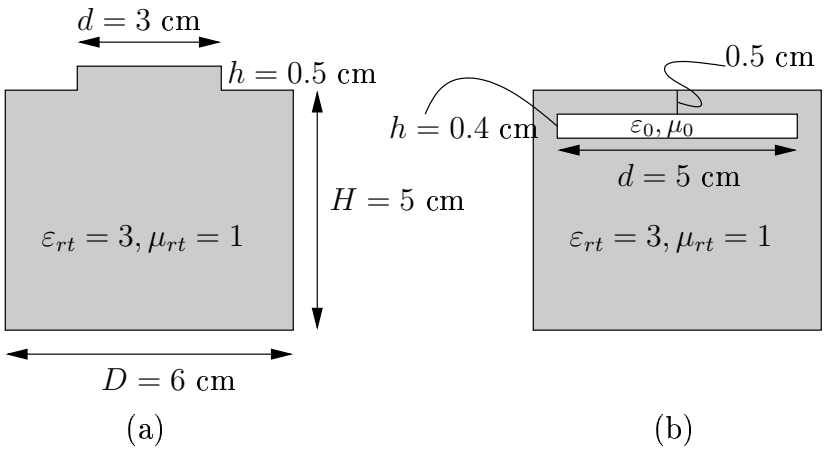

Figure 4.15: The modified AP mine geometries. (a) Small bump on top surface. (b) Air void in the AP mine.

decrease sharply with antenna-target horizontal distance. The losses in the soil further decrease these tails amplitudes, as the length of the propagation path in the soil increases with antenna-target horizontal distance.

In these extraction error and soil clutter studies, we have seen that the magnitude of the target response, taken relatively to that of the soil response, is an important factor in the quality assessment of the detection and signature extraction. It is therefore of significant interest to study the variations of these magnitudes with regards to the parameters that are susceptible to modify them through a parametric study of these responses. It would be expensive and time consuming to perform such a parametric study experimentally, as it would require a high degree of control in order to isolate the influence of each parameter and reduce the measurement errors. This, added to the fact that the GPR model has an excellent precision, has led us to choose to perform this parametric study with the help of our MoM code.

This parametric study, although particular to a given target ($\varepsilon_{rt} = 3$) and antenna currents (cosine distribution), and contained within determined frequency (0.5–3 GHz) and soil permittivity (2.5–10) ranges, has provided both expected and surprising results, summarized hereafter.

- If the soil is not lossy, an increase in its permittivity or in frequency results in an increase in both $|R_T|$ and $\left|\frac{R_T}{R_S}\right|$. When the soil is slightly lossy ($\tan\delta_s = 0.1$), the above conclusion still holds, but this is not

valid anymore for highly lossy soils ($\tan\delta_s = 0.3$), where an increase in frequency or soil permittivity can yield a decrease in both $|R_T|$ and $\left|\frac{R_T}{R_S}\right|$.

- The increase of the antenna-soil distance unsurprisingly yields a decrease in both $|R_T|$ and $\left|\frac{R_T}{R_S}\right|$.
- On the other hand, the study of the varying target depth yields a unexpected (not previously provided by experiments) result:
  - the multiple reflections between the target and the soil interface can be neglected in the target signature evaluation with an error mostly inferior to 5 %, and this error sharply drops with soil losses and/or target depth;
  - in other words, the characteristic MoM matrix of the buried target is very similar to the one that would have been obtained in a homogeneous medium having the same EM parameters as the layer containing the target;

  therefore, while the target signature depends upon the amplitude and angle of incidence of the excitation fields impinging on the target, it does not depend upon the target orientation with and distance from the soil interface. So, if someone is about to build a database of target signatures, he can do it by considering only an excitation field, the target orientation w.r.t. this field and the EM parameters of the "immediate vicinity" of the target, but does not have to consider the orientation and distance of the target w.r.t. the air-soil interface, the smallest distance (or target depth) being determined by a maximum acceptable error.
- The target orientation with respect to the incident fields has a strong effect on its signature, and this study has shown that the signature magnitude drops sharply when the reflection is not specular.
- The diameter of the target has an important effect on the signature magnitude, while its height only displaces the loci of the maxima and minima.
- A slight modification of the target geometry or inner structure can significantly change its radar response above a certain frequency.

Although performed for a simple target, this parametric study could be performed for more complicated objects presenting a better approximation of a real landmine internals. However, the goal here was to present the parametric

study itself. The qualitative conclusions of the parametric study can probably be extrapolated to more complicated targets, since the study is mainly focused on the consequences of the soil EM parameters variations or on the target relative position with respect to the radar system. Nevertheless, one could use much more complicated targets in the parametric study, *e.g.* real mine structures, as it does not make any difference to the numerical code. Such a study could also be performed for example for finding the best possible *geometry-radar antennas-frequency band* for a given target and a given soil. One could also use it for evaluating different equivalent currents distributions—corresponding to different antennas—, of for testing the influence of the soil roughness on R_T and on $\frac{R_T}{R_S}$. Finally, the numerical code could be used for finding the resonance frequencies of the buried target [63, 64, 65, 66].

Chapter 5

Summary and perspectives

5.1 Summary

The research work deals with the establishment of a complete, accurate, efficient and separable model of a monostatic SFCW GPR. The completeness, *i.e.* modeling from the EM quantities (fields and currents) up to the measured signal displayed to the operator, is important for providing the designer with a tool able to help him in creating or enhancing a particular design. The quantitative accuracy is a desired feature for the generation of predictive results, as well as for being able to access and precisely describe the high degree of complexity subtending the scattering processes at hand. The efficiency, related to the numerical method used in the model, should ensure that the accurate results are obtained within a reasonable computation time. The efficiency extends to the entire GPR model through the separability of its constitutive elements, which moreover allows for flexibility in the choice and modeling method of these elements.

In chapter 2, the setup of this accurate model of a monostatic SFCW GPR in presence of buried targets has been presented. The antenna modeling follows a mixed characterization-aperture equivalent currents approach: indeed it is described by its current distribution and by operational parameters that describe the complex radiation processes occurring in the presence of the soil and target. These parameters can be estimated by a simple calibration procedure, obviating the difficulty of setting up a precise numerical model of the antenna. The model, derived for arbitrary antenna equivalent current distributions, has been applied using dipole and cosinusoidal distributions. It yielded very good

quantitative similarities between estimated and simulated target signatures, especially for the cosinusoidal distribution, thereby validating the complete radar equation and its associated methodology for signature estimation, as well as the numerical algorithms used in the computations. The results also showed that accounting for the antenna-soil and to a lesser extent antenna-target multiple reflections in the process of target signature estimation slightly enhances the quality of the signature estimation with respect to a classical background subtraction. Finally, the decoupling of the antenna and target modeling allows for a great modularity in the use of the complete model, as the soil and target radar responses R_S and R_T can be computed independently and combined in (2.57) with the operational parameters H_i, H_t and H_f resulting from the characterization of a given radar system for having its complete simulated Γ.

The equations of the GPR model have been written for targets buried in arbitrary media, but the GPR model has been used in numerical computations involving flat multilayered media only. In principle, the GPR model and the numerical algorithms developed in this work allow for the computations of GPR responses of targets buried under rough soil interfaces. However, as said in section 1.5, the main reason for using a flat soil was the necessity of having experiments both *complex* and *controllable*, *i.e.* as free as possible of statistical variables. If in future works the soil roughness is introduced in the numerical computations and in the experiments, one should ensure that the statistical properties of the soil surface geometry are the same in the model and in the experiments.

The GPR model has been experimentally validated for antenna heights above the soil ranging from 40 cm down to 20 cm, and for a frequency band of 0.8–3 GHz. The lowest height to which the model is still correct for a given frequency has not been investigated, and the model remains to be validated—or modified—for antenna heights above the soil of a few centimeters.

In chapter 3, we have derived in section 3.2 the Huygens surface equivalence principle for a homogeneous medium in a manner slightly different than the development presented by Peterson *et al.* [51, chapter 1], in order to derive the principle for sources contained within the region for which the equivalence is built. In section 3.2.2 we extended the principle to multilayered media thanks to the source-field relationships written with help of the appropriate DGFs [27]. This equivalence principle has allowed us to write mixed-potential integral representations for the original electric and magnetic fields within a given volume as a sum of fields resulting from source-fields integrals of bounding surface

equivalent currents convoluted with the volume Green's functions, combined with the fields produced by the original sources if any. Applying the boundary conditions to the integral representations of these fields has naturally provided the surface electric and magnetic mixed-potential integral equations, namely the EMPIE and MMPIE, which in section 3.6 have further been combined under the form of a CFIE and PMCHWT formulation in order to obtain a resonance-free problem and the same number of unknowns and equations. The step-by-step approach followed has evolved from simple PEC scatterers embedded within multilayered media up to arbitrary combinations of dielectric and PEC bodies.

At section 3.7 we have introduced the MoM, which allows for solving the surface integral equations by discretizing the surface equivalent currents (which are the unknown quantities searched for) and testing the resulting discretized equations, thereby providing a linear system that has to be solved in order to retrieve the unknown coefficients of the discretized currents. First, the MoM expressions for the EMPIEs pertaining to an inhomogeneous dielectric body have been derived and written in a matrix system, conveniently subdivided into matrix blocks whose lines and columns are related to testing and source surfaces respectively. Explicit expressions of the terms appearing in these blocks are given at appendix B. Duality is then used to obtain the MoM matrix formulation for the corresponding MMPIEs; the MoM EMPIEs and MMPIEs matrix blocks are then combined following simple rules to form the MoM matrices for the CFIE and PMCHWT formulations. Although peculiar to the inhomogeneous dielectric body of section 3.4.1, the MoM matrix systems of section 3.7 are however easily generalizable to more complete geometries. Yet this is an unnecessary task, as the resulting submatrices assembling and combinations can be performed by a computer fed by the rules derived from the simpler inhomogeneous dielectric body case.

The MoM computer routines are indeed based on the simple rules of section 3.7 for constituting the MoM matrix systems from the matrix blocks, and on a programs library that computes efficiently the matrix blocks. The user must only draw the geometry at hand and mesh the surfaces, give values to the EM properties of the medium surrounding and filling the inhomogeneities, and define the source strength, distribution, position and orientation. These computer routines have been extensively tested and found to yield accurate solution for geometries involving several volumes (layered sphere), possibly with sharp edges and corners (cube). Although very general, these computer

routines still suffer some limitations that should be addressed in future work:

- the code does not handle bodies penetrating one or more interfaces of the multilayered medium;
- the code does not handle intersections between dielectric and/or metallic surfaces;
- the computational complexity and memory footprint of the code is $\mathcal{O}(N^2)$ if an iterative method is used for solving the linear system, where N is the number of basis functions, which can rapidly render resolution of problems involving electrically large objects slow or intractable.

Chapter 4 was oriented towards practical uses and limitations of the GPR model. We have shown in two laboratory experiments—a soil with varying moisture content containing a Russian PMN mine and a B-scan of a buried metal cylinder—that the subtraction of the antenna and soil contributions to the total radar signal significantly enhances the visual discrimination of the target. Moreover, the ability to retrieve the target signature opens the door to further signal processing treatment that could allow target identification.

However, errors on the estimation of the antenna operational parameters or of the soil radar response lead to errors on the estimated target response, as stated by the GPR determinate relative error equation. In that equation, the relative error on R_T is expressed as a weighted sum of the relative errors on the elements appearing in the GPR equation, namely, Γ, H_i, H_t, H_f and R_S, with all weights inversely proportional to $|R_T|$. The errors on the operational parameters find their source in changes in the radar setup between characterization and actual measurement, as well as in the assumed radar response of the target used in the characterization process. Apart from characterization errors, the error on the soil response can be due to the differences in the soil EM properties from point to point, or to the soil roughness, which induces random spatial variations in the soil response. This latter aspect was however not studied in this work, as one can choose a frequency band such that the soil roughness is without effect in that band.

With help of the monostatic GPR equation, we also have given special attention to the soil clutter, which arises when its response is not properly subtracted from the total radar signal, is the main source of target undetectability. We have explained how the target signature could be masked by the soil clutter in an A-scan, and how a B-scan can render the target space-time discernible, as long as the antenna is not too directive and the soil is not too lossy.

Finally, in these extraction error and soil clutter studies, we have seen that the magnitude of the target response, taken relatively to that of the soil response, is an important factor in the quality assessment of the detection and signature extraction. It is therefore of significant interest to study the variations of these magnitudes with regards to the parameters that are susceptible to modify them through a parametric study of these responses. As it would have been expensive and time consuming to perform such a parametric study experimentally, because of the high degree of control needed in order to isolate the influence of each parameter and reduce the measurement errors, we have used our numerical algorithms for this purpose. This parametric study, although particular to a given target and antenna currents, and contained within frequency and soil permittivity ranges, has provided both expected and surprising results, of which the most important are the facts that the multiple reflections between the target and the soil interface play a negligible role in the target signature and can therefore be neglected, and that the shape and inner structure of the target has an important impact on its signature above a given frequency.

Although performed for a simple target, this parametric study could be performed for more complicated objects presenting a better approximation of a real landmine internals. However, the goal of this work was to present the parametric study itself. The qualitative conclusions of the parametric study can probably be extrapolated to more complicated targets, since the study is mainly focused on the consequences of the soil EM parameters variations or on the target relative position with respect to the radar system. Nevertheless, one could use much more complicated targets in the parametric study, *e.g.* real mine structures, as it does not make any difference to the numerical code.

5.2 Perspectives

Future works on the GPR model should include its extension to bistatic or multistatic systems. The extension to more general antenna currents and incident fields, and the corresponding generalization of the characterization procedure, is also foreseen, this for taking into account multiple reflections in case of scattering by targets located away the main beam axis, as well as for allowing the use of the radar model for antennas located very close to the soil surface. In order to simplify the characterization we consider the possibility to partly compute $\underline{\underline{H}}_f$ by numerical modeling of the antenna.

Since the GPR model also yields a means for obtaining the target radar response, this latter should be studied (experimentally or numerically) for examining the possibilities of target identification. Moreover, research should seek a minimal set of parameters for characterizing the target signature. Finally, the practical usefulness of the GPR model should be further examined through experiments involving a commercial GPR, with the aim of predicting as precisely as possible the expected performances of the detector given the soil type, moisture level, type of targets and signal processing algorithms used.

On the point of view of the numerical algorithms, their capabilities could be greatly extended with additions such as the possibility of computing the scattering by targets penetrating interfaces, as well as the handling of volumes intersections. These additions demand a few men-weeks or men-months work. On another hand, the numerical efficiency of the code could be vastly improved by the use of numerical methods such as the multilevel fast multipole algorithm (MLFMA) or the adaptive integral method (AIM), however these extensions would require a significant amount of work, especially for targets embedded in multilayered media.

A last word concerns the possibility of using the methods developed in this work for modeling other microwave detectors, such as an active or passive radiometer. Indeed, the possibility of using a radiometer for detecting landmines is currently under investigation by the *Deutschen Zentrum für Luft- und Raumfahrt* (DLR) [67]. We have seen that accurate modeling can provide a number of benefits to the designer of a detection system, and while such models exist for passive and active radiometry for stratified media [11], such a work is still lacking for buried targets. First approximation models have been proposed in the past [67, 68], but they suffer severe limitations in their possibilities of application, precisely due to their lack of precision. Our personal opinion is that a numerical model, such as the one developed here, should be adapted to meet the modeling characteristics pertaining to the radiation properties of a buried inhomogeneity, namely, the incoherency of the surface equivalent currents that could represent the incoherent emission processes that arise in phenomena of natural radiation.

Appendixes

Appendix A

GPR modeling demonstrations

A.1 Integral on S_V

The integral on S_V, resulting from the reciprocity applied between fields from a state T and R, is written:

$$\int_{S_V} (\mathbf{E}_T \times \mathbf{H}_R - \mathbf{E}_R \times \mathbf{H}_T) \cdot \hat{\mathbf{n}} \, \mathrm{d}S. \tag{A.1}$$

As the measurement system and waveguide is coated by a perfect electric conductor (PEC) (h2), and since the tangential electric field over a PEC must be zero, the integration over S_V vanishes, excepted in the waveguide. Note that a surface impedance boundary condition would yield the same result. Within the waveguide, fields propagate following the fundamental mode (h3). The total fields in a single mode is a linear combination of the forward and backward mode fields [41, p. 538]. Using (12), (13), (45) and (46) of [41], we can write that

$$\begin{aligned}(\mathbf{E}_X, \mathbf{H}_X) &= (\mathbf{E}_{a_X} + \mathbf{E}_{b_X}, \mathbf{H}_{a_X} + \mathbf{H}_{b_X}) \\ &= \left(\frac{a_X + b_X}{\sqrt{\Re\{p_0\}}} \mathbf{e}_t, \frac{a_X - b_X}{\sqrt{\Re\{p_0\}}} \mathbf{h}_t \right)\end{aligned} \tag{A.2}$$

where X refers to state T or R, $\mathbf{e}_t$ and $\mathbf{h}_t$ are the transverse fields of the forward-propagating (towards antenna) mode, and a_X and b_X are the amplitudes of the

forward and backward traveling waves respectively. p_0 is defined as:

$$p_0 \triangleq \int_S \mathbf{e}_t \times \mathbf{h}_t^* \cdot \hat{\mathbf{n}} \, \mathrm{d}S \tag{A.3}$$

where $\hat{\mathbf{n}}$ is the normal to the waveguide section and points towards direction of propagation of traveling wave a, and S is the section of the waveguide.

We can now rewrite (A.1):

$$\begin{aligned} \int_{S_V} (\mathbf{E}_T \times \mathbf{H}_R - \mathbf{E}_R \times \mathbf{H}_T) \cdot \hat{\mathbf{n}} \, \mathrm{d}S = [(a_T + b_T)(a_R - b_R) \\ - (a_R + b_R)(a_T - b_T)] \frac{\int_S \mathbf{e}_t \times \mathbf{h}_t \cdot \hat{\mathbf{n}} \, \mathrm{d}S}{p_0} \\ = -2K(a_R b_T - a_T b_R) \end{aligned} \tag{A.4}$$

where the reciprocity factor

$$K \triangleq \frac{\int_S \mathbf{e}_t \times \mathbf{h}_t \cdot \hat{\mathbf{n}} \, \mathrm{d}S}{p_0}. \tag{A.5}$$

As said in [41, p. 547], $K = 1$ for most waveguides. For other waveguides, K can easily be computed.

A.2 Matrix inversion lemma and useful formulas

The matrix inversion lemma states that:

$$\left(\underline{\underline{A}} - \underline{\underline{BDC}}\right)^{-1} = \underline{\underline{A}}^{-1} + \underline{\underline{A}}^{-1}\underline{\underline{B}}\left(\underline{\underline{D}}^{-1} - \underline{\underline{CA}}^{-1}\underline{\underline{B}}\right)^{-1}\underline{\underline{CA}}^{-1}. \tag{A.6}$$

Particularizing this to $\underline{\underline{A}} = \underline{\underline{I}}$ and $\underline{\underline{D}} = \underline{\underline{I}}$ yields:

$$\left(\underline{\underline{I}} - \underline{\underline{BC}}\right)^{-1} = \underline{\underline{I}} + \underline{\underline{B}}\left(\underline{\underline{I}} - \underline{\underline{CB}}\right)^{-1}\underline{\underline{C}}. \tag{A.7}$$

Another useful relation is given by multiplying both sides of (A.7) by $\underline{\underline{C}}$:

$$\begin{aligned} \underline{\underline{C}}\left(\underline{\underline{I}} - \underline{\underline{BC}}\right)^{-1} &= \underline{\underline{C}} + \underline{\underline{CB}}\left(\underline{\underline{I}} - \underline{\underline{CB}}\right)^{-1}\underline{\underline{C}} \\ &= \left(\underline{\underline{I}} - \underline{\underline{CB}} + \underline{\underline{CB}}\right)\left(\underline{\underline{I}} - \underline{\underline{CB}}\right)^{-1}\underline{\underline{C}} \\ &= \left(\underline{\underline{I}} - \underline{\underline{CB}}\right)^{-1}\underline{\underline{C}} \end{aligned} \tag{A.8}$$

A.3 Computation of antenna feedback matrix in presence of multilayered medium

Consider sources $(\mathbf{J}_{\mathrm{exc}}, \mathbf{M}_{\mathrm{exc}})$ that produce fields $(\mathbf{E}_{\mathrm{exc}}^{(\mathrm{ml})}, \mathbf{H}_{\mathrm{exc}}^{(\mathrm{ml})})$ in presence of a multilayered medium. The coefficients of these fields in the field basis are

$\underline{F}^{(\mathrm{ml})}_{\mathrm{exc}}$. The soil may be replaced by equivalent currents $(\mathbf{J}_{\mathrm{soil,\ exc}}, \mathbf{M}_{\mathrm{soil,\ exc}})$. Hence, $\underline{F}^{(\mathrm{ml})}_{\mathrm{exc}} = \underline{F}^{(\mathrm{fs})}_{\mathrm{exc}} + \underline{F}^{(\mathrm{fs})}_{\mathrm{soil,\ exc}}$. If an antenna is introduced above the soil, additional equivalent currents $(\mathbf{J}_{AS}, \mathbf{M}_{AS})$ and $(\mathbf{J}_{\mathrm{soil,\ ant}}, \mathbf{M}_{\mathrm{soil,\ ant}})$ must be added respectively on the antenna and in the soil. The coefficients of $(\mathbf{J}_{AS}, \mathbf{M}_{AS})$ in the current basis are $\underline{I}^{(\mathrm{ml})}_{AS}$. By definition of $\underline{\underline{H}}^{(\mathrm{ml})}_{f}$, we have

$$\underline{I}^{(\mathrm{ml})}_{AS} = \underline{\underline{H}}^{(\mathrm{ml})}_{f}\, \underline{F}^{(\mathrm{ml})}_{\mathrm{exc}}. \tag{A.9}$$

Using the soil equivalent currents, we may equivalently consider that the antenna is in free space and is excited by $(\mathbf{J}_{\mathrm{exc}}, \mathbf{M}_{\mathrm{exc}}) + (\mathbf{J}_{\mathrm{soil,\ exc}}, \mathbf{M}_{\mathrm{soil,\ exc}}) + (\mathbf{J}_{\mathrm{soil,\ ant}}, \mathbf{M}_{\mathrm{soil,\ ant}})$, which produce the fields

$$\begin{aligned} \underline{F}^{(\mathrm{fs})}_{\mathrm{exc,\ fs}} &= \underline{F}^{(\mathrm{fs})}_{\mathrm{exc}} + \underline{F}^{(\mathrm{fs})}_{\mathrm{soil,\ exc}} + \underline{F}^{(\mathrm{fs})}_{\mathrm{soil,\ ant}} \\ &= \underline{F}^{(\mathrm{ml})}_{\mathrm{exc}} + \underline{F}^{(\mathrm{fs})}_{\mathrm{soil,\ ant}}. \end{aligned} \tag{A.10}$$

We may then write that

$$\underline{I}^{(\mathrm{ml})}_{AS} = \underline{\underline{H}}^{(\mathrm{fs})}_{f}\, \underline{F}^{(\mathrm{fs})}_{\mathrm{exc,\ fs}}. \tag{A.11}$$

Equating (A.9) and (A.11), we get:

$$\underline{\underline{H}}^{(\mathrm{fs})}_{f} \left(\underline{F}^{(\mathrm{ml})}_{\mathrm{exc}} + \underline{F}^{(\mathrm{fs})}_{\mathrm{soil,\ ant}} \right) = \underline{\underline{H}}^{(\mathrm{ml})}_{f}\, \underline{F}^{(\mathrm{ml})}_{\mathrm{exc}}. \tag{A.12}$$

Using $\underline{F}^{(\mathrm{fs})}_{\mathrm{soil,\ ant}} = \underline{\underline{G}}^{(\mathrm{soil})}\, \underline{I}^{(\mathrm{ml})}_{AS} = \underline{\underline{G}}^{(\mathrm{soil})}\, \underline{\underline{H}}^{(\mathrm{ml})}_{f}\, \underline{F}^{(\mathrm{ml})}_{\mathrm{exc}}$, we get

$$\underline{\underline{H}}^{(\mathrm{fs})}_{f} + \underline{\underline{H}}^{(\mathrm{fs})}_{f}\, \underline{\underline{G}}^{(\mathrm{soil})}\, \underline{\underline{H}}^{(\mathrm{ml})}_{f} = \underline{\underline{H}}^{(\mathrm{ml})}_{f} \tag{A.13}$$

where we have dropped the factor $\underline{F}^{(\mathrm{ml})}_{\mathrm{exc}}$, because (A.13) must be valid for any $\underline{F}^{(\mathrm{ml})}_{\mathrm{exc}}$. We then get $(\underline{\underline{I}} - \underline{\underline{H}}^{(\mathrm{fs})}_{f}\, \underline{\underline{G}}^{(\mathrm{soil})})\, \underline{\underline{H}}^{(\mathrm{ml})}_{f} = \underline{\underline{H}}^{(\mathrm{ml})}_{f}$ from which (2.53) follows.

A.4 Equality of total and recursive approach

First we demonstrate that expressions (2.49) and (2.52) for the antenna currents in presence of soil and target obtained by the total and recursive approaches are equivalent. By using (2.53) in (2.52) and the same current and field basis, one gets:

$$\begin{aligned} \underline{I}^{(\mathrm{ml,\ t})}_{AT} &= \left(\left(\underline{\underline{I}} - \underline{\underline{H}}_{f}\, \underline{\underline{G}}^{(\mathrm{soil})} \right)^{-1} \underline{\underline{H}}_{f}\, \underline{\underline{G}}^{(\mathrm{t})} \right)^{-1} \underline{I}^{(\mathrm{ml})}_{AT} \\ &= \left(\left(\underline{\underline{I}} - \underline{\underline{H}}_{f}\, \underline{\underline{G}}^{(\mathrm{soil})} \right)^{-1} \left(\underline{\underline{I}} - \underline{\underline{H}}_{f}\, \underline{\underline{G}}^{(\mathrm{soil,\ t})} \right) \right)^{-1} \underline{I}^{(\mathrm{ml})}_{AT} \\ &= \left(\underline{\underline{I}} - \underline{\underline{H}}_{f}\, \underline{\underline{G}}^{(\mathrm{soil,\ t})} \right)^{-1} \underline{I}_{AT} \end{aligned} \tag{A.14}$$

where the last line is due to (2.51). The demonstration is ended by noting that in (2.49), $\underline{I}_{AT}^{(\mathrm{fs},\ (\mathrm{soil},\ \mathrm{t}))} = \underline{I}_{AT}^{(\mathrm{ml},\ \mathrm{t})}$.

Using (2.40) in (2.50) and the same current and field basis for $\Gamma^{(\mathrm{soil})}$ and $\Gamma^{(\mathrm{t})}$, we can write that

$$\begin{aligned}\Gamma^{(\mathrm{soil})} + \Gamma^{(\mathrm{t})} &= \underline{I}_{AT}^{T}\underline{\underline{R}}_F\underline{\underline{G}}^{(\mathrm{soil})}\underline{I}_{AT}^{(\mathrm{ml})} + \left(\underline{I}_{AT}^{(\mathrm{ml})}\right)^T\underline{\underline{R}}_F\underline{\underline{G}}^{(\mathrm{t})}\underline{I}_{AT}^{(\mathrm{ml},\ \mathrm{t})} \\ &= \left(\underline{I}_{AT}^{(\mathrm{ml})}\right)^T\left[\underline{\underline{R}}_F\underline{\underline{G}}^{(\mathrm{soil})}\underline{I}_{AT} + \underline{\underline{R}}_F\underline{\underline{G}}^{(\mathrm{t})}\underline{I}_{AT}^{(\mathrm{ml},\ \mathrm{t})}\right]\end{aligned} \tag{A.15}$$

where the second line is obtained by transposing the first term (each term of the sum is a scalar), together with the fact that $\left(\underline{\underline{R}}_F\underline{\underline{G}}^{(\mathrm{soil})}\right)^T = \underline{\underline{R}}_F\underline{\underline{G}}^{(\mathrm{soil})}$. Using the last line of (A.14) for rewriting $\underline{I}_{AT}$ as function of $\underline{I}_{AT}^{(\mathrm{ml},\ \mathrm{t})}$, and factoring to the right this latter yields:

$$\begin{aligned}&\Gamma^{(\mathrm{soil})} + \Gamma^{(\mathrm{t})} = \\ &\left(\underline{I}_{AT}^{(\mathrm{ml})}\right)^T\left[\underline{\underline{R}}_F\underline{\underline{G}}^{(\mathrm{soil})}\left(\underline{\underline{I}} - \underline{\underline{H}}_f\underline{\underline{G}}^{(\mathrm{soil},\ \mathrm{t})}\right) + \underline{\underline{R}}_F\underline{\underline{G}}^{(\mathrm{t})}\right]\underline{I}_{AT}^{(\mathrm{ml},\ \mathrm{t})}\end{aligned} \tag{A.16}$$

which can be further developed by distributing $\left(\underline{\underline{I}} - \underline{\underline{H}}_f\underline{\underline{G}}^{(\mathrm{soil},\ \mathrm{t})}\right)$, factoring $\underline{\underline{G}}^{(\mathrm{soil},\ \mathrm{t})}$ to the right of the bracket, and rewriting $\left(\underline{I}_{AT}^{(\mathrm{ml})}\right)^T$ with help of (2.51):

$$\begin{aligned}\Gamma^{(\mathrm{soil})} + \Gamma^{(\mathrm{t})} = \underline{I}_{AT}^{T}&\left(\left(\underline{\underline{I}} - \underline{\underline{H}}_f\underline{\underline{G}}^{(\mathrm{soil})}\right)^{-1}\right)^T \\ &\left[\underline{\underline{R}}_F - \underline{\underline{R}}_F\underline{\underline{G}}^{(\mathrm{soil})}\underline{\underline{H}}_f\right]\underline{\underline{G}}^{(\mathrm{soil},\ \mathrm{t})}\underline{I}_{AT}^{(\mathrm{ml},\ \mathrm{t})}.\end{aligned} \tag{A.17}$$

Finally, noting that

$$\begin{aligned}\left[\underline{\underline{R}}_F - \underline{\underline{R}}_F\underline{\underline{G}}^{(\mathrm{soil})}\underline{\underline{H}}_f\right] &= \left[\underline{\underline{R}}_F - \left(\underline{\underline{G}}^{(\mathrm{soil})}\right)^T\underline{\underline{R}}_F^T\underline{\underline{H}}_f\right] \\ &= \left[\underline{\underline{R}}_F - \left(\underline{\underline{G}}^{(\mathrm{soil})}\right)^T\underline{\underline{H}}_f^T\underline{\underline{R}}_F\right]\end{aligned} \tag{A.18}$$

where the second line is due to the fact that $\underline{\underline{R}}_F^T\underline{\underline{H}}_f = \underline{\underline{H}}_f^T\underline{\underline{R}}_F$, and since $\left(\underline{\underline{A}}^{-1}\right)^T = \left(\underline{\underline{A}}^T\right)^{-1}$, we can rewrite (A.17) as:

$$\Gamma^{(\mathrm{soil})} + \Gamma^{(\mathrm{t})} = \underline{I}_{AT}^{T}\underline{\underline{R}}_F\underline{\underline{G}}^{(\mathrm{soil},\ \mathrm{t})}\underline{I}_{AT}^{(\mathrm{ml},\ \mathrm{t})} \tag{A.19}$$

which is exactly the same as (2.47) (without free space term).

A.5 Independence of $\Gamma^{(\mathrm{c})}$ from γ

Developing the contrast response (2.17) into the field and current basis, with the integral expression given by (2.44) where $\underline{\underline{H}}_f^{(\mathrm{bg})} = \underline{\underline{H}}_{f,\gamma}^{(\mathrm{bg})}$, and using (2.39),

we obtain the general expression:

$$\begin{aligned}\Gamma^{(c)} &= \frac{a^{(bg)}}{a^{(bg,\,c)}}\left(\underline{I}_{AT}^{(bg)}\right)^T \underline{\underline{R}}^{(c)}\left(\underline{I}-\underline{\underline{H}}_{f,\gamma}^{(bg)}\underline{\underline{G}}^{(c)}\right)^{-1}\underline{I}_{AT}^{(bg,\,c)} \\ &= \frac{1-\gamma\Gamma^{(bg,\,c)}}{1-\gamma\Gamma^{(bg)}}X_\gamma\end{aligned} \tag{A.20}$$

where the second equality has been obtained by using (A.35) and by defining:

$$X_\gamma \triangleq \left(\underline{I}_{AT}^{(bg)}\right)^T \underline{\underline{R}}^{(c)}\left(\underline{I}-\underline{\underline{H}}_{f,\gamma}^{(bg)}\underline{\underline{G}}^{(c)}\right)^{-1}\underline{I}_{AT}^{(bg,\,c)}. \tag{A.21}$$

Let us develop X_γ as function of $\Gamma^{(c)}$. For a reflection coefficient γ at the entrance of the VNA, the original traveling wave a will be augmented by a fraction of $b = b_{\text{exc}}\tau$ arriving at this entrance, that is, γb (see appendix A.6). Developing (2.34) and accounting for this effect allows us to find the expression of $\underline{\underline{H}}_{f,\gamma}^{(bg)}$:

$$\begin{aligned}\underline{I}_{AS}^{(c)} &= \underline{\underline{H}}_f^{(bg)}\underline{F}^{inc} + \underline{I}_{AT}\alpha\underbrace{\underline{I}_{AT}^T\underline{\underline{R}}_F\underline{F}^{inc}}_{b=b_{\text{exc}}\tau} \\ &= \underbrace{\left(\underline{\underline{H}}_f^{(bg)} + \alpha\underline{I}_{AT}\underline{I}_{AT}^T\underline{\underline{R}}_F\right)}_{\underline{\underline{H}}_{f,\gamma}^{(bg)}}\underline{F}^{inc}\end{aligned} \tag{A.22}$$

where $\underline{\underline{H}}_f^{(bg)} = \underline{\underline{H}}_{f,\gamma=0}^{(bg)}$. We rewrite $\left(\underline{I}-\underline{\underline{H}}_{f,\gamma}^{(bg)}\underline{\underline{G}}^{(c)}\right)^{-1}$ of (A.21) as:

$$\begin{aligned}\left(\underline{I}-\underline{\underline{H}}_{f,\gamma}^{(bg)}\underline{\underline{G}}^{(c)}\right)^{-1} &= \left(\underline{I}-\left(\underline{\underline{H}}_f^{(bg)}+\alpha\underline{I}_{AT}\underline{I}_{AT}^T\underline{\underline{R}}_F\right)\underline{\underline{G}}^{(c)}\right)^{-1} \\ &= (\underbrace{\underline{I}-\underline{\underline{H}}_f^{(bg)}\underline{\underline{G}}^{(c)}}_{\underline{\underline{A}}} - \underbrace{\alpha\underline{I}_{AT}\underline{I}_{AT}^T\underline{\underline{R}}_F\underline{\underline{G}}^{(c)}}_{\underline{\underline{B}}})^{-1}\end{aligned} \tag{A.23}$$

where the first equality is due to (A.22). Using the matrix inversion lemma with $\underline{\underline{C}}$ and $\underline{\underline{D}}$ equals to $\underline{\underline{I}}$, (A.23) becomes:

$$\begin{aligned}\left(\underline{I}-\underline{\underline{H}}_{f,\gamma}^{(bg)}\underline{\underline{G}}^{(c)}\right)^{-1} &= \left(\underline{I}-\underline{\underline{H}}_f^{(bg)}\underline{\underline{G}}^{(c)}\right)^{-1} + \\ &\left(\underline{I}-\underline{\underline{H}}_f^{(bg)}\underline{\underline{G}}^{(c)}\right)^{-1}\alpha\underline{I}_{AT}\underline{I}_{AT}^T\underline{\underline{R}}_F\underline{\underline{G}}^{(c)} \\ &\left(\underline{I}-\underbrace{\left(\underline{I}-\underline{\underline{H}}_f^{(bg)}\underline{\underline{G}}^{(c)}\right)^{-1}}_{X^{-1}}\underbrace{\alpha\underline{I}_{AT}\underline{I}_{AT}^T\underline{\underline{R}}_F\underline{\underline{G}}^{(c)}}_{Y}\right)^{-1} \\ &\left(\underline{I}-\underline{\underline{H}}_f^{(bg)}\underline{\underline{G}}^{(c)}\right)^{-1}.\end{aligned} \tag{A.24}$$

But, since

$$\begin{aligned}\left(\underline{\underline{I}} - \underline{\underline{X}}^{-1}\underline{\underline{Y}}\right)^{-1} &= \left(\underline{\underline{X}}^{-1}\left(\underline{\underline{X}} - \underline{\underline{Y}}\right)\right)^{-1} \\ &= \left(\underline{\underline{X}} - \underline{\underline{Y}}\right)^{-1}\underline{\underline{X}}\end{aligned} \tag{A.25}$$

we can write for (A.24)

$$\begin{aligned}\left(\underline{\underline{I}} - \underline{\underline{H}}_{f,\gamma}^{(\mathrm{bg})}\underline{\underline{G}}^{(\mathrm{c})}\right)^{-1} &= \left(\underline{\underline{I}} - \underline{\underline{H}}_{f}^{(\mathrm{bg})}\underline{\underline{G}}^{(\mathrm{c})}\right)^{-1} \\ &+ \left(\underline{\underline{I}} - \underline{\underline{H}}_{f}^{(\mathrm{bg})}\underline{\underline{G}}^{(\mathrm{c})}\right)^{-1}\alpha\underline{I}_{AT}\underline{I}_{AT}^{T}\underline{\underline{R}}_{F}\underline{\underline{G}}^{(\mathrm{c})} \\ &\left(\underline{\underline{I}} - \underline{\underline{H}}_{f,\gamma}^{(\mathrm{bg})}\underline{\underline{G}}^{(\mathrm{c})} - \alpha\underline{I}_{AT}\underline{I}_{AT}^{T}\underline{\underline{R}}_{F}\underline{\underline{G}}^{(\mathrm{c})}\right)^{-1}.\end{aligned} \tag{A.26}$$

Rewriting (A.21) with help of (A.26) and (A.22), one gets:

$$\begin{aligned}X_\gamma = \underline{I}_{AT}^{T}\underline{\underline{R}}^{(\mathrm{c})}&\left(\underline{\underline{I}} - \underline{\underline{H}}_{f}^{(\mathrm{bg})}\underline{\underline{G}}^{(\mathrm{c})}\right)^{-1}\underline{I}_{AT} \\ &+ \alpha\underline{I}_{AT}^{T}\underline{\underline{R}}^{(\mathrm{c})}\left(\underline{\underline{I}} - \underline{\underline{H}}_{f}^{(\mathrm{bg})}\underline{\underline{G}}^{(\mathrm{c})}\right)^{-1}\underline{I}_{AT} \\ &\underline{I}_{AT}^{T}\underline{\underline{R}}_{F}\underline{\underline{G}}^{(\mathrm{c})}\left(\underline{\underline{I}} - \underline{\underline{H}}_{f,\gamma}^{(\mathrm{bg})}\underline{\underline{G}}^{(\mathrm{c})}\right)^{-1}\underline{I}_{AT}.\end{aligned} \tag{A.27}$$

Finally, by using (A.20) and (A.21) in (A.27), we have that

$$X_\gamma = X_0 + \alpha X_0 X_\gamma \tag{A.28}$$

(with $X_0 = X_{\gamma=0}$), from which we finally get

$$X_\gamma = \frac{X_0}{1 - \alpha X_0}. \tag{A.29}$$

Since from appendix A.6 we have that

$$\alpha = \frac{\gamma}{1 - \gamma\Gamma^{(\mathrm{bg})}} \tag{A.30}$$

we can rewrite (A.29) as:

$$X_\gamma = X_0\frac{1 - \gamma\Gamma^{(\mathrm{bg})}}{1 - \gamma\Gamma^{(\mathrm{bg,\ c})}}. \tag{A.31}$$

Finally, plugging this result back into (A.20) gives the final result:

$$\begin{aligned}\Gamma^{(\mathrm{c})} &= X_0 \\ &= \left(\underline{I}_{AT}^{(\mathrm{bg})}\right)^{T}\underline{\underline{R}}^{(\mathrm{c})}\left(\underline{\underline{I}} - \underline{\underline{H}}_{f,\gamma=0}^{(\mathrm{bg})}\underline{\underline{G}}^{(\mathrm{c})}\right)^{-1}\underline{I}_{AT}^{(\mathrm{bg,\ c})}.\end{aligned} \tag{A.32}$$

This demonstrates that $\Gamma^{(\mathrm{c})}$ is independant of γ and therefore depends only upon the antenna characteristics, the background and the contrast.

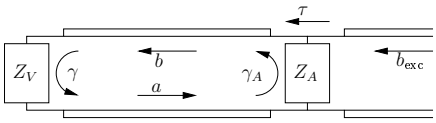

Figure A.1:

A.6 Computation of α

We can first write that $\frac{a}{b} = \gamma$, as seen at Fig. A.1. Since $b = b_{\text{exc}}\tau + a\gamma_A$, we have that $\frac{b - b_{\text{exc}}\tau}{a} = \gamma_A$, which we can further write as $\frac{1}{\gamma} - \frac{b_{\text{exc}}\tau}{a} = \gamma_A$. Since $\gamma_A = \Gamma^{(\text{bg})}$, we have that $\frac{b_{\text{exc}}\tau}{a} = \frac{1}{\gamma} - \Gamma^{(\text{bg})} = \frac{1 - \gamma\Gamma^{(\text{bg})}}{\gamma} = \frac{1}{\alpha}$.

A.7 Computation of $a^{(\text{bg})}/a^{(\text{bg, c})}$

Since

$$a^{(\text{bg, c})} = a_V + \gamma b^{(\text{bg, c})} \tag{A.33}$$

$$a^{(\text{bg})} = a_V + \gamma b^{(\text{bg})} \tag{A.34}$$

we have that

$$\begin{aligned} \frac{a^{(\text{bg})}}{a^{(\text{bg, c})}} &= \frac{a^{(\text{bg})}}{a_V}\frac{a_V}{a^{(\text{bg, c})}} \\ &= \frac{1 - \gamma\Gamma^{(\text{bg, c})}}{1 - \gamma\Gamma^{(\text{bg})}}. \end{aligned} \tag{A.35}$$

Appendix B

Method of moments solution terms

B.1 Computation of the homogeneous medium MoM matrix terms

In this section we are going to detail how to compute the terms of the MoM matrices that appear in (3.78) and (3.82) for inhomogeneities embedded in homogeneous media, namely

$$I_1^E = \left\{ \left\langle \mathbf{g}_m; \frac{\nabla\nabla\cdot + k^2}{j\omega\varepsilon_0\varepsilon_r} \langle G, \mathbf{f}_n \rangle_{D_n} \right\rangle_{D_m} \right\}_{S^\pm} \tag{B.1}$$

$$I_2 = \left\{ \langle \mathbf{g}_m; \nabla \times \langle G, \mathbf{f}_n \rangle_{D_n} \rangle_{D_m} \right\}_{S^\pm} \tag{B.2}$$

$$I_3 = \left\{ \langle \mathbf{g}_m; \hat{\mathbf{n}} \times \mathbf{f}_n \rangle_{D_m} \right\}_{S^\pm} \tag{B.3}$$

where $\{X\}_{S^\pm}$ means that we effectuate the testing on $D_m^\pm$, that is, for D_m being at an infinitesimal distance from the surface S along its normal $\hat{\mathbf{n}}$ on its positive or negative side. The positive side is the one into which $\hat{\mathbf{n}}$ points. The homogeneous space Green's function G is given by:

$$G = \frac{e^{-jk|\mathbf{r}-\mathbf{r}'|}}{4\pi\,|\mathbf{r}-\mathbf{r}'|}$$

where $k = \omega\sqrt{\varepsilon\mu} = \omega\sqrt{\varepsilon_0\varepsilon_r\mu_0\mu_r}$ (as usual, ε_r and μ_r are respectively the relative dielectric permittivity and magnetic permeability of the medium). Su-

perscript E of I_1 indicates that it is related to $\underline{\underline{Z}}^E$. I_1^H is obtained from I_1^E by the following relation: $I_1^H = \frac{\varepsilon_0\varepsilon_r}{\mu_0\mu_r} I_1^E$.

I_1^E is defined even when the triangles of D_m and the triangles of D_n overlap, *i.e.* $I_1^E\big|_{S^+} = I_1^E\big|_{S^-} = I_1^E\big|_S$ [45, 57]. I_2 is a discontinuous function around $S^\pm$ if the triangles of D_m and the triangles of D_n overlap. In that case, the value of I_2 on the surface S is undefined, and we need to compute its Cauchy principal value. It has been calculated in [52, p. 139] and is given by:

$$\lim_{\mathbf{r}\to S^\pm} \left\langle \mathbf{g}_m; \nabla \times \langle G, \mathbf{f}_n \rangle_{D_n} \right\rangle_{D_m} = \mp\frac{1}{2} \langle \mathbf{g}_m; \hat{\mathbf{n}} \times \mathbf{f}_n \rangle_{D_m} + \left\langle \mathbf{g}_m; \nabla \times \langle G, \mathbf{f}_n \rangle_{D_n} \right\rangle_{D_m}. \tag{B.4}$$

Reporting the above discontinuity on I_3 through (3.78b) or (3.82b) we can rewrite (B.1)–(B.3):

$$I_1^E = \left\langle \mathbf{g}_m; \frac{\nabla\nabla\cdot + k^2}{j\omega\varepsilon_0\varepsilon_r} \langle G, \mathbf{f}_n \rangle_{D_n} \right\rangle_{D_m} \tag{B.5}$$

$$I_2 = \left\langle \mathbf{g}_m; \nabla \times \langle G, \mathbf{f}_n \rangle_{D_n} \right\rangle_{D_m} \tag{B.6}$$

$$I_3 = \frac{1}{2} \langle \mathbf{g}_m; \hat{\mathbf{n}} \times \mathbf{f}_n \rangle_{D_m}. \tag{B.7}$$

B.1.1 Computation of I_1

First let us transform $\nabla\nabla\cdot\langle G, \mathbf{f}_n\rangle_{D_n}$. In full form it is written as:

$$\nabla\nabla\cdot\int_{D_n} G(\mathbf{r},\mathbf{r}')\,\mathbf{f}_n(\mathbf{r}')\ \mathrm{d}S', \tag{B.8}$$

where the integration is performed on the domain D_n of the RWG basis function (see Fig. 3.13). By using the fact that $\nabla\cdot G = -\nabla'\cdot G$ and basic vector identities, we can write the following sequence of equalities:

$$\begin{aligned}
\nabla\nabla\cdot\int_{D_n} G\mathbf{f}_n\ \mathrm{d}S' &= \nabla\int_{D_n} \nabla\cdot(G\mathbf{f}_n)\ \mathrm{d}S' \\
&= \nabla\int_{D_n} \nabla G\cdot\mathbf{f}_n\ \mathrm{d}S' \\
&= -\nabla\int_{D_n} \nabla' G\cdot\mathbf{f}_n\ \mathrm{d}S' \\
&= -\nabla\int_{D_n} \left[\nabla'\cdot(G\mathbf{f}_n) - G\nabla'_S\cdot\mathbf{f}_n\right]\ \mathrm{d}S' \\
&= -\nabla\oint_{\partial D_n} \hat{\mathbf{m}}_n\cdot G\mathbf{f}_n\ \mathrm{d}l + \nabla\int_{D_n} G\nabla'_S\cdot\mathbf{f}_n\ \mathrm{d}S'
\end{aligned}$$

where ∂D_n denotes integration on the border of D_n. Due to the properties of the RWG basis functions given at section 3.7.1.1, the contour integral yields zero. We can therefore write that

$$\nabla\nabla\cdot\int_{D_n} G\mathbf{f}_n \,\mathrm{d}S' = \nabla\int_{D_n} G\nabla'_S\cdot\mathbf{f}_n \,\mathrm{d}S', \tag{B.9}$$

which allows us to decompose I_1^E as follows:

$$I_1^E = \frac{1}{j\omega\varepsilon}\underbrace{\left\langle \mathbf{g}_m; \nabla\left\langle G, \nabla'_S\cdot\mathbf{f}_n\right\rangle_{D_n}\right\rangle_{D_m}}_{\triangleq I_{1,1}} + \frac{k^2}{j\omega\varepsilon}\underbrace{\left\langle \mathbf{g}_m; \left\langle G, \mathbf{f}_n\right\rangle_{D_n}\right\rangle_{D_m}}_{\triangleq I_{1,2}}. \tag{B.10}$$

$I_{1,1}$ and $I_{1,2}$ are common to I_1^E and I_1^H.

B.1.1.1 Testing with $\mathbf{g}_m = \mathbf{f}_m$

First we modify integral $I_{1,1}$. The gradient applied to the inside inner product can be applied on the testing function by integrating by parts and by applying Gauss' divergence theorem [45, 57]:

$$\begin{aligned}\int_{D_m}\mathbf{f}_m\cdot\nabla\phi \,\mathrm{d}S &= \int_{D_m}\nabla\cdot(\mathbf{f}_m\phi)\ \mathrm{d}S - \int_{D_m}\phi\nabla_S\cdot\mathbf{f}_m \,\mathrm{d}S \\ &= \int_{\partial D_m}(\mathbf{f}_m\phi)\cdot\hat{\mathbf{m}}\,\mathrm{d}l - \int_{D_m}\phi\nabla_S\cdot\mathbf{f}_m \,\mathrm{d}S\end{aligned} \tag{B.11}$$

where ϕ is a scalar function, ∂D_m is the contour of D_m and $\hat{\mathbf{m}} = \hat{\mathbf{l}}\times\hat{\mathbf{n}}$ is the normal to the contour of the basis function domain (see Fig. 3.13). The contour integral yields zero, due to the fact that, on the edges of the RWG basis function domain D_m, $\mathbf{f}_m$ is parallel to $\hat{\mathbf{l}}_m$. We therefore have that

$$I_{1,1} = -\left\langle \nabla_S\cdot\mathbf{f}_m, \left\langle G, \nabla'_S\cdot\mathbf{f}_n\right\rangle_{D_n}\right\rangle_{D_m}. \tag{B.12}$$

From the divergence properties of the RWG basis functions given by (3.72), it is easy to see that $I_{1,1}$ is constituted by the following sum:

$$I_{1,1} = \sum_{p,\, T_m^p\in D_m}\ \sum_{q,\, T_n^q\in D_n} -4C_m^pC_n^q\int_{T_m^p}\int_{T_n^q} G\,\mathrm{d}S'\mathrm{d}S \tag{B.13}$$

with $C_m^p = \frac{S_m^p l_m}{2A_m^p}$, where S_m^p is the sign of test function m in triangle p, l_m is the length of edge m, and A_m^p is the area of triangle T_m^p. The sums are performed on p and q for which T_m^p and T_n^q are the triangles that form half of D_m and D_n respectively. We can note that the term under the integration sign

is independent upon the basis function. This constatation leads us to remark that, instead of evaluating the MoM integrals basis-wise, we will perform them triangle-wise, and contribute back the terms into the MoM matrix with the appropriate coefficients for all basis and test functions that pertain to the two triangles [45]. Since for closed surfaces, there are three basis functions per triangle, and because the majority of the time is spent on these integrals, performing them triangle-wise will save a non-negligible amount of computation time. In the remainder of the text, the two summation symbols will be dropped for clarity.

One more comment must be made about (B.13). G is singular when $\mathbf{r} = \mathbf{r}'$, and this renders the numerical integration very imprecise if T_m^p is close to T_n^q. This singularity must be properly extracted. This is done thoroughly in [57] and will not be discussed here.

Now let us develop $I_{1,2}$. From definition (3.71) of the RWG basis functions, it is immediate to see that $I_{1,2}$ is constituted by combinations of the following term:

$$\begin{aligned} C_m^p C_n^q \int_{T_m^p} (\mathbf{r} - \mathbf{r}_m^p) \cdot \int_{T_n^q} G\,(\mathbf{r}' - \mathbf{r}_n^q)\,\mathrm{d}S'\mathrm{d}S \\ = C_m^p C_n^q \Bigg[\int_{T_m^p} \mathbf{r} \cdot \int_{T_n^q} G\,\mathbf{r}'\mathrm{d}S'\mathrm{d}S - \mathbf{r}_n^q \cdot \int_{T_m^p} \mathbf{r} \int_{T_n^q} G\,\mathrm{d}S'\mathrm{d}S \\ - \mathbf{r}_m^p \cdot \int_{T_m^p} \int_{T_n^q} G\,\mathbf{r}'\mathrm{d}S'\mathrm{d}S + \mathbf{r}_m^p \cdot \mathbf{r}_n^q \int_{T_m^p} \int_{T_n^q} G\,\mathrm{d}S'\mathrm{d}S \Bigg] \end{aligned} \tag{B.14}$$

where $\mathbf{r}_m^p$ is the vector position of the node belonging to triangle p and opposite to edge m. The four integrals on the right-hand side of the above equation are independent of the edges, and each can again be performed triangle-wise. Only their recombination is edge-dependent. Computationally speaking, this is an enormous advantage over computing directly the left-hand side term of the above equation, as there are always more edges than triangles (up to nine times more for closed bodies). Moreover, we can immediately see that the last term on the right-hand side of (B.14) is equal to (B.13).

B.1.1.2 Testing with $\mathbf{g}_m = \hat{\mathbf{n}} \times \mathbf{f}_m$

Rewriting explicitly $I_{1,1}$ with $\mathbf{g}_m = \hat{\mathbf{n}} \times \mathbf{f}_m$, we can see that it will be a combination of the following term:

$$2C_m^p C_n^q \int_{T_m^p} \left(\hat{\mathbf{n}}_m^p \times (\mathbf{r} - \mathbf{r}_m^p)\right) \cdot \int_{T_n^q} \nabla G\,\mathrm{d}S'\mathrm{d}S \tag{B.15}$$

This time we cannot move the gradient onto the testing function in $I_{1,1}$, because $\hat{\mathbf{n}} \times \mathbf{f}_m$ is not continuous on the triangle pair that forms D_m [57], as the triangles normals differ. The integral may be further decomposed as:

$$\begin{aligned}
&\int_{T_m^p} \left(\hat{\mathbf{n}}_m^p \times (\mathbf{r} - \mathbf{r}_m^p)\right) \cdot \int_{T_n^q} \nabla G \, \mathrm{d}S' \mathrm{d}S \\
&\quad = \int_{T_m^p} (\hat{\mathbf{n}}_m^p \times \mathbf{r}) \cdot \int_{T_n^q} \nabla G \, \mathrm{d}S' \mathrm{d}S - (\hat{\mathbf{n}}_m^p \times \mathbf{r}_m^p) \cdot \int_{T_m^p} \int_{T_n^q} \nabla G \, \mathrm{d}S' \mathrm{d}S \\
&\quad = \hat{\mathbf{n}}_m^p \cdot \left(\int_{T_m^p} \mathbf{r} \times \int_{T_n^q} \nabla G \, \mathrm{d}S' \mathrm{d}S - \mathbf{r}_m^p \times \int_{T_m^p} \int_{T_n^q} \nabla G \, \mathrm{d}S' \mathrm{d}S \right).
\end{aligned} \tag{B.16}$$

The kernel involved in the terms contained in (B.16) is highly singular, as it involves an integral of a $1/R^2$ singularity, in contrast with an integral of a $1/R$ singularity usually involved with G [57]. When domains of basis functions m and n are "sufficiently far away" from each other, a regular numerical integration of the terms appearing in (B.16) should not cause any trouble. But if the test and basis function overlap, we will not be able to extract analytically the singularity, and a numerical method will have to evaluate a great number of times the integrand for obtaining a precise value of the integral.

However, an elegant transformation may be applied to the integrand by noting that

$$\begin{aligned}
&\int_{T_m^p} \left(\hat{\mathbf{n}}_m^p \times (\mathbf{r} - \mathbf{r}_m^p)\right) \cdot \int_{T_n^q} \nabla G \, \mathrm{d}S' \mathrm{d}S \\
&\qquad = \hat{\mathbf{n}}_m^p \cdot \int_{T_m^p} (\mathbf{r} - \mathbf{r}_m^p) \times \int_{T_n^q} \nabla G \, \mathrm{d}S' \mathrm{d}S \\
&\qquad = -\hat{\mathbf{n}}_m^p \cdot \left[\int_{T_m^p} \int_{T_n^q} \nabla \times \left(G \left(\mathbf{r} - \mathbf{r}_m^p\right)\right) \mathrm{d}S' \mathrm{d}S \right. \\
&\qquad\qquad \left. - \int_{T_m^p} \int_{T_n^q} G \nabla \times (\mathbf{r} - \mathbf{r}_m^p) \, \mathrm{d}S' \mathrm{d}S \right] \\
&\qquad = -\hat{\mathbf{n}}_m^p \cdot \int_{\partial T_m^p} \left(\hat{\mathbf{m}}_m^p \times (\mathbf{r} - \mathbf{r}_m^p)\right) \int_{T_n^q} G \, \mathrm{d}S' \mathrm{d}l
\end{aligned} \tag{B.17}$$

where use of identity $\nabla \times (a\mathbf{b}) = a\nabla \times \mathbf{b} - \mathbf{b} \times \nabla a$ has been made. The last equality is due to the fact that the rotational of the position vector $(\mathbf{r} - \mathbf{r}_m^p)$ is

zero. By noting that $\hat{\mathbf{m}} = \hat{\mathbf{l}} \times \hat{\mathbf{n}}$ (Fig. 3.13), we finally obtain

$$\begin{aligned}\int_{T_m^p} \left(\hat{\mathbf{n}}_m^p \times (\mathbf{r} - \mathbf{r}_m^p)\right) \cdot \int_{T_n^q} \nabla G \, \mathrm{d}S' \mathrm{d}S \\ = \int_{\partial T_m^p} -\hat{\mathbf{l}}_m^p \cdot (\mathbf{r} - \mathbf{r}_m^p) \int_{T_n^q} G \, \mathrm{d}S' \mathrm{d}l \\ = \int_{\partial T_m^p} -\hat{\mathbf{l}}_m^p \cdot \mathbf{r} \int_{T_n^q} G \, \mathrm{d}S' \mathrm{d}l + \mathbf{r}_m^p \cdot \int_{\partial T_m^p} \hat{\mathbf{l}}_m^p \int_{T_n^q} G \, \mathrm{d}S' \mathrm{d}l\end{aligned} \tag{B.18}$$

which is a more elegant form than its counterpart (23) of [57]. Singularity $\frac{1}{R^2}$ has been reduced to $\frac{1}{R}$ and can therefore be analytically extracted even for overlapping basis and test functions.

Let us now develop $I_{1,2}$. We will have the following terms:

$$\begin{aligned}C_m^p C_n^q \int_{T_m^p} \left(\hat{\mathbf{n}}_m^p \times (\mathbf{r} - \mathbf{r}_m^p)\right) \cdot \int_{T_n^q} G(\mathbf{r}' - \mathbf{r}_n^q) \, \mathrm{d}S' \mathrm{d}S \\ = C_m^p C_n^q \Bigg[\int_{T_m^p} (\hat{\mathbf{n}}_m^p \times \mathbf{r}) \cdot \int_{T_n^q} G \, \mathbf{r}' \, \mathrm{d}S' \mathrm{d}S - \mathbf{r}_n^q \cdot \int_{T_m^p} (\hat{\mathbf{n}} \times \mathbf{r}) \int_{T_n^q} G \, \mathrm{d}S' \mathrm{d}S \\ - (\hat{\mathbf{n}}_m^p \times \mathbf{r}_m^p) \cdot \int_{T_m^p} \int_{T_n^q} G \, \mathbf{r}' \, \mathrm{d}S' \mathrm{d}S + \mathbf{r}_n^q \cdot (\hat{\mathbf{n}}_m^p \times \mathbf{r}_m^p) \int_{T_m^p} \int_{T_n^q} G \, \mathrm{d}S' \mathrm{d}S \Bigg].\end{aligned} \tag{B.19}$$

These terms do not pose any particular problems, and some of them are already present in (B.14).

B.1.2 Computation of I_2

Let us rewrite explicitly I_2:

$$\begin{aligned}I_2 &= \int_{D_m} \mathbf{g}_m \cdot \nabla \times \int_{D_n} G \mathbf{f}_n \, \mathrm{d}S' \mathrm{d}S \\ &= \int_{D_m} \mathbf{g}_m \cdot \int_{D_n} \nabla \times (G \mathbf{f}_n) \, \mathrm{d}S' \mathrm{d}S \\ &= \int_{D_m} \mathbf{g}_m \cdot \int_{D_n} \nabla G \times \mathbf{f}_n \, \mathrm{d}S' \mathrm{d}S\end{aligned} \tag{B.20}$$

where use of identity $\nabla \times (a\mathbf{b}) = a\nabla \times \mathbf{b} - \mathbf{b} \times \nabla a$ and the fact that $\mathbf{f}_n = \mathbf{f}_n(\mathbf{r}')$ has been made. Note that, if the two triangles T_m^p and T_n^q that form respectively half of D_m and half of D_n are coplanar, the corresponding contribution $I_2^{pq} = 0$, since in that case ∇G is contained in the same plane as $\mathbf{f}_n$ and $\mathbf{g}_m$, and therefore $\nabla G \times \mathbf{f}_n$ and $\mathbf{g}_m$ are perpendicular. *A fortiori*, I_2^{pq} will be zero if $T_m^p = T_n^q$.

B.1.2.1 Testing with $\mathbf{g}_m = \mathbf{f}_m$

After replacing $(\mathbf{r}' - \mathbf{r}_n^q)$ by $(\mathbf{r}' - \mathbf{r}) + (\mathbf{r} - \mathbf{r}_m^p) + (\mathbf{r}_m^p - \mathbf{r}_n^q)$, using $\nabla G = -\nabla' G$ and performing a few manipulations, it can be shown that (B.20) implies terms of type (see (20) of [57]):

$$\begin{aligned} & C_m^p C_n^q \int_{T_m^p} (\mathbf{r} - \mathbf{r}_m^p) \cdot \left[(\mathbf{r}_m^p - \mathbf{r}_n^q) \times \int_{T_n^q} \nabla' G \, \mathrm{d}S' \right] \, \mathrm{d}S \\ & = C_m^p C_n^q \, (\mathbf{r}_m^p - \mathbf{r}_n^q) \cdot \left[\int_{T_m^p} \mathbf{r} \times \int_{T_n^q} \nabla G \, \mathrm{d}S' \mathrm{d}S - \mathbf{r}_m^p \times \int_{T_m^p} \int_{T_n^q} \nabla G \, \mathrm{d}S' \mathrm{d}S \right]. \end{aligned} \tag{B.21}$$

B.1.2.2 Testing with $\mathbf{g}_m = \hat{\mathbf{n}} \times \mathbf{f}_m$

In this case, by using $\nabla G = -\nabla' G$ and by replacing $(\mathbf{r}' - \mathbf{r}_n^q)$ by $(\mathbf{r}' - \mathbf{r}) + (\mathbf{r} - \mathbf{r}_n^q)$, (B.20) implies terms of type:

$$\begin{aligned} & C_m^p C_n^q \int_{T_m^p} \left(\hat{\mathbf{n}}_m^p \times (\mathbf{r} - \mathbf{r}_m^p) \right) \cdot \left[(\mathbf{r} - \mathbf{r}_n^q) \times \int_{T_n^q} -\nabla G \, \mathrm{d}S' \right] \, \mathrm{d}S \\ & \qquad = -C_m^p C_n^q \left\{ \int_{T_m^p} (\hat{\mathbf{n}}_m^p \times \mathbf{r}) \cdot \left[\mathbf{r} \times \int_{T_n^q} \nabla G \, \mathrm{d}S' \right] \mathrm{d}S \right. \\ & + \mathbf{r}_n^q \cdot \int_{T_m^p} (\hat{\mathbf{n}}_m^p \times \mathbf{r}) \times \int_{T_n^q} \nabla G \, \mathrm{d}S' \mathrm{d}S - (\hat{\mathbf{n}}_m^p \times \mathbf{r}_m^p) \cdot \int_{T_m^p} \mathbf{r} \times \int_{T_n^q} \nabla G \, \mathrm{d}S' \mathrm{d}S \\ & \qquad \left. - \mathbf{r}_n^q \cdot \left[(\hat{\mathbf{n}} \times \mathbf{r}_m^p) \times \int_{T_m^p} \int_{T_n^q} \nabla G \, \mathrm{d}S' \mathrm{d}S \right] \right\}. \end{aligned} \tag{B.22}$$

Note that two terms of (B.22) are present in (B.21).

B.1.3 Computation of I_3

B.1.3.1 Testing with $\mathbf{g}_m = \mathbf{f}_m$

I_3 is nonzero only for overlapping triangles p and q, and will involve combinations of terms of the type

$$\begin{aligned} & C_m^p C_n^p \int_{T_m^p} (\mathbf{r} - \mathbf{r}_m^p) \cdot (\hat{\mathbf{n}}_m^p \times (\mathbf{r} - \mathbf{r}_n^p)) \, \mathrm{d}S \\ & \qquad = -C_m^p C_n^p \hat{\mathbf{n}}_m^p \cdot \left[(\mathbf{r}_n^p - \mathbf{r}_m^p) \times \int_{T_m^p} \mathbf{r} \, \mathrm{d}S + (\mathbf{r}_m^p \times \mathbf{r}_n^p) \int_{T_m^p} 1 \, \mathrm{d}S \right]. \end{aligned} \tag{B.23}$$

B.1.3.2 Testing with $\mathbf{g}_m = \hat{\mathbf{n}} \times \mathbf{f}_m$

We can immediately write that

$$\langle \hat{\mathbf{n}} \times \mathbf{f}_m ; \hat{\mathbf{n}} \times \mathbf{f}_n \rangle_{D_m} = \langle \mathbf{f}_m ; \mathbf{f}_n \rangle_{D_m} \tag{B.24}$$

where the right-hand term can be further decomposed using basic vector formulas as

$$\begin{aligned} & C_m^p C_n^p \int_{T_m^p} (\mathbf{r} - \mathbf{r}_m^p) \cdot (\mathbf{r} - \mathbf{r}_n^p) \ \mathrm{d}S \\ & = C_m^p C_n^p \left[\int_{T_m^p} |\mathbf{r}|^2 \ \mathrm{d}S - (\mathbf{r}_m^p + \mathbf{r}_n^p) \cdot \int_{T_m^p} \mathbf{r} \ \mathrm{d}S + (\mathbf{r}_m^p \cdot \mathbf{r}_n^p) \int_{T_m^p} 1 \ \mathrm{d}S \right]. \end{aligned} \tag{B.25}$$

B.2 Computation of the multilayered medium MoM matrix terms

In this section we are going to detail how to compute the terms of the MoM matrices that appear in (3.77) for inhomogeneities embedded in multilayered media, namely

$$I_4^E = -j\omega \left\langle \mathbf{g}_m ; \langle \overline{\boldsymbol{\mathcal{K}}}^{AJ} ; \mathbf{f}_n \rangle_{D_n} \right\rangle_{D_m} \tag{B.26}$$

$$I_5^E = \frac{1}{j\omega\varepsilon_0} \left\langle \mathbf{g}_m ; \nabla \left\langle K^{\Phi}, \nabla'_S \cdot \mathbf{f}_n \right\rangle_{D_n} \right\rangle_{D_m} \tag{B.27}$$

$$I_6^E = \left\langle \mathbf{g}_m ; \langle \overline{\boldsymbol{\mathcal{G}}}^{EM} ; \mathbf{f}_n \rangle_{D_n} \right\rangle_{D_m}. \tag{B.28}$$

Note that the term I_3 has been omitted, since it has been treated at the previous section. Terms pertaining to (3.81) can be obtained by duality applied to the Green's functions (appendix C.1). In the remainder of this section, I_i^E will be denoted I_i.

B.2.1 Computation of I_4

It is shown at appendix C.2 that, if the source and observation points, designated by $\mathbf{r}'$ and $\mathbf{r}$ respectively, are located within the same layer l, we can rewrite $\overline{\boldsymbol{\mathcal{K}}}^{AJ}$ as:

$$\overline{\boldsymbol{\mathcal{K}}}^{AJ} = \mu_0 \mu_m G_l \overline{\boldsymbol{\mathcal{I}}} + \overline{\boldsymbol{\mathcal{K}}}^{AJ,(\mathrm{ml})} \tag{C.24}$$

in which the direct and reflection terms have been separated. We can rewrite I_4 accordingly as:

$$\begin{aligned} I_4 &= -j\omega \left\langle \mathbf{g}_m; \left\langle \mu_0\mu_l G_l \overline{\boldsymbol{\mathcal{I}}}, \mathbf{f}_n \right\rangle_{D_n} \right\rangle_{D_m} - j\omega \left\langle \mathbf{g}_m; \left\langle \overline{\boldsymbol{\mathcal{K}}}^{AJ,(\mathrm{ml})}, \mathbf{f}_n \right\rangle_{D_n} \right\rangle_{D_m} \\ &= \frac{k_l^2}{j\omega\varepsilon_0\varepsilon_{rl}} \underbrace{\left\langle \mathbf{g}_m; \langle G_l, \mathbf{f}_n \rangle_{D_n} \right\rangle_{D_m}}_{I_{4,1}=I_{1,2}} - j\omega \underbrace{\left\langle \mathbf{g}_m; \left\langle \overline{\boldsymbol{\mathcal{K}}}^{AJ,(\mathrm{ml})}, \mathbf{f}_n \right\rangle_{D_n} \right\rangle_{D_m}}_{I_{4,2}} \end{aligned} \tag{B.29}$$

where $\overline{\boldsymbol{\mathcal{I}}}$ is the unit dyadic and has the property that $\mathbf{a} \cdot \overline{\boldsymbol{\mathcal{I}}} = \overline{\boldsymbol{\mathcal{I}}} \cdot \mathbf{a} = \mathbf{a}$, ε_{rl} is the relative dielectric permittivity of layer l, and $G_l = \frac{e^{-jk_l|\mathbf{r}-\mathbf{r}'|}}{4\pi|\mathbf{r}-\mathbf{r}'|}$. We can immediately recognize that the first term of the last equality is equal to $I_{1,2}$, which has been calculated previously: it is the direct term that pertains to homogeneous space. We will therefore concentrate on $I_{4,2}$ due to the reflections at the layer boundaries. If the source and observation points are not within the same layer, there are no singular terms and formulas derived for the reflexion term can be applied directly with $\overline{\boldsymbol{\mathcal{K}}}^{AJ}$ without decomposition into a direct and reflection term.

B.2.1.1 Testing with $\mathbf{g}_m = \mathbf{f}_m$

In this case, the reflexion term given by $I_{4,2}$ implies terms that can be written as:

$$\begin{aligned} & C_m^p C_n^q \int_{T_p} (\mathbf{r} - \mathbf{r}_m^p) \cdot \int_{T_q} \overline{\boldsymbol{\mathcal{K}}}^{AJ,(\mathrm{ml})} \cdot (\mathbf{r}' - \mathbf{r}_n^q) \ \mathrm{d}S'\mathrm{d}S \\ &= C_m^p C_n^q \Bigg[\int_{T_p} \mathbf{r} \cdot \int_{T_q} \overline{\boldsymbol{\mathcal{K}}}^{AJ,(\mathrm{ml})} \cdot \mathbf{r}' \ \mathrm{d}S'\mathrm{d}S - \mathbf{r}_n^q \cdot \int_{T_p} \mathbf{r} \cdot \int_{T_q} \overline{\boldsymbol{\mathcal{K}}}^{AJ,(\mathrm{ml})} \ \mathrm{d}S'\mathrm{d}S \\ & - \mathbf{r}_m^p \cdot \int_{T_p} \int_{T_q} \overline{\boldsymbol{\mathcal{K}}}^{AJ,(\mathrm{ml})} \cdot \mathbf{r}' \ \mathrm{d}S'\mathrm{d}S + \mathbf{r}_m^p \cdot \int_{T_p} \int_{T_q} \overline{\boldsymbol{\mathcal{K}}}^{AJ,(\mathrm{ml})} \ \mathrm{d}S'\mathrm{d}S \cdot \mathbf{r}_n^q \Bigg]. \end{aligned} \tag{B.30}$$

The reader will note that, when we use dyadics, the placement of position vectors is important and cannot be arbitrarily interchanged.

B.2.1.2 Testing with $\mathbf{g}_m = \hat{\mathbf{n}} \times \mathbf{f}_m$

In this case, the reflexion term given by $I_{4,2}$ implies terms that can be written as:

$$\begin{aligned} C_m^p C_n^q \int_{T_p} \left(\hat{\mathbf{n}}_m^p \times (\mathbf{r} - \mathbf{r}_m^p)\right) \cdot \int_{T_q} \overline{\boldsymbol{\mathcal{K}}}^{AJ,(\mathrm{ml})} \cdot (\mathbf{r}' - \mathbf{r}_n^q)\ \mathrm{d}S'\mathrm{d}S \\ = C_m^p C_n^q \Bigg[\int_{T_p} (\hat{\mathbf{n}}_m^p \times \mathbf{r}) \cdot \int_{T_q} \overline{\boldsymbol{\mathcal{K}}}^{AJ,(\mathrm{ml})} \cdot \mathbf{r}'\ \mathrm{d}S'\mathrm{d}S \\ - \mathbf{r}_n^q \cdot \int_{T_p} (\hat{\mathbf{n}}_m^p \times \mathbf{r}) \cdot \int_{T_q} \overline{\boldsymbol{\mathcal{K}}}^{AJ,(\mathrm{ml})}\ \mathrm{d}S'\mathrm{d}S - (\hat{\mathbf{n}}_m^p \times \mathbf{r}_m^p) \cdot \int_{T_p}\int_{T_q} \overline{\boldsymbol{\mathcal{K}}}^{AJ,(\mathrm{ml})} \cdot \mathbf{r}'\ \mathrm{d}S'\mathrm{d}S \\ + (\hat{\mathbf{n}}_m^p \times \mathbf{r}_m^p) \cdot \int_{T_p}\int_{T_q} \overline{\boldsymbol{\mathcal{K}}}^{AJ,(\mathrm{ml})}\ \mathrm{d}S'\mathrm{d}S \cdot \mathbf{r}_n^q \Bigg]. \end{aligned} \tag{B.31}$$

B.2.2 Computation of I_5

As for I_4, if $\mathbf{r}$ and $\mathbf{r}'$ are within the same layer l, it is possible to decompose I_5 as a sum of a direct term and a term involving the reflexions at the interfaces that bound layer l (appendix C.2):

$$K^{\Phi} = \frac{1}{\varepsilon_{rl}} G_l + K^{\Phi,(\mathrm{ml})}. \tag{C.25}$$

Using this decomposition, we can rewrite I_5 as follows:

$$\begin{aligned} I_5 &= \frac{1}{j\omega\varepsilon_0} \left\langle \mathbf{g}_m; \nabla \left\langle \frac{1}{\varepsilon_{rl}} G_l, \nabla'_S \cdot \mathbf{f}_n \right\rangle_{D_n} \right\rangle_{D_m} \\ &\quad + \frac{1}{j\omega\varepsilon_0} \left\langle \mathbf{g}_m; \nabla \left\langle K^{\Phi,(\mathrm{ml})}, \nabla'_S \cdot \mathbf{f}_n \right\rangle_{D_n} \right\rangle_{D_m} \\ &= \frac{1}{j\omega\varepsilon_0\varepsilon_{rl}} \underbrace{\left\langle \mathbf{g}_m; \nabla \left\langle G_l, \nabla'_S \cdot \mathbf{f}_n \right\rangle_{D_n} \right\rangle_{D_m}}_{I_{5,1} = I_{1,1}} \\ &\quad + \frac{1}{j\omega\varepsilon_0} \underbrace{\left\langle \mathbf{g}_m; \nabla \left\langle K^{\Phi,(\mathrm{ml})}, \nabla'_S \cdot \mathbf{f}_n \right\rangle_{D_n} \right\rangle_{D_m}}_{I_{5,2}}. \end{aligned} \tag{B.32}$$

Again, we recognize immediately that $I_{5,1} = I_{1,1}$, which was treated previously. Therefore we will concentrate on $I_{5,2}$. As for I_4, if the source and observation points are not within the same layer, we can use the formulas developed for $I_{5,2}$ but with the superscript "(ml)" suppressed.

B.2.2.1 Testing with $\mathbf{g}_m = \mathbf{f}_m$

In this case, using transformations (B.11) as for $I_{1,1}$, $I_{5,2}$ can be rewritten as follows

$$I_{5,2} = -\left\langle \nabla_S \cdot \mathbf{g}_m, \left\langle K^{\Phi,(\mathrm{ml})}, \nabla'_S \cdot \mathbf{f}_n \right\rangle_{D_n} \right\rangle_{D_m} \tag{B.33}$$

and it therefore involves terms of the type

$$-4C_m^p C_n^q \int_{T_m^p} \int_{T_n^q} K^{\Phi,(\mathrm{ml})} \, \mathrm{d}S' \mathrm{d}S. \tag{B.34}$$

B.2.2.2 Testing with $\mathbf{g}_m = \hat{\mathbf{n}} \times \mathbf{f}_m$

The gradient can not be transferred on the testing function anymore, and we get terms of the type:

$$\begin{aligned} 2C_m^p C_n^q \int_{T_m^p} \left(\hat{\mathbf{n}}_m^p \times (\mathbf{r} - \mathbf{r}_m^p) \right) \cdot \int_{T_n^q} \nabla K^{\Phi,(\mathrm{ml})} \, \mathrm{d}S' \mathrm{d}S \\ = 2C_m^p C_n^q \int_{T_m^p} (\hat{\mathbf{n}}_m^p \times \mathbf{r}) \cdot \int_{T_n^q} \nabla K^{\Phi,(\mathrm{ml})} \, \mathrm{d}S' \mathrm{d}S \\ - (\hat{\mathbf{n}}_m^p \times \mathbf{r}_m^p) \cdot \int_{T_m^p} \int_{T_n^q} \nabla K^{\Phi,(\mathrm{ml})} \, \mathrm{d}S' \mathrm{d}S. \end{aligned} \tag{B.35}$$

These integrals can be evaluated numerically since the direct terms have been extracted. Explicit formulas for $\nabla K^{\Phi,(\mathrm{ml})}$ can be obtained from appendix C.1.

B.2.3 Computation of I_6

Since $\overline{\boldsymbol{\mathcal{G}}}^{EM}$ can be obtained by duality applied to $\overline{\boldsymbol{\mathcal{G}}}^{HJ}$ following (C.8b), we can also separate $\overline{\boldsymbol{\mathcal{G}}}^{EM}$ in a direct and reflection terms thanks to the dual form of (C.23):

$$\overline{\boldsymbol{\mathcal{G}}}^{EM} = -\nabla G_l \times \overline{\boldsymbol{\mathcal{I}}} + \overline{\boldsymbol{\mathcal{G}}}^{EM,(\mathrm{ml})}. \tag{B.36}$$

We can therefore rewrite I_6 as follows:

$$\begin{aligned} I_6 &= \left\langle \mathbf{g}_m; \left\langle -\nabla G_l \times \overline{\boldsymbol{\mathcal{I}}}; \mathbf{f}_n \right\rangle_{D_n} \right\rangle_{D_m} + \left\langle \mathbf{g}_m; \left\langle \overline{\boldsymbol{\mathcal{G}}}^{EM,(\mathrm{ml})}; \mathbf{f}_n \right\rangle_{D_n} \right\rangle_{D_m} \\ &= \underbrace{-\left\langle \mathbf{g}_m; \left\langle \nabla G_l \times \mathbf{f}_n \right\rangle_{D_n} \right\rangle_{D_m}}_{I_{6,1}=I_2} + \underbrace{\left\langle \mathbf{g}_m; \left\langle \overline{\boldsymbol{\mathcal{G}}}^{EM,(\mathrm{ml})}; \mathbf{f}_n \right\rangle_{D_n} \right\rangle_{D_m}}_{I_{6,2}}. \end{aligned} \tag{B.37}$$

$I_{6,1}$ has been obtained by using the fact that, for any vector $\mathbf{a}$, $\mathbf{a} \times \overline{\boldsymbol{\mathcal{I}}} = -\left(\mathbf{a} \times \overline{\boldsymbol{\mathcal{I}}}\right)^T$, together with the identities $\mathbf{a} \cdot \overline{\boldsymbol{\mathcal{B}}} = \overline{\boldsymbol{\mathcal{B}}}^T \cdot \mathbf{a}$, $\mathbf{a} \cdot \left(\mathbf{b} \times \overline{\boldsymbol{\mathcal{C}}}\right) = (\mathbf{a} \times \mathbf{b}) \cdot \overline{\boldsymbol{\mathcal{C}}}$

and $\mathbf{a}\cdot\overline{\overline{\boldsymbol{\mathcal{I}}}}=\overline{\overline{\boldsymbol{\mathcal{I}}}}\cdot\mathbf{a}=\mathbf{a}$ [69], which have allowed us to write:

$$\left\langle -\nabla G_l \times \overline{\overline{\boldsymbol{\mathcal{I}}}}; \mathbf{f}_n \right\rangle_{D_n} = -\left\langle \nabla G_l \overset{\times}{,} \mathbf{f}_n \right\rangle_{D_n} . \tag{B.38}$$

Since $I_{6,1}=I_2$, we will concentrate on $I_{6,2}$.

B.2.3.1 Testing with $\mathbf{g}_m=\mathbf{f}_m$

In this case, $I_{6,2}$ will involve terms of the type:

$$\begin{aligned}
&C_m^p C_n^q \int_{T_m^p} (\mathbf{r}-\mathbf{r}_m^p)\cdot \int_{T_n^q} \overline{\boldsymbol{\mathcal{G}}}^{EM,(\mathrm{ml})}\cdot(\mathbf{r}'-\mathbf{r}_n^q)\ \mathrm{d}S'\mathrm{d}S \\
&= C_m^p C_n^q \Bigg[\int_{T_m^p} \mathbf{r}\cdot \int_{T_n^q} \overline{\boldsymbol{\mathcal{G}}}^{EM,(\mathrm{ml})}\cdot\mathbf{r}'\ \mathrm{d}S'\mathrm{d}S - \mathbf{r}_n^q\cdot\int_{T_m^p}\mathbf{r}\cdot\int_{T_n^q}\overline{\boldsymbol{\mathcal{G}}}^{EM,(\mathrm{ml})}\ \mathrm{d}S'\mathrm{d}S \\
&\quad - \mathbf{r}_m^p\cdot\int_{T_m^p}\int_{T_n^q}\overline{\boldsymbol{\mathcal{G}}}^{EM,(\mathrm{ml})}\cdot\mathbf{r}'\ \mathrm{d}S'\mathrm{d}S + \mathbf{r}_m^p\cdot\int_{T_m^p}\int_{T_n^q}\overline{\boldsymbol{\mathcal{G}}}^{EM,(\mathrm{ml})}\ \mathrm{d}S'\mathrm{d}S\cdot\mathbf{r}_n^q \Bigg].
\end{aligned} \tag{B.39}$$

B.2.3.2 Testing with $\mathbf{g}_m=\hat{\mathbf{n}}\times\mathbf{f}_m$

In this case, $I_{6,2}$ will involve terms of the type:

$$\begin{aligned}
&C_m^p C_n^q \int_{T_m^p} \left(\hat{\mathbf{n}}_m^p\times(\mathbf{r}-\mathbf{r}_m^p)\right)\cdot\int_{T_n^q}\overline{\boldsymbol{\mathcal{G}}}^{EM,(\mathrm{ml})}\cdot(\mathbf{r}'-\mathbf{r}_n^q)\ \mathrm{d}S'\mathrm{d}S \\
&\qquad = C_m^p C_n^q \Bigg[\int_{T_m^p}(\hat{\mathbf{n}}_m^p\times\mathbf{r})\cdot\int_{T_n^q}\overline{\boldsymbol{\mathcal{G}}}^{EM,(\mathrm{ml})}\cdot\mathbf{r}'\ \mathrm{d}S'\mathrm{d}S \\
&-\mathbf{r}_n^q\cdot\int_{T_m^p}(\hat{\mathbf{n}}_m^p\times\mathbf{r})\cdot\int_{T_n^q}\overline{\boldsymbol{\mathcal{G}}}^{EM,(\mathrm{ml})}\ \mathrm{d}S'\mathrm{d}S - (\hat{\mathbf{n}}_m^p\times\mathbf{r}_m^p)\cdot\int_{T_m^p}\int_{T_n^q}\overline{\boldsymbol{\mathcal{G}}}^{EM,(\mathrm{ml})}\cdot\mathbf{r}'\ \mathrm{d}S'\mathrm{d}S \\
&\qquad + (\hat{\mathbf{n}}_m^p\times\mathbf{r}_m^p)\cdot\int_{T_m^p}\int_{T_n^q}\overline{\boldsymbol{\mathcal{G}}}^{EM,(\mathrm{ml})}\ \mathrm{d}S'\mathrm{d}S\cdot\mathbf{r}_n^q \Bigg].
\end{aligned} \tag{B.40}$$

There are two terms of the right-hand side that are common with $\mathbf{f}_m$ testing.

B.3 Computation of the MoM excitation vectors

The nonzero terms involved in the computation of the excitation vectors $\underline{V}^E$ and $\underline{V}^H$ have the following generic form given by (3.79) and (3.83):

$$V_m^P = -\left\langle \mathbf{g}_m; \mathbf{P}^{\mathrm{inc}} \right\rangle_{D_m} \tag{B.41}$$

where $\mathbf{P}$ can be $\mathbf{E}$ or $\mathbf{H}$. If tested with $\mathbf{g}_m = \mathbf{f}_m$, we immediately have that

$$-\left\langle \mathbf{g}_m; \mathbf{P}^{\text{inc}} \right\rangle_{D_m} = -\frac{l_m}{2A_m^+} \int_{T_m^+} \left(\mathbf{r} - \mathbf{r}_m^+\right) \cdot \mathbf{P}^{\text{inc}} \, \mathrm{d}S + \frac{l_m}{2A_m^-} \int_{T_m^-} \left(\mathbf{r} - \mathbf{r}_m^-\right) \cdot \mathbf{P}^{\text{inc}} \, \mathrm{d}S. \tag{B.42}$$

If tested with $\mathbf{g}_m = \hat{\mathbf{n}} \times \mathbf{f}_m$, we have

$$\begin{aligned} -\left\langle \mathbf{g}_m; \mathbf{P}^{\text{inc}} \right\rangle_{D_m} = &-\frac{l_m}{2A_m^+} \int_{T_m^+} \left(\hat{\mathbf{n}}_m^+ \times \left(\mathbf{r} - \mathbf{r}_m^+\right)\right) \cdot \mathbf{P}^{\text{inc}} \, \mathrm{d}S \\ &+ \frac{l_m}{2A_m^-} \int_{T_m^-} \left(\hat{\mathbf{n}}_m^- \times \left(\mathbf{r} - \mathbf{r}_m^-\right)\right) \cdot \mathbf{P}^{\text{inc}} \, \mathrm{d}S. \end{aligned} \tag{B.43}$$

Appendix C

Multilayered Media Green's Functions

This chapter deals with the Dyadic Green's functions (DGFs) that link the electric and magnetic fields to electric and magnetic dipole currents in multilayered media. Numerous authors have derived those DGFs, and development is this area is mainly driven by applications linked to microstrip patch antennas [27]. The spatial domain DGFs are given in terms of Sommerfeld integrals of transmission-line Green's functions. Please note that in the remainder of the text, the relative constitutive parameters ε_{rj} and μ_{rj} of layer j will be denoted by ε_j and μ_j.

C.1 Dyadic Green's functions

For $\widetilde{\widetilde{\boldsymbol{\mathcal{G}}}}^{EJ}$ ($\overline{\boldsymbol{\mathcal{G}}}^{EJ}$ in the k_ρ-space, or spectrum-domain), the elements are given by using (28) and (14) of [27]:

$$\widetilde{\mathcal{G}}_{xx}^{EJ} = -\left(\frac{1}{2}+\frac{1}{2}\cos(2\xi)\right)V_i^e - \left(\frac{1}{2}-\frac{1}{2}\cos(2\xi)\right)V_i^h \tag{C.1a}$$

$$\widetilde{\mathcal{G}}_{yy}^{EJ} = -\left(\frac{1}{2}-\frac{1}{2}\cos(2\xi)\right)V_i^e - \left(\frac{1}{2}+\frac{1}{2}\cos(2\xi)\right)V_i^h \tag{C.1b}$$

$$\widetilde{\mathcal{G}}_{xy}^{EJ} = -\frac{1}{2}\sin(2\xi)\,V_i^e + \frac{1}{2}\sin(2\xi)\,V_i^h \tag{C.1c}$$

$$\widetilde{\mathcal{G}}_{yx}^{EJ} = \widetilde{\mathcal{G}}_{xy}^{EJ} \tag{C.1d}$$

$$\widetilde{\mathcal{G}}_{zx}^{EJ} = \cos(\xi)\,\frac{k_\rho}{\omega\varepsilon_0\varepsilon_m}I_i^e \tag{C.1e}$$

$$\widetilde{\mathcal{G}}_{zy}^{EJ} = \sin(\xi)\,\frac{k_\rho}{\omega\varepsilon_0\varepsilon_m} I_i^e \tag{C.1f}$$

$$\widetilde{\mathcal{G}}_{xz}^{EJ} = \cos(\xi)\,\frac{k_\rho}{\omega\varepsilon_0\varepsilon_n} V_v^e \tag{C.1g}$$

$$\widetilde{\mathcal{G}}_{yz}^{EJ} = \sin(\xi)\,\frac{k_\rho}{\omega\varepsilon_0\varepsilon_n} V_v^e \tag{C.1h}$$

$$\widetilde{\mathcal{G}}_{zz}^{EJ} = \frac{1}{j\omega\varepsilon_0\varepsilon_n}\left[\frac{k_\rho^2}{j\omega\varepsilon_0\varepsilon_m} - \delta(z-z')\right] \tag{C.1i}$$

where V_i^p, V_v^p and I_i^p $(p = e, h)$ are the transmission-line Green's functions whose derivation and properties are exposed at annex C.3 and are function of z (the observation point) and z' (the source point). In the above equations, indexes m and n of the constitutive parameters ε and μ pertain to the layers corresponding to observation point z and source point z' respectively. The space-domain DGF $\overline{\boldsymbol{\mathcal{G}}}^{PQ}$ is obtained from $\widetilde{\overline{\boldsymbol{\mathcal{G}}}}^{PQ}$ by applying the following Fourier transform:

$$\overline{\boldsymbol{\mathcal{G}}}^{PQ}(\mathbf{r}, \mathbf{r}') = \mathcal{F}^{-1}\left\{\widetilde{\overline{\boldsymbol{\mathcal{G}}}}^{PQ}(\mathbf{k}_\rho; z, z')\right\}. \tag{C.2}$$

where $\mathbf{r}$ and $\mathbf{r}'$ are respectively the observation and source points in the spatial domain, $\mathbf{k}_\rho = k_x\hat{\mathbf{x}} + k_y\hat{\mathbf{y}}$ is the wavenumber in the spectral domain, and z and z' are respectively the heights of the observation and source points in the spatial or spectral domain. The spectral integrals that arise in (C.2) are given by [27]:

$$\mathcal{F}^{-1}\left\{\begin{matrix}\sin\\ \cos\end{matrix}(n\xi)\,\widetilde{f}(k_\rho)\right\} = (-j)^n \begin{matrix}\sin\\ \cos\end{matrix}(n\varphi)\, S_n\left\{\widetilde{f}(k_\rho)\right\} \tag{C.3}$$

where $S_n\left\{\widetilde{f}(k_\rho)\right\}$ is the Sommerfeld integral of order n of function $\widetilde{f}(k_\rho)$ and is defined by:

$$S_n\left\{\widetilde{f}(k_\rho)\right\} = \frac{1}{2\pi}\int_0^\infty \widetilde{f}(k_\rho)\, J_n(k_\rho\rho)\, k_\rho\, \mathrm{d}k_\rho. \tag{C.4}$$

Here, J_n is the Bessel function of order n and (ρ, φ) are the cylindrical coordinates of the projection of the field point on the (x, y) plane. Those relations are demonstrated in appendix D. Applying these above formulas to $\widetilde{\overline{\boldsymbol{\mathcal{G}}}}^{EJ}$ yields the following terms for the spatial DGF $\overline{\boldsymbol{\mathcal{G}}}^{EJ}$:

$$\mathcal{G}_{xx}^{EJ} = -\frac{1}{2}S_0\{V_i^e + V_i^h\} + \frac{1}{2}\cos(2\varphi)\, S_2\{V_i^e - V_i^h\} \tag{C.5a}$$

$$\mathcal{G}_{yy}^{EJ} = -\frac{1}{2}S_0\{V_i^e + V_i^h\} - \frac{1}{2}\cos(2\varphi)\, S_2\{V_i^e - V_i^h\} \tag{C.5b}$$

$$\mathcal{G}_{xy}^{EJ} = \frac{1}{2}\sin(2\varphi)\, S_2\{V_i^e - V_i^h\} \tag{C.5c}$$

$$\mathcal{G}_{yx}^{EJ} = \mathcal{G}_{xy}^{EJ} \tag{C.5d}$$

$$\mathcal{G}_{zx}^{EJ} = -\frac{j\cos(\varphi)}{\omega\varepsilon_0\varepsilon_m} S_1\{k_\rho I_i^e\} \tag{C.5e}$$

$$\mathcal{G}_{zy}^{EJ} = -\frac{j\sin(\varphi)}{\omega\varepsilon_0\varepsilon_m} S_1\{k_\rho I_i^e\} \tag{C.5f}$$

$$\mathcal{G}_{xz}^{EJ} = -\frac{j\cos(\varphi)}{\omega\varepsilon_0\varepsilon_n} S_1\{k_\rho V_v^e\} \tag{C.5g}$$

$$\mathcal{G}_{yz}^{EJ} = -\frac{j\sin(\varphi)}{\omega\varepsilon_0\varepsilon_n} S_1\{k_\rho V_v^e\} \tag{C.5h}$$

$$\mathcal{G}_{zz}^{EJ} = -\frac{1}{\omega^2\varepsilon_0^2\varepsilon_m\varepsilon_n} S_0\{k_\rho^2 I_v^e\} - \frac{1}{j\omega\varepsilon_0\varepsilon_n}\mathcal{F}^{-1}\{\delta(z-z')\} \tag{C.5i}$$

Similarly, the elements of $\widetilde{\overline{\mathcal{G}}}^{HJ}$ are given by using (29) and (14) of [27]:

$$\widetilde{\mathcal{G}}_{xx}^{HJ} = \frac{1}{2}\sin(2\xi)\left(I_i^e - I_i^h\right) \tag{C.6a}$$

$$\widetilde{\mathcal{G}}_{yy}^{HJ} = -\widetilde{\mathcal{G}}_{xx}^{HJ} \tag{C.6b}$$

$$\widetilde{\mathcal{G}}_{xy}^{HJ} = \frac{1}{2}\left(I_i^e + I_i^h\right) - \frac{1}{2}\cos(2\xi)\left(I_i^e - I_i^h\right) \tag{C.6c}$$

$$\widetilde{\mathcal{G}}_{yx}^{HJ} = -\frac{1}{2}\left(I_i^e + I_i^h\right) - \frac{1}{2}\cos(2\xi)\left(I_i^e - I_i^h\right) \tag{C.6d}$$

$$\widetilde{\mathcal{G}}_{zx}^{HJ} = \sin(\xi)\frac{k_\rho}{\omega\mu_0\mu_m} V_i^h \tag{C.6e}$$

$$\widetilde{\mathcal{G}}_{zy}^{HJ} = -\cos(\xi)\frac{k_\rho}{\omega\mu_0\mu_m} V_i^h \tag{C.6f}$$

$$\widetilde{\mathcal{G}}_{xz}^{HJ} = -\sin(\xi)\frac{k_\rho}{\omega\varepsilon_0\varepsilon_n} I_v^e \tag{C.6g}$$

$$\widetilde{\mathcal{G}}_{yz}^{HJ} = \cos(\xi)\frac{k_\rho}{\omega\varepsilon_0\varepsilon_n} I_v^e \tag{C.6h}$$

$$\widetilde{\mathcal{G}}_{zz}^{HJ} = 0 \tag{C.6i}$$

and the space-domain DGF $\overline{\mathcal{G}}^{HJ}$ is then obtained by making the same transformations as for $\overline{\mathcal{G}}^{EJ}$:

$$\mathcal{G}_{xx}^{HJ} = -\frac{1}{2}\sin(2\varphi)\, S_2\{I_i^e - I_i^h\} \tag{C.7a}$$

$$\mathcal{G}_{yy}^{HJ} = -\mathcal{G}_{xx}^{HJ} \tag{C.7b}$$

$$\mathcal{G}_{xy}^{HJ} = \frac{1}{2}S_0\{I_i^e + I_i^h\} + \frac{1}{2}\cos(2\varphi)\, S_2\{I_i^e - I_i^h\} \tag{C.7c}$$

$$\mathcal{G}_{yx}^{HJ} = -\frac{1}{2}S_0\{I_i^e + I_i^h\} + \frac{1}{2}\cos(2\varphi)\, S_2\{I_i^e - I_i^h\} \tag{C.7d}$$

$$\mathcal{G}_{zx}^{HJ} = -\frac{j\sin(\varphi)}{\omega\mu_0\mu_m} S_1\{k_\rho V_i^h\} \tag{C.7e}$$

$$\mathcal{G}_{zy}^{HJ} = \frac{j\cos(\varphi)}{\omega\mu_0\mu_m} S_1\{k_\rho V_i^h\} \tag{C.7f}$$

$$\mathcal{G}_{xz}^{HJ} = \frac{j\sin(\varphi)}{\omega\varepsilon_0\varepsilon_n} S_1\{k_\rho I_v^e\} \tag{C.7g}$$

$$\mathcal{G}_{yz}^{HJ} = -\frac{j\cos(\varphi)}{\omega\varepsilon_0\varepsilon_n} S_1\{k_\rho I_v^e\} \tag{C.7h}$$

$$\mathcal{G}_{zz}^{HJ} = 0. \tag{C.7i}$$

Expressions for $\overline{\boldsymbol{\mathcal{G}}}^{HM}$ and $\overline{\boldsymbol{\mathcal{G}}}^{EM}$ can be obtained by applying duality to $\overline{\boldsymbol{\mathcal{G}}}^{EJ}$ and $\overline{\boldsymbol{\mathcal{G}}}^{HJ}$ respectively, that is, by making the following replacements: $\varepsilon \to \mu$, $\mu \to \varepsilon$, $V \to I$, $I \to V$, $v \to i$, $i \to v$, $e \to h$ and $h \to e$. This can be summarized by the following formulas:

$$\overline{\boldsymbol{\mathcal{G}}}^{HM} = \overline{\boldsymbol{\mathcal{G}}}^{EJ}_{\mu\to\varepsilon,\varepsilon\to\mu} \tag{C.8a}$$

$$\overline{\boldsymbol{\mathcal{G}}}^{EM} = -\overline{\boldsymbol{\mathcal{G}}}^{HJ}_{\mu\to\varepsilon,\varepsilon\to\mu}. \tag{C.8b}$$

Those relations can also be obtained by applying the Fourier transform to (28)–(31) in [27].

The mixed-potential formulation (5) in [27] allows one to rewrite $\overline{\boldsymbol{\mathcal{G}}}^{EJ}$ as

$$\begin{aligned}\overline{\boldsymbol{\mathcal{G}}}^{EJ} &= -j\omega\mu_0\overline{\boldsymbol{\mathcal{G}}}^{AJ} + \frac{1}{j\omega\varepsilon_0}\nabla\left(C^\Phi\hat{\mathbf{z}} + \nabla' K^\Phi\right) \\ &= -j\omega\overline{\boldsymbol{\mathcal{K}}}^{AJ} + \frac{1}{j\omega\varepsilon_0}\nabla\nabla' K^\Phi\end{aligned} \tag{C.9}$$

where the DGF for the magnetic vector potential is given by

$$\overline{\boldsymbol{\mathcal{K}}}^{AJ} = \mu_0\overline{\boldsymbol{\mathcal{G}}}^{AJ} + \frac{1}{\omega^2\varepsilon_0}\nabla C^\Phi\hat{\mathbf{z}} \tag{C.10}$$

and where the elements of $\overline{\boldsymbol{\mathcal{G}}}^{AJ}$ are given by applying the Fourier transform to the spectral DGF $\widetilde{\overline{\boldsymbol{\mathcal{G}}}}^{AJ}$ given by (41) in [27]:

$$\mathcal{G}_{xx}^{AJ} = \frac{1}{j\omega\mu_0} S_0\{V_i^h\} \tag{C.11a}$$

$$\mathcal{G}_{yy}^{AJ} = \mathcal{G}_{xx}^{AJ} \tag{C.11b}$$

$$\mathcal{G}_{xy}^{AJ} = 0 \tag{C.11c}$$

$$\mathcal{G}_{yx}^{AJ} = 0 \tag{C.11d}$$

$$\mathcal{G}_{zx}^{AJ} = -\mu_m\cos(\varphi)\, S_1\left\{\frac{I_i^h - I_i^e}{k_\rho}\right\} \tag{C.11e}$$

$$\mathcal{G}_{zy}^{AJ} = -\mu_m\sin(\varphi)\, S_1\left\{\frac{I_i^h - I_i^e}{k_\rho}\right\} \tag{C.11f}$$

$$\mathcal{G}_{xz}^{AJ} = 0 \tag{C.11g}$$
$$\mathcal{G}_{yz}^{AJ} = 0 \tag{C.11h}$$
$$\mathcal{G}_{zz}^{AJ} = \frac{\mu_m}{j\omega\varepsilon_0\varepsilon_n} S_0\{I_v^e\}\,. \tag{C.11i}$$

Moreover, since from [27] we have that

$$\widetilde{C}^{\Phi} = \frac{\omega^2\mu_0\varepsilon_0\mu_n}{k_\rho^2}\left(V_v^h - V_v^e\right) \tag{C.12}$$

and noting that $\widetilde{\nabla} = -jk_\rho\hat{\mathbf{u}} + \hat{\mathbf{z}}\frac{d}{dz}$, we can compute that

$$\widetilde{\nabla}\widetilde{C}^{\Phi} = \frac{j\omega^2\mu_0\varepsilon_0\mu_n}{k_\rho}\Bigg[-\left(V_v^h - V_v^e\right)\left(\cos(\xi)\,\hat{\mathbf{x}} + \sin(\xi)\,\hat{\mathbf{y}}\right) + \frac{1}{k_\rho}\left(\frac{k_{zm}^2}{\omega\varepsilon_0\varepsilon_m}I_v^e - \omega^2\mu_0\mu_m I_v^h\right)\hat{\mathbf{z}}\Bigg]. \tag{C.13}$$

Reverting to the spatial domain yields:

$$\mathcal{F}\left\{\widetilde{\nabla}\widetilde{C}^{\Phi}\right\} = j\omega^2\mu_0\varepsilon_0\mu_n\Bigg[S_1\left\{\frac{V_v^h - V_v^e}{k_\rho}\right\}\left(j\cos(\varphi)\,\hat{\mathbf{x}} + j\sin(\varphi)\,\hat{\mathbf{y}}\right) + S_0\left\{\frac{k_{zm}^2}{\omega\varepsilon_0\varepsilon_m k_\rho^2}I_v^e - \frac{\omega\mu_0\mu_m}{k_\rho^2}I_v^h\right\}\hat{\mathbf{z}}\Bigg]. \tag{C.14}$$

Therefore, we can write for $\overline{\boldsymbol{\mathcal{K}}}^{AJ}$ that:

$$\mathcal{K}_{xx}^{AJ} = \frac{1}{j\omega}S_0\{V_i^h\} \tag{C.15a}$$
$$\mathcal{K}_{yy}^{AJ} = \mathcal{K}_{xx}^{AJ} \tag{C.15b}$$
$$\mathcal{K}_{xy}^{AJ} = 0 \tag{C.15c}$$
$$\mathcal{K}_{yx}^{AJ} = 0 \tag{C.15d}$$
$$\mathcal{K}_{zx}^{AJ} = -\mu_0\mu_m\cos(\varphi)\,S_1\left\{\frac{I_i^h - I_i^e}{k_\rho}\right\} \tag{C.15e}$$
$$\mathcal{K}_{zy}^{AJ} = -\mu_0\mu_m\sin(\varphi)\,S_1\left\{\frac{I_i^h - I_i^e}{k_\rho}\right\} \tag{C.15f}$$
$$\mathcal{K}_{xz}^{AJ} = -\mu_0\mu_n\cos(\varphi)\,S_1\left\{\frac{V_v^h - V_v^e}{k_\rho}\right\} \tag{C.15g}$$
$$\mathcal{K}_{yz}^{AJ} = -\mu_0\mu_n\sin(\varphi)\,S_1\left\{\frac{V_v^h - V_v^e}{k_\rho}\right\} \tag{C.15h}$$
$$\mathcal{K}_{zz}^{AJ} = \frac{\mu_0\mu_m}{j\omega\varepsilon_0\varepsilon_n}S_0\{I_v^e\} + j\mu_0\mu_n S_0\left\{\frac{k_{zm}^2}{\omega\varepsilon_0\varepsilon_m k_\rho^2}I_v^e - \frac{\omega\mu_0\mu_m}{k_\rho^2}I_v^h\right\}. \tag{C.15i}$$

For K^{Φ} we have:

$$K^{\Phi} = j\omega\varepsilon_0 S_0 \left\{ \frac{V_i^e - V_i^h}{k_\rho^2} \right\}. \tag{C.16}$$

When testing with $\hat{\mathbf{n}}\times$ RWG basis functions, it is also necessary to have ∇K^{Φ} and $\nabla' K^{\Phi}$. We first write that:

$$\widetilde{\nabla}\widetilde{K}^{\Phi} = \frac{\omega\varepsilon_0}{k_\rho}\left(V_i^e - V_i^h\right)\left(\cos(\xi)\,\hat{\mathbf{x}} + \sin(\xi)\,\hat{\mathbf{y}}\right) - \frac{\omega\varepsilon_0}{k_\rho^2}\left(\omega\mu_0\mu_m I_i^h - \frac{k_{zm}^2}{\omega\varepsilon_0\varepsilon_m} I_i^e\right)\hat{\mathbf{z}} \tag{C.17a}$$

$$\widetilde{\nabla}'\widetilde{K}^{\Phi} = -\frac{\omega\varepsilon_0}{k_\rho}\left(V_i^e - V_i^h\right)\left(\cos(\xi)\,\hat{\mathbf{x}} + \sin(\xi)\,\hat{\mathbf{y}}\right) + \frac{\omega\varepsilon_0}{k_\rho^2}\left(\omega\mu_0\mu_n V_v^h - \frac{k_{zn}^2}{\omega\varepsilon_0\varepsilon_n} V_v^e\right)\hat{\mathbf{z}} \tag{C.17b}$$

both of which become after a Sommerfeld integration

$$\nabla K^{\Phi} = -j\omega\varepsilon_0 S_1 \left\{ \frac{V_i^e - V_i^h}{k_\rho} \right\}\left(\cos(\varphi)\,\hat{\mathbf{x}} + \sin(\varphi)\,\hat{\mathbf{y}}\right) - \omega\varepsilon_0 S_0 \left\{ \frac{\omega\mu_0\mu_m}{k_\rho^2} I_i^h - \frac{k_{zm}^2}{\omega\varepsilon_0\varepsilon_m k_\rho^2} I_i^e \right\}\hat{\mathbf{z}} \tag{C.18a}$$

$$\nabla' K^{\Phi} = j\omega\varepsilon_0 S_1 \left\{ \frac{V_i^e - V_i^h}{k_\rho} \right\}\left(\cos(\varphi)\,\hat{\mathbf{x}} + \sin(\varphi)\,\hat{\mathbf{y}}\right) + \omega\varepsilon_0 S_0 \left\{ \frac{\omega\mu_0\mu_n}{k_\rho^2} V_v^h - \frac{k_{zn}^2}{\omega\varepsilon_0\varepsilon_n k_\rho^2} V_v^e \right\}\hat{\mathbf{z}}. \tag{C.18b}$$

Expressions for the electric vector potential $\overline{\boldsymbol{\mathcal{K}}}^{FM}$ and scalar potential K^{Ψ} are again obtained by duality applied to $\overline{\boldsymbol{\mathcal{K}}}^{AJ}$ and K^{Φ} respectively.

C.2 Decomposition of the DGFs in direct and reflexion terms

Whenever the source point $\mathbf{r}'$ approaches the observation point $\mathbf{r}$, all the spatial domain DGFs and scalar Green's functions for multilayered media become singular. This is due to the presence of a *direct term* in the transmission-line Green's functions, which, after the Fourier transformation aiming at reverting to the spatial domain, correspond in fact to the *homogeneous space Green's*

function. Indeed, the spatial domain homogeneous space Green's function is given by the following Sommerfeld identity [46]:

$$S_0\left\{\frac{e^{-jk_{zm}|z-z'|}}{2jk_{zm}}\right\} = \frac{e^{-jk_m|\mathbf{r}-\mathbf{r}'|}}{4\pi\,|\mathbf{r}-\mathbf{r}'|} \tag{C.19}$$

where $k_{zm} = \sqrt{k_m^2 - k_\rho^2}$, with $k_m = \omega\sqrt{\varepsilon_0\varepsilon_m\mu_0\mu_m}$, and with the square root branch of k_{zm} specified by the condition that $-\pi < \arg\{k_{zm}\} \leq 0$. This direct term is present in the TLGFs V_i^h and its dual form I_v^e. Note that this direct term appears only when z and z' are located within the same layer m.

Taking a look at the explicit expression (C.11) given for $\overline{\boldsymbol{\mathcal{G}}}^{AJ}$ immediately shows that both $\mathcal{G}_{xx}^{AJ}$ and $\mathcal{G}_{yy}^{AJ}$ have that direct term, since they both involve V_i^h. Indeed, using (62) and (18) of [27], and identity (C.19) yields the following expression for spatial components $\mathcal{G}_{xx}^{AJ}$ and $\mathcal{G}_{yy}^{AJ}$:

$$\mathcal{G}_{xx}^{AJ} = \mathcal{G}_{yy}^{AJ} = \mu_m\frac{e^{-jk_m|\mathbf{r}-\mathbf{r}'|}}{4\pi\,|\mathbf{r}-\mathbf{r}'|} + \frac{1}{j\omega\mu_0}S_0\left\{V_i^{h,(\mathrm{ml})}\right\} \tag{C.20}$$

where $V_i^{h,(\mathrm{ml})}$ is the part of V_i^h that correspond to the partial reflections occuring at the boundaries of layer m. Likely, it is straightforward to show that

$$\mathcal{G}_{zz}^{AJ} = \mu_m\frac{e^{-jk_m|\mathbf{r}-\mathbf{r}'|}}{4\pi\,|\mathbf{r}-\mathbf{r}'|} + \frac{\mu_m}{j\omega\varepsilon_0\varepsilon_m}S_0\left\{I_v^{e,(\mathrm{ml})}\right\}. \tag{C.21}$$

We again stress on the fact that these relations hold only if $m = n$. It is also important to note that, while both I_i^h and I_i^e yield the same singularities in the spatial domain after a Sommerfeld transformation, those singularities cancel out in $\mathcal{G}_{zx}^{AJ}$ and $\mathcal{G}_{zy}^{AJ}$ due to the subtraction of I_i^h and I_i^e. Therefore, we can rewrite $\overline{\boldsymbol{\mathcal{G}}}^{AJ}$ as the sum of a homogeneous space DGF, which represents the direct contribution of the source to the field, and of a DGF that represents the partial reflections at the interfaces that bound layer m:

$$\overline{\boldsymbol{\mathcal{G}}}^{AJ} = \mu_m G_m\overline{\boldsymbol{\mathcal{I}}} + \overline{\boldsymbol{\mathcal{G}}}^{AJ,(\mathrm{ml})} \tag{C.22}$$

where $\overline{\boldsymbol{\mathcal{I}}} = \hat{\mathbf{x}}\hat{\mathbf{x}} + \hat{\mathbf{y}}\hat{\mathbf{y}} + \hat{\mathbf{z}}\hat{\mathbf{z}}$, which is the unit dyadic, and where $G_m = \frac{e^{-jk_m|\mathbf{r}-\mathbf{r}'|}}{4\pi|\mathbf{r}-\mathbf{r}'|}$.

The above equation has very important practical implications. For example, from (39) in [27], we can rewrite $\overline{\boldsymbol{\mathcal{G}}}^{HJ}$ as:

$$\begin{aligned}\overline{\boldsymbol{\mathcal{G}}}^{HJ} &= \frac{1}{\mu_m}\nabla\times\overline{\boldsymbol{\mathcal{G}}}^{AJ}\\ &= \nabla G_m\times\overline{\boldsymbol{\mathcal{I}}} + \frac{1}{\mu_m}\nabla\times\overline{\boldsymbol{\mathcal{G}}}^{AJ,(\mathrm{ml})}\\ &= \nabla G_m\times\overline{\boldsymbol{\mathcal{I}}} + \overline{\boldsymbol{\mathcal{G}}}^{HJ,(\mathrm{ml})}\end{aligned} \tag{C.23}$$

where $\overline{\boldsymbol{\mathcal{G}}}^{HJ,(\mathrm{ml})}$ is given by (C.7), in which the direct contributions of the TLGFs have been extracted. Practically, when using $\overline{\boldsymbol{\mathcal{G}}}^{HJ}$ in a MoM code, we can treat separately its direct contribution, which presents singularities when $\mathbf{r} = \mathbf{r}'$, and its contribution due to partial reflections, which is not singular unless $\mathbf{r} = \mathbf{r}'$ on an interface (this case is not considered in this work). Applying the same reasoning to $\overline{\boldsymbol{\mathcal{K}}}^{AJ}$ allows us to write:

$$\overline{\boldsymbol{\mathcal{K}}}^{AJ} = \mu_0\mu_m G_m \overline{\boldsymbol{\mathcal{I}}} + \overline{\boldsymbol{\mathcal{K}}}^{AJ,(\mathrm{ml})}. \tag{C.24}$$

Note that $\nabla C^{\Phi}\hat{\mathbf{z}}$, which contributes to $\overline{\boldsymbol{\mathcal{K}}}^{AJ}$, has direct terms that cancel out by subtraction.

Finally, the same separation can be done for K^{Φ}. We have, after separating the direct and reflection terms in the TLGFs, that

$$\begin{aligned} K^{\Phi} &= \frac{1}{\varepsilon_m} G_m + j\omega\varepsilon_0 S_0 \left\{ \frac{V_i^{e,(\mathrm{ml})} - V_i^{h,(\mathrm{ml})}}{k_\rho^2} \right\} \\ &= \frac{1}{\varepsilon_m} G_m + K^{\Phi,(\mathrm{ml})}. \end{aligned} \tag{C.25}$$

C.3 Transmission-line Green's functions

C.3.1 $V_i(z|z')\,, \quad m = n$

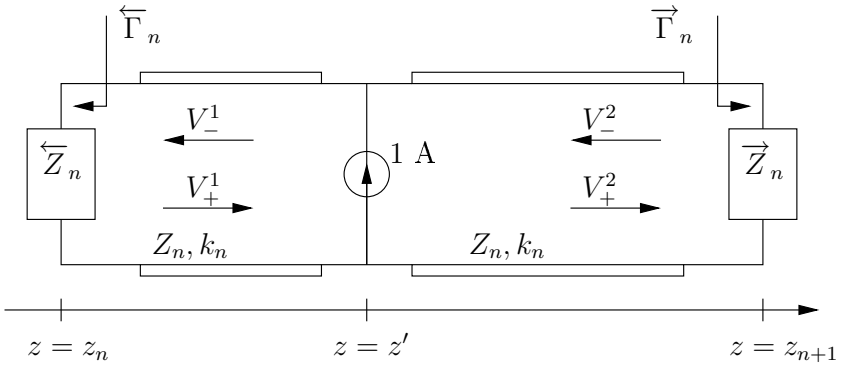

Figure C.1: Transmission-line problem.

For Fig. C.1 we have :

$$V^i(z) = V_+^i\, e^{-jk_n z} + V_-^i\, e^{jk_n z} \tag{C.26a}$$

$$I^i(z) = Y_n \left(V_+^i\, e^{-jk_n z} - V_-^i\, e^{jk_n z} \right) \tag{C.26b}$$

where

$$\begin{cases} i = 1 & z < z' \\ i = 2 & z > z'. \end{cases}$$

Before going any further, we must define $\overleftarrow{\Gamma}_n$ and $\overrightarrow{\Gamma}_n$:

$$\begin{cases} \overleftarrow{\Gamma}_n \triangleq \frac{\text{outgoing wave}}{\text{ingoing wave}} = \frac{V_+^1}{V_-^1}\, e^{-2jk_n z_n}, & \overleftarrow{\Gamma}_n(z) = \frac{V_+^1}{V_-^1}\, e^{-2jk_n z} = \overleftarrow{\Gamma}_n\, e^{-2jk_n(z-z_n)} \\ \overrightarrow{\Gamma}_n \triangleq \frac{V_-^2}{V_+^2}\, e^{2jk_n z_{n+1}}, & \overrightarrow{\Gamma}_n(z) = \frac{V_-^2}{V_+^2}\, e^{2jk_n z} = \overrightarrow{\Gamma}_n\, e^{2jk_n(z-z_{n+1})}. \end{cases} \tag{C.27}$$

We have four boundary conditions which allow us to find the expressions for the coefficients : a condition from the continuity of voltage across the abscissa $z = z'$, a condition from the continuity of current, one for $z = z_n$, one for $z = z_{n+1}$ (equation C.27). These four conditions are listed below :

$$V_+^1\, e^{-jk_n z'} + V_-^1\, e^{jk_n z'} = V_+^2\, e^{-jk_n z'} + V_-^2\, e^{jk_n z'} \tag{C.28}$$

$$1 + Y_n \left(V_+^1\, e^{-jk_n z'} - V_-^1\, e^{jk_n z'} \right) = Y_n \left(V_+^2\, e^{-jk_n z'} - V_-^2\, e^{jk_n z'} \right) \tag{C.29}$$

$$\frac{V_+^1}{V_-^1}\, e^{-2jk_n z_n} = \overleftarrow{\Gamma}_n \tag{C.30}$$

$$\frac{V_-^2}{V_+^2}\, e^{2jk_n z_{n+1}} = \overrightarrow{\Gamma}_n. \tag{C.31}$$

From (C.28), (C.30) and (C.31) we have that

$$V_+^1\, e^{-jk_n z'} + \frac{V_+^1}{\overleftarrow{\Gamma}_n}\, e^{jk_n z'}\, e^{-2jk_n z_n} = V_+^2\, e^{-jk_n z'} + V_+^2 \overrightarrow{\Gamma}_n\, e^{-2jk_n z_{n+1}}\, e^{jk_n z'} \tag{C.32}$$

and from (C.29), (C.30) and (C.31) we have

$$Z_n + V_+^1\, e^{-jk_n z'} - \frac{V_+^1}{\overleftarrow{\Gamma}_n}\, e^{jk_n z'}\, e^{-2jk_n z_n} = V_+^2\, e^{-jk_n z'} - V_+^2 \overrightarrow{\Gamma}_n\, e^{-2jk_n z_{n+1}}\, e^{jk_n z'}. \tag{C.33}$$

The two last equations form a linear system of two equations with two unknowns V_+^1 and V_+^2. In a matrix form, we have

$$\begin{bmatrix} e^{-jk_n z'} + \frac{e^{-2jk_n z_n}}{\overleftarrow{\Gamma}_n}\, e^{jk_n z'} & -\left(e^{-jk_n z'} + \overrightarrow{\Gamma}_n\, e^{-2jk_n z_{n+1}}\, e^{jk_n z'} \right) \\ e^{-jk_n z'} - \frac{e^{-2jk_n z_n}}{\overleftarrow{\Gamma}_n}\, e^{jk_n z'} & -\left(e^{-jk_n z'} - \overrightarrow{\Gamma}_n\, e^{-2jk_n z_{n+1}}\, e^{jk_n z'} \right) \end{bmatrix} \begin{bmatrix} V_+^1 \\ V_+^2 \end{bmatrix}$$

$$= \begin{bmatrix} 0 \\ \\ -Z_n \end{bmatrix}. \quad \text{(C.34)}$$

In order to find V_+^1 and V_+^2, we have to invert the matrix in the above equation. The determinant of the square matrix in (C.34) is

$$\begin{aligned}
&- \left(e^{-jk_n z'} + \frac{e^{-2jk_n z_n}}{\overleftarrow{\Gamma}_n}\, e^{jk_n z'} \right) \left(e^{-jk_n z'} - \overrightarrow{\Gamma}_n\, e^{-2jk_n z_{n+1}}\, e^{jk_n z'} \right) \\
&+ \left(e^{-jk_n z'} - \frac{e^{-2jk_n z_n}}{\overleftarrow{\Gamma}_n}\, e^{jk_n z'} \right) \left(e^{-jk_n z'} + \overrightarrow{\Gamma}_n\, e^{-2jk_n z_{n+1}}\, e^{jk_n z'} \right) \\
&= -e^{-2jk_n z'} + \overrightarrow{\Gamma}_n\, e^{-2jk_n z_{n+1}} - \frac{e^{-2jk_n z_n}}{\overleftarrow{\Gamma}_n} + \frac{\overrightarrow{\Gamma}_n}{\overleftarrow{\Gamma}_n}\, e^{-2jk_n (z_n + z_{n+1})}\, e^{2jk_n z'} \\
&\quad + e^{-2jk_n z'} + \overrightarrow{\Gamma}_n\, e^{-2jk_n z_{n+1}} - \frac{e^{-2jk_n z_n}}{\overleftarrow{\Gamma}_n} - \frac{\overrightarrow{\Gamma}_n}{\overleftarrow{\Gamma}_n}\, e^{-2jk_n (z_n + z_{n+1})}\, e^{2jk_n z'} \\
&= 2\overrightarrow{\Gamma}_n\, e^{-2jk_n z_{n+1}} - 2\frac{e^{-2jk_n z_n}}{\overleftarrow{\Gamma}_n} \\
&= 2\frac{e^{-2jk_n z_n}}{\overleftarrow{\Gamma}_n} \left(\overleftarrow{\Gamma}_n \overrightarrow{\Gamma}_n\, e^{-2jk_n (z_{n+1} - z_n)} - 1 \right) \\
&= 2\frac{e^{-2jk_n z_n}}{\overleftarrow{\Gamma}_n} \left(\overleftarrow{\Gamma}_n \overrightarrow{\Gamma}_n\, e^{-2jk_n d_n} - 1 \right)
\end{aligned}$$

The inverse of the matrix in (C.34) is then given by:

$$\frac{\overleftarrow{\Gamma}_n\, e^{2jk_n z_n}}{2\left(\overleftarrow{\Gamma}_n \overrightarrow{\Gamma}_n\, e^{-2jk_n d_n} - 1 \right)} \begin{bmatrix} -\left(e^{-jk_n z'} - \overrightarrow{\Gamma}_n\, e^{-2jk_n z_{n+1}}\, e^{jk_n z'} \right) & e^{-jk_n z'} + \overrightarrow{\Gamma}_n\, e^{-2jk_n z_{n+1}}\, e^{jk_n z'} \\ \\ -\left(e^{-jk_n z'} - \frac{e^{-2jk_n z_n}}{\overleftarrow{\Gamma}_n}\, e^{jk_n z'} \right) & e^{-jk_n z'} + \frac{e^{-2jk_n z_n}}{\overleftarrow{\Gamma}_n}\, e^{jk_n z'} \end{bmatrix}. \quad \text{(C.35)}$$

Multiplying this equation with the left and right-hand side of (C.34) gives us:

$$V_+^1 = -Z_n \frac{\overleftarrow{\Gamma}_n\, e^{2jk_n z_n}\, e^{-jk_n z'} + \overleftarrow{\Gamma}_n \overrightarrow{\Gamma}_n\, e^{-2jk_n d_n}\, e^{jk_n z'}}{2\left(\overleftarrow{\Gamma}_n \overrightarrow{\Gamma}_n\, e^{-2jk_n d_n} - 1 \right)} \quad \text{(C.36)}$$

$$V_+^2 = -Z_n \frac{\overleftarrow{\Gamma}_n\, e^{2jk_n z_n}\, e^{-jk_n z'} + e^{jk_n z'}}{2\left(\overleftarrow{\Gamma}_n \overrightarrow{\Gamma}_n\, e^{-2jk_n d_n} - 1\right)}. \tag{C.37}$$

It is then easy to find

$$V_-^1 = \frac{V_+^1\, e^{-2jk_n z_n}}{\overleftarrow{\Gamma}_n} = -Z_n \frac{e^{-jk_n z'} + \overrightarrow{\Gamma}_n\, e^{-2jk_n z_{n+1}}\, e^{jk_n z'}}{2\left(\overleftarrow{\Gamma}_n \overrightarrow{\Gamma}_n\, e^{-2jk_n d_n} - 1\right)} \tag{C.38}$$

$$V_-^2 = V_+^2 \overrightarrow{\Gamma}_n\, e^{-2jk_n z_{n+1}} = -Z_n \frac{\overleftarrow{\Gamma}_n \overrightarrow{\Gamma}_n\, e^{-2jk_n d_n}\, e^{-jk_n z'} + \overrightarrow{\Gamma}_n\, e^{-2jk_n z_{n+1}}\, e^{jk_n z'}}{2\left(\overleftarrow{\Gamma}_n \overrightarrow{\Gamma}_n\, e^{-2jk_n d_n} - 1\right)} \tag{C.39}$$

As it is written in equation (C.26), we have two regions to consider.

$\boxed{z_n < z < z'}$

$$\begin{aligned}
V^1(z) &= V_+^1\, e^{-jk_n z} + V_-^1\, e^{jk_n z} \\
&= -Z_n \frac{\overleftarrow{\Gamma}_n\, e^{2jk_n z_n}\, e^{-jk_n z'}\, e^{-jk_n z} + \overleftarrow{\Gamma}_n \overrightarrow{\Gamma}_n\, e^{-2jk_n d_n}\, e^{jk_n z'}\, e^{-jk_n z}}{2\left(\overleftarrow{\Gamma}_n \overrightarrow{\Gamma}_n\, e^{-2jk_n d_n} - 1\right)} \\
&\quad - Z_n \frac{e^{-jk_n z'}\, e^{jk_n z} + \overrightarrow{\Gamma}_n\, e^{-2jk_n z_{n+1}}\, e^{jk_n z'}\, e^{jk_n z}}{2\left(\overleftarrow{\Gamma}_n \overrightarrow{\Gamma}_n\, e^{-2jk_n d_n} - 1\right)} \\
&= \frac{Z_n}{2\left(1 - \overleftarrow{\Gamma}_n \overrightarrow{\Gamma}_n\, e^{-2jk_n d_n}\right)} \\
&\quad \Big[\overleftarrow{\Gamma}_n\, e^{2jk_n z_n}\, e^{-jk_n\left(z'+z\right)} + \overrightarrow{\Gamma}_n\, e^{-2jk_n z_{n+1}}\, e^{jk_n\left(z'+z\right)} \\
&\quad + e^{jk_n\left(z-z'\right)} + \overleftarrow{\Gamma}_n \overrightarrow{\Gamma}_n\, e^{-2jk_n d_n}\, e^{-jk_n\left(z-z'\right)} \\
&\quad - \overleftarrow{\Gamma}_n \overrightarrow{\Gamma}_n\, e^{-2jk_n d_n}\, e^{jk_n\left(z-z'\right)} + \overleftarrow{\Gamma}_n \overrightarrow{\Gamma}_n\, e^{-2jk_n d_n}\, e^{jk_n\left(z-z'\right)}\Big]
\end{aligned} \tag{C.40}$$

So we have for $V^1(z)$:

$$\begin{aligned}
V^1(z) = \frac{Z_n}{2} \Bigg[& e^{jk_n\left(z-z'\right)} + \frac{1}{\left(1 - \overleftarrow{\Gamma}_n \overrightarrow{\Gamma}_n\, e^{-2jk_n d_n}\right)} \\
& \Big[\overleftarrow{\Gamma}_n\, e^{2jk_n z_n}\, e^{-jk_n\left(z'+z\right)} + \overrightarrow{\Gamma}_n\, e^{-2jk_n z_{n+1}}\, e^{jk_n\left(z'+z\right)} \\
& + \overleftarrow{\Gamma}_n \overrightarrow{\Gamma}_n\, e^{-2jk_n d_n}\, e^{-jk_n\left(z-z'\right)} + \overleftarrow{\Gamma}_n \overrightarrow{\Gamma}_n\, e^{-2jk_n d_n}\, e^{jk_n\left(z-z'\right)}\Big]
\end{aligned} \tag{C.41}$$

$\boxed{z' < z < z_{n+1}}$

$$
\begin{aligned}
V^2(z) &= V_+^2\, e^{-jk_n z} + V_-^2\, e^{jk_n z} \\
&= \frac{Z_n}{2\left(1 - \overleftarrow{\Gamma}_n \overrightarrow{\Gamma}_n\, e^{-2jk_n d_n}\right)} \Big[\overleftarrow{\Gamma}_n\, e^{2jk_n z_n}\, e^{-jk_n\left(z'+z\right)} + e^{-jk_n\left(z-z'\right)} \\
&\quad + \overleftarrow{\Gamma}_n \overrightarrow{\Gamma}_n\, e^{-2jk_n d_n}\, e^{jk_n\left(z-z'\right)} + \overrightarrow{\Gamma}_n\, e^{-2jk_n z_{n+1}}\, e^{jk_n\left(z'+z\right)} \\
&\quad - \overleftarrow{\Gamma}_n \overrightarrow{\Gamma}_n\, e^{-2jk_n d_n} e^{-jk_n\left(z-z'\right)} + \overleftarrow{\Gamma}_n \overrightarrow{\Gamma}_n\, e^{-2jk_n d_n} e^{-jk_n\left(z-z'\right)}\Big] \\
&= \frac{Z_n}{2}\left[e^{-jk_n\left(z-z'\right)} + \frac{1}{\left(1 - \overleftarrow{\Gamma}_n \overrightarrow{\Gamma}_n\, e^{-2jk_n d_n}\right)}\right. \\
&\quad \Big[\overleftarrow{\Gamma}_n\, e^{2jk_n z_n}\, e^{-jk_n\left(z'+z\right)} + \overrightarrow{\Gamma}_n\, e^{-2jk_n z_{n+1}}\, e^{jk_n\left(z'+z\right)} \\
&\quad + \overleftarrow{\Gamma}_n \overrightarrow{\Gamma}_n\, e^{-2jk_n d_n}\, e^{-jk_n\left(z-z'\right)} + \overleftarrow{\Gamma}_n \overrightarrow{\Gamma}_n\, e^{-2jk_n d_n}\, e^{jk_n\left(z-z'\right)}\Big]
\end{aligned}
\tag{C.42}
$$

Finally, by merging the expressions for $V^1(z)$ and $V^2(z)$, we obtain Michalski's expression :

$$
\begin{aligned}
V_i(z|z') = \frac{Z_n}{2}&\left[e^{-jk_n|z-z'|} + \frac{1}{\left(1 - \overleftarrow{\Gamma}_n \overrightarrow{\Gamma}_n\, e^{-2jk_n d_n}\right)}\right. \\
&\Big[\overleftarrow{\Gamma}_n\, e^{2jk_n z_n}\, e^{-jk_n\left(z'+z\right)} + \overrightarrow{\Gamma}_n\, e^{-2jk_n z_{n+1}}\, e^{jk_n\left(z'+z\right)} \\
&+ \overleftarrow{\Gamma}_n \overrightarrow{\Gamma}_n\, e^{-2jk_n d_n}\, e^{-jk_n\left(z-z'\right)} + \overleftarrow{\Gamma}_n \overrightarrow{\Gamma}_n\, e^{-2jk_n d_n}\, e^{jk_n\left(z-z'\right)}\Big]
\end{aligned}
\tag{C.43}
$$

where the first term on the right-hand side of the equation is the direct term, and the others result from the partial reflections at the layer boundaries [27].

C.3.2 $I_i(z|z')\,, \quad m = n$

From equations (C.26), (C.36)-(C.39) we can express the current in the two regions

$\boxed{z_n < z < z'}$

$$
\begin{aligned}
I^1(z) &= Y_n \left(V_+^1 \, e^{-jk_n z} - V_-^1 \, e^{jk_n z} \right) \\
&= -\frac{\overleftarrow{\Gamma}_n \, e^{2jk_n z_n} \, e^{-jk_n z'} \, e^{-jk_n z} + \overleftarrow{\Gamma}_n \overrightarrow{\Gamma}_n \, e^{-2jk_n d_n} \, e^{jk_n z'} \, e^{-jk_n z}}{2\left(\overleftarrow{\Gamma}_n \overrightarrow{\Gamma}_n \, e^{-2jk_n d_n} - 1 \right)} \\
&\quad + \frac{e^{-jk_n z'} \, e^{jk_n z} + \overrightarrow{\Gamma}_n \, e^{-2jk_n z_{n+1}} \, e^{jk_n z'} \, e^{jk_n z}}{2\left(\overleftarrow{\Gamma}_n \overrightarrow{\Gamma}_n \, e^{-2jk_n d_n} - 1 \right)} \\
&= \frac{1}{2\left(1 - \overleftarrow{\Gamma}_n \overrightarrow{\Gamma}_n \, e^{-2jk_n d_n} \right)} \\
&\quad \Big[\overleftarrow{\Gamma}_n \, e^{2jk_n z_n} \, e^{-jk_n \left(z' + z \right)} - \overrightarrow{\Gamma}_n \, e^{-2jk_n z_{n+1}} \, e^{jk_n \left(z' + z \right)} \\
&\quad - e^{jk_n \left(z - z' \right)} + \overleftarrow{\Gamma}_n \overrightarrow{\Gamma}_n \, e^{-2jk_n d_n} \, e^{-jk_n \left(z - z' \right)} \\
&\quad - \overleftarrow{\Gamma}_n \overrightarrow{\Gamma}_n \, e^{-2jk_n d_n} \, e^{jk_n \left(z - z' \right)} + \overleftarrow{\Gamma}_n \overrightarrow{\Gamma}_n \, e^{-2jk_n d_n} \, e^{jk_n \left(z - z' \right)} \Big]
\end{aligned}
\tag{C.44}
$$

So we have for $I^1(z)$:

$$
\begin{aligned}
I^1(z) &= \frac{1}{2} \Bigg[-e^{jk_n \left(z - z' \right)} + \frac{1}{\left(1 - \overleftarrow{\Gamma}_n \overrightarrow{\Gamma}_n \, e^{-2jk_n d_n} \right)} \\
&\quad \Big[\overleftarrow{\Gamma}_n \, e^{2jk_n z_n} \, e^{-jk_n \left(z' + z \right)} - \overrightarrow{\Gamma}_n \, e^{-2jk_n z_{n+1}} \, e^{jk_n \left(z' + z \right)} \\
&\quad + \overleftarrow{\Gamma}_n \overrightarrow{\Gamma}_n \, e^{-2jk_n d_n} \, e^{-jk_n \left(z - z' \right)} - \overleftarrow{\Gamma}_n \overrightarrow{\Gamma}_n \, e^{-2jk_n d_n} \, e^{jk_n \left(z - z' \right)} \Big]
\end{aligned}
\tag{C.45}
$$

$\boxed{z' < z < z_{n+1}}$

$$
\begin{aligned}
I^2(z) &= Y_n \left(V_+^2 \, e^{-jk_n z} - V_-^2 \, e^{jk_n z} \right) \\
&= \frac{1}{2\left(1 - \overleftarrow{\Gamma}_n \overrightarrow{\Gamma}_n \, e^{-2jk_n d_n} \right)} \Big[\overleftarrow{\Gamma}_n \, e^{2jk_n z_n} \, e^{-jk_n \left(z' + z \right)} + e^{-jk_n \left(z - z' \right)} \\
&\quad - \overleftarrow{\Gamma}_n \overrightarrow{\Gamma}_n \, e^{-2jk_n d_n} \, e^{jk_n \left(z - z' \right)} - \overrightarrow{\Gamma}_n \, e^{-2jk_n z_{n+1}} \, e^{jk_n \left(z' + z \right)} \\
&\quad - \overleftarrow{\Gamma}_n \overrightarrow{\Gamma}_n \, e^{-2jk_n d_n} \, e^{-jk_n \left(z - z' \right)} + \overleftarrow{\Gamma}_n \overrightarrow{\Gamma}_n \, e^{-2jk_n d_n} \, e^{-jk_n \left(z - z' \right)} \Big] \\
&= \frac{1}{2} \Bigg[e^{-jk_n \left(z - z' \right)} + \frac{1}{\left(1 - \overleftarrow{\Gamma}_n \overrightarrow{\Gamma}_n \, e^{-2jk_n d_n} \right)} \\
&\quad \Big[\overleftarrow{\Gamma}_n \, e^{2jk_n z_n} \, e^{-jk_n \left(z' + z \right)} - \overrightarrow{\Gamma}_n \, e^{-2jk_n z_{n+1}} \, e^{jk_n \left(z' + z \right)} \\
&\quad + \overleftarrow{\Gamma}_n \overrightarrow{\Gamma}_n \, e^{-2jk_n d_n} \, e^{-jk_n \left(z - z' \right)} - \overleftarrow{\Gamma}_n \overrightarrow{\Gamma}_n \, e^{-2jk_n d_n} \, e^{jk_n \left(z - z' \right)} \Big]
\end{aligned}
\tag{C.46}
$$

By merging the two expressions we obtain :

$$I_i(z|z') = \frac{1}{2}\left[\pm e^{-jk_n|z-z'|} + \frac{1}{\left(1-\overleftarrow{\Gamma}_n\overrightarrow{\Gamma}_n\, e^{-2jk_nd_n}\right)}\right.$$
$$\left[\overleftarrow{\Gamma}_n\, e^{2jk_nz_n}\, e^{-jk_n(z'+z)} - \overrightarrow{\Gamma}_n\, e^{-2jk_nz_{n+1}}\, e^{jk_n(z'+z)}\right.$$
$$\left.\left.+\overleftarrow{\Gamma}_n\overrightarrow{\Gamma}_n\, e^{-2jk_nd_n}\, e^{-jk_n(z-z')} - \overleftarrow{\Gamma}_n\overrightarrow{\Gamma}_n\, e^{-2jk_nd_n}\, e^{jk_n(z-z')}\right]\right. \quad z\underset{<}{\overset{>}{}}z'. \tag{C.47}$$

C.3.3 $V_v(z|z')\,, \quad m = n$

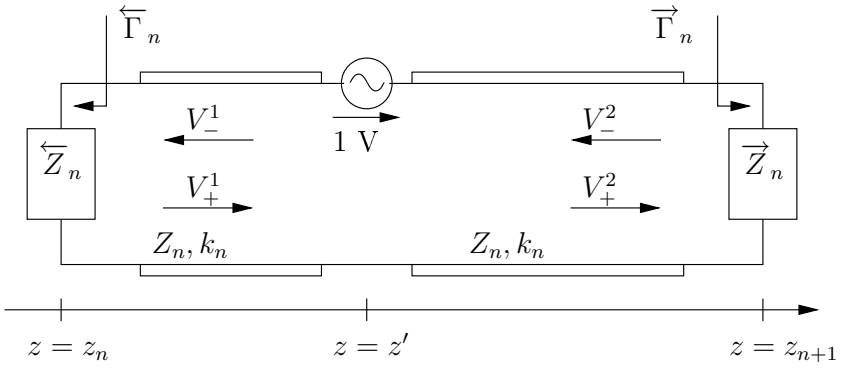

Figure C.2: Transmission-line problem.

The equations (C.26) and definitions (C.27) remain the same; only the boundary conditions (C.28) and (C.29) change into :

$$1 + V_+^1\, e^{-jk_nz'} + V_-^1\, e^{jk_nz'} = V_+^2\, e^{-jk_nz'} + V_-^2\, e^{jk_nz'} \tag{C.48}$$
$$Y_n\left(V_+^1\, e^{-jk_nz'} - V_-^1\, e^{jk_nz'}\right) = Y_n\left(V_+^2\, e^{-jk_nz'} - V_-^2\, e^{jk_nz'}\right) \tag{C.49}$$

which become, with the help of (C.30) and (C.31)

$$1 + V_+^1\, e^{-jk_nz'} + \frac{V_+^1}{\overleftarrow{\Gamma}_n}\, e^{jk_nz'}\, e^{-2jk_nz_n} = V_+^2\, e^{-jk_nz'} + V_+^2\,\overrightarrow{\Gamma}_n\, e^{-2jk_nz_{n+1}}\, e^{jk_nz'} \tag{C.50}$$

$$V_+^1\, e^{-jk_nz'} - \frac{V_+^1}{\overleftarrow{\Gamma}_n}\, e^{jk_nz'}\, e^{-2jk_nz_n} = V_+^2\, e^{-jk_nz'} - V_+^2\,\overrightarrow{\Gamma}_n\, e^{-2jk_nz_{n+1}}\, e^{jk_nz'}. \tag{C.51}$$

In matrix form it gives

$$e^{-jk_n z'}\begin{bmatrix} 1+\frac{e^{-2jk_n z_n}}{\overleftarrow{\Gamma}_n}\,e^{2jk_n z'} & -\left(1+\overrightarrow{\Gamma}_n\,e^{-2jk_n z_{n+1}}\,e^{2jk_n z'}\right) \\ 1-\frac{e^{-2jk_n z_n}}{\overleftarrow{\Gamma}_n}\,e^{2jk_n z'} & -\left(1-\overrightarrow{\Gamma}_n\,e^{-2jk_n z_{n+1}}\,e^{2jk_n z'}\right) \end{bmatrix}\begin{bmatrix} V_+^1 \\ V_+^2 \end{bmatrix} = \begin{bmatrix} -1 \\ 0 \end{bmatrix} \tag{C.52}$$

The coefficients matrix is the same as in equation (C.34), and has already been inverted in equation (C.35). We obtain

$$V_+^1 = \frac{\overleftarrow{\Gamma}_n\,e^{2jk_n z_n}\,e^{-jk_n z'} - \overleftarrow{\Gamma}_n\overrightarrow{\Gamma}_n\,e^{-2jk_n d_n}\,e^{jk_n z'}}{2\left(\overleftarrow{\Gamma}_n\overrightarrow{\Gamma}_n\,e^{-2jk_n d_n}-1\right)} \tag{C.53}$$

$$V_+^2 = \frac{\overleftarrow{\Gamma}_n\,e^{2jk_n z_n}\,e^{-jk_n z'} - e^{jk_n z'}}{2\left(\overleftarrow{\Gamma}_n\overrightarrow{\Gamma}_n\,e^{-2jk_n d_n}-1\right)}. \tag{C.54}$$

It is then easy to find

$$V_-^1 = \frac{V_+^1\,e^{-2jk_n z_n}}{\overleftarrow{\Gamma}_n} = \frac{e^{-jk_n z'} - \overrightarrow{\Gamma}_n\,e^{-2jk_n z_{n+1}}\,e^{jk_n z'}}{2\left(\overleftarrow{\Gamma}_n\overrightarrow{\Gamma}_n\,e^{-2jk_n d_n}-1\right)} \tag{C.55}$$

$$V_-^2 = V_+^2\overrightarrow{\Gamma}_n\,e^{-2jk_n z_{n+1}} = \frac{\overleftarrow{\Gamma}_n\overrightarrow{\Gamma}_n\,e^{-2jk_n d_n}\,e^{-jk_n z'} - \overrightarrow{\Gamma}_n\,e^{-2jk_n z_{n+1}}\,e^{jk_n z'}}{2\left(\overleftarrow{\Gamma}_n\overrightarrow{\Gamma}_n\,e^{-2jk_n d_n}-1\right)} \tag{C.56}$$

From (C.26) and (C.53)–(C.56) we can express the voltage in the two regions:

$\boxed{z_n < z < z'}$

$$
\begin{aligned}
V_v^1(z) &= V_+^1\, e^{-jk_n z} + V_-^1\, e^{jk_n z} \\
&= \frac{\overleftarrow{\Gamma}_n\, e^{2jk_n z_n}\, e^{-jk_n(z'+z)} - \overleftarrow{\Gamma}_n \overrightarrow{\Gamma}_n\, e^{-2jk_n d_n}\, e^{jk_n(z'-z)}}{-2D_n} \\
&\quad + \frac{e^{-jk_n(z'-z)} - \overrightarrow{\Gamma}_n\, e^{-2jk_n z_{n+1}}\, e^{jk_n(z'+z)}}{-2D_n} \\
&= -\frac{1}{2D_n}\Big[\overleftarrow{\Gamma}_n\, e^{2jk_n z_n}\, e^{-jk_n(z'+z)} - \overrightarrow{\Gamma}_n\, e^{-2jk_n z_{n+1}}\, e^{jk_n(z'+z)} \\
&\quad + e^{-jk_n(z'-z)} - \overleftarrow{\Gamma}_n \overrightarrow{\Gamma}_n\, e^{-2jk_n d_n}\, e^{jk_n(z'-z)} \\
&\quad - \overleftarrow{\Gamma}_n \overrightarrow{\Gamma}_n\, e^{-2jk_n d_n}\, e^{-jk_n(z'-z)} + \overleftarrow{\Gamma}_n \overrightarrow{\Gamma}_n\, e^{-2jk_n d_n}\, e^{-jk_n(z'-z)}\Big] \\
&= \frac{1}{2}\Bigg[-e^{-jk_n(z'-z)} - \frac{1}{D_n} \\
&\qquad \Big[\overleftarrow{\Gamma}_n\, e^{2jk_n z_n}\, e^{-jk_n(z'+z)} - \overrightarrow{\Gamma}_n\, e^{-2jk_n z_{n+1}}\, e^{jk_n(z'+z)} \\
&\qquad - \overleftarrow{\Gamma}_n \overrightarrow{\Gamma}_n\, e^{-2jk_n d_n}\, e^{jk_n(z'-z)} + \overleftarrow{\Gamma}_n \overrightarrow{\Gamma}_n\, e^{-2jk_n d_n}\, e^{-jk_n(z'-z)}\Big]\Bigg]
\end{aligned}
\tag{C.57}
$$

$\boxed{z' < z < z_{n+1}}$

$$
\begin{aligned}
V_v^2(z) &= V_+^2\, e^{-jk_n z} + V_-^2\, e^{jk_n z} \\
&= -\frac{1}{2D_n}\Big[\overleftarrow{\Gamma}_n\, e^{2jk_n z_n}\, e^{-jk_n(z'+z)} - e^{jk_n(z'-z)} \\
&\quad + \overleftarrow{\Gamma}_n \overrightarrow{\Gamma}_n\, e^{-2jk_n d_n}\, e^{-jk_n(z'-z)} - \overrightarrow{\Gamma}_n\, e^{-2jk_n z_{n+1}}\, e^{jk_n(z'+z)} \\
&\quad - \overleftarrow{\Gamma}_n \overrightarrow{\Gamma}_n\, e^{-2jk_n d_n}\, e^{jk_n(z'-z)} + \overleftarrow{\Gamma}_n \overrightarrow{\Gamma}_n\, e^{-2jk_n d_n}\, e^{jk_n(z'-z)}\Big] \\
&= \frac{1}{2}\Bigg[e^{jk_n(z'-z)} - \frac{1}{D_n} \\
&\qquad \Big[\overleftarrow{\Gamma}_n\, e^{2jk_n z_n}\, e^{-jk_n(z'+z)} - \overrightarrow{\Gamma}_n\, e^{-2jk_n z_{n+1}}\, e^{jk_n(z'+z)} \\
&\qquad - \overleftarrow{\Gamma}_n \overrightarrow{\Gamma}_n\, e^{-2jk_n d_n}\, e^{jk_n(z'-z)} + \overleftarrow{\Gamma}_n \overrightarrow{\Gamma}_n\, e^{-2jk_n d_n}\, e^{-jk_n(z'-z)}\Big]\Bigg].
\end{aligned}
\tag{C.58}
$$

By merging the two equations we obtain

$$
\begin{aligned}
V_v(z|z') = \frac{1}{2}\Bigg[&\pm e^{-jk_n|z'-z|} - \frac{1}{D_n} \\
&\Big[\overleftarrow{\Gamma}_n\, e^{2jk_n z_n}\, e^{-jk_n(z'+z)} - \overrightarrow{\Gamma}_n\, e^{-2jk_n z_{n+1}}\, e^{jk_n(z'+z)}
\end{aligned}
$$

$$-\overleftarrow{\Gamma}_n \overrightarrow{\Gamma}_n \, e^{-2jk_n d_n} \, e^{jk_n(z'-z)} + \overleftarrow{\Gamma}_n \overrightarrow{\Gamma}_n \, e^{-2jk_n d_n} \, e^{-jk_n(z'-z)}\Big]\Big] \qquad z \gtrless z' \quad \text{(C.59)}$$

C.3.4 $I_v(z|z')\,, \quad m = n$

From equations (C.26), (C.53)–(C.56) we can express the current in the two regions

$\boxed{z_n < z < z'}$

$$\begin{aligned}
I_v^1(z) &= Y_n \left(V_+^1 \, e^{-jk_n z} - V_-^1 \, e^{jk_n z}\right) \\
&= Y_n \left[\frac{\overleftarrow{\Gamma}_n \, e^{2jk_n z_n} \, e^{-jk_n(z'+z)} - \overleftarrow{\Gamma}_n \overrightarrow{\Gamma}_n \, e^{-2jk_n d_n} \, e^{jk_n(z'-z)}}{-2D_n}\right. \\
&\quad \left. - \frac{e^{-jk_n(z'-z)} - \overrightarrow{\Gamma}_n \, e^{-2jk_n z_{n+1}} \, e^{jk_n(z'+z)}}{-2D_n}\right] \\
&= -\frac{Y_n}{2D_n}\Big[\overleftarrow{\Gamma}_n \, e^{2jk_n z_n} \, e^{-jk_n(z'+z)} + \overrightarrow{\Gamma}_n \, e^{-2jk_n z_{n+1}} \, e^{jk_n(z'+z)} \\
&\quad - e^{-jk_n(z'-z)} - \overleftarrow{\Gamma}_n \overrightarrow{\Gamma}_n \, e^{-2jk_n d_n} \, e^{jk_n(z'-z)} \\
&\quad - \overleftarrow{\Gamma}_n \overrightarrow{\Gamma}_n \, e^{-2jk_n d_n} \, e^{-jk_n(z'-z)} + \overleftarrow{\Gamma}_n \overrightarrow{\Gamma}_n \, e^{-2jk_n d_n} \, e^{-jk_n(z'-z)}\Big] \\
&= \frac{Y_n}{2}\Big[e^{-jk_n(z'-z)} - \frac{1}{D_n} \\
&\qquad \Big[\overleftarrow{\Gamma}_n \, e^{2jk_n z_n} \, e^{-jk_n(z'+z)} + \overrightarrow{\Gamma}_n \, e^{-2jk_n z_{n+1}} \, e^{jk_n(z'+z)} \\
&\qquad - \overleftarrow{\Gamma}_n \overrightarrow{\Gamma}_n \, e^{-2jk_n d_n} \, e^{jk_n(z'-z)} - \overleftarrow{\Gamma}_n \overrightarrow{\Gamma}_n \, e^{-2jk_n d_n} \, e^{-jk_n(z'-z)}\Big]\Big]
\end{aligned} \quad \text{(C.60)}$$

$\boxed{z' < z < z_{n+1}}$

$$
\begin{aligned}
I_v^2(z) &= Y_n \left(V_+^2\, e^{-jk_n z} - V_-^2\, e^{jk_n z}\right) \\
&= -\frac{Y_n}{2D_n}\Big[\overleftarrow{\Gamma}_n\, e^{2jk_n z_n}\, e^{-jk_n(z'+z)} - e^{jk_n(z'-z)} \\
&\quad - \overleftarrow{\Gamma}_n \overrightarrow{\Gamma}_n\, e^{-2jk_n d_n}\, e^{-jk_n(z'-z)} + \overrightarrow{\Gamma}_n\, e^{-2jk_n z_{n+1}}\, e^{jk_n(z'+z)} \\
&\quad - \overleftarrow{\Gamma}_n \overrightarrow{\Gamma}_n\, e^{-2jk_n d_n}\, e^{jk_n(z'-z)} + \overleftarrow{\Gamma}_n \overrightarrow{\Gamma}_n\, e^{-2jk_n d_n}\, e^{jk_n(z'-z)}\Big] \\
&= \frac{Y_n}{2}\Bigg[e^{jk_n(z'-z)} - \frac{1}{D_n} \\
&\qquad \Big[\overleftarrow{\Gamma}_n\, e^{2jk_n z_n}\, e^{-jk_n(z'+z)} + \overrightarrow{\Gamma}_n\, e^{-2jk_n z_{n+1}}\, e^{jk_n(z'+z)} \\
&\qquad - \overleftarrow{\Gamma}_n \overrightarrow{\Gamma}_n\, e^{-2jk_n d_n}\, e^{jk_n(z'-z)} - \overleftarrow{\Gamma}_n \overrightarrow{\Gamma}_n\, e^{-2jk_n d_n}\, e^{-jk_n(z'-z)}\Big]\Bigg]
\end{aligned}
\tag{C.61}
$$

By merging the two equations we obtain

$$
\begin{aligned}
I_v(z|z') = \frac{Y_n}{2}\Bigg[&e^{-jk_n|z'-z|} - \frac{1}{D_n} \\
&\Big[\overleftarrow{\Gamma}_n\, e^{2jk_n z_n}\, e^{-jk_n(z'+z)} + \overrightarrow{\Gamma}_n\, e^{-2jk_n z_{n+1}}\, e^{jk_n(z'+z)} \\
&- \overleftarrow{\Gamma}_n \overrightarrow{\Gamma}_n\, e^{-2jk_n d_n}\, e^{jk_n(z'-z)} - \overleftarrow{\Gamma}_n \overrightarrow{\Gamma}_n\, e^{-2jk_n d_n}\, e^{-jk_n(z'-z)}\Big]\Bigg].
\end{aligned}
\tag{C.62}
$$

C.3.5 $V_i(z|z')$ $I_i(z|z')$ $m < n$

Let us first find the transfer function relating $V(z_{q-1})$ to $V(z_q)$. In the $q-1$ layer of the transmission-line system, we have that

$$
V(z_{q-1}) = V_+^{q-1}\, e^{-jk_{q-1}z_{q-1}} + V_-^{q-1}\, e^{jk_{q-1}z_{q-1}} \tag{C.63}
$$

and

$$
\overleftarrow{\Gamma}_{q-1} \triangleq \frac{V_+^{q-1}}{V_-^{q-1}}\, e^{-2jk_{q-1}z_{q-1}}. \tag{C.64}
$$

So we have

$$
\begin{aligned}
V(z_{q-1}) &= V_+^{q-1}\, e^{-jk_{q-1}z_{q-1}} + \frac{V_+^{q-1}}{\overleftarrow{\Gamma}_{q-1}}\, e^{-jk_{q-1}z_{q-1}} \\
&= V_+^{q-1}\, e^{-jk_{q-1}z_{q-1}} \left(1 + \frac{1}{\overleftarrow{\Gamma}_{q-1}}\right)
\end{aligned}
\tag{C.65}
$$

$$
\Longrightarrow \quad V_+^{q-1} = V(z_{q-1})\; e^{jk_{q-1}z_{q-1}} \frac{\overleftarrow{\Gamma}_{q-1}}{1 + \overleftarrow{\Gamma}_{q-1}} \tag{C.66}
$$

$$\Longrightarrow \quad V_-^{q-1} = V(z_{q-1})\ e^{-jk_{q-1}z_{q-1}} \frac{1}{1+\overleftarrow{\Gamma}_{q-1}} \tag{C.67}$$

But we also have that

$$\begin{aligned} V(z_q) &= V_+^{q-1}\ e^{-jk_{q-1}z_q} + V_-^{q-1}\ e^{jk_{q-1}z_q} \\ &= \frac{V(z_{q-1})}{1+\overleftarrow{\Gamma}_{q-1}} \left[e^{-jk_{q-1}d_{q-1}} \overleftarrow{\Gamma}_{q-1} + e^{jk_{q-1}d_{q-1}} \right]. \end{aligned} \tag{C.68}$$

We thus finally obtain

$$\frac{V(z_{q-1})}{V(z_q)} = \overleftarrow{T}_{q-1} = \frac{\left(1+\overleftarrow{\Gamma}_{q-1}\right)\ e^{-jk_{q-1}d_{q-1}}}{1+\overleftarrow{\Gamma}_{q-1}\ e^{-2jk_{q-1}d_{q-1}}}. \tag{C.69}$$

We have the transfer function relating the ends of two transmission-line sections. Now we wish to find the transfer function relating one end of a section z_{m+1} and an arbitrary point z in that section m. We already know from (C.66) and (C.67) that

$$V_+^m = V(z_m)\ e^{jk_m z_m} \frac{\overleftarrow{\Gamma}_m}{1+\overleftarrow{\Gamma}_m} \tag{C.70}$$

$$V_-^m = V(z_m)\ e^{-jk_m z_m} \frac{1}{1+\overleftarrow{\Gamma}_m}. \tag{C.71}$$

But

$$\begin{aligned} V^m(z) &= V_+^m\ e^{-jk_m z} + V_-^m\ e^{jk_m z} \\ &= \frac{V(z_m)}{1+\overleftarrow{\Gamma}_m} \left[e^{jk_m z_m}\ e^{-jk_m z} \overleftarrow{\Gamma}_m + e^{-jk_m z_m}\ e^{jk_m z} \right] \\ &= V(z_{m+1}) \frac{\left(1+\overleftarrow{\Gamma}_m\right)\ e^{-jk_m d_m}}{1+\overleftarrow{\Gamma}_m\ e^{-2jk_m d_m}} \quad \frac{e^{-jk_m(z_m-z)}}{1+\overleftarrow{\Gamma}_m} \left[e^{-2jk_m(z-z_m)} \overleftarrow{\Gamma}_m + 1 \right] \\ &= V(z_{m+1}) \frac{e^{-jk_m(d_m+z_m-z)}}{1+\overleftarrow{\Gamma}_m\ e^{-2jk_m d_m}} \left[1+\overleftarrow{\Gamma}_m\ e^{-2jk_m(z-z_m)} \right] \\ &= V(z_{m+1}) \frac{e^{-jk_m(z_{m+1}-z)}}{1+\overleftarrow{\Gamma}_m\ e^{-2jk_m d_m}} \left[1+\overleftarrow{\Gamma}_m\ e^{-2jk_m(z-z_m)} \right] \end{aligned} \tag{C.72}$$

which is the same as [27].

The total transfer function from the left end of section n to a point z in

section m with $m < n$ is therefore given by :

$$\begin{aligned} V^m(z) &= \prod_{q=m+1}^{n-1} \frac{V(z_q)}{V(z_{q+1})} \quad \frac{V^m(z)}{V(z_{m+1})} \\ &= \prod_{q=m+1}^{n-1} \overleftarrow{T}_q \quad \frac{e^{-jk_m(z_{m+1}-z)}}{1+\overleftarrow{\Gamma}_m\, e^{-2jk_m d_m}} \left[1+\overleftarrow{\Gamma}_m\, e^{-2jk_m(z-z_m)}\right]. \end{aligned} \tag{C.73}$$

Therefore we finally have

$$V_i(z|z') = V_i(z_n|z') \prod_{q=m+1}^{n-1} \overleftarrow{T}_q \frac{e^{-jk_m(z_{m+1}-z)}}{1+\overleftarrow{\Gamma}_m\, e^{-2jk_m d_m}} \left[1+\overleftarrow{\Gamma}_m\, e^{-2jk_m(z-z_m)}\right]. \tag{C.74}$$

Proceeding the same way for $I_i(z|z')$, we can find :

$$I_i(z|z') = V_i(z_n|z') \prod_{q=m+1}^{n-1} \overleftarrow{T}_q \frac{e^{-jk_m(z_{m+1}-z)}}{1+\overleftarrow{\Gamma}_m\, e^{-2jk_m d_m}} (-Y_m) \left[1-\overleftarrow{\Gamma}_m\, e^{-2jk_m(z-z_m)}\right]. \tag{C.75}$$

To end this section, note that the transfer functions are also valid for $V_v(z|z')$ and $I_v(z|z')$.

C.3.6 $I_i(z|z')$ $V_v(z|z')$ $I_v(z|z')$ $m = n$. Alternative method

We know from article [27] that

$$\begin{aligned} \frac{dV_i}{dz} &= -jk_z Z I_i \\ \frac{dI_i}{dz} &= -jk_z Y V_i + \delta(z-z') \\ \frac{dV_v}{dz} &= -jk_z Z I_v + \delta(z-z') \\ \frac{dI_v}{dz} &= -jk_z Y V_v \end{aligned}$$

and that the following reciprocity properties are met

$$\begin{aligned} V_i(z|z') &= V_i(z'|z) \\ I_v(z|z') &= I_v(z'|z) \\ V_v(z|z') &= -I_i(z'|z) \\ I_i(z|z') &= -V_v(z'|z)\,. \end{aligned}$$

We find for $I_i(z|z')$:

$$I_i(z|z') = \frac{1}{2}\left[\pm e^{-jk_n|z-z'|} + \frac{1}{\left(1-\overleftarrow{\Gamma}_n\overrightarrow{\Gamma}_n\, e^{-2jk_nd_n}\right)}\right.$$
$$\left[\overleftarrow{\Gamma}_n\, e^{2jk_nz_n}\, e^{-jk_n\left(z'+z\right)} - \overrightarrow{\Gamma}_n\, e^{-2jk_nz_{n+1}}\, e^{jk_n\left(z'+z\right)}\right.$$
$$\left.\left.+\overleftarrow{\Gamma}_n\overrightarrow{\Gamma}_n\, e^{-2jk_nd_n}\, e^{-jk_n\left(z-z'\right)} - \overleftarrow{\Gamma}_n\overrightarrow{\Gamma}_n\, e^{-2jk_nd_n}\, e^{jk_n\left(z-z'\right)}\right] \quad z\underset{<}{>}z' \tag{C.76}$$

so

$$-I_i(z'|z) = -\frac{1}{2}\left[\pm e^{-jk_n|z-z'|} + \frac{1}{\left(1-\overleftarrow{\Gamma}_n\overrightarrow{\Gamma}_n\, e^{-2jk_nd_n}\right)}\right.$$
$$\left[\overleftarrow{\Gamma}_n\, e^{2jk_nz_n}\, e^{-jk_n\left(z'+z\right)} - \overrightarrow{\Gamma}_n\, e^{-2jk_nz_{n+1}}\, e^{jk_n\left(z'+z\right)}\right.$$
$$\left.\left.+\overleftarrow{\Gamma}_n\overrightarrow{\Gamma}_n\, e^{-2jk_nd_n}\, e^{-jk_n\left(z'-z\right)} - \overleftarrow{\Gamma}_n\overrightarrow{\Gamma}_n\, e^{-2jk_nd_n}\, e^{jk_n\left(z'-z\right)}\right] \quad z'\underset{<}{>}z \tag{C.77}$$

where z and z' have been interchanged, and which is equivalent to

$$-I_i(z'|z) = \frac{1}{2}\left[\mp e^{-jk_n|z-z'|} - \frac{1}{\left(1-\overleftarrow{\Gamma}_n\overrightarrow{\Gamma}_n\, e^{-2jk_nd_n}\right)}\right.$$
$$\left[\overleftarrow{\Gamma}_n\, e^{2jk_nz_n}\, e^{-jk_n\left(z'+z\right)} - \overrightarrow{\Gamma}_n\, e^{-2jk_nz_{n+1}}\, e^{jk_n\left(z'+z\right)}\right.$$
$$\left.\left.+\overleftarrow{\Gamma}_n\overrightarrow{\Gamma}_n\, e^{-2jk_nd_n}\, e^{-jk_n\left(z'-z\right)} - \overleftarrow{\Gamma}_n\overrightarrow{\Gamma}_n\, e^{-2jk_nd_n}\, e^{jk_n\left(z'-z\right)}\right] \quad z\underset{>}{<}z' \tag{C.78}$$

therefore

$$V_v(z|z') = \frac{1}{2}\left[\pm e^{-jk_n|z-z'|} - \frac{1}{\left(1-\overleftarrow{\Gamma}_n\overrightarrow{\Gamma}_n\, e^{-2jk_nd_n}\right)}\right.$$
$$\left[\overleftarrow{\Gamma}_n\, e^{2jk_nz_n}\, e^{-jk_n\left(z'+z\right)} - \overrightarrow{\Gamma}_n\, e^{-2jk_nz_{n+1}}\, e^{jk_n\left(z'+z\right)}\right.$$
$$\left.\left.+\overleftarrow{\Gamma}_n\overrightarrow{\Gamma}_n\, e^{-2jk_nd_n}\, e^{-jk_n\left(z'-z\right)} - \overleftarrow{\Gamma}_n\overrightarrow{\Gamma}_n\, e^{-2jk_nd_n}\, e^{jk_n\left(z'-z\right)}\right] \quad z\underset{<}{>}z'. \tag{C.79}$$

C.3.7 $I_i(z|z')$ $V_v(z|z')$ $I_v(z|z')$ $m < n$. Alternative method

Let us calculate $\frac{dV_i}{dz}$ from equation (C.74).

$$\begin{aligned}\frac{dV_i(z|z')}{dz} =& \frac{V_i(z_n|z')}{1+\overleftarrow{\Gamma}_m\, e^{-2jk_m d_m}} \prod_{q=m+1}^{n-1} \overleftarrow{T}_q \\ & \Big[jk_m e^{-jk_m(z_{m+1}-z)}\left(1+\overleftarrow{\Gamma}_m\, e^{-2jk_m(z-z_m)}\right) \\ & + e^{-jk_m(z_{m+1}-z)}\overleftarrow{\Gamma}_m\,(-2jk_m)\, e^{-2jk_m(z-z_m)}\Big] \\ =& \frac{V_i(z_n|z')}{1+\overleftarrow{\Gamma}_m\, e^{-2jk_m d_m}} \prod_{q=m+1}^{n-1} \overleftarrow{T}_q\, jk_m\, e^{-jk_m(z_{m+1}-z)}\left(1-\overleftarrow{\Gamma}_m\, e^{-2jk_m d_m}\right) \\ =& -jk_m Z_m I_i(z|z')\end{aligned} \tag{C.80}$$

where the last equality is found by comparison to equation (C.75).

C.4 Derivations of the TLGFs with respect to z'

For the derivation of the integral equations it is necessary to derive the TLGFs with respect to z'. This is the subject of this section.

C.4.1 $m = n$

We know that (section C.3.6)

$$\frac{dV_i(z|z')}{dz} = -jk_n Z_n I_i(z|z')\,.$$

By interchanging z and z' this equation becomes

$$\frac{dV_i(z'|z)}{dz'} = -jk_n Z_n I_i(z'|z)\,.$$

Taking into account the fact that $V_i(z|z') = V_i(z'|z)$ we finally get

$$\frac{dV_i(z|z')}{dz'} = -jk_n Z_n I_i(z'|z) = jk_n Z_n V_v(z|z') \tag{C.81}$$

Let us do the same thing for $V_v(z|z')$, by writing

$$\frac{dI_i(z|z')}{dz} = -jk_n Y_n V_i(z|z') + \delta(z-z')\,.$$

Interchanging z and z', we write :

$$\frac{dI_i(z'|z)}{dz'} = -jk_nY_nV_i(z'|z) + \delta(z'-z)$$

or

$$-\frac{dV_v(z|z')}{dz'} = -jk_nY_nV_i(z|z') + \delta(z-z')\,. \tag{C.82}$$

We can also find

$$\frac{dI_v(z|z')}{dz'} = jk_nY_nI_i(z|z') \tag{C.83}$$

$$-\frac{dI_i(z|z')}{dz'} = -jk_nZ_nI_v(z|z') + \delta(z-z')\,. \tag{C.84}$$

C.4.2 $m < n$

With the results of the preceding section, the derivations are straightforward:

$$\begin{aligned}\frac{dV_i(z|z')}{dz'} &= \frac{dV_i(z_n|z')}{dz'}\prod_{q=m+1}^{n-1}\overleftarrow{T}_q\,\frac{e^{-jk_m(z_{m+1}-z)}}{1+\overleftarrow{\Gamma}_m\,e^{-2jk_md_m}}\left[1+\overleftarrow{\Gamma}_m\,e^{-2jk_m(z-z_m)}\right]\\ &= jk_nZ_nV_v(z_n|z')\prod_{q=m+1}^{n-1}\overleftarrow{T}_q\,\frac{e^{-jk_m(z_{m+1}-z)}}{1+\overleftarrow{\Gamma}_m\,e^{-2jk_md_m}}\left[1+\overleftarrow{\Gamma}_m\,e^{-2jk_m(z-z_m)}\right]\end{aligned} \tag{C.85}$$

$$\frac{dV_v(z|z')}{dz'} = \big(jk_nY_nV_i(z_n|z') - \delta(z_n-z')\big)\overleftarrow{T}(z\leftarrow z_n) \tag{C.86}$$

$$\frac{dI_v(z|z')}{dz'} = jk_nY_nI_i(z_n|z')\,\overleftarrow{T}(z\leftarrow z_n) \tag{C.87}$$

$$\frac{dI_i(z|z')}{dz'} = \big(jk_nZ_nI_v(z_n|z') - \delta(z_n-z')\big)\overleftarrow{T}(z\leftarrow z_n) \tag{C.88}$$

where

$$\overleftarrow{T}(z\leftarrow z_n) = \prod_{q=m+1}^{n-1}\overleftarrow{T}_q\,\frac{e^{-jk_m(z_{m+1}-z)}}{1+\overleftarrow{\Gamma}_m\,e^{-2jk_md_m}}\left[1+\overleftarrow{\Gamma}_m\,e^{-2jk_m(z-z_m)}\right].$$

C.5 Continuity of $V_i(z|z')$

This part, although quite tedious, is necessary in order to extract useful features of formulation A and B. The purpose is to demonstrate that $V_i(z|z')$ is continuous with respect to z and z' or, in equation :

$$V_i^{m,n}(z_m\leftarrow z|z') = V_i^{m-1,n}(z\rightarrow z_m|z')$$
$$V_i^{m,n}(z|z_n\leftarrow z') = V_i^{m,n-1}(z|z'\rightarrow z_n)$$

This is done in the next two sections. We assume that $m < n$.

C.6 Continuity with respect to z

This demonstration is rather straightforward. It is easy to show, with the help of equation (C.74) that in order to prove

$$V_i^{m,n}(z_m \leftarrow z|z') = V_i^{m-1,n}(z \rightarrow z_m|z') \tag{C.89}$$

we have to prove that

$$\frac{e^{-jk_m(z_{m+1}-z)}}{1+\overleftarrow{\Gamma}_m\, e^{-2jk_m d_m}}\left[1+\overleftarrow{\Gamma}_m\, e^{-2jk_m(z-z_m)}\right]\Bigg|_{z_m\leftarrow z} =$$
$$\overleftarrow{T}_m\frac{e^{-jk_{m-1}(z_m-z)}}{1+\overleftarrow{\Gamma}_{m-1}\, e^{-2jk_{m-1}d_{m-1}}}\left[1+\overleftarrow{\Gamma}_{m-1}\, e^{-2jk_{m-1}(z-z_{m-1})}\right]\Bigg|_{z\rightarrow z_m} \tag{C.90}$$

or

$$\frac{e^{-jk_m d_m}}{1+\overleftarrow{\Gamma}_m\, e^{-2jk_m d_m}}\left[1+\overleftarrow{\Gamma}_m\right]$$
$$=$$
$$\frac{\left(1+\overleftarrow{\Gamma}_m\right)e^{-jk_m d_m}}{1+\overleftarrow{\Gamma}_m\, e^{-2jk_m d_m}}\,\frac{1}{1+\overleftarrow{\Gamma}_{m-1}\, e^{-2jk_{m-1}d_{m-1}}}\left[1+\overleftarrow{\Gamma}_{m-1}\, e^{-2jk_{m-1}d_{m-1}}\right] \tag{C.91}$$

which is immediate.

C.7 Continuity with respect to z'

The problem is schematically represented figure C.3. It is easy to show, with the help of equation (C.74) that in order to prove

$$V_i^{m,n}(z|z_n \leftarrow z') = V_i^{m,n-1}(z|z' \rightarrow z_n) \tag{C.92}$$

we have to prove that

$$Z_n\frac{\overbrace{1+\overleftarrow{\Gamma}_n+\overrightarrow{\Gamma}_n\, e^{-2jk_n d_n}+\overleftarrow{\Gamma}_n\overrightarrow{\Gamma}_n\, e^{-2jk_n d_n}}^{[1]}}{\underbrace{D_n}_{[2]}}\,\frac{1+\overleftarrow{\Gamma}_{n-1}}{1+\overleftarrow{\Gamma}_{n-1}\, e^{-2jk_{n-1}d_{n-1}}}$$
$$= Z_{n-1}\frac{\overbrace{1+\overleftarrow{\Gamma}_{n-1}+\overrightarrow{\Gamma}_{n-1}+\overleftarrow{\Gamma}_{n-1}\overrightarrow{\Gamma}_{n-1}}^{[3]}}{\underbrace{D_{n-1}}_{[4]}}. \tag{C.93}$$

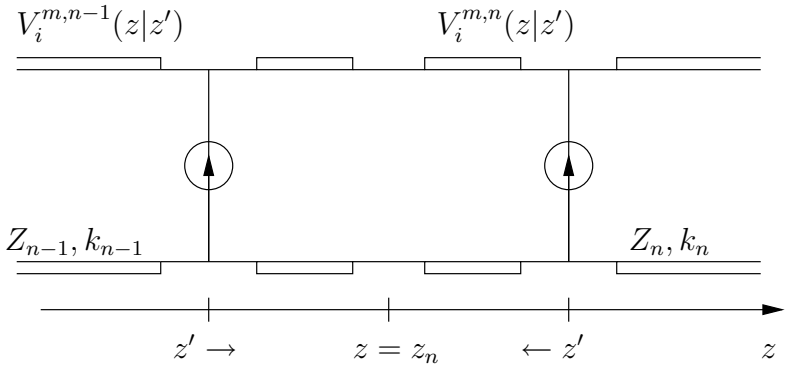

Figure C.3: Current source in two adjacent layers.

In order to do this, we are going to calculate each term of the above equation separately, after having replaced

$$\overleftarrow{\Gamma}_n \quad \text{by} \quad \frac{Z_{n-1} - Z_n + (Z_{n-1} + Z_n)\,\overleftarrow{\Gamma}_{n-1}\,e^{-2jk_{n-1}d_{n-1}}}{Z_{n-1} + Z_n + (Z_{n-1} - Z_n)\,\overleftarrow{\Gamma}_{n-1}\,e^{-2jk_{n-1}d_{n-1}}}$$

and

$$\overrightarrow{\Gamma}_{n-1} \quad \text{by} \quad \frac{Z_n - Z_{n-1} + (Z_n + Z_{n-1})\,\overrightarrow{\Gamma}_n\,e^{-2jk_n d_n}}{Z_n + Z_{n-1} + (Z_n - Z_{n-1})\,\overrightarrow{\Gamma}_n\,e^{-2jk_n d_n}}$$

following their definition given in [27].

C.7.1 Term [1]

We have

$$[1] = \frac{Z_{n-1} + Z_n + (Z_{n-1} - Z_n)\,\overleftarrow{\Gamma}_{n-1}\,e^{-2jk_{n-1}d_{n-1}} + \ldots}{\ldots + Z_{n-1} - Z_n + (Z_{n-1} + Z_n)\,\overleftarrow{\Gamma}_{n-1}\,e^{-2jk_{n-1}d_{n-1}} + \ldots}$$

$$\frac{\ldots + \left[Z_{n-1} + Z_n + (Z_{n-1} - Z_n)\,\overleftarrow{\Gamma}_{n-1}\,e^{-2jk_{n-1}d_{n-1}}\right]\overrightarrow{\Gamma}_n\,e^{-2jk_n d_n} + \ldots}{\ldots + \left[Z_{n-1} - Z_n + (Z_{n-1} + Z_n)\,\overleftarrow{\Gamma}_{n-1}\,e^{-2jk_{n-1}d_{n-1}}\right]\overrightarrow{\Gamma}_n\,e^{-2jk_n d_n}}$$

$$\left[Z_{n-1} + Z_n + (Z_{n-1} - Z_n)\,\overleftarrow{\Gamma}_{n-1}\,e^{-2jk_{n-1}d_{n-1}}\right]$$

the denominator being under the whole fraction bar.

Simplifying this long expression, we find

$$[1] = 2Z_{n-1}\frac{\left(1+\overleftarrow{\Gamma}_{n-1}\,e^{-2jk_{n-1}d_{n-1}}\right)\left(1+\overrightarrow{\Gamma}_{n}\,e^{-2jk_{n}d_{n}}\right)}{Z_{n-1}+Z_n+(Z_{n-1}-Z_n)\,\overleftarrow{\Gamma}_{n-1}\,e^{-2jk_{n-1}d_{n-1}}}. \tag{C.94}$$

C.7.2 Term [2]

$$\begin{aligned}
D_n &= 1-\overleftarrow{\Gamma}_n\overrightarrow{\Gamma}_n\,e^{-2jk_nd_n}\\
&= \frac{Z_{n-1}+Z_n+(Z_{n-1}-Z_n)\,\overleftarrow{\Gamma}_{n-1}\,e^{-2jk_{n-1}d_{n-1}}-Z_{n-1}\overrightarrow{\Gamma}_n\,e^{-2jk_nd_n}+\dots}{\dots+Z_n\overrightarrow{\Gamma}_n\,e^{-2jk_nd_n}-(Z_{n-1}+Z_n)\,\overleftarrow{\Gamma}_{n-1}\,e^{-2jk_{n-1}d_{n-1}}\overrightarrow{\Gamma}_n\,e^{-2jk_nd_n}}\\
&\qquad\qquad Z_{n-1}+Z_n+(Z_{n-1}-Z_n)\,\overleftarrow{\Gamma}_{n-1}\,e^{-2jk_{n-1}d_{n-1}}\\
&= \frac{Z_{n-1}\left(1-\overrightarrow{\Gamma}_n\,e^{-2jk_nd_n}\right)+Z_n\left(1+\overrightarrow{\Gamma}_n\,e^{-2jk_nd_n}\right)\dots}{\dots+Z_{n-1}\overleftarrow{\Gamma}_{n-1}\,e^{-2jk_{n-1}d_{n-1}}\left(1-\overrightarrow{\Gamma}_n\,e^{-2jk_nd_n}\right)\dots}\\
&\qquad\qquad \frac{\dots-Z_n\overleftarrow{\Gamma}_{n-1}\,e^{-2jk_{n-1}d_{n-1}}\left(1+\overrightarrow{\Gamma}_n\,e^{-2jk_nd_n}\right)}{Z_{n-1}+Z_n+(Z_{n-1}-Z_n)\,\overleftarrow{\Gamma}_{n-1}\,e^{-2jk_{n-1}d_{n-1}}}\\
&= \frac{Z_{n-1}\left(1+\overleftarrow{\Gamma}_{n-1}\,e^{-2jk_{n-1}d_{n-1}}\right)\left(1-\overrightarrow{\Gamma}_n\,e^{-2jk_nd_n}\right)\dots}{\dots+Z_n\left(1-\overleftarrow{\Gamma}_{n-1}\,e^{-2jk_{n-1}d_{n-1}}\right)\left(1+\overrightarrow{\Gamma}_n\,e^{-2jk_nd_n}\right)}.\\
&\qquad\qquad Z_{n-1}+Z_n+(Z_{n-1}-Z_n)\,\overleftarrow{\Gamma}_{n-1}\,e^{-2jk_{n-1}d_{n-1}}
\end{aligned}$$

We therefore have

$$\frac{[1]}{[2]} = 2Z_{n-1}\frac{\left(1+\overleftarrow{\Gamma}_{n-1}\,e^{-2jk_{n-1}d_{n-1}}\right)\left(1+\overrightarrow{\Gamma}_{n}\,e^{-2jk_{n}d_{n}}\right)}{Z_{n-1}\left(1+\overleftarrow{\Gamma}_{n-1}\,e^{-2jk_{n-1}d_{n-1}}\right)\left(1-\overrightarrow{\Gamma}_{n}\,e^{-2jk_{n}d_{n}}\right)\dots} \tag{C.95}$$
$$\dots+Z_n\left(1-\overleftarrow{\Gamma}_{n-1}\,e^{-2jk_{n-1}d_{n-1}}\right)\left(1+\overrightarrow{\Gamma}_n\,e^{-2jk_nd_n}\right)$$

C.7.3 Term [3]

Proceeding the same way as for term [1], we find :

$$[3] = 2Z_n\frac{\left(1+\overleftarrow{\Gamma}_{n-1}\right)\left(1+\overrightarrow{\Gamma}_{n}\,e^{-2jk_{n}d_{n}}\right)}{Z_n+Z_{n-1}+(Z_n-Z_{n-1})\,\overrightarrow{\Gamma}_n\,e^{-2jk_nd_n}}. \tag{C.96}$$

C.7.4 Term [4]

$$
\begin{aligned}
D_{n-1} &= 1 - \overleftarrow{\Gamma}_{n-1}\overrightarrow{\Gamma}_{n-1} \\
&= \frac{Z_n + Z_{n-1} + (Z_n - Z_{n-1})\,\overrightarrow{\Gamma}_n\, e^{-2jk_nd_n}\dots}{\dots - \left[Z_n - Z_{n-1} + (Z_n + Z_{n-1})\,\overrightarrow{\Gamma}_n\, e^{-2jk_nd_n}\right]\overleftarrow{\Gamma}_{n-1}\, e^{-2jk_{n-1}d_{n-1}}} \\
&\qquad\qquad Z_n + Z_{n-1} + (Z_n - Z_{n-1})\,\overrightarrow{\Gamma}_n\, e^{-2jk_nd_n} \\
&= \frac{Z_n\left(1 - \overleftarrow{\Gamma}_{n-1}\, e^{-2jk_{n-1}d_{n-1}}\right) + Z_{n-1}\left(1+\overleftarrow{\Gamma}_{n-1}\, e^{-2jk_{n-1}d_{n-1}}\right)\cdots}{\dots + Z_n\,\overrightarrow{\Gamma}_n\, e^{-2jk_nd_n}\left(1 - \overleftarrow{\Gamma}_{n-1}\, e^{-2jk_{n-1}d_{n-1}}\right)\dots} \\
&\qquad\qquad \frac{\dots - Z_{n-1}\,\overrightarrow{\Gamma}_n\, e^{-2jk_nd_n}\left(1 + \overleftarrow{\Gamma}_{n-1}\, e^{-2jk_{n-1}d_{n-1}}\right)}{Z_n + Z_{n-1} + (Z_n - Z_{n-1})\,\overrightarrow{\Gamma}_n\, e^{-2jk_nd_n}} \\
&= \frac{Z_{n-1}\left(1 + \overleftarrow{\Gamma}_{n-1}\, e^{-2jk_{n-1}d_{n-1}}\right)\left(1 - \overrightarrow{\Gamma}_n\, e^{-2jk_nd_n}\right)\dots}{\dots + Z_n\left(1 - \overleftarrow{\Gamma}_{n-1}\, e^{-2jk_{n-1}d_{n-1}}\right)\left(1 + \overrightarrow{\Gamma}_n\, e^{-2jk_nd_n}\right)} \\
&\qquad\qquad \frac{}{Z_n + Z_{n-1} + (Z_n - Z_{n-1})\,\overrightarrow{\Gamma}_n\, e^{-2jk_nd_n}}.
\end{aligned}
$$

We therefore have

$$
\begin{aligned}
\frac{[3]}{[4]} = 2Z_n \frac{\left(1 + \overleftarrow{\Gamma}_{n-1}\right)\left(1 + \overrightarrow{\Gamma}_n\, e^{-2jk_nd_n}\right)}{Z_{n-1}\left(1 + \overleftarrow{\Gamma}_{n-1}\, e^{-2jk_{n-1}d_{n-1}}\right)\left(1 - \overrightarrow{\Gamma}_n\, e^{-2jk_nd_n}\right)\dots} \\
\frac{}{\dots + Z_n\left(1 - \overleftarrow{\Gamma}_{n-1}\, e^{-2jk_{n-1}d_{n-1}}\right)\left(1 + \overrightarrow{\Gamma}_n\, e^{-2jk_nd_n}\right)}.
\end{aligned}
\tag{C.97}
$$

It is then easy to see that equation (C.93) is verified, providing the continuity of V_i with respect to z'.

Appendix D

Fourier transforms and Sommerfeld integrals

Since the medium under consideration is homogeneous and of infinite extent in any (transverse to z) plane, the analysis is facilitated by the Fourier transformation of all fields with respect to the transverse coordinate. Hence, we express any scalar field component as $f(\mathbf{r}) \equiv f(\rho, z)$ where $\rho = x\,\hat{\mathbf{x}} + y\,\hat{\mathbf{y}}$ is the projection of $\mathbf{r}$ on the x, y plane. We introduce the Fourier transform pair

$$\begin{aligned} \mathcal{F}\{f(\mathbf{r})\} &\equiv \tilde{f}(\mathbf{k}_\rho, z) \\ &= \iint_{-\infty}^{+\infty} f(\mathbf{r})\, e^{j\mathbf{k}_\rho \cdot \rho}\, dx\, dy \end{aligned} \tag{D.1}$$

$$\begin{aligned} \mathcal{F}^{-1}\left\{\tilde{f}(\mathbf{k}_\rho, z)\right\} &\equiv f(\mathbf{r}) \\ &= \frac{1}{(2\pi)^2} \iint_{-\infty}^{+\infty} \tilde{f}(\mathbf{k}_\rho, z)\, e^{-j\mathbf{k}_\rho \cdot \rho}\, dk_x\, dk_y. \end{aligned} \tag{D.2}$$

Now let us transform definition (D.2). Making the substitutions

$$x = \rho\cos\varphi \quad k_x = k_\rho \cos\xi$$

$$y = \rho\sin\varphi \quad k_y = k_\rho \sin\xi$$

we have

$$\frac{1}{(2\pi)^2}\iint_{-\infty}^{+\infty}\tilde{f}(\mathbf{k}_\rho,z)\,e^{-j\mathbf{k}_\rho\cdot\rho}\,dk_x\,dk_y$$
$$=\frac{1}{2\pi}\int_0^\infty k_\rho\,dk_\rho\,\tilde{f}(\mathbf{k}_\rho,z)\,\frac{1}{2\pi}\int_0^{2\pi}d\xi\;e^{-j\rho k_\rho\cos(\xi-\varphi)}. \quad \text{(D.3)}$$

Let us set $\omega=\xi-\varphi$. We then have

$$f(\mathbf{r})=\frac{1}{2\pi}\int_0^\infty k_\rho\,dk_\rho\,\tilde{f}(\mathbf{k}_\rho,z)\quad\underbrace{\frac{1}{2\pi}\int_{-\varphi}^{2\pi-\varphi}d\omega\;e^{-j\rho k_\rho\cos(\omega)}}_{\text{Bessel function of order 0: } J_0(\mathbf{k}_\rho\rho)}. \quad \text{(D.4)}$$

Next we calculate different transforms that are needed in the main body of this text.

$$\mathcal{F}^{-1}\left\{\frac{k_x}{k_\rho}\tilde{f}(\mathbf{k}_\rho,z)\right\}=\frac{1}{(2\pi)^2}\iint_{-\infty}^{+\infty}\frac{k_x}{k_\rho}\tilde{f}(\mathbf{k}_\rho,z)\,e^{-j\mathbf{k}_\rho\cdot\rho}\,dk_x\,dk_y$$
$$=\frac{1}{2\pi}\int_0^\infty k_\rho\,dk_\rho\,\tilde{f}(\mathbf{k}_\rho,z)\,\frac{1}{2\pi}\int_0^{2\pi}\cos\xi\;e^{-j\rho k_\rho\cos(\xi-\varphi)}\,d\xi$$
$$=\frac{1}{2\pi}\int_0^\infty k_\rho\,dk_\rho\,\tilde{f}(\mathbf{k}_\rho,z)\quad\underbrace{\frac{1}{2\pi}\int_0^{2\pi}\frac{e^{j\xi}+e^{-j\xi}}{2}\;e^{-j\rho k_\rho\cos(\xi-\varphi)}\,d\xi}_{X}.$$
$$\text{(D.5)}$$

Let us take a look at X, defining $\omega = \xi - \varphi$:

$$\begin{aligned}
X &= \frac{1}{2\pi}\int_{-\varphi}^{2\pi-\varphi} \frac{e^{j(\omega+\varphi)} + e^{-j(\omega+\varphi)}}{2}\; e^{-jk_\rho\rho\cos\omega}\, d\omega \\
&= \frac{1}{2}\left[\frac{1}{2\pi}\int_{-\varphi}^{2\pi-\varphi} e^{j\varphi}\; e^{j\omega}\; e^{-jk_\rho\rho\cos\omega}\, d\omega \right. \\
&\qquad \left. + \frac{1}{2\pi}\int_{-\varphi}^{2\pi-\varphi} e^{-j\varphi}\; e^{-j\omega}\; e^{-jk_\rho\rho\cos\omega}\, d\omega\right] \\
&= \frac{1}{2}\left[\frac{1}{2\pi}\; e^{j\varphi}\; e^{j\frac{\pi}{2}} \int_{-\varphi}^{2\pi-\varphi} e^{j\left(\omega-\frac{\pi}{2}\right)}\; e^{-jk_\rho\rho\cos\omega}\, d\omega \right. \\
&\qquad \left. + \frac{1}{2\pi}\; e^{-j\varphi}\; e^{-j\frac{\pi}{2}} \int_{-\varphi}^{2\pi-\varphi} e^{-j\left(\omega-\frac{\pi}{2}\right)}\; e^{-jk_\rho\rho\cos\omega}\, d\omega\right] \\
&= \frac{1}{2}\left[e^{j\varphi}\; e^{j\frac{\pi}{2}} J_{-1}(k_\rho\rho) + e^{-j\varphi}\; e^{-j\frac{\pi}{2}} J_1(k_\rho\rho)\right] \\
&= \frac{1}{2}\left[-e^{j\varphi}\; e^{j\frac{\pi}{2}} + e^{-j\varphi}\; e^{-j\frac{\pi}{2}}\right] \\
&= -j\cos\varphi J_1(k_\rho\rho)\,.
\end{aligned}$$

Thus we have

$$\mathcal{F}^{-1}\left\{\frac{k_x}{k_\rho}\tilde{f}(\mathbf{k}_\rho, z)\right\} = -j\cos\varphi\frac{1}{2\pi}\int_0^\infty \tilde{f}(\mathbf{k}_\rho, z)\, J_1(k_\rho\rho)\, k_\rho\, dk_\rho. \tag{D.6}$$

Following the same method we find

$$\mathcal{F}^{-1}\left\{\frac{k_y}{k_\rho}\tilde{f}(\mathbf{k}_\rho, z)\right\} = -j\sin\varphi\frac{1}{2\pi}\int_0^\infty \tilde{f}(\mathbf{k}_\rho, z)\, J_1(k_\rho\rho)\, k_\rho\, dk_\rho. \tag{D.7}$$

We can also calculate

$$\begin{aligned}
\mathcal{F}^{-1}\left\{\left(\frac{k_x}{k_\rho}\right)^2\tilde{f}(\mathbf{k}_\rho, z)\right\} &= \frac{1}{(2\pi)^2}\iint_{-\infty}^{+\infty}\left(\frac{k_x}{k_\rho}\right)^2\tilde{f}(\mathbf{k}_\rho, z)\; e^{-j\mathbf{k}_\rho\cdot\rho}\, dk_x\, dk_y \\
&= \frac{1}{2\pi}\int_0^\infty k_\rho\, dk_\rho\; \tilde{f}(\mathbf{k}_\rho, z) \\
&\qquad \frac{1}{2\pi}\int_0^{2\pi}\cos^2\xi\; e^{-jk_\rho\rho\cos(\xi-\varphi)}\, d\xi \\
&= \frac{1}{2\pi}\int_0^\infty k_\rho\, dk_\rho\; \tilde{f}(\mathbf{k}_\rho, z) \\
&\qquad \frac{1}{2\pi}\int_0^{2\pi}\frac{(1+\cos 2\xi)}{2}\; e^{-jk_\rho\rho\cos(\xi-\varphi)}\, d\xi.
\end{aligned} \tag{D.8}$$

We already recognize an integral representation of a Bessel function multiplied

by a $\frac{1}{2}$ factor. Let us make the change

$$\frac{1}{4\pi}\int_0^{2\pi}\cos 2\xi\; e^{-jk_\rho\rho\cos(\xi-\varphi)}\;d\xi = \frac{1}{4\pi}\int_{-\varphi}^{2\pi-\varphi}\cos 2\left(\omega+\varphi\right)\; e^{-jk_\rho\rho\cos\omega}\;d\omega$$

then

$$\begin{aligned}
&\frac{1}{4\pi}\int_{-\varphi}^{2\pi-\varphi}\frac{e^{j2(\omega+\varphi)}+e^{-j2(\omega+\varphi)}}{2}\;e^{-jk_\rho\rho\cos\omega}\;d\omega\\
&=\frac{1}{4}\left[\frac{1}{2\pi}\int_{-\varphi}^{2\pi-\varphi}e^{j2\varphi}\;e^{j2\omega}\;e^{-jk_\rho\rho\cos\omega}\;d\omega\right.\\
&\qquad\left.+\frac{1}{2\pi}\int_{-\varphi}^{2\pi-\varphi}e^{-j2\varphi}\;e^{-j2\omega}\;e^{-jk_\rho\rho\cos\omega}\;d\omega\right]\\
&=\frac{1}{4}\left[\frac{1}{2\pi}\;e^{j2\varphi}\;e^{j2\frac{\pi}{2}}\int_{-\varphi}^{2\pi-\varphi}e^{j2\left(\omega-\frac{\pi}{2}\right)}\;e^{-jk_\rho\rho\cos\omega}\,d\omega\right.\\
&\qquad\left.+\frac{1}{2\pi}\;e^{-j2\varphi}\;e^{-j2\frac{\pi}{2}}\int_{-\varphi}^{2\pi-\varphi}e^{-j2\left(\omega-\frac{\pi}{2}\right)}\;e^{-jk_\rho\rho\cos\omega}\,d\omega\right]\\
&=\frac{1}{4}\left[e^{j2\varphi}\;e^{j2\frac{\pi}{2}}J_{-2}(k_\rho\rho)+e^{-j2\varphi}\;e^{-j2\frac{\pi}{2}}J_2(k_\rho\rho)\right]\\
&=-\frac{1}{2}\cos 2\varphi J_2(k_\rho\rho)
\end{aligned}$$

because $J_{-n}(x)=(-1)^n J_n(x)$ [70]. We finally get

$$\begin{aligned}
\mathcal{F}^{-1}\left\{\left(\frac{k_x}{k_\rho}\right)^2\tilde{f}(\mathbf{k}_\rho,z)\right\} &= \frac{1}{4\pi}\int_0^\infty \tilde{f}(\mathbf{k}_\rho,z)\,J_0(k_\rho\rho)\;k_\rho\;dk_\rho\\
&\quad-\cos 2\varphi\frac{1}{4\pi}\int_0^\infty\tilde{f}(\mathbf{k}_\rho,z)\,J_2(k_\rho\rho)\;k_\rho\;dk_\rho. \qquad \text{(D.9)}
\end{aligned}$$

In the same way we can obtain (because $\sin^2\xi=\frac{1-\cos 2\xi}{2}$)

$$\begin{aligned}
\mathcal{F}^{-1}\left\{\left(\frac{k_y}{k_\rho}\right)^2\tilde{f}(\mathbf{k}_\rho,z)\right\} &= \frac{1}{4\pi}\int_0^\infty \tilde{f}(\mathbf{k}_\rho,z)\,J_0(k_\rho\rho)\;k_\rho\;dk_\rho\\
&\quad+\cos 2\varphi\frac{1}{4\pi}\int_0^\infty\tilde{f}(\mathbf{k}_\rho,z)\,J_2(k_\rho\rho)\;k_\rho\;dk_\rho. \qquad \text{(D.10)}
\end{aligned}$$

The last thing we need to examine is

$$\begin{aligned}
\mathcal{F}^{-1}\left\{\frac{k_x k_y}{k_\rho^2}\tilde{f}(\mathbf{k}_\rho,z)\right\} &= \frac{1}{(2\pi)^2}\iint_{-\infty}^{+\infty}\frac{k_x k_y}{k_\rho^2}\tilde{f}(\mathbf{k}_\rho,z)\; e^{-j\mathbf{k}_\rho\cdot\rho}\; dk_x\, dk_y \\
&= \frac{1}{2\pi}\int_0^\infty k_\rho\; dk_\rho\; \tilde{f}(\mathbf{k}_\rho,z) \\
&\quad \frac{1}{2\pi}\int_0^{2\pi}\cos\xi\sin\xi\; e^{-jk_\rho\rho\cos(\xi-\varphi)}\; d\xi \\
&= \frac{1}{2\pi}\int_0^\infty k_\rho\; dk_\rho\; \tilde{f}(\mathbf{k}_\rho,z) \\
&\quad \frac{1}{2\pi}\int_0^{2\pi}\frac{\sin 2\xi}{2}\; e^{-jk_\rho\rho\cos(\xi-\varphi)}\; d\xi \\
&= \frac{1}{2\pi}\int_0^\infty k_\rho\; dk_\rho\; \tilde{f}(\mathbf{k}_\rho,z) \\
&\quad \underbrace{\frac{1}{2\pi}\int_0^{2\pi}\frac{e^{j2\xi}-e^{-j2\xi}}{4j}\; e^{-jk_\rho\rho\cos(\xi-\varphi)}\; d\xi}_{X}\,.
\end{aligned} \tag{D.11}$$

We now develop X, making the change of variable $\omega = \xi - \varphi$:

$$\begin{aligned}
X &= \frac{1}{2\pi}\int_{-\varphi}^{2\pi-\varphi}\frac{e^{j2(\omega+\varphi)}-e^{-j2(\omega+\varphi)}}{4j}\; e^{-jk_\rho\rho\cos\omega}\; d\omega \\
&= \frac{1}{4j}\left[\frac{1}{2\pi}\int_{-\varphi}^{2\pi-\varphi} e^{j2\varphi}\; e^{j2\omega}\; e^{-jk_\rho\rho\cos\omega}\; d\omega\right. \\
&\quad \left. -\frac{1}{2\pi}\int_{-\varphi}^{2\pi-\varphi} e^{-j\varphi}\; e^{-j\omega}\; e^{-jk_\rho\rho\cos\omega}\; d\omega\right] \\
&= \frac{1}{4j}\left[\frac{1}{2\pi}\; e^{j2\varphi}\; e^{j2\frac{\pi}{2}}\int_{-\varphi}^{2\pi-\varphi} e^{j2\left(\omega-\frac{\pi}{2}\right)}\; e^{-jk_\rho\rho\cos\omega}\; d\omega\right. \\
&\quad \left. -\frac{1}{2\pi}\; e^{-j2\varphi}\; e^{-j2\frac{\pi}{2}}\int_{-\varphi}^{2\pi-\varphi} e^{-j2\left(\omega-\frac{\pi}{2}\right)}\; e^{-jk_\rho\rho\cos\omega}\; d\omega\right] \\
&= \frac{1}{4j}\left[e^{j2\varphi}\; e^{j2\frac{\pi}{2}}J_{-2}(k_\rho\rho) - e^{-j2\varphi}\; e^{-j2\frac{\pi}{2}}J_2(k_\rho\rho)\right] \\
&= \frac{1}{4j}\left[e^{j2\varphi}\; e^{j2\frac{\pi}{2}} - e^{-j2\varphi}\; e^{-j2\frac{\pi}{2}}\right]J_2(k_\rho\rho) \\
&= -\frac{1}{2}\sin 2\varphi J_2(k_\rho\rho)
\end{aligned} \tag{D.12}$$

so

$$\mathcal{F}^{-1}\left\{\frac{k_x k_y}{k_\rho^2}\tilde{f}(\mathbf{k}_\rho,z)\right\} = -\sin 2\varphi\frac{1}{4\pi}\int_0^\infty \tilde{f}(\mathbf{k}_\rho,z)\, J_2(k_\rho\rho)\, k_\rho\; dk_\rho. \tag{D.13}$$

Bibliography

[1] The U.S. Department of State. Humanitarian Mine Action: The Landmine Threat and the Response to It. July 2002. `http://www.state.gov/t/pm/rls/fs/`.

[2] M. Acheroy. Mine action: status of sensor technology for close-in and remote detection of anti-personnel mines. In S. Lambot, A. G. Gorriti, editor, *Proceedings of the Third International Workshop on Advanced Ground-Penetrating Radar*, pages 3–13, TU Delft, The Netherlands, May 2005.

[3] B. Scheers. *Ultra-wideband ground penetrating radar with application to the detection of anti personal landmines.* Catholic University of Louvain – Royal Military Academy, Brussels, Belgium, 2001. Ph.D. dissertation.

[4] P. Druyts, L. Merlat, and M. Acheroy. Modeling considerations for imaging with a standard metal detector. In SPIE Press, editor, *Proceedings of DEtection and Remediation Technologies for Mines and Minelike Targets*, pages 1431–1451, Orlando, Florida, USA, April 2000.

[5] D. J. Daniels. *Surface Penetrating Radar.* IEE, London, 1996.

[6] Delft University of Technology. *Proceedings of the second International Workshop on Advanced Ground Penetrating Radar.* The International Research Centre for Telecommunications-Transmissions and Radar (IRCTR), TU Delft, the Netherlands, 2003.

[7] Delft University of Technology. *Proceedings of the Tenth International Conference on Ground Penetrating Radar, Volume I and II.* IEEE, TU Delft, the Netherlands, 2004.

[8] Delft University of Technology. *Proceedings of the third International Workshop on Advanced Ground Penetrating Radar*. IEEE, TU Delft, the Netherlands, 2005.

[9] D. J. Daniels. *Ground Penetrating Radar*. IEE, London, 2004. 2nd edition.

[10] M. T. Hallikainen, F. T. Ulaby, M. C. Dobson, M. A. El-Rayes, and L. K. Wu. Microwave dielectric behavior of wet soil—part I: empirical models and experimental observations. *IEEE Transactions on Geoscience and Remote Sensing*, GE-23:25–34, 1985.

[11] F. T. Ulaby, R. K. Moore, and A. K. Fung. *Microwave remote sensing: active and passive. Fundamentals and Radiometry*, volume 1. Artech House, 1981.

[12] David D. Daniels. Affordable GPR technology. In S. Lambot, A. G. Gorriti, editor, *Proceedings of the Third International Workshop on Advanced Ground-Penetrating Radar*, pages 15–19, TU Delft, The Netherlands, May 2005.

[13] F. L. Teixeira, Weng Cho Chew, M. Straka, M. L. Oristaglio, and T. Wang. Finite-difference time-domain simulation of ground penetrating radar on dispersive, inhomogeneous, and conductive soils. *IEEE Transactions on Geoscience and Remote Sensing*, 36(6):1928–1937, November 1998.

[14] Levent Gürel and Ugur Oguz. Three-dimensional fdtd modeling of a ground-penetrating radar. *IEEE Transactions on Geoscience and Remote Sensing*, 38(4):1190–1197, July 2000.

[15] Levent Gürel and Ugur Oguz. Simulations of ground-penetrating radars over lossy and heterogeneous grounds. *IEEE Transactions on Geoscience and Remote Sensing*, 39(6):1190–1197, June 2001.

[16] Ugur Oguz and Levent Gürel. Frequency responses of ground-penetrating radars operating over highly lossy grounds. *IEEE Transactions on Geoscience and Remote Sensing*, 40(6):1385–1394, June 2002.

[17] Traian Dogaru and Lawrence Carin. Time-domain sensing of targets buried under a rough air-ground interface. *IEEE Transactions on Antennas and Propagation*, 46(3):360–372, March 1998.

[18] Jacqueline M. Bourgeois and Glenn S. Smith. A fully three-dimensional simulation of a ground-penetrating radar: FDTD theory compared with experiment. *IEEE Transactions on Geoscience and Remote Sensing*, 34(1):36–44, January 1996.

[19] Jacqueline M. Bourgeois and Glenn S. Smith. A complete electromagnetic simulation of the separated-aperture sensor for detecting buried land mines. *IEEE Transactions on Antennas and Propagation*, 46(10):1419–1426, October 1998.

[20] Thomas P. Montoya and Glenn S. Smith. Land mine detection using a ground-penetrating radar based on resistively loaded vee dipoles. *IEEE Transactions on Antennas and Propagation*, 47(12):1795–1806, December 1999.

[21] Bo Yang and Carey Rappaport. Response of realistic soil for GPR applications with 2-D FDTD. *IEEE Transactions on Geoscience and Remote Sensing*, 39(6):1198–1205, June 2001.

[22] Krzysztof A. Michalski and Dalian Zheng. Electromagnetic scattering and radiation by surfaces of arbitrary shapes in layered media. *IEEE Transactions on Antennas and Propagation*, 38(3):335–352, March 1990.

[23] Stanislav Vitebskiy, Keith Sturgess, and Lawrence Carin. Short-pulse plane-wave scattering from buried perfectly conducting bodies of revolution. *IEEE Transactions on Antennas and Propagation*, 44(2):143–151, February 1996.

[24] Magda El-Shenawee. Scattering from Multiple Objects Buried Beneath Two-Dimensional Random Rough Surface Using the Steepest Descent Path Method. *IEEE Transactions on Antennas and Propagation*, 51(4):802–809, April 2003.

[25] Anders Sullivan, Raju Damarla, Norbert Geng, Yanting Dong, and Lawrence Carin. Ultrawide-band synthetic aperture radar for detection of unexploded ordnance: Modeling and measurements. *IEEE Transactions on Antennas and Propagation*, 48(9):1306–1315, September 2000.

[26] Lawrence Carin, Jeffrey Sichina, and James F. Harvey. Microwave underground propagation and detection. *IEEE Transactions on Microwave Theory and Techniques*, 50(3):945–952, March 2002.

[27] Krzysztof A. Michalski and Juan R. Mosig. Multilayered media green's functions in integral equation formulations. *IEEE Transactions on Antennas and Propagation*, 45(3):508–519, March 1997.

[28] Christian Bruns, Pascal Leuchtmann, and Rüdiger Vahldieck. Comprehensive analysis and simulation of a 1–18 ghz broadband parabolic reflector horn antenna system. *IEEE Transactions on Antennas and Propagation*, 51(6):1418–1422, June 2003.

[29] I. van den Bosch, S. Lambot, M. Acheroy, I. Huynen, and P. Druyts. Accurate electromagnetic modeling of a monostatic ground-penetrating radar for targets buried in stratified media. *IEEE Transactions on Geoscience and Remote Sensing*, 2005. In Preparation.

[30] I. van den Bosch, P. Druyts, S. Lambot, I. Huynen, and M. Acheroy. Accurate and efficient modeling of monostatic GPR signal of dielectric targets embedded in stratified media. In , editor, *Proceedings of the Progress in Electromagnetics Research Symposium (PIERS)*, pages 251–255, Hangzhou, Zhejiang, China, August 2005.

[31] I. van den Bosch, S. Lambot, and A. Vander Vorst. A new approach for extracting landmine signature from ground penetrating radar signal. In E. Slob, A. Yarovoy, and J. Rhebergen, editors, *Proceedings of the Tenth International Conference on Ground Penetrating Radar*, pages 287–290, TU Delft, the Netherlands, June 2004.

[32] I. van den Bosch, S. Lambot, P. Druyts, I. Huynen, and M. Acheroy. Buried target signature extraction from ground-penetrating radar signal. measurements and simulations. *Near Surface Geophysics (special issue)*, 2005. accepted for publication.

[33] Norbert Geng and Lawrence Carin. Wideband electromagnetic scattering from a dielectric bor buried in a layered lossy, dispersive medium. *IEEE Transactions on Antennas and Propagation*, 47(4):610–619, April 1999.

[34] Neelakantam V. Venkatarayalu, Chi-Chih Chen, Fernando L. Texeira, and Robert Lee. Numerical modeling of ultrawide-band dielectric horn antenna using FDTD. *IEEE Transactions on Antennas and Propagation*, 52(5):1318–1323, May 2004.

[35] Kwan-Ho Lee, Chi-Chih Chen, Fernando L. Texeira, and Robert Lee. Modeling and investigation of a geometrically complex UWB GPR antenna using FDTD. *IEEE Transactions on Antennas and Propagation*, 52(8):1983–1991, August 2004.

[36] Kefeng Liu, Constantine A. Balanis, Craig R. Birtcher, and George C. Barber. Analysis of pyramidal horn antennas using moment methods. *IEEE Transactions on Antennas and Propagation*, 41(10):1379–1389, October 1993.

[37] Arun K. Bhattacharyya and Gordon Zeeman Rollins. Accurate radiation and impedance characteristics of horn antennas—a moment methods model. *IEEE Transactions on Antennas and Propagation*, 44(4):523–531, April 1996.

[38] S. Lambot, E. C. Slob, I. van den Bosch, B. Stockbroeckx, and M. Vanclooster. Modeling of GPR signal for accurate characterization of the subsurface dielectric properties. *IEEE Transactions on Geoscience and Remote Sensing*, 42(11):2555–2568, November 2004.

[39] Constantine A. Balanis. *Antenna Theory: Analysis and Design.* Harper & Row, New York, 1982.

[40] R. E. Collin. *Antennas and Radiowave Propagation.* Electrical Engineering. McGraw-Hill, 1985.

[41] Roger B. Marks and Dylan F. Williams. A General Waveguide Circuit Theory. *Journal of Research of the National Institute of Standards and Technology*, 97(5):533–562, September 1992.

[42] W. C. Chew and J. A. Kong. Electromagnetic field of a dipole on a two-layer earth. *Geophysics*, 46(3):309–315, March 1981.

[43] R. F. Harrington. *Time-Harmonic Electromagnetic Fields.* IEEE, 1961.

[44] Xing Qing Sheng, Jian-Ming Jin, Jiming Song, Weng Cho Chew, and Cai-Cheng Lu. Solution of Combined-Field Integral Equation Using Multilevel Fast Multipole Algorithm for Scattering by Homogeneous Bodies. *IEEE Transactions on Antennas and Propagation*, 46(11):1718–1726, November 1998.

[45] Sadasiva M. Rao, Donald R. Wilton, and Allen W. Glisson. Electromagnetic scattering and radiation by surfaces of arbitrary shapes. *IEEE Transactions on Antennas and Propagation*, 30(3):409–418, May 1982.

[46] Krzysztof A. Michalski. Extrapolation methods for sommerfeld integral tails. *IEEE Transactions on Antennas and Propagation*, 46(10):1405–1418, October 1998.

[47] S. Lambot, E. C. Slob, I. van den Bosch, B. Stockbroeckx, B. Scheers, and M. Vanclooster. Estimating soil electric properties from monostatic ground-penetrating radar signal inversion in the frequency domain. *Water Resources Research*, 40, April 2004. W04205, doi10.1029/2003WR002095.

[48] Weng Cho Chew, Jian-Ming Jin, Eric Michielssen, and Jiming Song. *Fast and Efficient Algorithms in Computational Electromagnetics*. Artech House, Norwood, MA 02062, 2001.

[49] W.-B. Ewe, L.-W. Li, and M.-S. Leong. Solving mixed dielectric/conducting scattering problem using adaptive integral method. *Progress in Electromagnetics Research*, 46:143–163, 2004.

[50] Pasi Ylä-0ijala, Matti Taskinen, and J. Sarvas. Surface integral equation method for general composite metallic and dielectric structures with junctions. *Progress in Electromagnetics Research*, June 2004. Submitted.

[51] Andrew F. Peterson, Scott L. Ray, and Raj Mittra. *Computational Methods for Electromagnetics*. IEEE/OUP Series on Electromagnetic Wave Theory. IEEE Press, New York, 1998.

[52] N. Morita, N. Kumagai, and J. R. Mautz. *Integral Equation Methods for Electromagnetics*. Artech House, Boston, 1990.

[53] A. J. Poggio and E. K. Miller. *Integral equations solutions of three dimensional scattering problems*. Computer Techniques for Electromagnetics. Pergamon, Oxford, U.K., 1973. chapter 4.

[54] Y. Chang and R. F. Harrington. A surface formulation for characteristic modes of material bodies. *IEEE Transactions on Antennas and Propagation*, 25:789–795, 1977.

[55] T. K. Wu and L. L. Tsai. Scattering from arbitrarily-shaped lossy dielectric bodies of revolution. *Radio Science*, 12:709–718, 1977.

[56] R. F. Harrington. *Field Computation by Moment Methods.* MacMillan, New York, 1968.

[57] Pasi Ylä-0ijala and Matti Taskinen. Calculation of cfie impedance matrix elements with rwg and $\hat{\mathbf{n}} \times$ RWG functions. *IEEE Transactions on Antennas and Propagation*, 51(8):1837–1846, August 2003.

[58] Pascal Druyts. *Modeling of Metal Detectors for Humanitarian Demining.* Catholic University of Louvain – Royal Military Academy, Brussels, Belgium. Ph.D. dissertation. In preparation.

[59] Feng Ling and Jian-Ming Jin. Discrete complex image method for green's functions of general multilayer media. *IEEE Microwave and Guided Wave Letters*, 10(10):400–402, October 2000.

[60] Tomasz M. Grzegorczyk and Juan R. Mosig. Full-wave analysis of antennas containing horizontal and vertical metallizations embedded in planar multilayered media. *IEEE Transactions on Antennas and Propagation*, 51(11):3047–3054, November 2003.

[61] Ling Li, Jiangqi He, Zhijun Liu, Xiaolong Dong, and Lawrence Carin. MLFMA analysis of scattering from multiple targets in the presence of a half-space. *IEEE Transactions on Antennas and Propagation*, 51(4):810–819, April 2003.

[62] Christoph Rauscher. *Fundamentals of Spectrum Analysis.* Rohde & Schwarz GmbH & Co. KG, München, Germany, 2002. `www.rohde-schwarz.com`.

[63] I. Huynen, J. Steisel, and B. Stockbroeckx. A simple detection method of buried cylindrical targets applicable to landmines. *Microwave and Optical Technology Letters*, 38(1):80–83, July 2003.

[64] Yong Wang, I. Dennis Longstaff, Christopher J. Leat, and Nicholas V. Shuley. Complex natural resonances of conducting planar objects buried in a dielectric half-space. *IEEE Transactions on Geoscience and Remote Sensing*, 39(6):1183–1189, June 2001.

[65] S. Vitebskiy and L. Carin. Resonance of perfectly conducting wires and bodies of revolution buried in a lossy dispersive half-space. *IEEE Transactions on Antennas and Propagation*, 44:1575–1583, December 1996.

[66] N. Geng, D. R. Jackson, and L. Carin. On the resonances of a dielectric BOR buried in a dispersive layered medium. *IEEE Transactions on Antennas and Propagation*, 47:1305–1313, August 1999.

[67] M. Peichl, S. Dill, and H. Süss. Application of microwave radiometry for buried landmine detection. In *Proceedings of the 2nd International Workshop on Advanced Ground Penetrating Radar*, TU Delft, the Netherlands, May 2003.

[68] D. Firre and A. Goyens. Conception de radiomètres hyperfréquences en vue de la détection de mines antipersonnel. Master's thesis, Microwaves UCL, Louvain-la-Neuve, Belgium, June 2000.

[69] Chen-To Tai. *Dyadic Green Functions in Electromagnetic Theory.* Oxford University Press, 1996.

[70] I. S. Gradshteyn and I. M. Ryzhik. *Tables of Integrals, Series, and Products.* Academic Press, 1980. Corrected and enlarged edition.